



**FIELD OF SCIENCE: Natural sciences**

SCIENTIFIC DISCIPLINE: Physical sciences

## **DOCTORAL THESIS**

*The influence of endogenous and exogenous factors on  
the activity of photosystem II and its heterogeneity*

Author: Sonia Krysiak

First supervisor: prof. dr hab. Květoslava Burda

Second supervisor: prof. dr hab. Nika Spiridis

Completed in: AGH University of Krakow, Faculty of Physics and Applied  
Computer Science, Department of Applied Nuclear Physics

Krakow, 2023



# Declaration of the author

Aware of legal responsibility for making untrue statements I hereby declare that I am the legitimate author of this dissertation and that it is my original work.

---

*date*

*author's signature*

# Declaration of the supervisors

This dissertation is ready to be reviewed.

---

*date*

*1<sup>st</sup> supervisor's signature*

---

*date*

*2<sup>nd</sup> supervisor's signature*



# Acknowledgements

I would like to express my sincere gratitude to all the people who have supported the creation of this dissertation. First and foremost, I am deeply grateful to my supervisor Prof. dr hab. Květoslava Burda for introducing me to the fascinating world of photosynthesis and for many years of guidance.

I would like to especially thank Prof. Gerardo Goya and his group for hosting me on numerous occasions at the Instituto de Nanociencia y Materiales de Aragon, Zaragoza, Spain. I am indebted to Ana Carolina for her help with the TEM measurements.

I would like to express my thank to dr Aleksandra Orzechowska, dr Joanna Fiedor, and dr hab. Renata Szymańska for the friendly atmosphere and valuable tips.

I would like to highlight the importance of my fellow PhD students, many of whom became my friends. My special thanks go to Julek, who often saves me in helpless situations, and to Beata, who supports me a lot. I would like to thank Sławek, Magda, and Mateusz for their support and the time we spent together.

Finally I would like to dedicate this work to my family. You are always there for me. You give me motivation and strength to achieve my goals. Thank you.

This PhD thesis has been completed in the framework of the POWER Program, project No. POWR.03.02.00-00-I004/16, co-financed by the European Union.



Unia Europejska  
Europejski Fundusz Społeczny





# List of publications and achievements

## 1. Publications

Krysiak, S. & Burda, K. (2023). How extrinsic proteins influence heterogeneity of oxygen evolution in tobacco. Under submission.

Krysiak, S., Gotić, M., Madej, E., Moreno Maldonado, A. C., Goya, G. F., Spiridis, N., & Burda, K. (2023). The effect of ultrafine WO<sub>3</sub> nanoparticles on the organization of thylakoids enriched in photosystem II and energy transfer in photosystem II complexes. *Microsc. Res. Tech.*, 1–16. <https://doi.org/10.1002/jemt.24394>.

Jamrozik, A., Przewoznik, J., Krysiak, S., Korecki, J., Trykowski, G., Małolepszy, A., Stobiński, L., Burda, K. (2021). Effect of Grinding and the Mill Type on Magnetic Properties of Carboxylated Multiwall Carbon Nanotubes. *Materials*, 14, 4057. <https://doi.org/10.3390/ma14144057>.

## 2. Conferences

no.	The conference	Place, date	Title of the presentation	The form	Authors
1.	Bioinorganic redox control: international workshop on "Bioinorganic redox control - implications for medicinal chemistry and environmental protection	20-21.04. 2017, Krakow	Heterogeneity of oxygen evolution in photosynthetic process	poster	S. Krysiak, A. Orzechowska, J. Fiedor, R. Szymańska, K. Burda
2.	2 <sup>nd</sup> International Caparica Conference on Pollutant Toxic Ions & Molecules	03-06.11. 2017, Lisbon	Influence of TiO <sub>2</sub> nanoparticles on activity of photosystem II and heterogeneity of oxygen evolution	oral speech - awarded	S. Krysiak, K. Burda
3.	2 <sup>nd</sup> International Caparica Conference on Pollutant Toxic Ions & Molecules	03-06.11. 2017, Lisbon	Influence of TiO <sub>2</sub> nanoparticles on activity of photosystem II and heterogeneity of oxygen evolution	poster	S. Krysiak, K. Burda
4.	First European Congress on Photosynthesis Research, ePS-1	25-28.06. 2018, Uppsala	Influence of TiO <sub>2</sub> nanoparticles on photosystem II activity and heterogeneity of O <sub>2</sub> evolution	poster	S. Krysiak, K. Burda
5.	EBS Workshop on Nuclear Resonance Scattering	11-12.03 2018, Grenoble	Differences in the influence of Cu <sup>2+</sup> and Cd <sup>2+</sup> ions on properties of non-heme iron in reaction centres of type II	poster	S. Krysiak, A. Hałas, A. Orzechowska, A. Chumakov, D. Bessas,

					V. Derrien, P. Sebban, J. Korecki, T. Ślęzak, K. Burda
6.	Sunrise Poland Stakeholder Workshop CeNT UW	05-06.06 2019, Warszawa	Influence of Cd <sup>2+</sup> ions on properties of non-heme iron in bacterial reaction centres of type II	poster	S. Krysiak, A. Hałas, A. Orzechowska, A. Chumakov, D. Bessas, V. Derrien, P. Sebban, J. Korecki, T. Ślęzak, K. Burda
7.	Dokonania naukowe doktorantów: edycja VIII	27-28.04. 2020, Kraków	Badania układów hybrydowych złożonych z tylakoidów izolowanych z roślin wyższych oraz nanocząstek TiO <sub>2</sub>	oral speech - awarded	S. Krysiak, K. Burda
8.	Dokonania naukowe doktorantów: edycja VIII	27-28.04. 2020, Kraków	Wpływ białek zewnętrznych na funkcjonowanie fotosystemu II w procesie fotosyntezy	oral speech	S. Krysiak, K. Burda
9.	Dokonania naukowe doktorantów: edycja VIII	27-28.04. 2020, Kraków	Wpływ jonów Cd <sup>2+</sup> na właściwości żelaza niehemowego (NHFe) w bakteryjnych centrach reakcji typu II	poster	S. Krysiak, A. Hałas, A. Orzechowska, A. Chumakov, D. Bessas, V. Derrien, P. Sebban, J. Korecki, T. Ślęzak, K. Burda
10.	Nowe trendy w badaniach naukowych - streszczenia wystąpień młodych naukowców	20-21.06. 2020, Krakow	Liniiowy transport elektronów pomiędzy chinonami QA i QB w roślinach wyższych	oral speech	S. Krysiak, K. Burda
11.	Nowe trendy w badaniach naukowych - streszczenia wystąpień młodych naukowców	20-21.06. 2020, Krakow	Termoluminescencja w badaniach układów fotosyntetycznych	poster	S. Krysiak, K. Burda
12.	Nowe trendy w badaniach naukowych - streszczenia wystąpień młodych naukowców	20-21.06. 2020, Krakow	Wpływ białek zewnętrznych na funkcjonowanie fotosystemu II w procesie fotosyntezy	oral speech	S. Krysiak, K. Burda

13.	Analiza zagadnień i wyników - streszczenia wystąpień młodych naukowców 3	12-13.06. 2021, Krakow	<i>Układy hybrydowe składające się z fotosystemu II oraz nanocząstek TiO<sub>2</sub> i WO<sub>3</sub></i>	poster	S. Krysiak, K. Burda
14.	Analiza zagadnień i wyników - streszczenia wystąpień młodych naukowców 3	12-13.06. 2021, Krakow	<i>Wpływ nanocząstek TiO<sub>2</sub> i WO<sub>3</sub> na kinetykę transportu elektronów w fotosystemie II</i>	oral speech	S. Krysiak, K. Burda
15.	Analiza zagadnień i wyników - streszczenia wystąpień młodych naukowców 3	12-13.06. 2021, Krakow	Izolowane błony tylakoidów do pomiarów kinetyki transportu elektronów w fotosystemie II	oral speech	S. Krysiak, K. Burda
16.	4 <sup>th</sup> International Caparica Conference on Pollutant Toxic Ions & Molecules	01-04.11 2021, Lisbon	Effects of TiO <sub>2</sub> and WO <sub>3</sub> nanoparticles on electron transport kinetics within the photosystem II of higher plants	oral speech	S. Krysiak, K. Burda
17.	2 <sup>nd</sup> Workshop: Resource recovery from waste and wastewater and downstream procedures for PPB biomass	06.07. 2023 Madrid	-	participation	-

### 3. Awards

'The excellent Shotgun Communication' award at the 2<sup>nd</sup> International Caparica Conference on Pollutant Toxic Ions & Molecules in Lisbon. The title of the awarded speech: *Influence of TiO<sub>2</sub> nanoparticles on activity of photosystem II and heterogeneity of oxygen evolution.*

The awarded oral presentation '*Badania układów hybrydowych złożonych z tylakoidów izolowanych z roślin wyższych oraz nanocząstek TiO<sub>2</sub>*' at Dokonania naukowe doktorantów: edycja VIII.

### 4. Internships and projects and summer schools

no.	Host	Dates	Aim
1.	BOKU-University of Natural Resources and Life Sciences, Vienna	06-20.03.2017	Internship
2.	Instituto de Nanociencia de Aragón - Universidad de Zaragoza, Zaragoza	03-21.02.2020 17-30.09.2022 25.03-01.04.2023	Internship
3.	European Synchrotron Radiation Facility (ESRF)	25.08-02.09.2018	Project
4.	Narodowe Centrum Promieniowania Synchrotronowego Solaris, Kraków	05-09.11.2018	Summer school

5.	European Synchrotron Radiation Facility (ESRF), Grenoble	17-21.06.2019	Summer school
6.	Purple Gain, Cost action, Madrid	03-05.07.2023	Summer school

# Table of contents

<b>ABBREVIATIONS &amp; ACRONYMS</b>	<b>13</b>
<b>STRESZCZENIE</b>	<b>17</b>
<b>ABSTRACT</b>	<b>21</b>
<b>1. BACKGROUND AND MOTIVATION</b>	<b>25</b>
<b>2. THE AIM OF THE STUDIES</b>	<b>29</b>
<b>3. INTRODUCTION TO OXYGENIC PHOTOSYNTHESIS</b>	<b>31</b>
1.1 OXYGENIC PHOTOSYNTHESIS	32
1.2 PHOTOSYSTEM II IN HIGHER PLANTS	36
3.2.1 Acceptor side of PSII – Fe-quinone complex	41
3.2.2 Oxygen Evolving Complex	42
<b>4. INORGANIC SEMICONDUCTIVE SYSTEMS</b>	<b>49</b>
<b>5. MATERIALS &amp; METHODS</b>	<b>53</b>
5.1 BIOLOGICAL MATERIAL	53
5.2 WO <sub>3</sub> NANOPARTICLES	55
5.3 ELECTROPHORESIS	55
5.4 X – RAY PHOTON SPECTROSCOPY – WO <sub>3</sub> NPS CHARACTERISATION	59
5.5 DYNAMIC LIGHT SCATTERING – WO <sub>3</sub> NPS CHARACTERISATION	62

5.6 ABSORPTION SPECTROSCOPY	65
5.7 FLUORESCENCE SPECTROSCOPY	67
5.8 PULSE – AMPLITUDE MODULATED FLUORESCENCE	69
5.9 FAST POLAROGRAPHY (JOLIOT’S TYPE)	71
5.10 TRANSMISSION ELECTRON MICROSCOPY	74
5.11 ATOMIC FORCE MICROSCOPY	76
<b>6. RESULTS AND DISCUSSION</b>	<b>79</b>
6.1 THE ROLE OF THE EXTRINSIC PROTEINS ON THE HETEROGENEITY OF OXYGEN RELEASE	79
6.2 THE ACTION OF WO <sub>3</sub> NPS ON PSII BBY	100
6.2.1 WO <sub>3</sub> NPs influence on PSII organisation	100
6.2.2 WO <sub>3</sub> NPs influence on PSII functioning	103
6.6.2.1 Energy utilisation and photosynthetic efficiency	103
6.6.2.1 Oxygen evolution	110
6.2.3. Discussion	114
<b>7. CONCLUSIONS</b>	<b>123</b>
<b>8. PROSPECTS FOR THE FUTURE</b>	<b>127</b>
<b>REFERENCES</b>	<b>129</b>

# Abbreviations & acronyms

AB solution	solution of acrylamide and N, N-methylenebisacrylamide
Abs	absorption spectroscopy
ADP	adenosine diphosphate
AFM	Atomic Force Microscopy
APS	ammonium peroxydisulfate
ATP	adenosine triphosphate
C <sub>2</sub> S <sub>2</sub> M <sub>2</sub>	LHCII trimmers
CE	continuum electrostatics
Chl/Chls	chlorophyll/chlorophylls
CP24	antenna complexes of PSII
CP26	antenna complexes of PSII
CP29	antenna complexes of PSII
Crt/Crts	carotenoid/carotenoids
cryo-EM	Cryo-Electron Microscopy
Cyt. b <sub>6</sub> f	cytochrome b <sub>6</sub> f
DNA	deoxyribonucleic acid
DLS	Dynamic Light Scattering
DTT	1,4-Dithiothreitol
E <sub>g</sub>	energy band gap
EPR	Electron Paramagnetic Resonance
ESCA/XPS	Electron Spectroscopy for Chemical Analysis/X-ray Photoelectron Spectroscopy
EXAFS	extended X-ray absorption fine structure
Fd	ferredoxin
FEL	free-electron laser
FeS	iron(II) sulphide
FNR	enzyme ferredoxin-NADP <sup>+</sup> -reductase
FTIR	Fourier-Transform Infrared Spectroscopy
HEPES	4-(2-hydroxyethyl)-1-piperazineethanesulfonic acid

kDa	(kilo)Dalton, a non-SI unified atomic mass unit
HS	high spin
LHC	Light-Harvesting Complex
LS	low spin
MC	Monte Carlo studies
MD	molecular dynamics
MM	molecular mechanics
Mn <sub>4</sub> CaO <sub>5</sub>	manganese complex, a cubane-like structure
MS	mass spectroscopy
NADPH	nicotinamide adenine dinucleotide phosphate
NH Fe	non-heme iron
NIR	near infra – red light
NPQ	non-photochemical fluorescence quenching
NPs	nanoparticles
OEC	Oxygen Evolving Complex
P680	PSII reaction centre
P700	PSI reaction centre
PAM FL	Pulse-Amplitude Modulated Fluorescence
PC	plastocyanin
Pheo	pheophytin
PSI	Photosystem I
PSII	Photosystem II
PSII BBY	PSII-enriched thylakoids
PsbA or D1	PSII reaction centre core protein
PsbB or CP47	PSII antenna complexes protein
PsbC or CP43	PSII antenna complexes protein
PsbD or D2	PSII reaction centre core protein
PsbO	~33 kDa extrinsic unit of Mn <sub>4</sub> CaO <sub>5</sub>
PsbQ	~16 kDa extrinsic unit of Mn <sub>4</sub> CaO <sub>5</sub>
PsbP	~23 kDa extrinsic unit of Mn <sub>4</sub> CaO <sub>5</sub>
PsbV	extrinsic protein in cyanobacteria
PQ	plastoquinone molecule
PQH <sub>2</sub>	plastoquinol

Q	quinone
Q <sub>A</sub>	plastoquinone molecule bound at a Q <sub>A</sub> site
Q <sub>B</sub>	plastoquinone molecule bound at a Q <sub>B</sub> site
QM	quantum mechanics
RC	Reaction Centre
ROS	Reactive Oxygen Species
SDS – PAGE	sodium dodecyl sulphate – polyacrylamide gel electrophoresis
S <sub>i</sub> states	OEC transient states
tebpmcn	tetraethyl N,N'-bis(2-methylpyridyl-4-phosphonate) –N,N'-dimethylcyclohexyldiamine
TEM	Transmission Electron Microscopy
TEMED	N,N,N',N'-Tetramethylethane-1,2-diamine
Tris	2-amino-2-(hydroxymethyl)propane-1,3-diol
TRITON X-100	(C <sub>14</sub> H <sub>22</sub> O(C <sub>2</sub> H <sub>4</sub> O) <sub>n</sub> ), a nonionic surfactant
UV-VIS	ultraviolet (UV) to visible (Vis) region of electromagnetic radiation
WOC	Water Oxidising Complex
XPS	X – Ray Photoelectron Spectroscopy
Y <sub>D</sub> or Tyr <sub>D</sub>	tyrosine of peptide D1
Y <sub>Z</sub> or Tyr <sub>Z</sub>	tyrosine of peptide D2



# Streszczenie

Kierunek rozwoju życia na Ziemi został zdeterminowany przez fotosyntezę tlenową. Pierwsze organizmy zdolne do jej przeprowadzenia pojawiły się ponad 3 mld lat temu. Sinice, glony i rośliny wyższe potrafią wykorzystywać światło słoneczne do pobierania elektronów z wody, gdyż posiadają fotosystem II (PSII). Produktem ubocznym tego procesu jest  $O_2$ . PSII jest nie bez powodu nazywane "sercem" fotosyntezy, której dalsze etapy są uzależnione od aktywności kompleksu wydzielającego tlen (OEC - oxygen evolving complex). Zrozumienie struktury i mechanizmu działania OEC pozostaje największym wyzwaniem współczesnej nauki, pomimo ogromnego postępu, jaki dokonał się w ostatnich latach dzięki połączonym wysiłkom wielu grup badawczych z różnych dyscyplin i stosujących różne podejścia badawcze. Trudność w zrozumieniu funkcjonowania OEC, który stanowi kompleks  $Mn_4CaO_5$ , polega na pozyskiwaniu eksperymentalnych danych, które pozwalałyby jednoznacznie przypisać je do jego pośrednich stanów katalitycznych. Nie ma wciąż spójnego modelu OEC, który dałoby się stworzyć w oparciu o dostępne dane. Głównym problemem jest rozpad kompleksu  $Mn_4CaO_5$  podczas procesu izolacji z PSII, jego struktura ulega degradacji. Tylko wtedy, gdy jest związany z matrycą białkową PSII, istnieje jako wysoce aktywny związek zdolny do gromadzenia czterech ładunków dodatnich i ekstrakcji elektronów z wody. Pytania, które pozostają wciąż otwarte: (i) jak zmieniają się stany kompleksu  $Mn_4CaO_5$  w cyklu Koka, (ii) jakie są drogi odprowadzania protonów i  $O_2$  oraz przyłączania cząsteczek wody, (iii) jakie mechanizmy regulujące są odpowiedzialne za wysoką efektywność OEC i wreszcie (iv) który etap w cyklu Koka jest 'wąskim gardłem' (ang. *bottleneck*) i co jest tego przyczyną.

Mechanizm działania OEC jest niezwykle inspirujący i poznanie go będzie miało ogromny wpływ na projektowanie wydajnych ogniw paliwowych. Obecnie jednymi z najbardziej rozpowszechnionych układów są związki półprzewodnikowe bazujące na metalach, zdolne do utleniania wody. Między innymi zalicza się do nich związki wolframu. Niestety ich wydajność w produkcji  $O_2$  jest zwykle o ok. pięć rzędów wielkości mniejsza niż ta osiągnięta przez naturalny układ PSII wyposażony w kompleks  $Mn_4CaO_5$ . Innym problemem jest wąski zakres długości fal promieniowania elektromagnetycznego, które je aktywują, podczas gdy superkompleksy PSII przyswajają światło w szerokim zakresie spektralnym (w zakresie światła widzialnego) z dużą wydajnością dzięki obecności kompleksów antenowych. Dlatego też podejmowanych jest coraz więcej prób wytwarzania układów bio-nano-hybrydowych z połączenia półprzewodników z izolowanymi bądź całymi strukturami aparatu fotosyntetycznego.

Niniejsza praca koncentruje się na badaniu wpływu czynników endogennych i egzogennych na wydajność i heterogeniczność wytwarzania tlenu przez PSII BBY

(tylakoidy wzbogacone w PSII). W pierwszym przypadku badany był wpływ białek zewnętrznych (PsbO, PsbP i PsbQ), o których wiadomo z jednej strony, że stabilizują kompleks  $Mn_4CaO_5$ , a z drugiej strony, że mogą być odpowiedzialne za formowanie kanałów, którymi dostarczana jest woda w pobliże kompleksu manganowego i odbierane są protony i  $O_2$ . Jako czynnik egzogeny zostały wybrane nanocząstki (NPs)  $WO_3$ , gdyż znana są ich zdolność do utleniania wody i odporność na środowisko wodne. Czyni je to atrakcyjnym kandydatem do wytwarzania układu hybrydowego PSII BBY –  $WO_3$  NPs, który mógłby wykazywać zwiększone wydzielanie tlenu stymulowane oddziaływaniami z PSII w porównaniu do czystego układu półprzewodnikowego. Ze względu na rozmiary nanocząstek od ok. 1-3 nm można było się spodziewać, że będą się one wbudowywać w błony i będą mogły oddziaływać zarówno ze strona donorową, jak i akceptorową PSII. Aby móc bezpośrednio badać udział oraz kinetykę wydzielania tlenu w PSII wolną i szybką ścieżką, opracowano nowy protokół pomiarowy wykorzystujący szybką polarografię trójelektrodową (elektrodę typu Joliot). Eksperymenty przeprowadzono na PSII BBY izolowanych ze świeżych liści tytoniu (*Nicotiana tabacum* var. *John William's Broadleaf (JWB)*) w przypadku badań wpływu białek zewnętrznych na aktywność PSII oraz ze świeżych liści szpinaku (*Spinacia oleracea*) w badaniach układów hybrydowych PSII BBY -  $WO_3$  NPs. W żadnym z eksperymentów nie dodawano akceptorów zewnętrznych, które mogłyby wpłynąć na pracę PSII.

W pracy osiągnięto dwa ważne wyniki. Jeden jest związany z bezpośrednimi pomiarami heterogeniczności uwalniania tlenu przy użyciu szybkiej polarografii i identyfikacją czynników wpływających na przełączanie PSII między szybkimi i wolnymi fazami produkcji tlenu. Drugie osiągnięcie dotyczy nowego podejścia do rozwoju systemów biohybrydowych wykorzystujących mechanizmy PSII niezbędne do optymalizacji wydajności hybrydy w warunkach zbliżonych do naturalnych, tj. środowiskowych.

Wykorzystując heterogeniczny 5-cio stanowy rozszerzony model Koka, uwzględniający istnienie metastabilnego stanu  $S_4$ , przeprowadzono analizę oscylacji ewolucji tlenu pod wpływem krótkich wysycających błysków białego światła uzyskanych dla PSII BBY niepoddanego wymyciu białek i pozbawionego zewnętrznych białek otaczających kompleks  $Mn_4CaO_5$ . W próbie kontrolnej wszystkie przejścia pomiędzy stanami  $S_i \rightarrow S_{i+1}$  są wysoce efektywne poza przejściem ze stanu  $S_2$  do  $S_3$ , co świadczy o jego wyjątkowym charakterze. Co więcej, prawdopodobieństwo tego przejścia jest niezależne od obecności białek zewnętrznych. Zaobserwowano, że usunięcie dwóch białek PsbQ i PsbP powoduje w różnym stopniu spadek prawdopodobieństwa przejścia pomiędzy stanami  $S_0 \rightarrow S_1$ ,  $S_1 \rightarrow S_2$  i  $S_3 \rightarrow S_0$ . Największe zmiany zaobserwowano dla przejścia  $S_0 \rightarrow S_1$ . Usunięcie dodatkowo trzeciego białka spowodowało znaczny spadek aktywności PSII BBY o ok. 60%. Nie miało to jednak wpływu na efektywność przejść pomiędzy stanami  $S_i \rightarrow S_{i+1}$ . Natomiast ponad 80% udział szybkiej fazy wydzielania tlenu w kontrolnej próbie PSII BBY zmniejszył się prawie 4-rotnie w PSII pozbawionych PsbP

i PbQ. Wymycie wszystkich trzech białek spowodowało prawie całkowity zanik fazy szybkiej wydzielania  $O_2$ . Także wyniki z pomiarów zależności zmian amplitudy wydzielania tlenu pod wpływem trzeciego błysku w funkcji odległości pomiędzy pierwszym i drugim błyskiem, jak i pomiędzy drugim i trzecim błyskiem potwierdziły podobny zanik szybkiej fazy uwalniania  $O_2$  w badanych próbkach. Jednocześnie jego niezależność od przyjętego protokołu pomiarowego potwierdza sekwencyjny przebieg cyklu Koka. Stała czasowa szybkiej ścieżki wydzielania tlenu wyznaczona dla próbki kontrolnej z ok. 4 ms wzrosła do ok. 6 ms w PSII BBY pozbawionych dwóch białek zewnętrznych. Zaskakująca jest zmiana wolnej stałej czasowej, która w próbce kontrolnej wynosi ok. 60 ms, a następnie przyspiesza odpowiednio prawie 2 i 4-krotnie w PSII–PsbQ, PsbP i PSII – PsbQ, PsbP, PsbO. Wszystkie zaobserwowane zmiany zostały omówione w odniesieniu do przyjętej wiedzy na temat budowy kompleksu  $Mn_4CaO_5$  i funkcjonowania PSII oraz istniejących modeli opisujących przejścia pomiędzy stanami  $S_i \rightarrow S_{i+1}$ . Wyjaśnienie tych zjawisk wymagało wzięcia pod uwagę zarówno zmian organizacyjnych kompleksu  $Mn_4CaO_5$  z uwzględnieniem bliższych i dalszych sfer koordynacyjnych manganu i wapnia, jak i zmian w funkcjonowaniu rozpoznanych kanałów O1, O4 i Cl1 oraz ich roli kontrolnej w doprowadzaniu  $H_2O$  do i odprowadzaniu protonów i  $O_2$  poza OEC.

Praca ta dostarcza również nowych informacji na temat projektowania systemów nano-biohybrydowych wykorzystujących fotosystem II do produkcji  $O_2$ . Powszechnie badane nanostruktury półprzewodnikowe 2D/3D wymagają dużej powierzchni aktywnej wykazującej wysoce specyficzne połączenie z PSII w celu uzyskania prawidłowo zorientowanych systemów PSII o wysokiej gęstości upakowania. Wymaga to, z jednej strony, funkcjonalizacji tych mezo-nano powierzchni, a z drugiej strony, genetycznej modyfikacji samego PSII. Zazwyczaj wprowadza się mediatory elektronowe, aby zapewnić cykliczny obieg elektronów. Niemniej jednak, najwyższe tempo uwalniania tlenu zarejestrowane dla tych systemów, które osiągnęły w początkowej fazie działania, przeliczone na g katalizatora, tj. superkompleksu PSII, pozostaje o 2-3 rzędy wielkości niższe niż to wykazywane przez izolowane systemy PSII w ich natywnych warunkach. W niniejszej pracy zademonstrowano nowe podejście do konstruowania systemów hybrydowych opartych na naturalnym PSII BBY, który wykazuje najwyższą zdolność do ewolucji tlenu zademonstrowaną do tej pory. Superdrobne nanocząstki  $WO_3$  zostały wprowadzone do PSII BBY. Wykazano zależny od ich stężenia wpływ na organizację tych błon i funkcjonowanie PSII. Największe zmiany wywołane działaniem NPs zaobserwowano dla procesu ewolucji  $O_2$ . Maksymalną wydajność  $O_2$  na poziomie 70% odnotowano dla próbki kontrolnej oraz dla stężeń 0,02-0,03  $\mu g$  NPs/ $\mu g$  Chl i 0,15-0,3  $\mu g$  NPs/ $\mu g$  Chl. Korelowało to z niewielkim spadkiem wydajności fotochemicznej, co pozwoliło zidentyfikować mechanizm odpowiedzialny za to zjawisko. Mianowicie, wysoce specyficzne działanie  $WO_3$  NPs po stronie donorowej, ich zdolność do pobierania elektronów z OEC oraz tworzenie łańcuchów przewodzących docierających do strony akceptorowej PSII, umożliwiło im przenoszenie elektronów do chinonów związanych w

miejscach  $Q_A$  i  $Q_B$ . Wpływ NPs na zawartość superkompleksów PSII ma ogromne znaczenie. W ten sposób NPs mogą modyfikować potencjały redoks  $Q_A$  i  $Q_B$ , a także regulować dostęp PQ z zewnętrznej puli chinonów do miejsca wiązania  $Q_B$ . Zaproponowane podejście może przynieść korzyści w projektowaniu systemów biohybrydowych, które przekształcają energię słoneczną w paliwo. Pozwala ono na wykorzystanie całego spektrum długości fal emitowanych przez słońce w zakresie UV-VIS z wysoką wydajnością kwantową reakcji rozszczepiania wody i produkcji tlenu na poziomie natywnej aktywności PSII. System działa przy pH 6,5 i nie wymaga dodatkowych akceptorów elektronów. Oczywiście stabilność takiego układu hybrydowego jest kluczowa i zależy między innymi od szybkości wychwytu  $O_2$  (mniejszy wychwyty  $O_2$  = mniejsza generacja ROS) oraz zdolności do regeneracji  $PQ_{ox}$ , co może wymagać zewnętrznego mediatora elektronów. W tym drugim przypadku wymaga to interakcji dwóch systemów, z których drugim może być system zdolny do produkcji  $H_2$  (wymagałoby to ich separacji przestrzennej) lub energii elektrycznej przy użyciu odpowiedniej elektrody zdolnej do ekstrakcji elektronów z  $PQH_2$ .

# Abstract

The direction of life on Earth was determined by oxygenic photosynthesis. The first organisms capable of carrying out this process appeared more than 3 billion years ago. Cyanobacteria, algae and higher plants are able to use sunlight to extract electrons from water, as they have photosystem II (PSII). A side-product of this process is O<sub>2</sub>. PSII is not without reason called the 'heart' of photosynthesis. The following steps which occur during photosynthesis depend on the activity of the oxygen-evolving complex (OEC). Understanding the structure and mechanism of action of the OEC remains the greatest challenge of modern science, despite the enormous progress made in recent years thanks to the combined efforts of many research groups from different disciplines and using different research approaches. The difficulty in understanding the functioning of the OEC, which is formed from the Mn<sub>4</sub>CaO<sub>5</sub> complex, lies in obtaining experimental data that would allow it to be unambiguously assigned to intermediate catalytic states. There is still no consistent model of the OEC that can be constructed from the available data. The main problem is that the Mn<sub>4</sub>CaO<sub>5</sub> complex cannot be isolated from PSII; it degrades. Only when bound to the PSII protein matrix, does it exist as a highly active compound capable of accumulating four positive charges and extracting electrons from water. Questions that remain open are: (i) how do the states of the Mn<sub>4</sub>CaO<sub>5</sub> complex change in the Kok cycle, (ii) what are the pathways of proton and oxygen release and water molecule binding, (iii) what are the regulatory mechanisms responsible for the high efficiency of the OEC, and finally (iv) which stage in the Kok cycle is the bottleneck and what is the cause of this.

The mechanism of action of the OEC is fascinating, and its understanding will have a massive impact on the design of efficient fuel cells. Currently, the most widespread systems are semiconductor compounds capable of oxidising water. These include tungsten compounds. Unfortunately, compared to a natural PSII system equipped with the Mn<sub>4</sub>CaO<sub>5</sub> complex, their efficiency in O<sub>2</sub> production is usually about five orders of magnitude lower. Another problem is the narrow range of wavelengths that activate them. PSII supercomplexes absorb light in a wide spectral range (visible light range) with high efficiency due to the presence of antenna complexes. This is why attempts are increasingly made to create bio-nano-hybrid systems in combination with isolated or entire structures of the photosynthetic apparatus. For this reason, more and more attempts are being made to produce bio-nano-hybrid systems by combining semiconductors with isolated or whole structures of a photosynthetic apparatus.

This work focuses on studying endogenous and exogenous factors in the efficiency and heterogeneity of oxygen production by PSII B68 (in PSII-enriched thylakoids). In the first case, the influence of external proteins (PsbO, PsbP and PsbQ)

was investigated. These proteins are known to stabilise the  $Mn_4CaO_5$  complex and may be responsible for forming channels through which water is supplied near the manganese complex and  $H^+$  and  $O_2$  are extracted.  $WO_3$  nanoparticles (NPs) were chosen as the exogenous agent because of their known ability to oxidise water and their resistance to aquatic environments. This makes them an attractive candidate for the PSII BBY -  $WO_3$  NPs hybrid system, which could exhibit enhanced oxygen release stimulated by interactions with PSII compared to a pure semiconductor system. The size of the nanoparticles is about 1-3 nm. It was expected that they would be able to incorporate into the membranes and interact with both the donor and acceptor side of PSII. A new measurement protocol using fast three-electrode polarography (Joliot-type electrodes) was developed to directly study the contribution and kinetics of oxygen release in PSII via the slow and fast pathways. Experiments have been carried out using PSII BBY isolated from fresh tobacco leaves (*Nicotiana tabacum* var. *John William's Broadleaf* (JWB)) to study the effect of external proteins on PSII activity and from fresh spinach leaves (*Spinacia oleracea*) to study PSII BBY -  $WO_3$  NPs hybrid systems. No external acceptors were added in any of the experiments, which could alter the acceptor side of the PSII and thus alter how it works.

There are two main achievements of this work. One is related to direct measurements of oxygen release heterogeneity using fast polarography and identifying factors influencing PSII switching between fast and slow phases of oxygen production. The other is related to a new approach to developing biohybrid systems using the PSII mechanisms necessary to optimise hybrid performance under near-natural, i.e. environmental, conditions.

Using the heterogeneous  $5S$  – state extended Kok model, which considers the existence of a metastable  $S_4$  state, an analysis of oxygen evolution oscillations under the influence of short saturating flashes of white light has been carried out. The data were obtained for untreated PSII BBY and depleted of external proteins surrounding the  $Mn_4CaO_5$  complex. All transitions between the  $S_i \rightarrow S_{i+1}$  states are highly efficient in the control sample, except the transition from the  $S_2$  to the  $S_3$  state, proving its unique nature. Moreover, the probability of this transition is independent of the presence of external proteins. It was observed that the removal of the two proteins PsbQ and PsbP caused a decrease in the transition probability between the states  $S_0 \rightarrow S_1$ ,  $S_1 \rightarrow S_2$  and  $S_3 \rightarrow S_0$  to different degrees. The most considerable changes were observed for the  $S_0 \rightarrow S_1$  transition. However, the contribution of the fast phase of oxygen evolution of more than 80% in control PSII BBYs decreased almost 4-fold in PSII depleted of PsbP/PbQ. The elution of all three proteins almost entirely abolished the fast phase of  $O_2$  yield. A similar disappearance of the fast phase of  $O_2$  release in the samples studied was also confirmed by the results from measurements of the dependence of the changes in the amplitude of oxygen release under the third flash as a function of the distance between the 1<sup>st</sup> and 2<sup>nd</sup> flashes and between the 2<sup>nd</sup> and 3<sup>rd</sup> flashes. At the same time, its independence from

the measurement protocol adopted confirms the sequential nature of the Kok cycle. The time constant of the fast oxygen evolution pathway determined for the control sample increased from about 4 ms to about 6 ms in PSII BBY depleted of the two external proteins. The change in the slow time constant is surprising, which is about 60 ms in the control sample and then accelerates almost 2 and 4 times in PSII-PsbQ, PsbP and PSII-PsbQ, PsbP, and PsbO, respectively. All of the observed changes were discussed in relation to the accepted knowledge of the structure of the  $Mn_4CaO_5$  complex and the functioning of the PSII, as well as existing models describing the transitions between the  $S_i \rightarrow S_{i+1}$  states. To explain these phenomena, it was necessary to take into account both the organisational changes in the  $Mn_4CaO_5$  complex, including other coordination spheres of manganese and calcium besides the immediate ones, as well as changes in the functioning of the identified O1, O4 and Cl1 channels and their controlling role in the supply of  $H_2O$  to and removal of  $H^+$  and  $O_2$  from the OEC.

This work also provides new insights into the design of nano-biohybrid systems using photosystem II for  $O_2$  production. Commonly studied 2D/3D semiconductor nanostructures require a large active surface showing a highly specific junction with PSII in order to obtain correctly oriented PSII systems with high packing density. This requires, on one hand, the functionalisation of these meso-nano surfaces and, on the other hand, genetic modification of the PSII itself. Usually, electron mediators are introduced to ensure electron cycling. Nevertheless, the highest rate of oxygen release recorded for these systems, which they achieved in their initial phase of operation, converted per g of catalyst, i.e. PSII supercomplex, remains 2-3 orders of magnitude lower than that exhibited by isolated PSII systems under their native conditions. This work demonstrated a new approach to constructing hybrid systems based on natural PSII BBY, which displays the highest oxygen evolution capacity observed so far. Superfine  $WO_3$  nanoparticles were introduced in PSII BBY. They have been shown to have a concentration-dependent effect on the organisation of these membranes and the functioning of PSII. The most remarkable NP-induced changes were observed for  $O_2$  evolution. The maximum  $O_2$  yield of 70% was detected for the control sample and for concentrations of 0.02-0.03  $\mu g$  NPs/ $\mu g$  Chl and 0.15-0.3  $\mu g$  NPs/ $\mu g$  Chl. This correlated with a slight decrease in photochemical yield, which made it possible to identify the mechanism responsible for this phenomenon. Namely, the highly specific action of  $WO_3$  NPs on the donor side, their ability to take up electrons from the OEC, and the formation of conducting chains reaching the acceptor side of PSII enabled them to transfer electrons to quinones bound at the  $Q_A$  and  $Q_B$  sites. The effect of NPs on the compactness of PSII supercomplexes is of great importance here. Thus, NPs can modify the redox potentials of  $Q_A$  and  $Q_B$  and regulate PQ's access from the external quinone pool to the  $Q_B$  binding site. This approach can benefit the design of biohybrid systems that convert solar energy into fuel. It allows the use of the entire spectrum of wavelengths emitted by the sun in the UV-VIS range with a high quantum efficiency of water-splitting reactions and oxygen production at the level of native PSII activity. The

system operates at pH 6.5 and requires no additional electron acceptors. Of course, the stability of such hybrid systems is crucial. It depends, among other things, on the rate of O<sub>2</sub> uptake (lower O<sub>2</sub> uptake = lower ROS generation) and the ability to regenerate PQ<sub>ox</sub>, which may require an external electron mediator. In the latter case, it requires the interaction of two systems; the second could be a system capable of producing H<sub>2</sub> (this would require their spatial separation) or electricity using a suitable electrode capable of extracting electrons from PQH<sub>2</sub>.

# 1. Background and motivation

The greatest challenge of humankind in sustaining the development of civilisation is finding efficient, safe, and widely available energy sources. Given the depletion of hydrocarbon resources or nuclear fuels currently used for energy production, scientists are working on renewable energy sources, which would additionally provide countries with independence and security. Renewable and effective energy sources are also an opportunity to develop poor regions of the world (Shahsavari & Akbari, 2018). On-site energy generation is essential due to other unresolved issues, namely the lack of large-scale energy storage capacity (Burheim, 2017) and long-distance transmission and distribution losses, which depend on the energy conversion efficiency in the various supply pathways (DeSantis, James, Houchins, Saur, & Lyubovsky, 2021). In addition, environmentally friendly solutions are being sought, especially as human activity is responsible for accelerating the greenhouse effect, climate change, and environmental pollution (Akella, Saini, & Sharma, 2009; Shahsavari & Akbari, 2018).

Fuel cells are a perfect solution for developing a clean, renewable, and, therefore, continuous source of energy that comes from storable compounds produced using solar energy (Lewis & Nocera, 2006). These solar collectors and solar fuel reactors based on a photoelectrochemical process that is a biomimicry of the light phase of photosynthesis seem to be the expected solution (Fujishima & Honda, 1972; Grätzel, 2001; Jafari et al., 2016; Krasnovskii & Brin, 1962; Lewis & Nocera, 2006; Zamaraev & Parmon, 1980; Zeradjanin, Masa, Spanos, & Schlögl, 2021). In photosynthetic organisms, their reaction centres (RCs) trap energy and use it for charge separation. With the presence of light-harvesting complexes (LHCs) that transfer energy to RCs, the energy capture cross-section is increased. In addition, pigments such as chlorophylls (Chls) or carotenoids (Crts) embedded in the LHC extend the range of absorbed sunlight. It is estimated that about 50% of the wavelength range of sunlight reaching the Earth's surface is used by photosynthetic organisms. The high efficiency of light absorption and charge separation in RCs makes photosynthetic systems very attractive for their application in biohybrid solar cells/reactors (Gust, Moore, & Moore, 2009; J. Liu & van Iersel, 2021; McCree, 1972; Sager, Smith, Edwards, & Cyr, 1988; Wasilewski, 2009; Y. Xu et al., 2017).

Photosystem II (PSII) has the most efficient light transformative capability on Earth (energy efficiency for absorbed photons with respect to charge separation is  $\sim 84\%$ ) (McConnell, Li, & Brudvig, 2010). Moreover, it can drive the solar water splitting process due to its extremely high oxidative power (highest among natural photosynthetic systems: 1.8 V at each photochemical step) and the presence of a  $\text{Mn}_4\text{CaO}_5$  cluster (called oxygen-evolving complex – OEC or water oxidising complex – WOC) located on its donor side. Under environmental conditions, PSII is able to use 75% of the energy absorbed by its reaction centre to split water and has 1.2 V of its oxidising power to do so at each oxidation step (Pecoraro, Baldwin, Caudle, Hsieh, & Law, 1998). Mimicking the action of photosystem II (PSII) is a likely strategy for the production of renewable fuels, mainly  $\text{H}_2$  and  $\text{O}_2$ , using water as an electron and proton donor (Z. Han, Qiu,

Eisenberg, Holland, & Krauss, 2012; He, Zhao, & Hou, 2013; Hou, 2017; D. Kim, Sakimoto, Hong, & Yang, 2015; Tachibana, Vayssieres, & Durrant, 2012; Y. Wang et al., 2020).

It is challenging to develop 'super-catalysts' for the anodic reaction to increase the kinetics of O<sub>2</sub> evolution and avoid the formation of other chemicals on the photoanode surface. The disadvantage of metal oxides (mainly TiO<sub>2</sub>, ZnO, or WO<sub>3</sub>) working as a photoanode is their high overpotential. This directly impacts the conversion efficiency. The current direction of research on photocatalytic water splitting focuses on designing a photoanode with efficient charge separation and fast charge transfer kinetics, activated by a wide range of visible light and operating under ambient conditions. These problems were addressed through various attempts, including doping, surface functionalisation, use of dyes, deposition of noble metals, and construction of cooperative heterostructures according to the Z-scheme [reviews:(Jafari et al., 2016; B.-H. Lee et al., 2019; Y. Li & Tsang, 2020; Sumathi, Prakasam, & Anbarasan, 2019; Y. Wang et al., 2020)].

Photo-catalysts producing even approx. 1 mmol O<sub>2</sub> g<sub>cat</sub><sup>-1</sup>h<sup>-1</sup> are still too inefficient to be used in fuel cells. Photosystem II shows a much higher activity in recovering O<sub>2</sub> from water than the known anode photocatalysts. Isolated photosynthetic membranes, thylakoids, depending on various cofactors (for example, the way of preparation, nutrients, buffer composition, light conditions, external acceptors used, and presence of external proteins), have oxygen evolution activity ranging from about 250 to 10000 mmol O<sub>2</sub> g<sub>chl</sub><sup>-1</sup> h<sup>-1</sup> (per gram of chlorophyll, Chl). Thylakoids enriched in PSII (PSII BBY) usually show an O<sub>2</sub> yield > 500 mmol g<sub>chl</sub><sup>-1</sup> h<sup>-1</sup> (Berthold, Babcock, & Yocum, 1981; Ghanotakis & Yocum, 1986; Ikeuchi, Yuasa, & Inoue, 1985). For a review, see also (Croce & van Amerongen, 2011). By rough estimation<sup>a</sup>, one may find a rate of oxygen evolution per gram of RC<sub>CaMn4O5</sub>-CP43-CP47 (reaction centre including inner light-harvesting antennae CP47 and CP43), the photocatalyst of PSII. It gives > ~1950 mmol O<sub>2</sub> g<sub>cat</sub><sup>-1</sup>h<sup>-1</sup> in PSII BBY.

It seems natural, therefore, for the first approach, involving bionanotechnologies to develop a new generation of systems capable of oxidising water with efficiency equal to evolutionarily selected photosystems, to explore biohybrid systems based on natural PSII and n-semiconductors known for their advantages. In particular, they should be materials that show high stability in aqueous environments over a wide pH range. By coupling to PSII and external photosynthetic antennas, biohybrid anodes have no limitation in the range of sunlight absorbed, whereas most efficient semiconductors absorb below 500 nm. There is growing interest in the possibility of photocurrent generation by photoelectrodes and H<sub>2</sub> production by combining semiconductor

---

<sup>a</sup> A rough estimate of the oxygen evolution rate per gram of RC-CP43-CP47 (PSII + two internal light collecting antennas CP43 and CP47, binding a total of 35 Chls) in thylakoids enriched in PSII (BBY PSII) isolated from higher plants was performed assuming that per one BBY PSII reaction center there are additionally 13 LHCII units (units of external light harvesting complex - each unit contains 12 Chls) forming two tetramers and one heptamer and three minor antennas CP29, CP26 and CP24 (three monomers containing 27 Chls in total) (Cinque, Croce, Holzwarth, & Bassi, 2000; Croce & van Amerongen, 2011; Saito, Kikuchi, Nakayama, Mukai, & Sumi, 2006), review: (Müh & Zouni, 2020; V. H. R. Schmid, 2008) The mass of protein units forming RC, CP43 and CP47 (in total 17 proteins) was taken from (Ke, 2001).

compounds with isolated photosynthetic structures or even whole chloroplasts, mainly due to the increased use of sunlight by such biohybrids [for review, see: (Gonçalves Silva et al., 2022; Y. Liu, Daye, Jenson, & Fong, 2018; Pang et al., 2018; J. Z. Zhang & Reisner, 2020)]. Biohybrid systems that combine inorganic semiconductors/metals and naturally occurring photosynthetic isolated antenna complexes or more complex protein-lipid-pigment systems open up a promising area for new research on water photocatalysis (Badura et al., 2006; Grimme, Lubner, Bryant, & Golbeck, 2008; Ihara et al., 2006; Iwuchukwu et al., 2010; M. Kato, Cardona, Rutherford, & Reisner, 2013; Kawahara et al., 2020; J. Li et al., 2016; Miyachi et al., 2017; Nagakawa et al., 2019; Riedel et al., 2019; Tahara et al., 2017; Terasaki et al., 2008; Tian et al., 2021; Utschig et al., 2011; Vittadello et al., 2010; Voloshin et al., 2022; Yehezkeli et al., 2012; Yehezkeli, Willner, Tel-Vered, Michaeli, & Nechushtai, 2014; J. Z. Zhang & Reisner, 2020). The biohybrid system should be self-organising, environmentally safe, and efficiently utilise radiation energy close to 100%.

However, there are few reports on the effectiveness of such systems in splitting water to produce O<sub>2</sub> for fuel cells (M. Kato, Cardona, Rutherford, & Reisner, 2012; M. Kato et al., 2013; R. Liu et al., 2011; Mersch et al., 2015; Noji et al., 2011; Sokol et al., 2018; Tian et al., 2021; W. Wang et al., 2016). Mainly, they focus on the problem of light-to-current conversion efficiency (Gonçalves Silva et al., 2022; Pang et al., 2018). This is one of the reasons to study the effect of tungsten oxide nanoparticles (WO<sub>3</sub> NPs) on PSII activity. This photosystem is responsible for the uptake of electrons and protons from water and the evolution of O<sub>2</sub>. Secondly, the operation of such solid-state biohybrids has so far been studied in configurations where photosynthetic systems were deposited on non-functionalized or functionalised surfaces, which limited the density of photosystems that could attach to and come into direct contact with flat electrodes. This also forced the orientation and packing pattern of the photosystems. The porosity of inorganic substrates has been shown to be an essential factor in enhancing the activity of engineered biohybrids, as it allows them to increase their contact area with biological molecules (Hardee & Bard, 1977; Huang et al., 2015; M. Kato et al., 2012; Pang et al., 2018; Tian et al., 2021; W. Wang et al., 2015; J. Z. Zhang & Reisner, 2020).

In the presented approach, a colloidal system was used, i.e. superfine WO<sub>3</sub> NPs suspended with PSII-enriched thylakoids (PSII BBY) in an aqueous buffer. This ensures that the biohybrid system works as a photoanode self-organizes, and the superfine NPs have complete contact with the photosynthetic membrane and its photoactive protein-dye complexes (i.e. the PSII reaction centre and light-harvesting complexes).

Tungsten oxide nanoparticles (NPs) were chosen to investigate their impact on the efficiency of charge separation and oxygen evolution, driven by the visible region of sunlight, in a hybrid system formed by PSII BBY and WO<sub>3</sub> NPs. WO<sub>3</sub> belongs to 'chromogenic' materials and has found many applications, including optoelectronics and microelectronics (Bourdin et al., 2020; Chang, Sun, Dong, Dong, & Yansheng Yin, 2014; Deb, 2008; Granqvist et al., 2018; Sánchez Martínez, Martínez-de la Cruz, & López Cuéllar, 2011; C.-K. Wang et al., 2013). Nanomaterials based on low-dimensional WO<sub>3</sub> structures exhibit chemical sensing properties and are being widely studied for applications as sensors in environmental engineering (L. Zhang et al., 2011). Due to their catalytic properties, they are among the materials with potential applications for water photolysis and H<sub>2</sub> production (in combined systems), as well as degradation of organic

pollutants [for review, see (Huang et al., 2015) and references therein; (Isari et al., 2020)]. Therefore, tungsten oxide nanoparticles may be a key material in fuel cell technologies in the near future.

In these colloidal systems,  $\text{WO}_3$  NPs were expected to interact with both the acceptor and donor side of PSII. That duality of the  $\text{WO}_3$  NPs functioning would stimulate the evolution of oxygen from water in this biohybrid system without any additional intermediate molecules. This may have profound consequences for the understanding of the system. Mn-oxo complexes/tungsten oxide heterostructures have been shown to be robust catalysts for the photodissociation of water, although the exact mechanism of the process is not fully elucidated (Chou et al., 2012; R. Liu et al., 2011).

However, to be able to design new generation biohybrid systems that are self-regulating, using the working capabilities of the PSII donor side with particular emphasis on the OEC, it is desirable to fully understand the mechanism of  $\text{O}_2$  evolution and which factors are triggers/regulators of this process. Understanding the relationship between the structural changes in the  $\text{Mn}_4\text{CaO}_5$  complex and the protein-water matrix in which it is located could provide a breakthrough in designing n-type semiconductor systems for renewable energy. Research efforts over the last few decades have provided a broad and diverse understanding of the functioning of PSII, including its donor side (for review, see: (Guo, Messinger, Kloo, & Sun, 2023; Pantazis, 2018)). The study of photosynthetic water oxidation is an interdisciplinary field. The interpretation of experimental results often depends on the theoretical approach used to develop them. Different research methods, including *in silico*, naturally lead to other suggestions regarding how the OEC works (more details are given in Chapter 6.1.2). However, all of these studies have one overarching cognitive objective in common. Indeed, a major step forward in understanding the functioning of the OEC was Joliot's observation of periodic oscillations of oxygen evolution in dark-adapted chloroplasts under the influence of short saturating flashes (P. Joliot, Barbieri, & Chabaud, 1969) and the linear four-step model of the oxidation cycle proposed by Kok et al. (Kok, Forbush, & McGloin, 1970). Extending the Kok model to a 5S - state model by explicitly including the metastable  $S_4$  state resulted in an excellent reproduction of the experimentally observed patterns of  $\text{O}_2$  release (Burda & Schmid, 1996). The presented studies focused on investigating the effects of the external proteins PsbO (~33 kDa), PsbP (~23 kDa) and PsbQ (~16 kDa) on the heterogeneity of the process of oxygen evolution in a higher plant. Although the role of these proteins is not yet fully understood, it is known that they play a protective role in stabilising the binding site of the  $\text{Mn}_4\text{O}_5\text{Ca}$  complex, ensuring ionic balance in its environment (mainly preventing the loss of calcium and chlorine ions). In addition, they are probably involved in regulating the access of water molecules to the OEC and removing  $\text{O}_2$  and hydrogen ions from it (Barry, Brahmachari, & Guo, 2017; Bricker & Frankel, 1998; Cammarata & Cheniae, 1987; Enami, Tomo, Kitamura, & Katoh, 1994; Hussein et al., 2021; Ifuku & Noguchi, 2016; Kruk, Burda, Jemioła-Rzemińska, & K., 2003; Sakashita, Watanabe, Ikeda, & Ishikita, 2017; Vass, Ono, & Inoue, 1987). Studying the heterogeneity of the OEC functioning modulated by endogenous factors, in this case external proteins, will contribute to a deeper understanding of the mechanism of water oxidation by PSII. In particular, they will provide insight into how long- and short-range interactions influence the OEC to ensure its operation under less favourable conditions.

## 2. The aim of the studies

Light-driven processes in the light phase of photosynthesis are the subject of research. In particular, the studies focused on Photosystem II (PSII) activity. Water is essential for the functioning of PSII. It is not only an electron donor for PSII. It is also crucial for transporting protons to and from the OEC catalytic centre and maintaining the entire network of hydrogen bonds involving amino acid residues responsible for the structure and dynamics of the protein matrix.

Although much is known about how PSII works, many questions remain to be answered before we can say that the fascinating mystery of water oxidation has been solved. The static picture of the functioning of the oxygen-generating complex containing the  $Mn_4CaO_5$  complex is widely discussed. However, it is already known that to understand how it works, it is necessary to consider the coordinated cooperation of its entire environment. For example, the heterogeneity of  $Mn_4CaO_5$  complex states at different stages of the Kok cycle is well documented, but its significance is unknown. This raises the question of whether these states, which can change dynamically in response to PSII conditions, are transient states that serve to optimise the functioning of the OEC enzyme or whether they determine two separate pathways of oxygen evolution within the system.

***Aim 1:*** *How does the heterogeneity of oxygen release depend on external proteins that stabilise the  $Mn_4CaO_5$  complex and participate in forming water channels?*

In order to achieve this goal, PSII BBY isolated from tobacco (*Nicotiana tabacum* var. *John William's Broadleaf (JWB)*) was studied using a fast three-electrode polarographic system with a standard measurement protocol and a newly developed protocol to measure the kinetics of different oxygen release pathways.

Another critical aspect of the research presented, in which PSII plays a significant role, is the design of an n-type self-organising semiconductor system that would operate in environmentally friendly conditions with the efficiency of oxygen release from water comparable to natural PSII and stimulated by electromagnetic radiation from a wide range of visible light. A colloidal system is the simplest of all. This allows the selected compound to interact with PSII without needing additional functionalisation or genetic modification of the biomaterial. A known semiconducting material stable in aqueous environments at neutral pH is  $WO_3$ .

***Aim 2:*** *How do  $WO_3$  NPs affect the organisation of the PSII BBY membrane? How does this affect light harvesting? How does this affect the process of oxygen*

*evolution? Can WO<sub>3</sub> NPs modify the heterogeneity of O<sub>2</sub> release? Under what conditions can WO<sub>3</sub> NPs stimulate oxygen production?*

To answer these questions, the effect of different concentrations of WO<sub>3</sub> nanoparticles on the activity of PSII BBY isolated from spinach (*Spinacia oleracea L.*) was investigated. Several complementary imaging techniques (AFM – atomic force microscopy, TEM – transmission electron microscopy), spectroscopic methods (absorption and steady-state fluorescence spectroscopy, light-induced variable fluorescence) and different measurement protocols using fast electrode polarography were applied.

### 3. Introduction to oxygenic photosynthesis

Photosynthesis is crucial for the existence of life on Earth as it is the primary energy source for most living organisms. Photosynthetic organisms convert solar energy into chemical energy in the form of organic compounds, such as glucose, which can be used to power cellular processes. Simultaneously, it plays a critical role in regulating the Earth's atmosphere by removing carbon dioxide and releasing oxygen as a byproduct, which maintains the conditions necessary for the development of life on our planet. In addition, photosynthesis is an essential food source and fossil fuel for humans.

The earliest forms of photosynthesis likely evolved in single-celled organisms around 3.8 – 3.5 billion years ago. These autotrophs possessed only one type of reaction centre (RC). Organisms capable of carrying out the currently known anaerobic photosynthesis absorb near infrared (NIR) light and use, among others, as electron donors: hydrogen sulfide or iron compounds. Unlike organisms capable of oxygenic photosynthesis, they cannot use water as a source of electrons. This is due to the low redox potential of their reaction centre and the lack of a structure capable of catalytic oxidation of water. (Björn & Govindjee, 2008, 2009) In Figure 1 the evolution direction of photosynthetic organisms is presented.

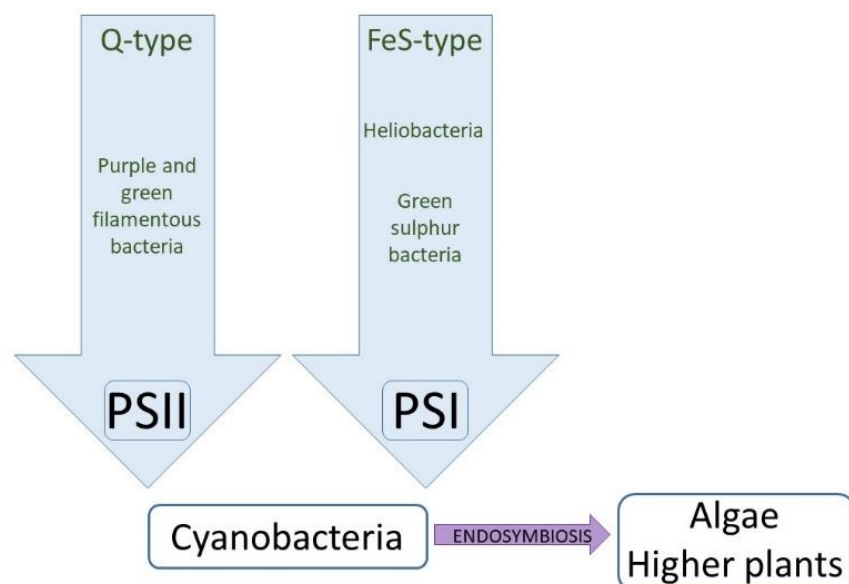
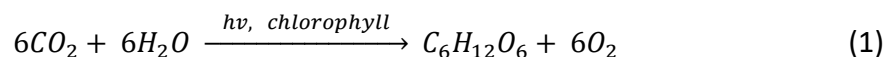


Figure 1 The evolution from anoxygenic to oxygenic photosynthesis. The scheme was based on (Björn & Govindjee, 2008, 2009) and references therein.

## 1.1 Oxygenic photosynthesis

Even though we use a simple notation to describe the oxygenic photosynthesis (Equation 1), it is a convolution of extremely complex biochemical processes.



where  $CO_2$  is carbon dioxide,  $H_2O$  is water molecule and  $C_6H_{12}O_6$  is glucose.

Oxygenic photosynthesis is a two-phase process. The light energy is absorbed in the light-phase by pigments such as chlorophylls (Chls), or carotenoids (Crt), which are embedded in the thylakoid membranes. The captured energy is then converted into chemical energy in the form of adenosine triphosphate (ATP) and nicotinamide adenine dinucleotide phosphate (NADPH). ATP and NADPH are used in the second phase of photosynthesis, called the dark phase or the Calvin cycle, and provide the energy and reducing power needed to fix carbon dioxide into organic molecules (e.g. glucose).

### *Protein-pigments complexes organisation in thylakoid membranes*

Chloroplasts' inner membranes, called thylakoids (Figure 2), are flattened, interconnected sac-like structures stacked together, forming grana. Grana are connected by intergranal lamellae (regions of unstacked thylakoids) (Staehein & Paolillo, 2020). Over the years, many theories and models have been developed to define the structure of thylakoids. Nowadays, the helical model of higher plants' thylakoid membranes presented in Figure 2b is widely accepted.

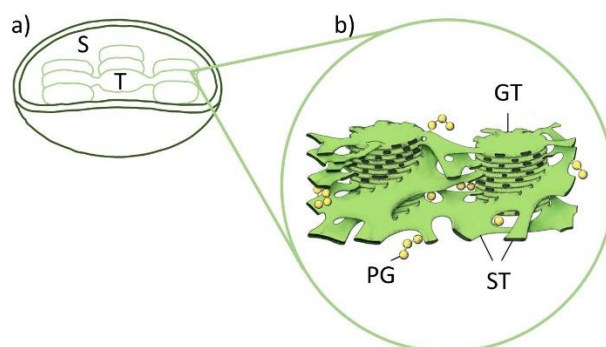


*Figure 2 The structures responsible for running photosynthesis are chloroplasts (a). Their inner membranes, thylakoids (T), contain complexes of proteins, lipids and pigments activated by light, called photosystems. The fluid-filled internal space within the chloroplasts is called stroma (S). It encircles the thylakoids. b) Grana thylakoids (GT) are stacks of thylakoid discs. They are primarily enriched in PSII, while unstacked thylakoid membranes, stroma thylakoids (ST), contain PSI and ATP synthase. Plastoglobules [PG] are lipoprotein subcompartments of the chloroplasts. The helical model of higher plants' thylakoid membranes was adapted from (Staehein & Paolillo, 2020).*

Thylakoid membranes comprise highly specific complexes of proteins, lipids and pigments activated by light, called photosystems. Photosystems contain specialised chlorophyll molecules and associated proteins that initiate light-dependent reactions by absorbing photons and transferring the energy to RCs. Thylakoids stacked in discs

(grana) include PSII – LHCII supercomplexes and PSII monomers, while PSI is embedded in unstacked parts of the membrane (Staelin & Paolillo, 2020). Figure 3 presents a detailed description of *Chlamydomonas reinhardtii* thylakoid membranes and their embedded complexes.

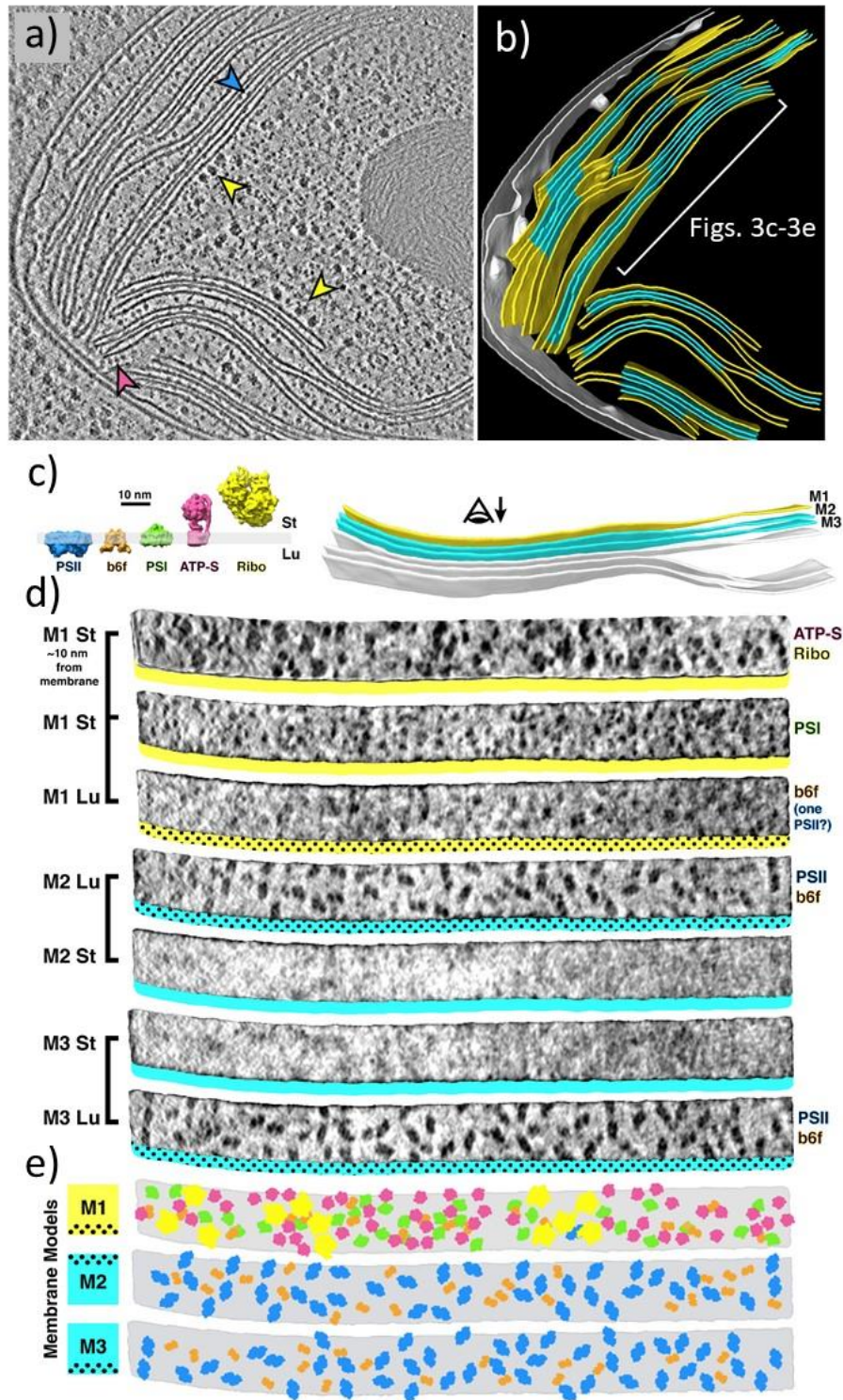


Figure 3 Architecture of photosynthetic apparatus. The native architecture of thylakoid membranes was obtained using cryo-electron tomography. All the pictures are taken from [4]. A chloroplast tomogram a) cross-section was obtained from an undamaged *Chlamydomonas* cell. The arrowheads indicate ribosomes bound to the membrane (yellow), ATP synthase (magenta), and PSII (blue). In the corresponding 3D segmentation of the chloroplast b), the

non-appressed membranes facing the stroma are represented in yellow, and the stacked membranes in close contact are depicted in blue. The diagram on the left (c) illustrates the extension of each molecular complex from the thylakoid membrane into the stroma (St) and lumen (Lu). In the lumen, large PSII (~4 nm) and smaller Cyt.  $b_6f$  (~3 nm) are observed. Thylakoid-bound ribosomes (Ribo) extend roughly 25 nm into the stroma. Also, PSI and the F1 region of ATP synthase (ATP-S) extend into the stroma at about 3 nm and 15 nm, respectively. Three segmented thylakoids from the region indicated in c) are examined on the right. Membranes 1-3 (M1-M3) are colour-coded to correspond to the (b). The eye symbol and arrow indicate the viewing direction. Membranogram renderings of M1-M3 are shown in d). All membranograms depict densities approximately 2 nm above the membrane surface, except for the top membranogram, which is expanded to display densities around 10 nm into the stroma. The stromal surfaces are underlined with solid colours, while the luminal surfaces are highlighted with a dotted colour pattern. The identified complexes on each surface are indicated on the right. A model representation of M1-M3 is provided in e), illustrating the organisation of all the thylakoid complexes. The colours used in the model correspond to the schematic in part c) (Wietrzynski et al., 2020).

### Linear and cyclic electron transfer

The primary role of the photosynthetic pigments is to absorb sunlight. Absorbed energy activates charge separation within PSII, which is the first step of the photosynthetic process. A linear electron transfer from PSII to PSI via cytochrome  $b_6f$  complex starts, and so does proton pumping from the stroma to the lumen (Figure 4).

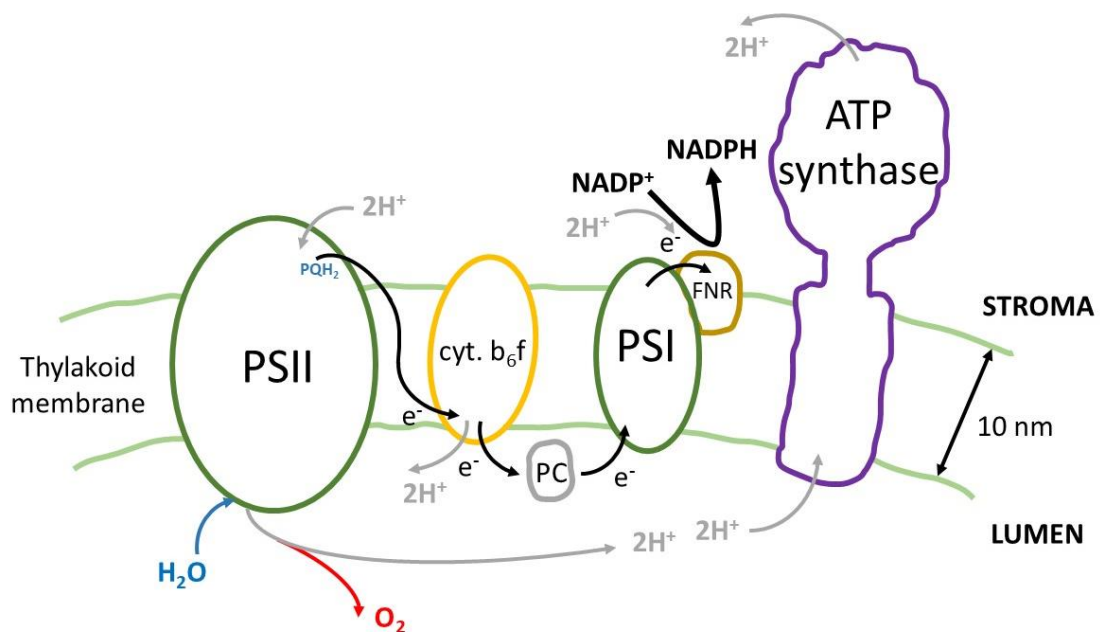


Figure 4 Electrons are extracted from water molecules in OEC embedded on the donor side of PSII. They are linearly transferred through PSII, cyt.  $b_6f$ , plastocyanin (PC) and then PSI. After absorbing a photon, PSI continue an electron transfer to FNR (ferredoxin – NADP<sup>+</sup> reductase). FNR completes the reduction of NADP<sup>+</sup> to NADPH. The dotted arrows indicate the pathway of cyclic electron transport around PSI. Simultaneously, an occurring proton gradient is used by ATP synthase to form ATP. The scheme was based on (Shikanai & Yamamoto, 2017).

When the pigment molecules in PSII absorb light energy, it excites electrons, raising them to a higher energy level. These excited electrons are then passed through a series of electron carriers in the thylakoid membrane, collectively known as the linear electron transport chain. As the electrons move along this chain, they release energy, which is used to pump protons ( $H^+$ ). The electron transport chain culminates in PSI, where the electrons are re-energised by absorbing more light energy. This energised

state allows the electrons to be transferred to a final electron acceptor, ferredoxin (Fd), and next to be used to reduce  $\text{NADP}^+$  to NADPH. This reduction reaction is catalysed by the enzyme ferredoxin-NADP<sup>+</sup>-reductase (FNR) (Shevela, Kern, Govindjee, & Messinger, 2023; Shikanai & Yamamoto, 2017).

Considering structures shown in Figure 4 as redox carriers characterised by their redox potential, one can construct a Z – scheme. The Z – scheme in Figure 5 visualises photosynthesis from an energetic perspective. Chlorophylls in P680 and P700 reaction centres are excited as a result of absorbing photons, and therefore, they increase their energy (Shevela et al., 2023).

Excited P680\* is a highly reducing agent that passes an electron to a pheophytin (Pheo). This electron is further transported via a primary electron quinone acceptor (a plastoquinone molecule, (PQ) bound at a Q<sub>A</sub> site to a secondary electron quinone acceptor (PQ) bound at a Q<sub>B</sub> site. After accepting two electrons and two protons from the stroma, plastoquinol (PQH<sub>2</sub>) is released from the Q<sub>B</sub> site. Plastoquinol delivers two electrons to cytochrome cyt. b<sub>6</sub>f and ‘pumps’ two protons from the stroma to the lumen (inner side of thylakoids). Plastoquinol delivers two electrons to cytochrome cyt. b<sub>6</sub>f and ‘pumps’ two protons from the stroma to the lumen (inner side of thylakoids). Plastocyanin (PC) accepts an electron from cyt. b<sub>6</sub>f and passes it to the PSI reaction centre, P700. Only after absorbing a photon is PSI able to continue electron transfer from PC to ferredoxin (FD). The following protein which transfers the electron is ferredoxin-NADP<sup>+</sup> reductase (FNR). FNR completes the reduction of NADP<sup>+</sup> to NADPH (Shevela et al., 2023).

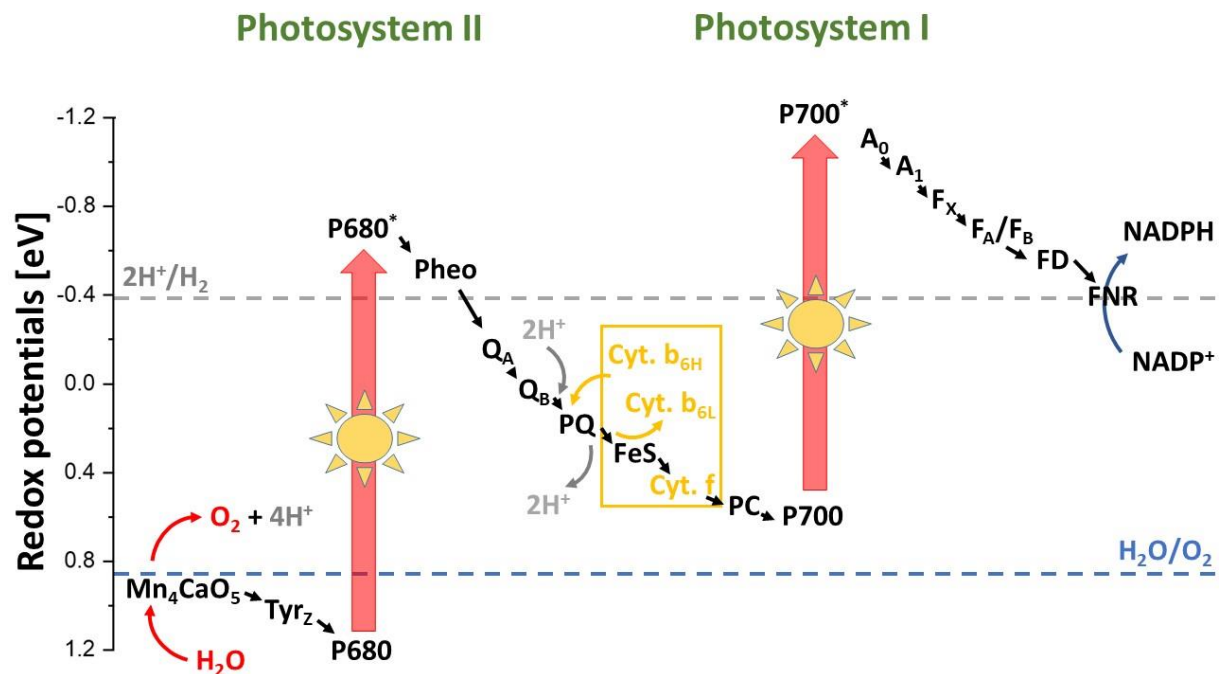


Figure 5 Z-Scheme is an electron pathway from OEC in PSII to NADP<sup>+</sup>. It shows the change of chemical potential in light-dependent reactions, which indicates the ability of a molecule to transport electrons. A linear electron transfer is marked with a solid black line. The diagram was based on Z-scheme by Govindjee, available on <https://www.life.illinois.edu/govindjee/textzsch.htm>.

## 1.2 Photosystem II in higher plants

Photosystem II is a crucial pigment-lipid-protein complex where photosynthesis starts. It contains about 20 subunits and has a molecular weight of about 300-350 kDa (Umena, Kawakami, Shen, & Kamiya, 2011). Mechanisms which occur in PSII are particularly noteworthy because of the PSII's ability to oxidise water. The structure of PSII is known from crystallographic measurements at 3.8, 2.9 and 1.9 Å resolutions (Ferreira, Iverson, Maghlaoui, Barber, & Iwata, 2004; Umena et al., 2011). The material used in those experiments originates from cyanobacteria as it is more stable and less complicated than photosystems in higher plants. By combining data from X-ray crystallography, Cryo-Electron Microscopy (cryo-EM) or X-ray free electron laser (XFEL), researchers have been able to determine the structure of PSII in higher plants (with an average resolution of 2.79 Å), providing detailed insights into its organisation, arrangement of protein subunits, and the positions of pigments and cofactors involved in light harvesting and electron transfer (Graça, Hall, Persson, & Schröder, 2021).

### Structure & functions

In higher plants, LHCII is a PSII antenna complex located on its periphery (Figure 6). The primary role of the light-harvesting system is to absorb a photon and transfer energy to the P680 reaction centre. Figure 6 presents plant PSII-LHCII supercomplexes of market spinach (a) and *Arabidopsis thaliana* (b) obtained using cryo-EM.

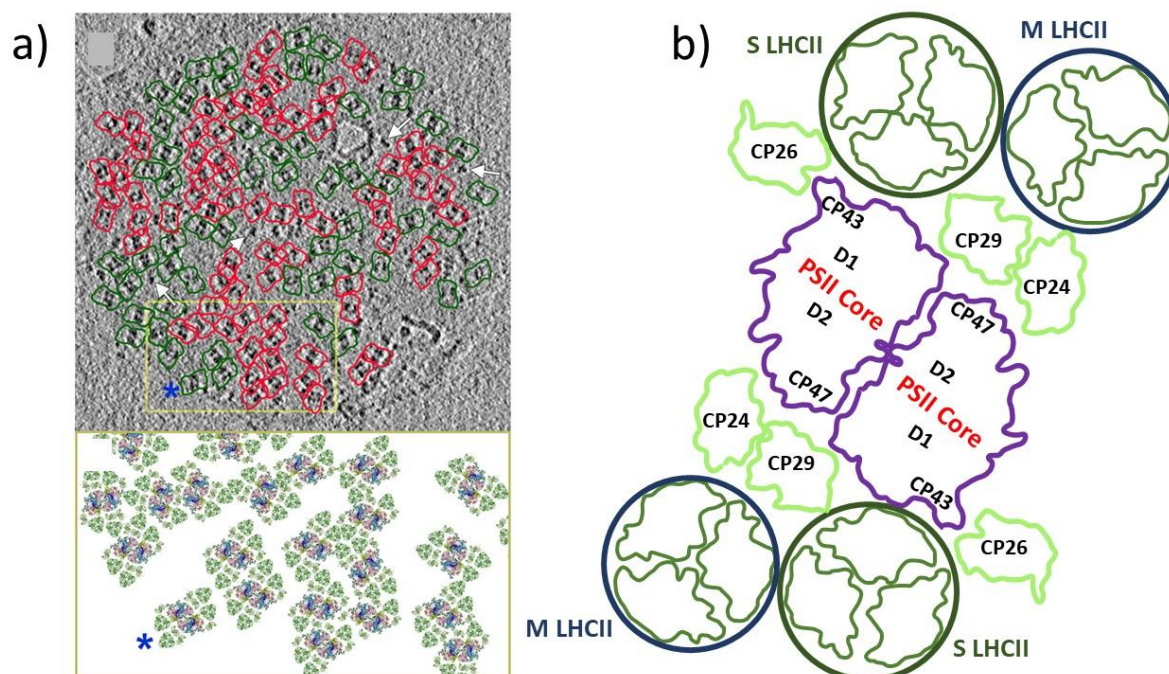


Figure 6 PSII supercomplexes. a) the upper part presents the contours of the complete C2S2M2 supercomplex in the tomographic slice of grana thylakoids. Green and red contours represent the positions of PSII complexes with no or significant clashes with neighbouring PSII complexes, respectively. White arrows point to smaller densities that have not been assigned but could potentially represent PSII monomers. At the bottom, a model illustrating the higher organisation of PSII supercomplexes is presented. A blue asterisk marks the corresponding area of the tomographic

data (Kouřil, Oostergetel, & Boekema, 2011). Figure b) shows an exemplary PSII – LHCII megacomplex ( $C_2S_2M_2$ ) model found in green plants and algae based on (C. -K. Lee, C. -W. Pao, & B. Smit, 2015b). Large PSII supercomplex is strongly (S) or moderately (M) bound to LHCII trimers.

Thylakoid macro-organization depends on environmental stimuli, so thylakoids are dynamic structures (Anderson, Horton, Kim, & Chow, 2012; Dekker & Boekema, 2005). Their optimal architecture is determined by PSII supercomplexes, which can vary in size depending on the number of LHCII trimers attached. The largest supercomplex contains strongly and moderately-bound LHCII trimers ( $C_2S_2M_2$ , Figure 6), and the minimal unit ( $C_2S_2$ ) is separated from the two moderately-bound LHCII trimers (2M). Still, intermediate states ( $C_2S_2M_1$ ,  $C_2S_1M_1$ ,  $C_2M_1$ ) and much smaller ones ( $C_2S_1$ ,  $C_2M_1$ ,  $C_2$ ,  $C_1S_1$ ) and larger supercomplexes are possible (Pagliano, Saracco, & Barber, 2013). The transformation between these different forms of PSII supercomplexes and their temporal and spatial stabilisation under specific conditions, depending on internal and external factors, aims to regulate and optimise the harvest and utilisation of light to facilitate diffusion processes inside and outside the membrane and to keep diffusion times short supporting the repair of light-damaged PSII [reviews: (Kirchhoff, 2008; Mullineaux, 2005)]. At the same time, LHCII aggregates may form (Johnson et al., 2011), and PSII core dimers can be reorganised, even leading to PSII monomerisation (Caffarri, Kouřil, Kereiche, Boekema, & Croce, 2009). Dissociation of the PSII supercomplex  $C_2S_2M_2$  is one of the photoprotective mechanisms essential for triggering non-photochemical fluorescence quenching (NPQ) (Betterle, Ballottari, Morosinotto, Zorzan, & Bassi, 2009). A significant challenge is to experimentally follow the different mechanisms that control the self-assembly of PSII-LHCII supercomplexes. In this case, the modelling approach has proven to be very helpful. Using a coarse-grained model of thylakoids, including two LHCII trimers (S2) firmly bound to the PSII core on antenna complexes CP26 and CP43 and two LHCII trimers (2M) moderately bound to the PSII core on antenna complexes CP24 and CP29 (see Figure 6), it was reported that there is a correlation between the free LHCII:PSII ratios, the membrane protein packing fraction, and the transitions between the ordered and disordered PSII supercomplex structures. It has been shown that the shifts of the equilibrium states between the individual superstructures  $C_2S_2 + 2M \leftrightarrow C_2S_2M_1 + M \leftrightarrow C_2S_2M_2$  are reversible and that the long-range order depends on the fluidity of the membrane, and thus, in particular on temperature (C. -K. Lee, C. -W. Pao, & B. Smit, 2015a). In addition, different conformers may occur within the supercomplexes. For example, it has been shown that in eukaryotic PSII, a monomeric CP29 antenna can switch between two different  $C_2S_2$  conformations, stretched  $C_2S_2str$  and compact  $C_2S_2comp$ , by changing its orientation, each of which may exhibit additional structural heterogeneity (Caspy, Fadeeva, Mazor, & Nelson, 2021). This flexibility of the PSII dimer core most likely ensures its optimal functioning under global as well as local variable conditions, including (i) efficient utilisation of light for charge separation, (ii) access of water and plastoquinones to the donor and acceptor PSII sides, respectively, and (iii) discharge of  $O_2$  and  $H^+$  outside the OEC.

Figure 7 presents the most famous cyanobacterial structures of Photosystem II at 1.9 Å resolution and 3.5 Å. The core complex of Photosystem II (Figure 8) in higher plants consists of several integral membrane proteins and cofactors responsible for light absorption, electron transfer, and water splitting. It includes the following major components:

- D1 and D2 proteins also known as PsbA and PsbD, respectively, are the core reaction centre proteins that coordinate the electron transfer process. They consist of transmembrane helices spanning the thylakoid membrane, with their N-termini facing the lumen (inside the thylakoid). D1 and D2 proteins harbour several redox-active cofactors, including chlorophyll a, pheophytin, plastoquinone, and iron-sulphur clusters, facilitating electron transfer within the reaction centre. Additionally, the D1 protein plays a critical role in the water-splitting process of oxygenic photosynthesis. It is associated with the OEC (Knoppová et al., 2022).
- CP43 (PsbC) and CP47 (PsbB) proteins form the core antenna system, which consists of chlorophyll and carotenoid pigments that capture light energy. CP43 and CP47 proteins play a role in stabilising the overall structure of the PSII complex. They provide a scaffold for assembling other PSII subunits and help maintain the integrity and functionality of the entire complex (Bricker & Frankel, 2002).
- Extrinsic proteins: They are a group of proteins associated with the PSII complex but located on the luminal side of the thylakoid membrane. They are involved in regulating water-splitting and thus oxygen evolution, and protecting the OEC from various environmental stresses. By interacting with the core components of PSII, these extrinsic proteins contribute to the overall efficiency of the photosynthetic process in plants. The main extrinsic proteins in plant PSII are PsbO, PsbP, and PsbQ (De Las Rivas, Balsera, & Barber, 2004; Enami et al., 2008; Nagao, Tomo, & Noguchi, 2015).
- Oxygen-Evolving Complex (OEC): The OEC is responsible for the water-splitting reaction that releases molecular oxygen. It comprises manganese ions (Mn), calcium ions (Ca), oxo-bridges and associated protein subunits (Umena et al., 2011).

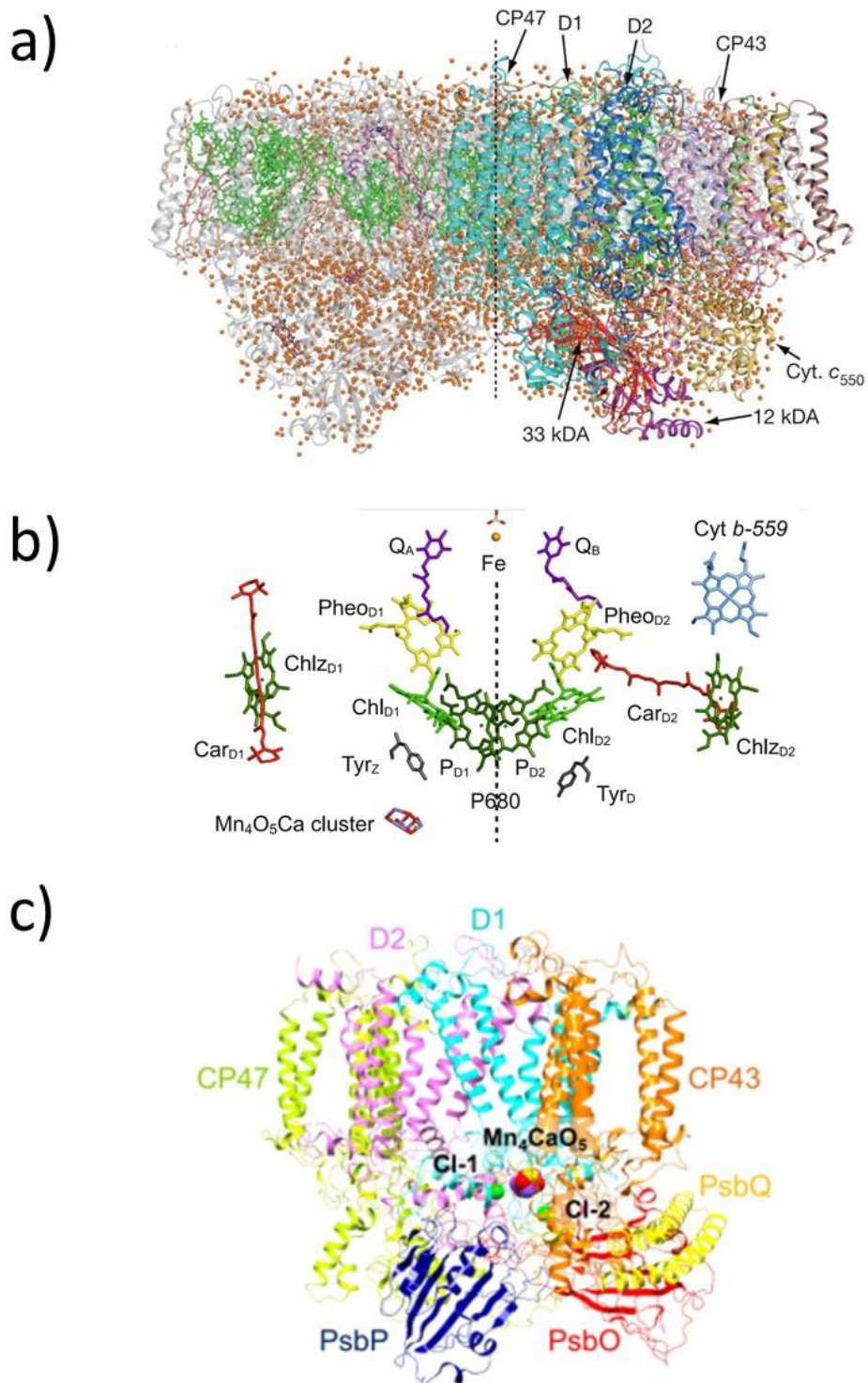


Figure 7 a) PSII structure isolated from thermophilic cyanobacteria *Thermosynechococcus vulcanus* at 1.9 Å resolution. The round orange points represent water molecules. There are visible two layers of water separated from each other with a layer of proteins (D1/D2- reaction core subunits, CP43/CP47- the proximal antenna proteins, cyt. c550, 12 and 33 kDa proteins). In higher plants, 33kDa accompanies two additional external proteins: 16 kDa and 23 kDa instead of 12 kDa, and cyt. c550. The left side of the figure shows green cofactors, invisible on the other side from the dashed line. The proteins are designated by colourful units on the right. Adapted from (Umena et al., 2011). b) The electron transfer cofactors are depicted perpendicular to the internal pseudo-twofold axis. Adapted from (Lubitz, Pantazis, & Cox, 2023). c) The cryo-electron microscopic structure of the spinach PSII protein complex (PDB: 3jcu<sup>1</sup>)(Taguchi et al., 2020).

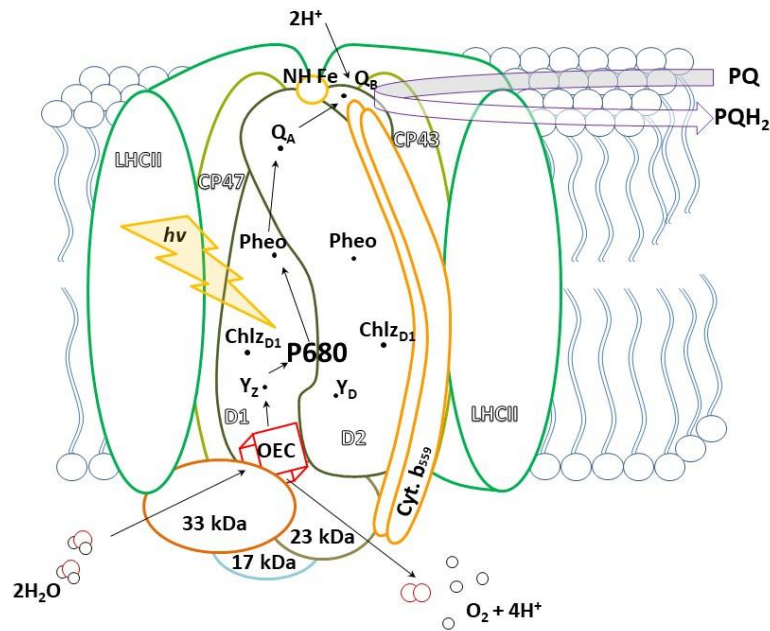


Figure 8 The core of the PSII reaction centre (RC) is a heterodimer D1/D2. Cytochrome b559 (cyt. b559) and proximal antenna proteins CP47 and CP43 are located in the vicinity of the RC core, as shown in the picture. The scheme also presents LHCII (light-harvesting complex II). Components of the donor side: OEC- oxygen-evolving complex,  $Y_Z$ - tyrosine 161 of the D1. The extrinsic proteins (33, 23, and 16 kDa) protect the OEC on the lumen side. The acceptor side consists of Pheo- pheophytin, PQ- plastoquinone,  $Q_A$ - plastoquinone bounded at the  $Q_A$  site, and  $Q_B$ - plastoquinone at the  $Q_B$  site. Additional components, plastoquinol ( $PQH_2$ ) and tyrosine 160 ( $Y_Z$ ) of the D2 protein are shown in the presented picture. A non-heme iron is located between  $Q_A$  (D2 protein) and  $Q_B$  (D1 protein) plastoquinones. Black arrows indicate the direction of linear electron transport.

### Electron transport within PSII

The processes which occur both on the donor and acceptor sides of PSII are marked in Figure 8. Although D1 and D2 proteins form a symmetrical reaction centre that provides two potential electron transport pathways, only one of them, whose components are located mainly on D1, is active (Allen & Williams, 1998). Excited  $P680^*$  is an electron donor to pheophytin (Pheo), a primary electron acceptor bound on the D1 protein. Pheophytin has a structure of Chl *a* compound without a central magnesium atom. Instead of magnesium, two hydrogen ions are attached inside the tetrapyrrole ring. After electron acceptance, pheophytin becomes a radical ( $Pheo^{\bullet-}$ ).  $P680^{*+}$  reacts with electrons provided by molecules from the reducing side of PSII, while  $Pheo^{\bullet-}$  reduces compounds on the oxidising side of PSII. These processes are responsible for the charge separation within photosystem II (Vinyard, Ananyev, & Dismukes, 2013).

An electron from  $Pheo^{\bullet-}$  is transferred to a primary electron acceptor, a plastoquinone (PQ) tightly bound at the  $Q_A$  site on the D2 unit. Finally,  $Q_A^{\bullet-}$  reduces a secondary plastoquinone acceptor, PQ, at the  $Q_B$  site on the D1 peptide. A non-heme iron atom supports the reaction between  $Q_A$  and  $Q_B$ . After receiving the first electron, partly reduced PQ remains at the  $Q_B$  site in a semiquinone form ( $PQ^{\bullet-}$ ), waiting for a

second electron from  $Q_A$ .  $Q_B$  is the only component of the system which can be double-reduced. After accepting two electrons, the secondary quinone acceptor binds two protons from the thylakoid stroma. Oxidised PQ exchanges reduced  $PQH_2$  at the  $Q_B$  site from an external plastoquinone pool in the membrane. Radical cation  $P680^{•+}$  is an even more potent oxidant than molecular oxygen. It is reduced by tyrosine  $Y_Z$  (D1- Tyr161) bound on the D1 protein.  $Y_Z$  accepts an electron from the OEC (Heathcote & Jones, 2012).

### 3.2.1 Acceptor side of PSII – Fe-quinone complex

The  $Q_A$  and  $Q_B$  binding sites in Photosystem II (PSII) play crucial roles in the electron transfer process. The plastoquinone molecule that binds to the PSII complex in  $Q_A$  binding site accepts an electron from the primary electron acceptor,  $P680^{•+}$ . Once  $Q_A$  receives the electron, it becomes reduced ( $Q_A^{•-}$ ). From there, it transfers the electron to the plastoquinone bound to the  $Q_B$  binding site. It accepts the electron from  $Q_A^{•-}$  and becomes reduced ( $Q_B^{•-}$ ).  $Q_B$  can undergo a two-electron reduction process, accepting two electrons and two protons from the surrounding medium. This reduction reaction converts  $Q_B$  to plastoquinol ( $Q_BH_2$ ), which then is released from its binding site and migrates to Cyt.  $b_6f$ . Once  $Q_BH_2$  is released, the binding site becomes vacant and ready to accept a new plastoquinone molecule (Q) from the surrounding pool of plastoquinone molecules in the thylakoid membrane (Vinyard et al., 2013).

There can be structural differences between  $Q_A$  and  $Q_B$  sites in plants, cyanobacteria, and algae. The  $Q_A$  and  $Q_B$  sites are located on the D2 and D1 protein subunits, respectively, within the PSII complex in plants and cyanobacteria (Grabolle & Dau, 2005; Umena et al., 2011).

As one can see in Figure 8, there is a non-heme iron (NHFe) molecule between  $Q_A$  and  $Q_B$  binding sites. Figure 9 provides a closer look at the NHFe vicinity. The exact role of NHFe is still under investigation.

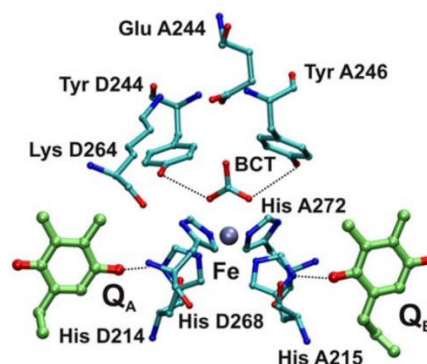
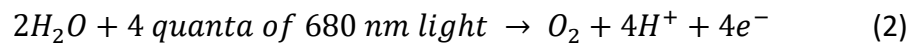


Figure 9 The scheme of *Thermosynechococcus vulcanus* PSII acceptor side (Müh & Zouni, 2020; Umena et al., 2011). The ligand environment of non-hem iron (Fe) is also visible.

### 3.2.2 Oxygen Evolving Complex

The process of water oxidation is the greatest mystery of photosynthesis. The unit responsible for water splitting is called an oxygen-evolving complex (OEC). Many scientific groups try to solve the puzzle and explain how it works. Frédéric Joliot made the most significant contribution to our understanding of the OEC mechanisms. His experiments and subsequent theoretical work (Kok model, thermodynamic calculations) show that the extraction of electrons from 2H<sub>2</sub>O can be summarised in a simple notation, as in Equation 2 (P. Joliot et al., 1969; Kok et al., 1970):



#### *Organisation & structure*

Despite the extensive work of different groups worldwide and their laboratory experiments, the complete structure and mechanisms of the OEC still need to be resolved. For now, this insuperable obstacle makes the OCE mechanisms impossible to explain thoroughly. However, constant progress is being made. To examine the OEC, a lot of experimental techniques are used, like: electron paramagnetic resonance (EPR), electron nuclear double resonance (ENDOR), extended X-ray absorption fine structure (EXAFS), mass spectroscopy (MS), polarography, or free-electron laser (FEL), for example, see: (Narzi, Mattioli, Bovi, & Guidoni, 2017; Pantazis, 2019; Yang, Lakshmi, Brudvig, & Batista, 2021).

The OEC is bound to the D1 protein from the lumen side of the thylakoid membrane and the CP43 protein. It consists of four manganese atoms, a calcium atom, and five oxygen atoms, creating a Mn<sub>4</sub>CaO<sub>5</sub> cluster, also referred to as a manganese complex (or Mn-cluster). Its environment is highly specific. It provides particular catalytic features of the OEC, such as the ability to split water molecules. This cubane-like structure is presented in Figure 10a. All manganese and calcium atoms are linked by di-μ-oxo- or mono-μ-oxo- bridges. Due to some significant differences in bond lengths, the cubane-like structure is not ideal but resembles a distorted chair. There are other molecules visible in the surrounding of the Mn<sub>4</sub>CaO<sub>5</sub> cluster, for example, chloride atoms, as well as many water molecules (Umena et al., 2011).

#### *Possible models of oxygen evolution. S – states*

The OEC undergoes a series of redox reactions and structural changes during the four-step water oxidation process. Kok observed that oxygen production in dark-adapted PSII systems exhibits damped oscillations with a periodicity of four (Kok et al., 1970). Kok et al. proposed a linear 4-step model that allowed coupling the four-electron oxidation of water to the single-electron turnover of the PSII reaction centre components under a photon absorption by the RC chlorophylls. This model assumes the successive accumulation of four positive charges through the OEC transient states called S<sub>i</sub> states, where (*i* = 0, 1, 2, 3, 4) indicates the number of positive charges stored in the

OEC on the  $\text{Mn}_4\text{CaO}_5$  complex). When sufficient oxidising power is accumulated, water molecules are split, an O - O bond is formed, and  $\text{O}_2$  is released (Kok et al., 1970).

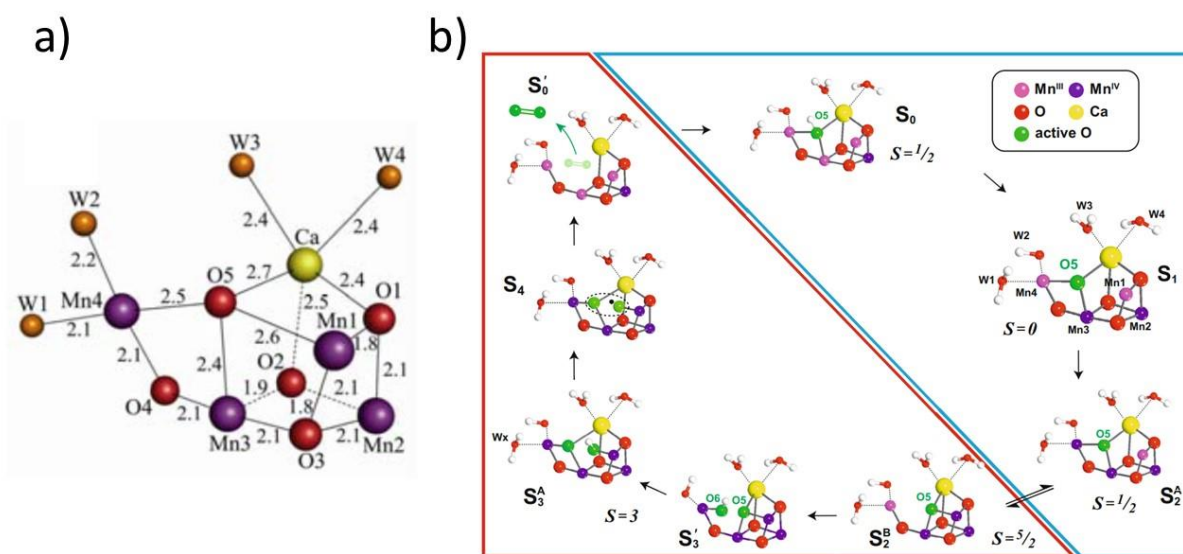


Figure 10 a) the OEC structure isolated from thermophilic cyanobacteria *Thermosynechococcus vulcanus* at 1.9 Å resolution (Umena et al., 2011). The distances are provided in Å. The labels Mn1-Mn4, O1-O5, Ca and W1-W4 follow the standard notation. b) The currently accepted scenario consists of open and closed conformations of the  $S_2$  and  $S_3$  states, and their possible transformations upon attaching a water molecule are adapted from (Lubitz et al., 2023) after modifications.

Some believe that forming a bond between two oxygen atoms is possible only after the accumulation of 4 positive charges, i.e. during the manganese complex's transition to the  $S_4$  state (de Lichtenberg, Avramov, et al., 2021; Ibrahim et al., 2020; Kusunoki, 2007; Vinyard, Khan, & Brudvig, 2015; B. Zhang & Sun, 2018). In contrast, others think it can already happen during the formation of the  $S_3$  state, which shows heterogeneity like the  $S_2$  state (Corry & O'Malley, 2018; Cox et al., 2014; Klaus, Haumann, & Dau, 2012; Mandal, Saito, & Ishikita, 2020; Pantazis, 2019; Pérez-Navarro, Neese, Lubitz, Pantazis, & Cox, 2016; Pushkar, Davis, & Palenik, 2018; Renger, 2012; Shoji, Isobe, & Yamaguchi, 2015; P. E. M. Siegbahn, 2008, 2009, 2018; Suga et al., 2017). Based on the crystal studies, it was concluded that the  $\text{Mn}_4\text{CaO}_5$  complex, which accumulates two positive charges and is in the  $S_2$  state, can adopt two different forms, open and closed. Examples of possible  $\text{Mn}_4\text{CaO}_5$  cluster configurations that can coexist are shown in Figure 10b. Each of the possible configurations of the  $\text{Mn}_4\text{CaO}_5$  complex at the various stages of its reorganisation associated with the accumulation of positive charge, the attachment of further water molecules and the release of protons is closely related to the valence changes of specific Mn ions, and consequently to the magnetic properties of the entire manganese cluster [for review see (Pantazis, 2019)]. Due to the very short lifetime of the  $S_4$  state, one can only try to determine the organisation of the OEC by modelling. This means it is impossible to say unequivocally what the actual stage of O=O formation and  $\text{O}_2$  release looks like.

The failure rate  $\alpha$  of the trapping centres (called misses) leads to a redistribution of the  $S_i$  states and, consequently, to a damping of the oscillations of the  $O_2$  release. In prolonged darkness, the OEC is mainly in the  $S_1$  state (usually  $\sim 75\%$ ) due to the oxidation of the  $S_0$  state by an electron carrier Tyr D (tyrosine of peptide D2, Figure 8) (Vermaas, Renger, & Dohnt, 1984; Zimmermann & Rutherford, 1985). So, the  $S_0$  state remains occupied at about 25%. Therefore, the first maximum is observed under the third flash. A small occupancy of the  $S_2$  state is also detected (a small  $O_2$  yield is observed under the second flash), but the higher states are unstable (Burda & Schmid, 1996). The original Kok model assumed equal misses for light-driven transitions  $S_n \rightarrow S_{n+1}$  and doubled effective excitation in a fraction  $\gamma$  of the centres in the  $S_0$  and  $S_1$  states (called double hits and equal). However, it has been shown that when this homogeneous model is used, there are significant discrepancies between the theoretical and experimental  $O_2$  yield patterns (Thibault, 1978). Moreover, it has been shown that the progressive damping of the oscillations is mainly due to misses. The heterogeneous model with different  $\alpha_i$  misses, omitting double hits, gives a better quantitative agreement with the experimental data obtained for other systems (Burda & Schmid, 1996; Delrieu, 1974, 1983; Lavorel, 1976, 1978). Additionally, it was found that the extension of the 4S-state Kok model to the 5S-state model (Figure 11), when the  $S_4$  state is introduced explicitly and its longer living isomer is considered, results in a much better fit between the theoretical and experimental data (Burda & Schmid, 1996).

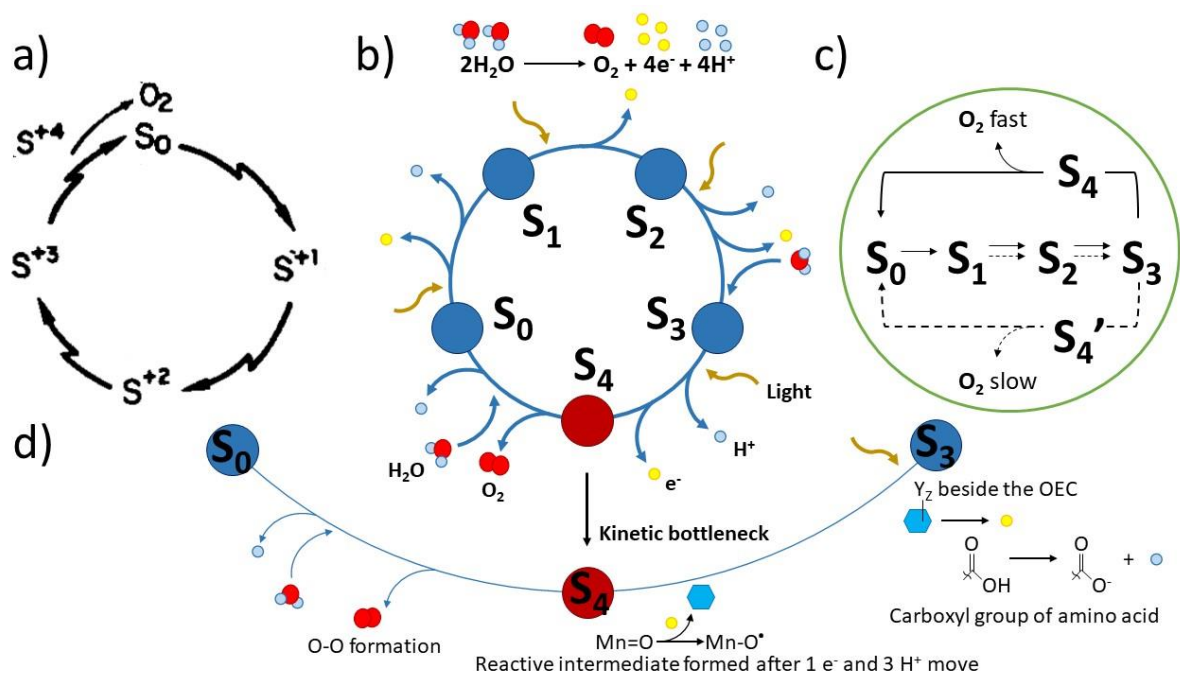


Figure 11 The OEC undergoes cycling between different states, referred to as S-states. a) The original 'Kok clock' was adapted from (Kok et al., 1970). b) One of the contemporary representations of the extended Kok model adapted from (Pantazis, 2023). The sequence and timing of individual steps during the transition from  $S_3$  to  $S_4$  and then to  $S_0$  have been shown by Bhowmick et al (Bhowmick et al., 2023). and Greife et al. (Greife et al., 2023). These events encompass movements of both  $e^-$  and  $H^+$ , involving transfers and exits in the vicinity of the OEC, which includes  $Y_z$  and other amino acid residues. A crucial reactive group ( $Mn-O^*$ ) is generated at the  $S_4$  stage, and this specific step serves as the rate-limiting factor, being the representation of a kinetic bottleneck for the entire reaction. The wavy line running through

*the bond of the carboxyl group presents its attachment to an amino-acid residue (Pantazis, 2023). c) The  $S_i$  state is assigned to a specific arrangement and oxidation state of the OEC, where  $i = 1, 2, 3, 4$ . After the OEC accumulates 4 positive charges, the  $O_2$  molecule is evolved, and the complex returns to its initial state. The model assumes two ways of oxygen evolution: fast and slow. Solid and dashed lines indicate a heterogeneous character of the OEC. The scheme is adapted from (Burda & Schmid, 2001).*

### *Channels for $H^+$ and $O_2$ and water transfer*

In Photosystem II, water,  $O_2$ , and proton channels are structural features that play essential roles during water oxidation process. There are many channels recognised within the whole complex and its vicinity (Hussein et al., 2023; Hussein et al., 2021; Sakashita, Watanabe, Ikeda, & Ishikita, 2017). Exemplary visualisations are presented in Figure 12. Water channels in PSII refer to specific pathways through which water network connects the OEC with the lumen side. These channels can provide routes for water molecules to reach the catalytic site where water splitting occurs. The water channels ensure a continuous supply of water molecules to sustain the oxygen-evolving reaction.  $O_2$  channels are channels through which molecular oxygen is released as a byproduct of the water-splitting. These channels allow the  $O_2$  molecules to exit the PSII complex and diffuse out of the thylakoid membrane. The proton channels in PSII are pathways that facilitate the movement of protons within the protein complex (Hussein et al., 2021; Sakashita, Watanabe, Ikeda, Saito, & Ishikita, 2017).

W1 ligand of  $Mn_4$  (Figure 10) is located at the entrance of the so-called 'narrow channel' (or O4 water chain) and is thought to be involved in proton removal from the OEC to the lumen and water entry (Dilbeck et al., 2012; Flesher et al., 2022; Ho & Styring, 2008; Vassiliev, Zaraiskaya, & Bruce, 2012; Yang et al., 2021). In cyanobacteria, the O4 channel is formed by residues of D1, D2, CP43, CP47, PsbO (a 33 kDa external protein, MSP - manganese stabilising protein) and PsbU (external protein subunits) connecting D1-D61 to the lumen. Still, on the other side of D1-D61, a 'broad channel', called also Cl1 channel, exists at the interface of the D2 and PsbO subunits (Ho & Styring, 2008; Umena et al., 2011; Vogt, Vinyard, Khan, & Brudvig, 2015). The ligand O5 is nominally closest to the Cl1 channel entrance. The Cl1 channel with its branching arms is indicated as an  $H^+$ -channel rather than a water delivery path (Bondar & Dau, 2012; Ishikita, Saenger, Loll, Biesiadka, & Knapp, 2006; Vogt et al., 2015), but the latter function cannot be ruled out either (Sakashita, Watanabe, Ikeda, Saito, et al., 2017). The so-called 'large channel' (or O1 water chain), a branched network, is formed in cyanobacteria by the identical protein subunits as the Cl1 channel with one difference: instead of PsbO, the PsbV subunit is involved. This channel is thought to remove  $O_2$  and deliver water to the OEC (A. G. Gabdulkhakov, Kljashtorny, & Dontsova, 2015a, 2015b; Ho & Styring, 2008; Vassiliev, Zaraiskaya, & Bruce, 2013). On the other hand, the sometimes recognised so-called 'back channel' appears to be inaccessible to water but permeable to  $O_2$  (Ho & Styring, 2008; Murray & Barber, 2007). Among the many water channels reported in cyanobacteria, the organisation of amino acids that form narrow and large channels is evolutionarily conserved in higher plants. In this case, a smaller number of PSII subunits

are involved in their formation. The subunits D1, CP43, PsbP (23 kDa external protein), and PsbQ (16 kDa external protein) are involved in the formation of the O1 water chain and D1, CP43, PsbP, and D2 in the construction of the O4 water chain (Sakashita, Watanabe, Ikeda, & Ishikita, 2017). The small radius of the O4 channel of about  $\sim 1.4$  Å in spinach suggests that water molecules are also arranged as a single chain in higher plants. A rigid water chain with powerful hydrogen bonds between the initial water molecules near the  $Mn_4CaO_5$  cluster and with its O4 atom indicates that the 'narrow channel' can transport protons via the Grotthuss mechanism since the activation energy of proton transfer is lowest when all water molecules are firmly bound in the H-bond network (Saito, Rutherford, & Ishikita, 2015; Stuchebrukhov, 2009; Takaoka, Sakashita, Saito, & Ishikita, 2016). Recently, a fascinating observation has been made. Namely, glycerol (commonly used as a cryoprotectant and stabiliser of isolated PSII), incorporated into the 'narrow channel' in cyanobacteria at a distance  $> 10$  Å from the OEC, affects the LS stabilisation of the  $S_2$  state of the  $Mn_4CaO_5$  complex, which adopts the 'open' conformation (Figure 10) as a result of disruption of the hydrogen bond network involving D1-D61 when it remains protonated. In the absence of glycerol (D1-D61 becomes deprotonated), both states of  $S_2$ , i.e. LS and HS (open and closed conformations), are virtually isoenergetic (Flesher et al., 2022). An analogous effect of regulation of the  $Mn_4CaO_5$  complex by allosteric interactions may also occur in higher plants, as indicated by the usual occurrence in their case of both spin states of the  $S_2$  state and the disappearance of the HS signal for  $S_2$  with an increase in the concentration of glycerol (Zimmermann & Rutherford, 1985).

The search for water, proton, and  $O_2$  transport pathways continues to be carried out by *in silico* experiments with various computational methods - including QM (quantum mechanics) / MM (molecular mechanics), MD (molecular dynamics), and CE (continuum electrostatics) / MC (Monte Carlo studies) using available PSII structures, even PSII thylakoid membrane model (Ogata, Yuki, Hatakeyama, Uchida, & Nakamura, 2013). Various research groups have pointed out similar patterns of water channels in cyanobacteria, but their purpose can only sometimes be clearly determined. Some counterparts have been found in higher plants. Still, even minor differences from cyanobacteria may be relevant to their precise control of protons and  $O_2$  output during water oxidation or water delivery to the OEC. Identifying these mechanisms is the greatest challenge. Learning about them is the key to getting a complete picture of how the OEC and PSII as a whole function. In general, water diffusion tends to require water-filled channels. Each water channel can potentially evacuate  $O_2$ , but its diffusion can also occur through hydrophobic pathways. It has been suggested that lipid clusters within PSII, due to their predominantly hydrophobic nature, may serve as an oxygen drain and mediate efficient, PSII-safe, and rapid release of  $O_2$  (A. Gabdulkhakov et al., 2009). A highly conserved small hydrophobic pathway in cyanobacteria and algae (prokaryotes and eukaryotes) has been identified at the beginning of the O1 channel and suggested to be responsible for facilitating  $O_2$  release from the OEC (Caspary et al., 2021).

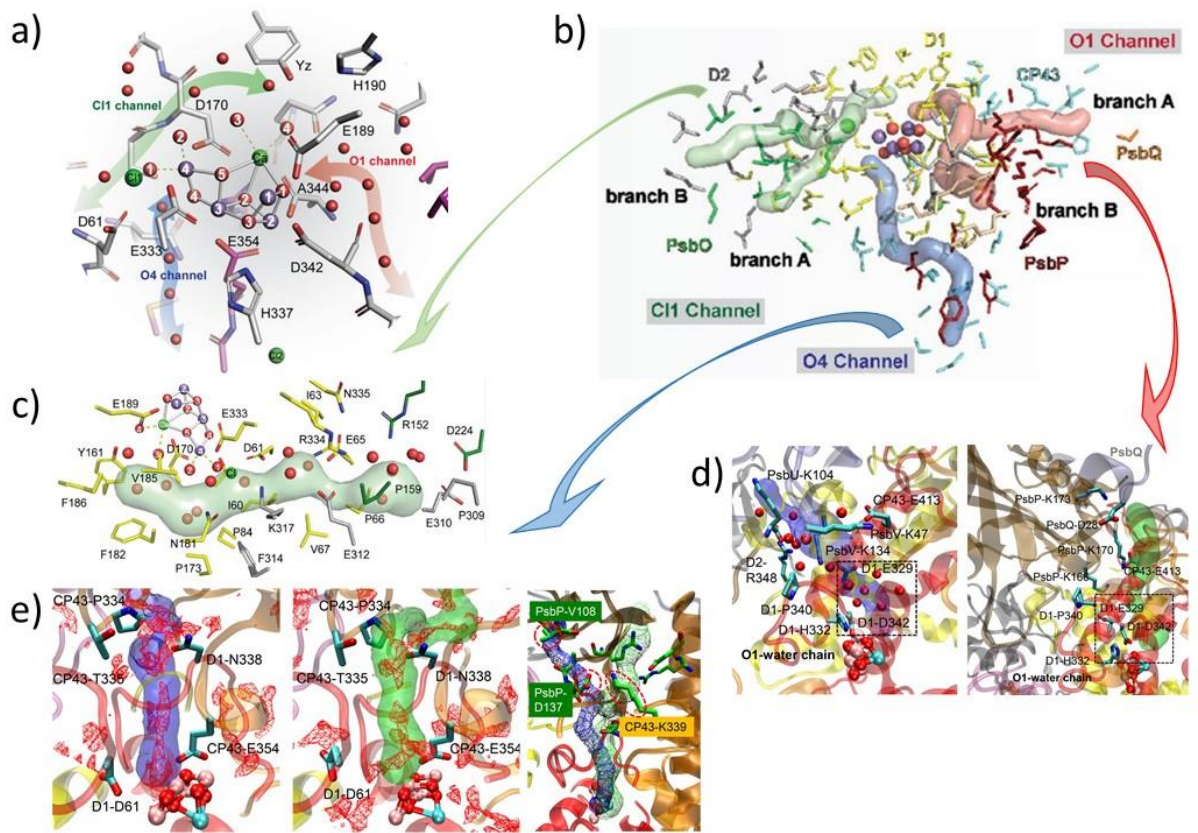


Figure 12 The figure presents different channels recognised in PSII of different species. A map a) adapted from (Hussein et al., 2023) reveals the presence of the three main water channels conserved in all species (the exact location, shape, and length can vary depending on the species). The O1 channel (branches A and B) is called ‘the large channel’ by some researchers. The O4 channel can be named ‘the narrow channel’, and branch A of the C1 channel is also referred to as ‘the broad channel’. b) The channels present in the plant *Spinacia oleracea* adapted from (Hussein et al., 2023). c) The calculated CIA channel and its surrounding environment in cyanobacteria *Thermosynechococcus vestitus* are coloured green, adapted from (Hussein et al., 2023). The d) panel depicts the O1-PsbU/V channel in cyanobacteria, coloured in violet, compared to the O1-PsbP channel in plants coloured in green (Sakashita, Watanabe, Ikeda, & Ishikita, 2017). The dotted squares demonstrate the D1 protein region. The panels presented in e) deliver the O4 channel: cyanobacterial O4-PsbU (left) and plant O4-PsbP (middle) channels. Also, on the right, the cyanobacterial O4-PsbU channel space is superposed into the plant cryo-EM structure (with a well-visible O4-PsbP channel) adapted from (Sakashita, Watanabe, Ikeda, & Ishikita, 2017; Wei et al., 2016).



## 4. Inorganic semiconductive systems

Nanomaterials based on low-dimensional  $\text{WO}_3$  structures exhibit chemical sensing properties and are being widely studied for applications as sensors in environmental engineering (L. Zhang et al., 2011). Due to their catalytic properties, they are among the materials with potential applications for water photolysis and  $\text{H}_2$  production, as well as degradation of organic pollutants [for review, see (Huang et al., 2015) and references therein; (Isari et al., 2020)]. Therefore, tungsten oxide nanoparticles may be a key material in fuel cell technologies in the near future. Moreover, it is considered a non-toxic, inexpensive material with good light resistance. It is chemically stable in aqueous media at  $\text{pH} < 7.0$  (Chen et al., 2016; Hardee & Bard, 1977; Hill & Choi, 2012).  $\text{WO}_3$  NPs possess different physicochemical properties depending on their size and structure (triclinic, monoclinic, orthorhombic, or tetragonal) (Cong, Tian, Li, Zhao, & Geng, 2014; Gullapalli, Vemuri, & Ramana, 2010). In  $\text{WO}_3$  (a stoichiometric compound), the metal centre is +VI and has no valence electrons ( $6s^05d^0$ ). Therefore, the energy band gap corresponds to electronic transitions from the top of the valence band formed by filled O 2p orbitals to the conduction band formed by empty W 5d orbitals (Deepa, Srivastava, Kar, & Agnihotry, 2006; Washizu, Yamamoto, Abe, Kawamura, & Sasaki, 2003). The observed size-phase-property correlation indicated that the decrease of grain size from about 50 nm to 9 nm results in a phase transition from a tetragonal to a monoclinic phase and an increase of the energy band gap ( $E_g$ ) from about 2.92 to 3.25 eV (Gullapalli et al., 2010). In contrast, the  $E_g$  value for  $\text{WO}_3$  bulk was estimated to be 2.62 eV (Koffyberg, Dwight, & Wold, 1979). Furthermore, quantum size effects determine the superiority of tungsten oxide NPs over bulk  $\text{WO}_3$  due to the increased efficiency of photoelectrochemical processes taking place in them. This is related to the increased stability of the photogenerated electron-hole pairs and the higher concentration of carriers on the grain surface (S.-H. Lee et al., 2006; Park et al., 2018; Sánchez Martínez et al., 2011; Zheng et al., 2011). In bulk tungsten oxide material, there is the problem of high electron-hole pair recombination rate or low electron transfer rate to molecular oxygen (Sclafani, Marci, & Venezia, 1998). Oxygen vacancies in nanostructured  $\text{WO}_3$  photoanode may modulate the charge carrier densities and the recombination kinetics across (Deb, 2008; Joya, Joya, Ocakoglu, & van de Krol, 2013). It was reported that a concentration of oxygen vacancies on the level of about  $\sim 2\%$  in the tungsten oxide provides optimal photoelectrochemical water oxidation in 0.1 M  $\text{H}_2\text{SO}_4$  solution (Corby, Francàs, Kafizas, & Durrant, 2020).

As early as the 1960s,  $\text{WO}_3$  was reported as an inorganic semiconductor capable of oxidising water in the presence of  $\text{Fe}^{3+}/\text{Fe}^{2+}$  as an electron acceptor (Krasnovskii & Brin, 1962). The quantum yield of  $\text{O}_2$  production from  $\text{H}_2\text{O}$  reached  $\sim 3\%$ . It was also observed that the deposition of 0.1%  $\text{RuO}_2$  or prior stirring of the  $\text{WO}_3$  powder for three

days in water increased the oxygen evolution rate by 2.5 and 2.0 times, respectively (Darwent & Mills, 1982). In these experiments, the highest observed rate of O<sub>2</sub> evolution was about 4.8 μmol g<sub>cat</sub><sup>-1</sup>h<sup>-1</sup> (per mass of catalyst, i.e. WO<sub>3</sub>). Low visible light utilisation and low O<sub>2</sub> production make tungsten oxide an unattractive material for commercial use in fuel cells. The formation of Z-scheme heterojunction composites/complexes of WO<sub>3</sub> with inorganic or organic compounds does not significantly change oxygen yield in these systems. For example, the performance of CuO/WO<sub>3</sub> and FePc/P-WO<sub>3</sub> was 2.79 and 3.6 μmol g<sub>cat</sub><sup>-1</sup>h<sup>-1</sup>, respectively (B. Li et al., 2020; Shi et al., 2019). Functionalisation of WO<sub>3</sub> by covalently anchoring a phosphonate-derivatized complex, Fe(tebppm<sub>cn</sub>)Cl<sub>2</sub> (tebppm<sub>cn</sub> = tetraethyl N,N'-bis(2-methylpyridyl-4-phosphonate) -N,N'-dimethylcyclohexyldiamine) increased the rate of water oxidation by 60% (Klepser & Bartlett, 2014). A stable and reproducible rate of O<sub>2</sub> evolution at 18 μmol g<sub>cat</sub><sup>-1</sup>h<sup>-1</sup> from water over 14 h was observed in the system consisting of Pt-doped WO<sub>3</sub> and g-C<sub>3</sub>N<sub>4</sub> at a weight ratio 1:1 (Martin, Reardon, Moniz, & Tang, 2014). In an optimised system composed of co-doped WO<sub>3</sub> with B and N anions, graphene (rGO), and CdSe quantum dots (6%CDSe/1%rGO3%BN-WO<sub>3</sub>), the oxygen evolution was 10-times higher than in WO<sub>3</sub>, i.e. 25.5 μmol O<sub>2</sub> g<sub>cat</sub><sup>-1</sup>h<sup>-1</sup>, but in the presence of cocatalyst 0.5%Rh<sub>x</sub>Cr<sub>2</sub>O<sub>3</sub>(0.5RCr) (Raziq et al., 2022). An order of magnitude higher efficiency of oxygen yield was detected in a two-step photocatalytic water splitting system (Z-scheme) consisting of a modified ZrO<sub>2</sub>/TaON and Pt-loaded WO<sub>3</sub> (Pt/WO<sub>3</sub>), working as H<sub>2</sub> and O<sub>2</sub> evolution photocatalyst, respectively, in the NaI presence ( ~ 266 μmol O<sub>2</sub> g<sub>cat</sub><sup>-1</sup>h<sup>-1</sup>) (Maeda, Higashi, Lu, Abe, & Domen, 2010). But nano WO<sub>3</sub> yellow-green powder from Aldrich Chemicals (estimated size of the grains: ~33 nm) in an aqueous solution of AgNO<sub>3</sub> showed even higher O<sub>2</sub> production, about 468 μmol g<sub>cat</sub><sup>-1</sup>h<sup>-1</sup>(Mills & Valenzuela, 2004). However, tungsten oxide nanoparticles from the same source with a radius five times greater exhibited twice less efficiency under the same experimental conditions.

For comparison, three examples of other Z-type heterojunction catalysts operating under optimised conditions, for which a significant increase in molecular oxygen emission under radiation in the visible spectral range was observed, are presented below. The rates of O<sub>2</sub> release given below have been converted, as before, per hour and gram of catalyst. For example, a high rate of oxygen evolution was reported for BiVO<sub>4</sub>/Au/CdS heterostructure, 138 μmol O<sub>2</sub> g<sub>cat</sub><sup>-1</sup>h<sup>-1</sup>, for long-term water overall splitting (X. Xu et al., 2021). 2D/2D polymeric Z-scheme heterostructures composed of ultrathin carbon nitride (g-C<sub>3</sub>N<sub>4</sub>) nanosheets (CNN) with varying levels of boron and nitrogen defects dopants (BDCNN<sub>350</sub>/BDCNN<sub>425</sub>) achieved excellent performance for catalytic O<sub>2</sub> evolution up to 700 μmol g<sub>cat</sub><sup>-1</sup>h<sup>-1</sup> in the presence of Pt and Co(OH)<sub>2</sub> co-catalysts (Zhao et al., 2021). However, a rate of O<sub>2</sub> production in 50Nb-TiO<sub>2</sub>/50 g-C<sub>3</sub>N<sub>4</sub> (mole percentage of Nb-TiO<sub>2</sub>/(Nb-TiO<sub>2</sub> + g-C<sub>3</sub>N<sub>4</sub>) was 50/50) was more than 2.4-time higher than in CNN, i.e. 1702 μmol O<sub>2</sub> g<sub>cat</sub><sup>-1</sup>h<sup>-1</sup> (Thanh Truc et al., 2019). The most efficient catalyst mimicking the activity of Mn<sub>4</sub>CaO<sub>5</sub>, i.e. the natural OEC, [OH<sub>2</sub>(terpy)Mn(O)<sub>2</sub>Mn(terpy)OH<sub>2</sub>] (NO<sub>3</sub>)<sub>3</sub>•6H<sub>2</sub>O in a solution of 0.07 M NaCl evolved O<sub>2</sub>

with an initial rate  $15 \text{ mmol/ g}_{\text{cat}}^{-1}\text{h}^{-1}$  within the first 15 minutes. However, during the first 2 hours, its activity dropped to about  $1.5 \text{ mmol/ g}_{\text{cat}}^{-1}\text{h}^{-1}$  (Limburg et al., 1999).

This shows that the rate of oxygen evolution under the influence of light per gram of active unit (i.e.  $\text{CR}_{\text{CaMn4O5}}\text{-CP43-CP47}$  complex) in PSII BBY is three to five orders of magnitude higher than that of  $\text{WO}_3$ -based catalysts and other inorganic or organic anode catalysts with high performance in water splitting systems.



# 5. Materials & methods

## 5.1 Biological material

The research was conducted on higher plants: a) freshly harvested laboratory-grown tobacco, *Nicotiana tabacum* var. *John William's Broadleaf* (JWB) and b) spinach *Spinacia oleracea*, purchased from the local market, freshly harvested (Figure 13).

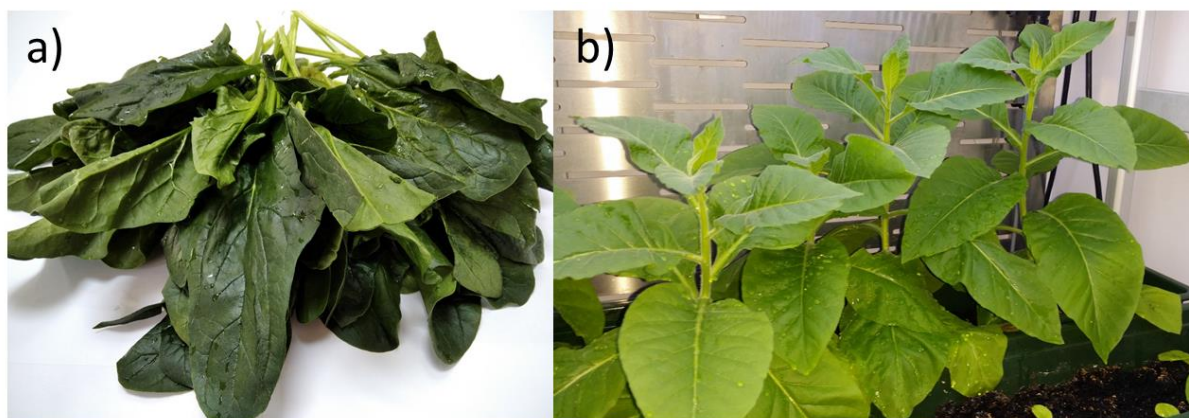


**Figure 13** Spinach purchased from the local market (a) and tobacco grown in laboratory conditions (b) were prepared for the studies presented in this work. Tobacco plants were grown in a plant growth chamber under moderate insolation conditions at 25 °C.

### Thylakoids isolation

Thylakoid membranes enriched with photosystem II (PSII BBY) were isolated from spinach or tobacco according to the procedure described in (Berthold et al., 1981) with some minor modifications. Tobacco PSII BBY samples were used to study the effect of proteins on oxygen evolution. PSII BBY from spinach were used in experiments on  $WO_3$  – PSII hybrid systems.

Freshly picked leaves were stored in the fridge at 4°C for an hour. They were then cut and mixed with cold elution buffer containing 10 mM NaCl, 5 mM  $MgCl_2 \cdot 6H_2O$ , 0.4 mM sucrose and 50 mM TRIS, pH 7.8 (Table 1). The obtained suspension was centrifuged at 1,500 rpm for 3 minutes at 4°C to separate the chloroplasts from the starch, and then the supernatant was centrifuged at 3,500 rpm for 10 minutes at 4°C. The sediment was washed twice with HEPES I buffer (pH 6.5). It was centrifuged at 3500 rpm for 10 minutes at 4°C. The chloroplasts were washed with HEPES II buffer (pH 6.5) and treated with 25% Triton X-100 for 20 min on ice. After incubation in Triton, the sample was centrifuged at

3500 rpm for 10 min. at 4 °C. The supernatant was centrifuged at 35,000 rpm for 12 min. at 4°C. The last step was repeated until the supernatant was colourless and clear.

Table 1 The buffers and solutions used in the thylakoid isolation procedure.

Buffer/Solution	Ingredients
HEPES I	15 mM NaCl
	5 mM MgCl <sub>2</sub>
	20 mM HEPES
HEPES II	15 mM NaCl
	5 mM MgCl <sub>2</sub>
	20 mM HEPES
	400 nM SUCROSE
ELUTION BUFFER	10 mM NaCl
	5 mM MgCl <sub>2</sub>
	400 mM Sucrose
	50 mM TRIS
TRITON X-100	25% TRITON X-100 in HEPES II

### Chlorophyll concentration determination

The chlorophyll concentration in the samples was determined by absorption spectroscopy according to (G. H. Schmid, 1971). The suspensions contained MeOH, distilled water and the sample were mixed in a Vortex-Mixer (PV-1 – MLS) and centrifuged (5000 rpm, 4 min, MiniSpin Plus – Eppendorf).

The following Equations 3 and 4 were used to determine the concentration of *Chl a* and *Chl b* in the sample:

$$[Chl a] = \frac{(E_{663} \times 45.6 - E_{645} \times 9.25) \times 1.16 \times V_R}{3585 \times V_S} \quad (3)$$

$$[Chl b] = \frac{(E_{645} \times 82.04 - E_{663} \times 16.75) \times 1.07 \times V_R}{3585 \times V_S} \quad (4)$$

where  $E_{663}$  stands for the absorption intensity for the wavelength 663 nm, and  $E_{645}$  stands for the absorption intensity for the wavelength 645 nm.  $V_R$  is a total solution

volume equal to 3 ml (methanol-based: 2.7 ml of 90% MeOH, 270  $\mu$ l of distilled water), and  $V_s$  is a sample volume equal to 0.03 ml.

The samples were diluted with HEPES II to a final total chlorophyll concentration of 2 mg/ml (PSII BBY from tobacco) and 1.13 mg/ml (PSII BBY from spinach), and stored at  $-80\text{ }^{\circ}\text{C}$ .

#### *Elution of the external PSII proteins*

Part of the PSII BBY sample from *Nicotiana tabacum* was used to prepare samples with eluted PSII extrinsic proteins according to the procedure described in (Burda, Strzałka, & Schmid, 1995; Ono & Inoue, 1983). Three sets of samples were prepared:

- PSII BBY control (all extrinsic proteins intact)
- PSII BBY depleted of two extrinsic proteins 16 kDa (PsbQ) and 23 kDa (PsbP), called later PSII BBY – 16,23;  
PSII BBY were washed with 1.5 M NaCl for 30 min.
- PSII BBY depleted of three extrinsic proteins 16 kDa (PsbQ), 23 kDa (PsbP) and 33 kDa (PsbO), called later BBY PSII – 16,23,33;  
PSII BBY were washed with 1.5 M  $\text{MgCl}_2$  for 30 min.

## 5.2 $\text{WO}_3$ nanoparticles

$\text{WO}_3$  NPs were obtained from tungsten trioxide hydrate. A complete synthesis procedure is given in (Gotic, Ivanda, Popovic, & Music, 2000), sample W3600. Briefly, 300 ml of 0.7 M HCl was added to 100 ml of the 1.0 M  $\text{Na}_2\text{WO}_4 \cdot 2\text{H}_2\text{O}$  solution until the final pH of the clear solution was 1.4. The obtained solution was autoclaved at  $60\text{ }^{\circ}\text{C}$  for 48 h, then isolated by centrifugation, and then dried in a Petri dish at  $60\text{ }^{\circ}\text{C}$ . This white powder sample ( $\text{WO}_3 \cdot 0.33\text{H}_2\text{O}$ ) was thermally treated at  $600\text{ }^{\circ}\text{C}$  to obtain yellowish  $\text{mWO}_3$  nanoparticles.

## 5.3 Electrophoresis

#### *Sample purification determination by SDS – PAGE*

Sodium dodecyl sulphate – polyacrylamide gel electrophoresis (**SDS – PAGE**) is an electrophoretic method developed by U. K. Laemmli in 1970 (Laemmli, 1970). It is commonly used to separate any proteins with molecular masses ranging from 5 – 250 kDa. The SDS–PAGE method was used to determine the elution efficiency of the three external proteins (PsbQ, PsbP and PsbO) from the PSII–LHCII complexes. Qualitative electrophoretic gel analysis aims to show the presence of a given protein by comparing

individual bands visible in a gel and the marker description provided by its manufacturer (Walkowiak B. & V., 2002).

### Experimental setup

Denaturing SDS – PAGE was performed in a vertical polyacrylamide gel system, [<https://www.bio-rad.com/en-pl/product/mini-protean-tetra-cell>] a Mini – Protean Tetra Cell apparatus (BioRad) presented in Figure 14. The setup consists of a buffer tank, an electrode assembly, a lid with power cables, a cell buffer dam, and a power supply. It enables researchers to perform electrophoretic separation on gels with 8.6 x 6.8 cm dimensions and a 0.75 – 1.5 mm thickness.

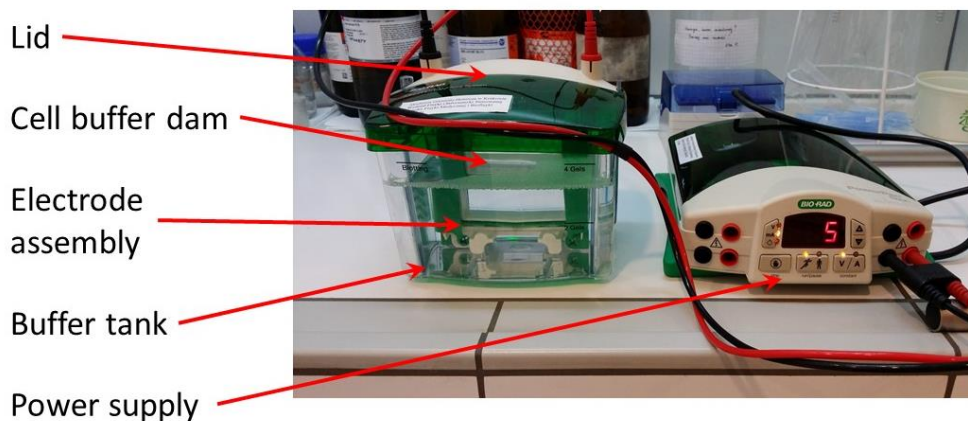


Figure 14 A Mini – Protean Tetra Cell apparatus.

### Measurement protocol

The detailed SDS-PAGE protocol based on (Laemmli, 1970) used in the present study was kindly provided by prof. Elżbieta Romanowska from the Department of Molecular Plant Physiology, Faculty of Biology, University of Warsaw. Minor changes were made to adapt the procedure to the biological material tested.

30% acrylamide solution (30 % AB solution) consisting of 29.2% acrylamide (Carl Roth) and 0.8% N, N-methylenebisacrylamide (Carl Roth) was used to prepare the running gels for the samples isolated from spinach 40% AB solution (38.9% acrylamide and 1.1% N, N-methylenebisacrylamide) was used to prepare the gradient running gel for the samples isolated from tobacco. Tables 2 and 4 show the compositions of running gels; Table 3 shows the composition of gel buffer used to prepare the gradient gel, and Table 5 shows the composition of stacking gels.

Table 2 The composition of the standard running gel, 1 mm thick, given in quantities (ml) to prepare 1 gel.

	15 %
30% AB solution	2.5

1.5 M Tris, pH 8.8 (Carl Roth)	1.3
H <sub>2</sub> O	1.1
10% SDS (POCH)	0.05
10% APS (Carl Roth)	0.05
TEMED (Carl Roth)	0.002

*Table 3 The composition of a gel buffer used to prepare the 10-20% gradient gel, given in quantities ml or g.*

1 M HCl	24 ml
Tris	18.2 g
SDS	0.4 g
TEMED	230 µl
H <sub>2</sub> O	Fill up to 100 ml, adjust pH to 9.4

*Table 4 The composition of a 10-20% gradient running gel, 1 mm thick, given in quantities (ml) to prepare 1 gel.*

	10 %	20%
Gel buffer	1.9	1.6
40% AB	1.9	3.7
1.5% APS	1.9	1.6
H <sub>2</sub> O	1.9	0.7

*Table 5 The composition of a stacking gel given in quantities (ml) to prepare 1 gel.*

	5%
30% AB solution	0.33
1.0 M Tris, pH 6.8	0.25
H <sub>2</sub> O	1.4
10% SDS	0.02
10% APS	0.02
TEMED	0.002

Before pouring the stacking gel, a 10-well comb was placed between the glass plates. The maximum volume of such a gel well was approximately 35 µl.

Protein samples were suspended in a 1:1 volume ratio in a denaturation buffer. The composition of the buffer is given in Table 6. Then, the samples were incubated at a high temperature (50°C) for 30 min and centrifuged at 12.000 x g, at room temperature, for 2 min. The adjusted amount of supernatant containing different concentrations of subsequent samples was injected into wells. Two wells were filled with the same amount of commercial protein ladder (ThermoFisher Scientific). The electrophoresis separation was conducted at 4°C, for 110 min, with constant current (30 mA for two gel

plates), using a running buffer composed of 192 mM glycine (POCH), 25 mM Tris (pH 8.3), and 0.1% SDS.

Table 6 The composition of a denaturation buffer given in quantities ml or g.

Glycerine (Lach:ner)	10 ml
SDS	2 g
Bromophenol Blue (POCH)	0.01 g
1.0 M Tris, pH 6.8	complete the buffer up to 100 ml
DTT (Carl Roth)	0.015 g per 1 ml of the buffer

After the separation, the gels were stained in the staining buffer (0.1% Coomassie Brilliant Blue G-250, POCH) for 3 hours. Then, the gels were decolourised by washing them in a 7% acetic acid (POCH) solution.

### Results

The electrophoretic separations performed confirm the correct procedure for isolating PSII BBY and eluting external proteins (Figure 15). Figure 15a shows the electrophoresis result obtained for the C1 control for PSII BBY isolated from spinach. Figure 15b shows the electrophoresis result obtained for the C3 control for PSII BBY isolated from tobacco and PSII BBY – 16, 23 (washed with NaCl) and PSII BBY - 16, 23, 33 (washed with MgCl<sub>2</sub>), second and third column respectively. M1 and M2 are the protein ladders.

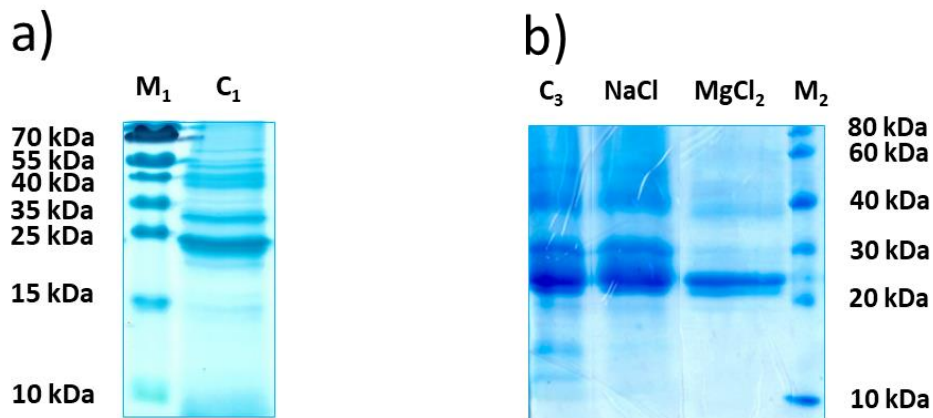


Figure 15 The SDS – PAGE results for the PSII BBY isolated from a) spinach and PSII BBY isolated from b) tobacco. In b) the results for PSII BBY - 16,23 and PSII BBY - 16,23,33 are also shown.

Both C<sub>1</sub>, and C<sub>3</sub> Controls have well-visible bands representing PSII RC and its accessory components, i.e. LHCII or extrinsic proteins (Caffarri et al., 2009). There are PsbO (33 kDa), PsbP (23 kDa), and PsbQ (16 kDa) bands visible. The second column in Figure 15b shows BBY PSII – 16, 23 sample where PsbP and PsbQ were disassembled from the complex. The third column in Figure 15b shows that the three extrinsic

proteins were removed in the sample PSII – 16, 23, 33) (Z. G. Wang, Xu, Liu, & Yang, 2010).

## 5.4 X – Ray Photon Spectroscopy – WO<sub>3</sub> NPs characterisation

X – Ray Photoelectron Spectroscopy (**XPS**) is an analytical technique based on the photoelectric effect and uses the radiation discovered by W. Röntgen. XPS was developed by Kai Siegbahn's group at Uppsala University in Sweden in the late 1960s (K. Siegbahn & Edvarson, 1956). By studying the energy of the photoelectrons, XPS can provide information about the sample's chemical composition, as different elements and chemical states have distinct binding energies (Hrynkiewicz & Rokita, 2013). In the presented research, XPS was used to determine the chemical composition of WO<sub>3</sub> nanoparticles. These WO<sub>3</sub> NPs were used to create colloidal systems with biological membranes. The XPS measurements were performed at the Jerzy Haber Institute of Catalysis and Surface Chemistry Polish Academy of Sciences in Kraków.

### *Experimental setup*

The atomic composition and the chemical state analysis of the samples were carried out using an Electron Spectroscopy for Chemical Analysis/X-ray Photoelectron Spectroscopy (ESCA/XPS) spectrometer equipped with a hemispherical analyser SES R4000 (Gammadata Scienta), pass energy 100 eV, presented in Figure 16. Core excitations were generated using an unmonochromatised Al K $\alpha$  X-ray source (1486 eV, 12 kV, 15 mA) without a charge neutraliser. The energy resolution of the system, measured as the full width at half maximum Ag 3d<sub>5/2</sub> excitation line, was 0.9 eV. The spectra were calibrated for a carbon C 1s excitation at a binding energy of 285 eV.

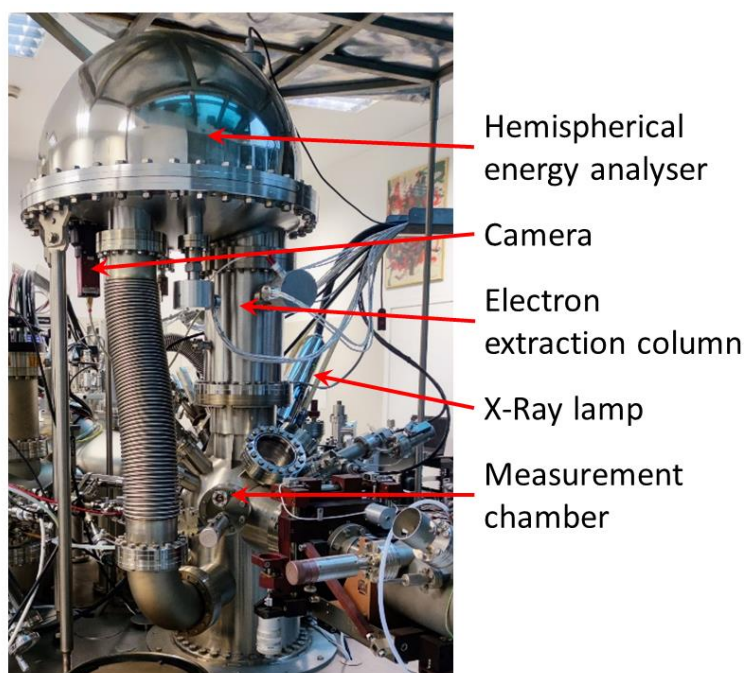


Figure 16 The ESCA/XPS spectrometer equipment. The photo provided by dr inż. Ewa Madej from IKiFP PAN.

### Measurement protocol

For XPS measurements, powder samples were pressed using a steel roller into a 99.9% pure indium piece. The prepared sample was mounted on a molybdenum holder (Figure 17).



Figure 17 A steel roller a), an exemplary sample pressed into an indium piece b), a molybdenum holder c).

The holder with the sample was pumped for several hours (4-12 hours) to achieve a vacuum of  $3 \times 10^{-7}$  mbar. Subsequently, the sample was transferred to the measurement chamber, where the base vacuum is  $6 \times 10^{-10}$  mbar. The standard photoelectron spectrum was collected at an angle of  $90^\circ$  relative to the sample surface. The analysed surface area was  $3 \text{ mm}^2$ . The overall spectrum was measured for each sample with a sampling step of 0.25 eV. The sampling step for the detailed spectrum in a narrow range was 0.025 eV.

### Data analysis

The spectra were analysed using the CasaXPS software and later presented using OriginLab. The background was approximated using the Shirley algorithm, and the

spectral lines were fitted using the Voigt function (a combination of Gaussian and Lorentzian functions in a 70:30 ratio).

### Results

In the overview spectrum of the WO<sub>3</sub> NPs sample (Figure 18), tungsten, oxygen and carbon predominate, accounting for 11.2%, 39.9%, and 44.1%, respectively. The sample also contains sodium 2.8% and nitrogen 1.8%.

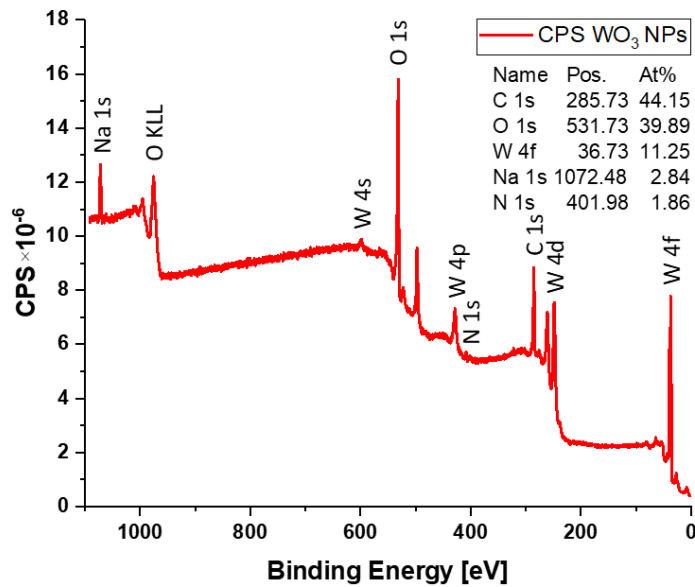


Figure 18 The high-resolution X-ray photoelectron spectrum of the WO<sub>3</sub> NPs.

On the tungsten core level line (Figure 19), a W 4f doublet is visible at an energy of 36.1 eV (W 4f<sub>7/2</sub>) and 38.2 eV (W 4f<sub>5/2</sub>). The intensity ratio of the lines is 0.75, and the spin-orbit splitting of the W 4f line is 2.1 eV, indicating that tungsten is in a 6<sup>+</sup> oxidation state (Cai, Li, Yang, & Guo, 2015; Keereeta, Thongtem, & T., 2015). This indicates the monoclinic structure of these WO<sub>3</sub> NPs.

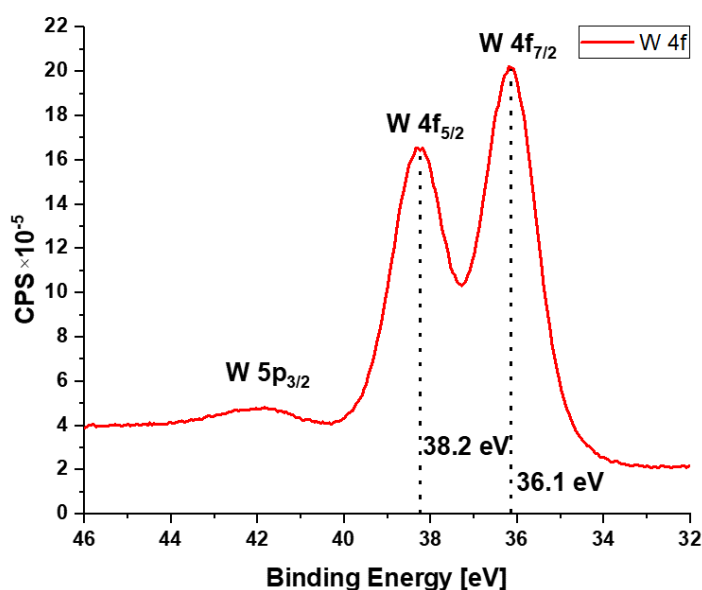


Figure 19 The high-resolution X-ray photoelectron spectrum of W 4f core level of the  $\text{WO}_3$  NPs sample.

## 5.5 Dynamic Light Scattering – $\text{WO}_3$ NPs characterisation

Dynamic Light Scattering (**DLS**) is based on light scattering and Brownian motion principles. The concept was first proposed by British physicist Peter Debye in 1947, but the first experiments validating its theoretical foundations were conducted in the 1960s (Berne & Pecora, 200). DLS is widely used in various fields of science and industry, including nanoparticle characterisation, protein aggregation studies, colloidal stability analysis, and biomolecular interactions. It provides valuable insights into particle sizes, size distributions, and molecular dynamics in solution (D., 2010; Lim, Yeap, Che, & Low, 2013). Together with XPS, the DLS method was used in presented studies to characterise  $\text{WO}_3$  NPs. The DLS experiments were carried out at the Jerzy Haber Institute of Catalysis and Surface Chemistry Polish Academy of Sciences in Kraków with the kind permission and assistance of prof. P. Warszyński.

The applied analyser Zetasizer Nano ZS (Malvern Panalytical Instruments) presented in Figure 20 can detect NPs sizes from 0.3 nm to 10  $\mu\text{m}$ . The instrument is equipped with a 4 mW He-Ne laser. The laser wavelength is 633 nm, and the scattered light is measured at a distance of 173 degrees [<https://apinstruments.pl/aparatura/malvern-panalytical/rodzina-zetasizer/zetasizer-nano/>].

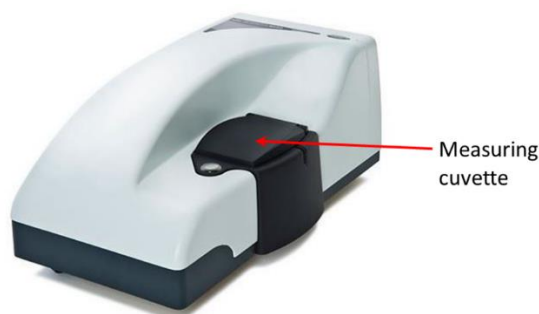


Figure 20 The Zetasizer Nano ZS analyser. The photo provided by [<https://www.malvernpanalytical.com/en/support/product-support/zetasizer-range/zetasizer-nano-range/zetasizer-nano-zs>].

### Measurement protocol

WO<sub>3</sub> NPs were suspended in the HEPES I buffer (15 mM NaCl, 5 mM MgCl<sub>2</sub>, 20 mM HEPES) at the initial 2 mg/ml concentration. Before each experiment, they were sonicated in a water bath for 20 min at 20°C. The DLS method checked their size distribution in the aqueous environment. After sonication and shaking, the samples were placed in a cuvette with an optical path length of 10 mm. The time of the measurements ranged from 70 to 80 s for solutions with NPs concentration  $2 \frac{\mu\text{g}}{\text{ml}}$  and  $0.2 \frac{\mu\text{g}}{\text{ml}}$ , and from 150 to 170 s for solutions with NPs concentration  $0.02 \frac{\mu\text{g}}{\text{ml}}$  and  $0.002 \frac{\mu\text{g}}{\text{ml}}$ .

### Data analysis

The data were automatically analysed in the Zetasizer software provided by Malvern Panalytical Instruments. The obtained parameters were the size of the nanoparticles, the standard deviation of that size, and the contribution. The data were later presented in OriginLab.

### Results

The intensity distribution can be converted into a volume or particle number distribution using the Mie scattering theory, refractive index and absorption. Due to the nature of the sample (polydispersity, aggregation of nanoparticles), the contributions of the fractions of NPs with different size are given by volume, instead of the intensity. Figure 21 presents the example data obtained for NPs samples containing  $0.002 \frac{\mu\text{g}}{\text{ml}}$  and  $0.02 \frac{\mu\text{g}}{\text{ml}}$  WO<sub>3</sub> NPs

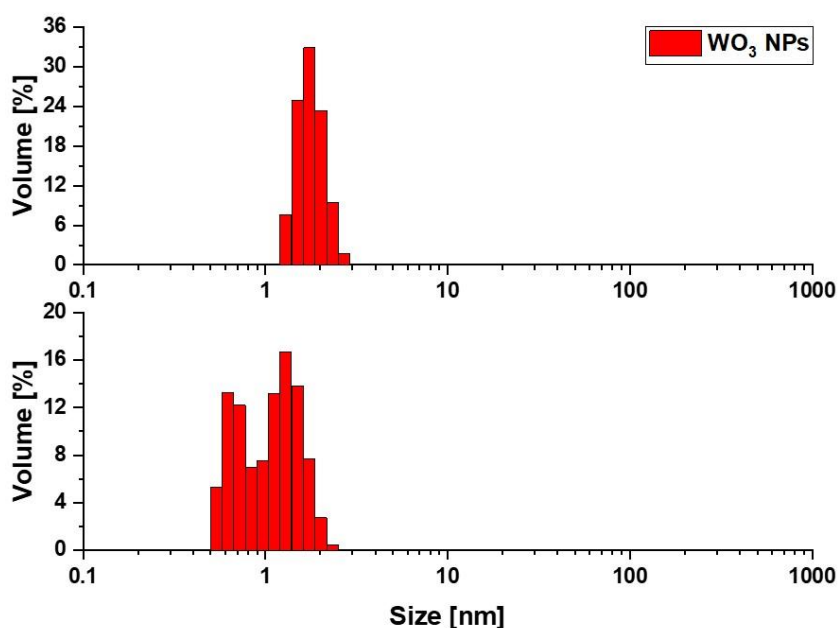


Figure 21 An example DLS results for monoclinic  $WO_3$  NPs suspended in HEPES I observed after sonification; the upper and lower graphs are for the concentration used:  $0.02$  and  $0.002 \frac{\mu g}{ml}$ , respectively.

Example volume distributions for nanoparticles with concentrations corresponding to the ratio  $1 \mu g$  NPs/ $\mu g$  Chl and  $0.1 \mu g$  NPs/ $\mu g$  Chl in the hybrid systems are shown in the upper and lower graphs, respectively (Figure 21). The HEPES I buffer gave no signal in DLS measurements. In the lower graph, the contribution of the NPs with an average size of about  $0.7$  nm and  $1.3$  nm is about  $35\%$  and  $65\%$ , respectively.

The results of DLS measurements of sonicated NPs suspended in the HEPES I buffer showed the presence of ultrafine  $WO_3$  NPs with sizes of  $0.68 \pm 0.10$  nm,  $1.30 \pm 0.30$  nm, and  $1.78 \pm 0.31$  nm. They accounted for  $70$  to  $100\%$  of the volume fraction in samples containing the highest nanoparticle concentrations tested. The fractions of larger nanoparticles and their sizes depended mainly on the time since sonication. However, larger crystalline structures were also present in the samples. In the DLS measurements, the larger nanoparticles observed had a size of about  $80 \pm 9$  nm or from about  $130 \pm 50$  to  $530 \pm 150$  nm, having a large dispersion. Theoretical calculations show that in monoclinic  $WO_3$  crystals the W-O bond distance is about  $1.8 \text{ \AA}$ , and the W-W distance between two corner  $[WO_6]$ -octahedra about  $3.8 \text{ \AA}$  (Juelsholt et al., 2021). Theoretical data usually yield parameters slightly overestimated than the experimental data, which for W-O distances vary between  $1.72$  and  $2.15 \text{ \AA}$  (Loopstra & Boldrini, 1966). The experimentally determined size of  $WO_3$  elemental cell is about  $7.3 \text{ \AA} \times 7.53 \text{ \AA} \times 7.68 \text{ \AA}$  (Tanisaki, 1960). Thus, the smallest  $WO_3$  nanostructures observed correspond to a cell containing eight molecules of  $WO_3$ . A similar result is obtained by assuming that the tungsten trioxide nanoparticles are spherical with a diameter of about  $0.7$  nm (a volume of  $\sim 0.179 \text{ nm}^3$ ), the average radius of a  $WO_3$  particle is about  $1.8 \text{ \AA}$  (a volume of  $\sim 0.024 \text{ nm}^3$ ) and the distance of the W-O-W bond is about  $3.6 \text{ \AA}$ . Similarly, it can be estimated that the

nanoparticles with diameters of about 1.3 nm (a volume of  $\sim 1.150 \text{ nm}^3$ ) and 1.78 nm (a volume of  $\sim 2.953 \text{ nm}^3$ ) contain about 48 and 123  $\text{WO}_3$  particles, respectively. Note that these numbers are of the same order as  $4^3$  and  $5^3$ , which would result from a dimensional analysis.  $\text{WO}_3$

NPs solutions, consist of small nanoparticles ( $\sim 1\text{-}3 \text{ nm}$ ); therefore, it can be concluded that they both are able to penetrate inside the thylakoid membranes.

## 5.6 Absorption Spectroscopy

Absorption spectroscopy is a technique used to study the interaction of electromagnetic radiation (typically in the ultraviolet (UV) or visible (Vis) regions) with the matter. It involves measuring the amount of light absorbed by a sample as a function of the wavelength or frequency of the incident light. The sample absorbs specific light wavelengths, corresponding to the energy required to promote electrons from lower to higher energy states. The absorption spectrum obtained provides information about the electronic and molecular structure of the sample and its activity in charge separation and recombination (Dittrich, 1988; Kozak & Niedzielski, 2011).

### *Experimental setup*

The influence of NPs on the PSII BBY was monitored by absorption measurements using UV-VIS Spectrophotometer Varian Cary 50 Bio (USA) presented in Figure 22. A 1 cm path-length quartz cuvette was used.

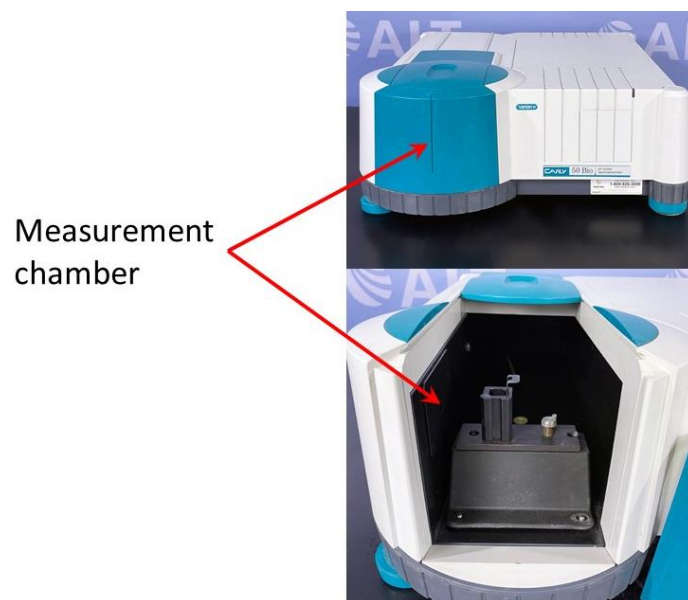


Figure 22 UV-VIS Spectrophotometer Varian Cary 50 Bio [<https://americanlaboratorytrading.com/lab-equipment-products/varian-cary-50-bio-uv-visible-spectrophotometer-6069>].

### Measurement protocol

PSII BBY untreated or treated with NPs, suspended in the HEPES I buffer (3 ml volume), were incubated on ice for 7 minutes in the darkness. During this time, they were shaken. They were then placed in the measuring chamber under dim light conditions and incubated again for 10 minutes in the darkness before measurement. The experiments were conducted in the wavelength range from 200 nm to 800 nm.

### Data analysis

Collected absorption spectra were analysed using OriginLab. The HEPES I spectrum was subtracted from the spectrum of the solution. Subsequently, the exponential part was removed from the resulting plots.

### Results

For the nanoparticle solutions, the wavelength value was then converted to energy units. This operation allowed determining the energy gap values for  $\text{WO}_3$  NPs used in the research. Figure 23 shows the relationship between  $(Ah\nu)^2$  and  $h\nu$  of  $\text{WO}_3$  NPs at a concentration of  $0.1 \mu\text{g NPs}/\mu\text{g Chl}$  suspended in HEPES I buffer, pH 6.5. Parameter  $A$  is the absorption intensity,  $h$  is Planck's constant,  $\nu$  is the photon frequency, and  $E_g$  is the band gap. The optical absorption for the direct transition has the following form near the band edge:  $Ah\nu \approx (h\nu - E_g)^{1/2}$  (Butler, 1977). From this relation, the optical band gap was determined. In our case, it is  $\sim 3.45 \text{ eV}$ , which is larger than the bulk  $\text{WO}_3$ .

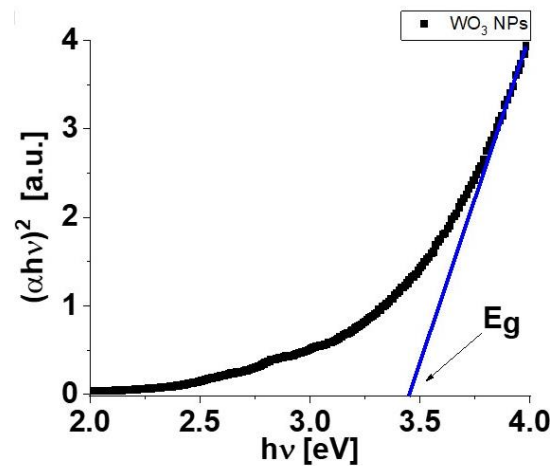


Figure 23 Energy gap values defined for  $\text{WO}_3$  NPs.

The exemplary absorption spectrum for a photosynthetic sample is presented in Figure 24. The results and discussion of the data can be found in Chapter 6, *Results and Discussion*.

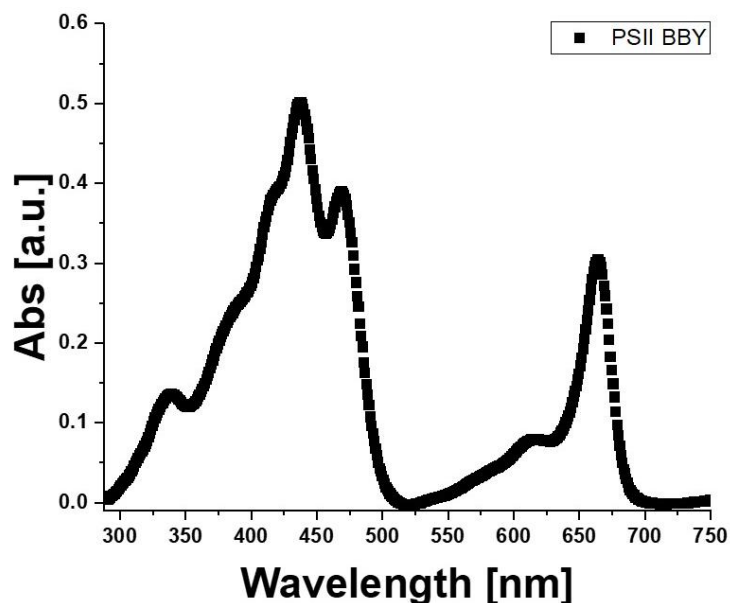


Figure 24 An example absorption spectrum of PSII BBY sample.

## 5.7 Fluorescence Spectroscopy

Fluorescence spectroscopy measures the emission of light from the sample after it has absorbed light energy. It provides information about the wavelengths and intensity of the emitted light. When a sample absorbs light at a specific wavelength, it can become excited to higher energy states. As the excited state is typically unstable, the sample relaxes back to its ground state by emitting light at longer wavelengths, usually in the visible or near-infrared regions. This emitted light during the transition of an excited molecule between the lowest level of the first excited singlet state ( $S_1$ ) and the ground singlet state ( $S_0$ ) is known as fluorescence. Fluorescence spectroscopy is widely used in photosynthetic research to assess energy transfer dynamics and efficiency of energy transition from light-harvesting complexes to reaction centres (Maxwell & Johnson, 2000).

### *Experimental setup*

A fluorometer Cary Eclipse Fluorescence Spectrometer Agilent (USA) is shown in Figure 25. For the measurements, a 1 cm path-length quartz cuvette was used.



Figure 25 Cary Eclipse Fluorescence Spectrometer Agilent (USA) [<https://www.agilent.com/en/product/molecular-spectroscopy/fluorescence-spectroscopy/fluorescence-systems/cary-eclipse-fluorescence-spectrophotometer>].

### *Measurement protocol*

Untreated or NP-treated PSII BBY samples, suspended in a 3 mL volume of HEPES I buffer, were incubated for 7 min on ice in the dark with gentle shaking. Subsequently, the samples were transferred to the measuring chamber under dim light conditions and incubated for an additional 10 minutes in the darkness prior to the measurement. Emission fluorescence experiments were conducted in the wavelength range from 600 nm to 850 nm, under excitation radiation varying from 375 nm to 495 nm in 5 nm increments.

### *Data analysis*

The fluorescence spectroscopy data were collected as 3D fluorescence maps presented in Chapter 6, *Results and Discussion*. Collected absorption spectra were analysed using OriginLab. An exemplary fluorescence spectrum for PSII BBY isolated from spinach excited with the radiation of a 480 nm wavelength is shown in Figure 26.

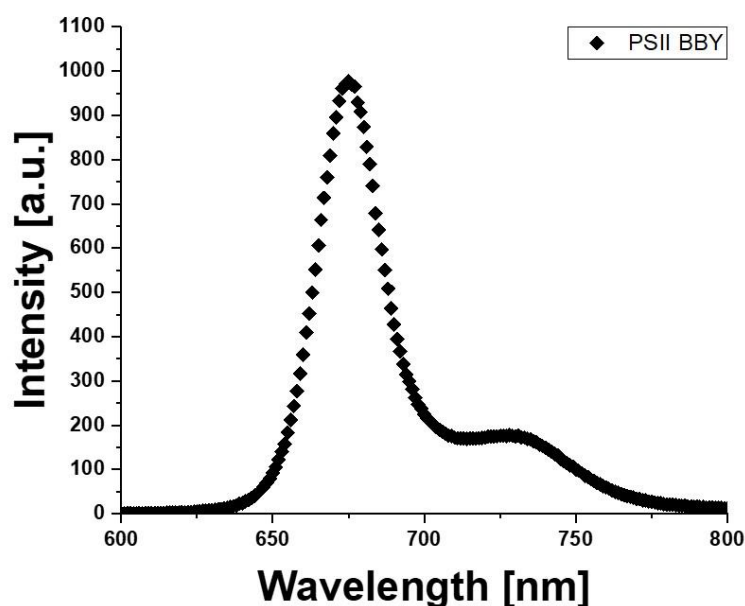


Figure 26 An example fluorescence spectrum of PSII BBY isolated from spinach.

The spectra for excitation radiation 440 and 480 nm were extracted for further analysis to obtain information on the energy transfer from LHCII and the minor antenna to PSII RC in the PSII BBY samples. Next, they were normalised to the value registered for an emission wavelength of 720 nm. The difference spectra  $\Delta = 480-440$  nm were prepared from such normalised spectra obtained for PSII BBY control sample and the colloidal systems PSII BBY-  $\text{WO}_3$  NPs.

## 5.8 Pulse – Amplitude Modulated Fluorescence

In Pulse-Amplitude Modulated (**PAM**) fluorescence, a modulated light source excites the photosynthetic pigments, typically chlorophylls. The modulation involves periodic light pulses with varying intensities, typically in the form of rapid on-off cycles. The fluorescence emitted by the sample is detected and analysed to derive several parameters that reflect the photosynthetic performance. A characteristic rise in chlorophyll fluorescence emission due to transitions from a dark-adapted state to an illuminated state is a visualisation of the Kautsky effect (Kautsky & Hirsch, 1931).

### Experimental setup

The double modulation fluorometer FL 3300 (Photon Systems Instruments, Czech Republic) used in the experiments is presented in Figure 27. The fluorometer allows recording the initial fluorescence signal with a 20  $\mu\text{s}$  time resolution.

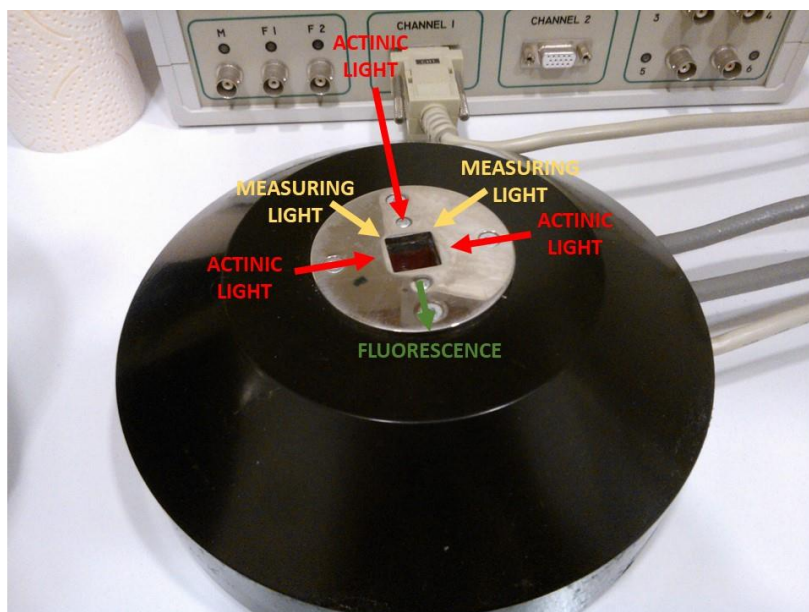


Figure 27 The measuring head of double modulation fluorometer FL 3300 with the scheme of light sources (Trtilek, Kramer, Koblizek, & Nedbal, 1997).

The instrumentation applies continuous actinic light (time duration up to several seconds,  $2300 \mu\text{Em}^{-2}\text{s}^{-1}$ ) having a wavelength maximum at 480 nm and measuring orange flashes ( $\lambda_{\text{max}} = 620 \text{ nm}$ ) of 2-5  $\mu\text{s}$  length. It uses two light sources to separate photosynthesis-driving reactions (actinic light) and fluorescence emission (low-power light).

#### Measurement protocol

The fluorescence induction curves were observed in dark-adapted samples. PSII BBY untreated and treated with various  $\text{WO}_3$  NPs concentrations were suspended in the HEPES I buffer (7 ml volume) and incubated on ice for 7 minutes in the darkness. They were then placed in the measuring chamber and incubated again for 10 minutes in the dark before measurement.

#### Data analysis

The collected data were analysed using OriginLab. They are presented and discussed in Chapter 6, *Results and Discussion*. An exemplary fluorescence induction curve of the Kautsky effect is shown in Figure 28:

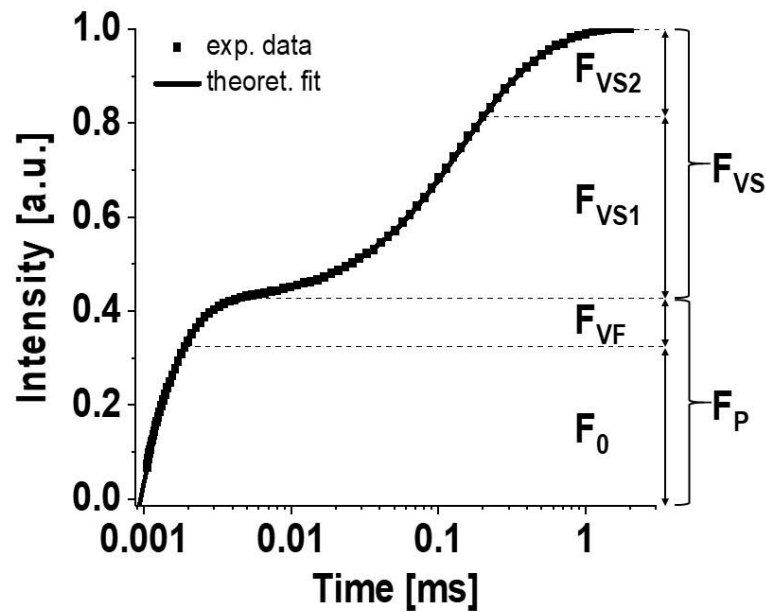


Figure 28 The Kautsky curve of the PSII BBY fluorescence. The plateau of fluorescence  $F_P$  value includes the initial fluorescence  $F_0$  (related to the amount of 'closed' RCs) and  $F_{VF}$  – fast fluorescence variable.  $F_{VS}$  stands for slow fluorescence variable.

Photosynthetic activity spectra were evaluated with the theoretical fit described by Equation 5:

$$y(t) = y_0 + \sum_{i=1}^n A_i \left(1 - e^{-\frac{t-t_0}{t_i}}\right) \quad (5)$$

where  $y_0$  stands for the value of the dark signal (equals 0 for normalised curves),  $n$  stands for the minimal number of components necessary for fitting the data,  $A_i$  is the contribution of a component 'i', and  $t_i$  is a time constant of a component 'i'.

## 5.9 Fast Polarography (Joliot's Type)

The three-electrode system developed by Pierre Joliot in the mid-20th century is a modification of the traditional Clark electrode, explicitly used to measure photosynthetic oxygen evolution in by oxygenic photosynthetic organisms under short saturating flashes. The system consists of a platinum working electrode, an Ag/AgCl reference electrode and a silver auxiliary electrode. By measuring the current generated at the working electrode due to the oxygen evolution reaction, the rate of photosynthetic oxygen production can be determined (P. Joliot et al., 1969).

### Experimental setup

The scheme of the three-electrode system based on (G. H. Schmid & Thibault, 1979) is presented in Figure 29. The disc-shaped Pt electrode placed in the centre is

surrounded by a concentric Ag/AgCl electrode. They are both set in an epoxy resin and linked by an electrolyte solution (KCl). The potential of the working electrode is settled at -680 mV. Thus, oxygen can be efficiently reduced, forming H<sub>2</sub>O<sub>2</sub>. The polarity changes during measurements, and the voltage difference is proportional to the amount of reduced O<sub>2</sub>.

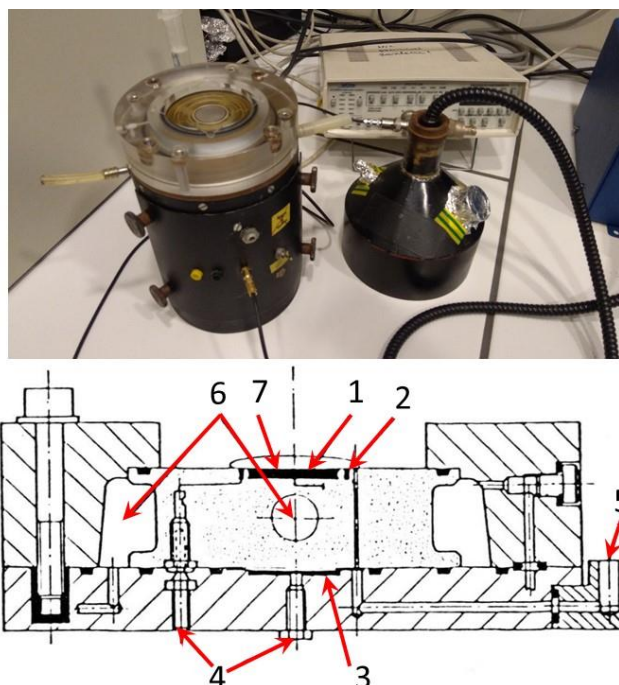


Figure 29 A scheme of the three-electrode setup: 1 – the Pt electrode, 2 – the Ag/AgCl electrode, 3 – the Ag electrode, 4 – electric connections, 5 – the KCl inlet, 6 – thermoregulation, 7 – the sample.

The applied flashes with an intensity of 1200  $\mu\text{Em}^{-2}\text{s}^{-1}$  and duration of  $\sim 3 \mu\text{s}$  at half intensity were generated by a xenon lamp (X-strobe. Perkin Elmer, Salem, MA, USA).

### Measurement protocol

The PSII BBY membranes were suspended in the HEPES I buffer for all fast polarography experiments. To test the NPs' influence on oxygen evolution, the specified amounts of NPs were added to the suspension. In each case, the total volume of the sample was 500  $\mu\text{l}$ . After 7 min dark incubation on ice and sedimentation on a filter, samples were transferred to the electrode in dim light conditions (the filter was centred on two external electrodes) and incubated for another 10 min in darkness. The measurement procedure (Figure 30) differs depending on the tested sample.

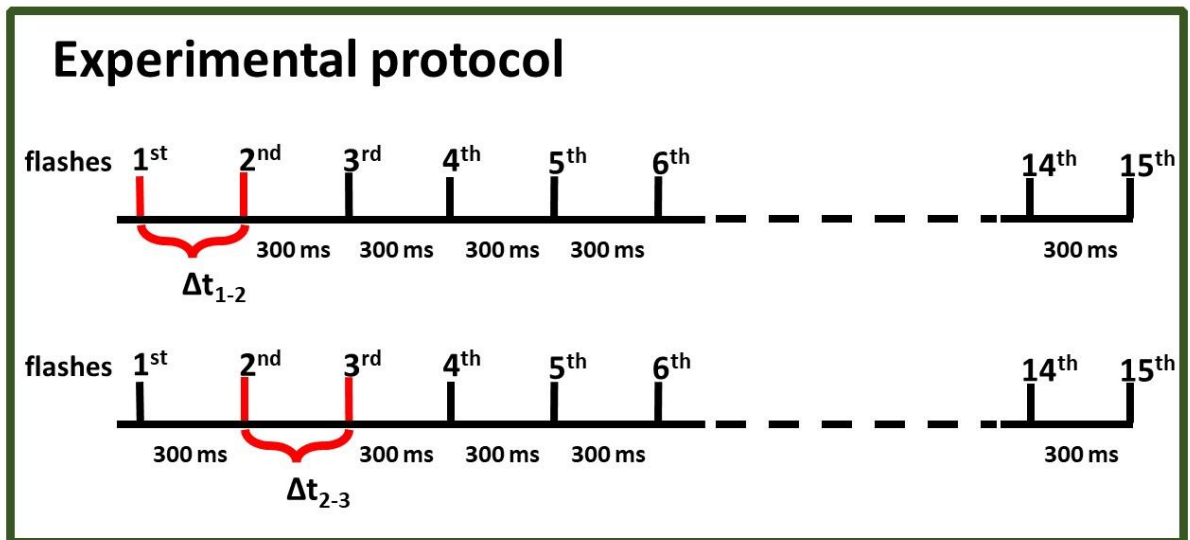


Figure 30 The experimental protocol for oxygen evolution experiments. The time separation between the 1<sup>st</sup> and the 2<sup>nd</sup> or the 2<sup>nd</sup> and the 3<sup>rd</sup> flash varied from 10 to 500 ms.

Two protocols were applied to measure oxygen evolution under 15 short saturating flashes in PSII BBY isolated from tobacco (control samples and depleted of extrinsic proteins) consisted of two parts:

- (i) time between the first and the second flash was changed,
- (ii) the time between the second and the third flash was changed.

In both cases the time intervals varied from about 10 to 500 ms. The intervals between the remaining flashes were constant, equal to 300 ms. In the standard protocol (which is the reference protocol), the distance between flashes was constant. It was 300 ms.

In the measurements studying the influence of NPs on oxygen evolution, only the second protocol was applied.

### Data analysis

As a result of a singular experiment, a plot of picks representing the amount of evolved oxygen is obtained (Figure 31a). The data for the samples depleted of extrinsic proteins were analysed using the 5S-state model (Burda & Schmid, 1996) presented in Chapter 3, Figure 11c, assuming the heterogeneity of oxygen evolution. The parameter  $d$  was introduced, representing the fraction of the O<sub>2</sub> released through the fast transition, whereas  $1-d$  corresponds to the slower transition.

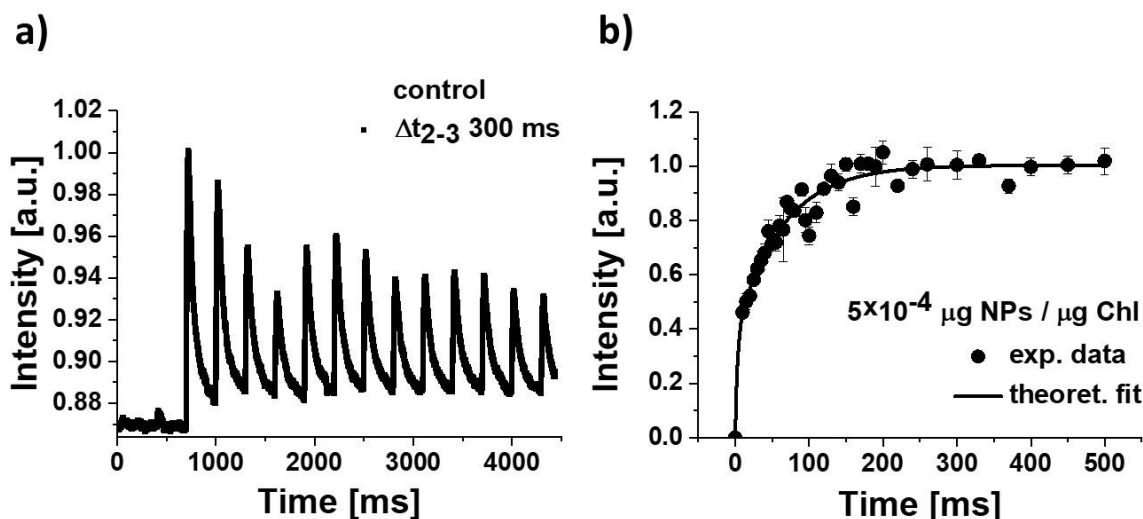


Figure 31 a) The flash-induced  $O_2$  yield oscillations in the control sample for the interval between the 2<sup>nd</sup> and the 3<sup>rd</sup> flash equal 300 ms. b) The exemplary normalised amplitudes of  $O_2$  evolution under the 3<sup>rd</sup> flash for BBY PSII. The solid line represents a theoretical fit using the biexponential function.

The intensities of peaks were evaluated for all sets of the collected data (for the samples depleted of extrinsic proteins as well as for the samples treated with NPs). Then, the amplitude of the oxygen evolution under the third flash was normalised to the sum of all amplitudes for each run of the experiment. The exemplary normalised amplitudes for the control sample are presented in Figure 31b. These data was fitted using Equation 6:

$$y(t) = \sum_{i=1}^n A_i \left(1 - e^{-\frac{x-x_0}{t_i}}\right) \quad (6)$$

where  $n$  stands for the minimal number of components necessary for fitting the data,  $A_i$  is the contribution of a component 'i', and  $t_i$  is the time constant of a component 'i'. In detecting a multiexponential behaviour of oxygen evolution under the third saturating flash, we should be able to get the contribution of different phases and characterizing them time constants. This protocol allows to directly check the heterogeneous character of the  $O_2$  yield suggested earlier in (Burda & Schmid, 1996).

## 5.10 Transmission Electron Microscopy

Transmission Electron Microscopy (**TEM**) is a powerful imaging technique used to study the fine structure of materials at the nanometer to atomic scale. It is a type of electron microscopy that involves the transmission of electrons through a thin sample to create detailed images and gather information about the sample's internal structure. For the last decades, TEM has been widely used in various scientific fields, such as materials science, nanotechnology, biology, and metallurgy (M. Li et al., 2020). In the

studies here performed TEM was applied to follow possible changes in thylakoid membrane architecture due to action of  $\text{WO}_3$  NPs).

### *Experimental setup*

The measurements were performed in Instituto de Nanociencia y Materiales de Aragon, Zaragoza, Spain, using The FEI Tecnai T20 (ThermoFisher Scientific) with an image resolution of 0.24 nm at 200 kV (Figure 32).

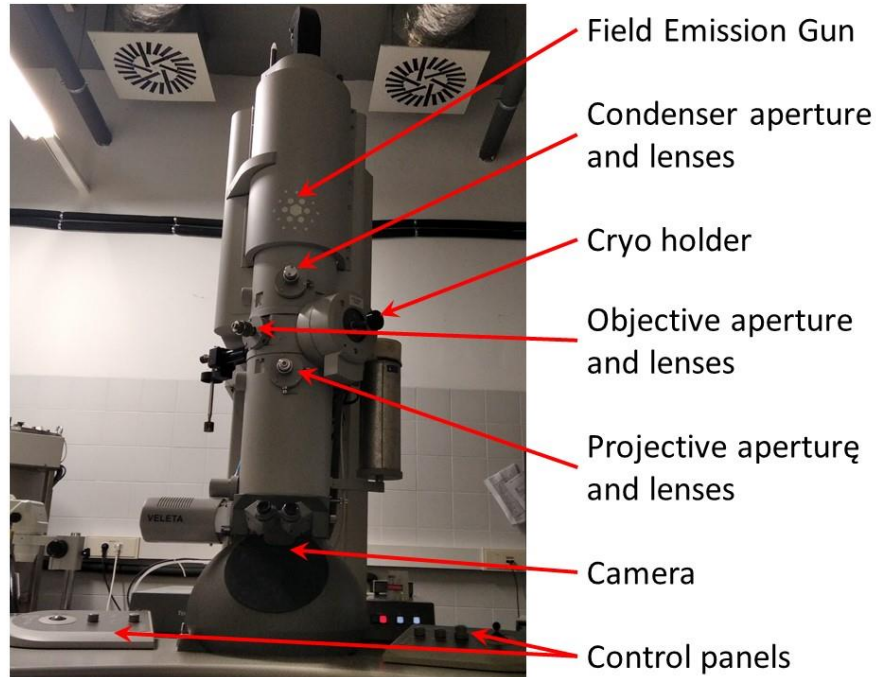


*Figure 32 The body of Tecnai T20 TEM, the column, consists of a FEG (Field Emission Gun), apertures and lenses, a cryo holder, a camera, and control panels.*

The condenser lenses and apertures control the spot size and beam size. The objective lens focuses the beam to transmit through the specimen, while the objective aperture selects electrons near the optical axis, enhancing image contrast. Finally, the projectors form the image's ultimate magnification.

### *Measurement protocol*

The native and NPs-treated thylakoid membranes enriched in PSII (PSII BBY) were initially fixed by immersing them in a solution of 4% glutaraldehyde in 0.2 M sodium cacodylate for 2 hours at 4 °C. After fixation, the membranes were centrifuged at 180 G for 10 minutes and then rinsed with 2 ml of a 2% glutaraldehyde solution in 0.1 M sodium cacodylate buffer. Then, they were centrifuged and washed with 0.1 M sodium cacodylate buffer three times.

The samples' staining and inclusion in resin were performed in Centro de Investigación Príncipe Felipe, **Valencia, Spain**. The fixed membranes were stained using Osmium Tetroxide 2% solution (EMS) and Uranyl Acetate 2% solution (EMS), embedded in Epoxy resin and dried in the oven at 70°C for 48h. After drying, the samples were cut

into ultrathin 60-80 nm sections and mounted on carbon-coated copper grids with a mesh structure for microscopic analysis.

Before the measurement, the grid is fastened on the specimen holder, inserted into the TEM column and pumped for several minutes to achieve a vacuum of  $\sim 10^{-6}$  mbar in the column and  $\sim 10^{-3}$  mbar in the camera. Setting microscope parameters includes, e.g. adjusting magnification, spot size, aperture, centring the beam, and adjusting Z-height. The images are recorded with a digital camera.

#### *Data analysis*

The recorded data were analysed using ImageJ software. The images of thylakoid membranes were evaluated in terms of their resistance to the isolation from the leaves process and the study of the difference of their dimensions depending on the variable concentration of nanoparticles introduced into the system. The results were presented in OriginLab software.

## 5.11 Atomic Force Microscopy

Atomic Force Microscopy (**AFM**) is a powerful imaging and probing technique for nanoscale characterisation and manipulation. It was invented in the 1980s and has since become a widely used tool in nanotechnology, materials science, and biology to study surfaces at the nanoscale level. The advantages of AFM include its high spatial resolution (typically down to atomic scales), ability to work in various environments (air, liquid, vacuum), and versatility in characterising materials, such as polymers, metals, semiconductors, and biological samples [<https://www.azonano.com/article.aspx?ArticleID=5182>]. AFM was used to monitor the organisation of PSII BBY untreated and treated with different  $\text{WO}_3$  NPs concentrations.

#### *Experimental setup*

The topography of the samples was examined in a liquid cell with AFM 5500 (Agilent, USA), presented in Figure 33.

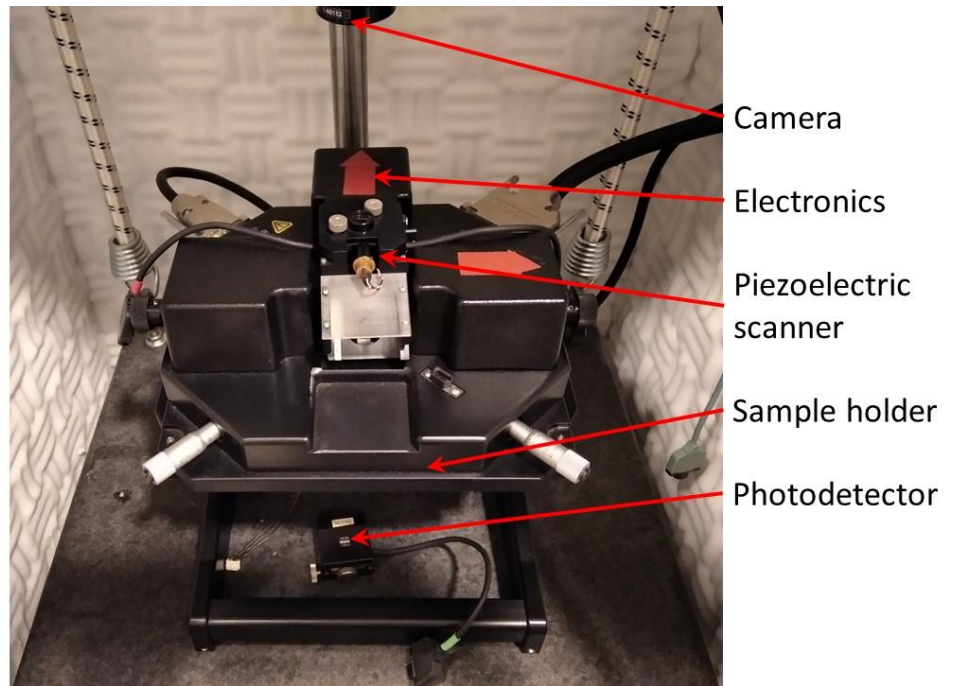


Figure 33 AFM 5500, Agilent, USA.

Silicon nitride probes with a soft triangular cantilever (Veeco, model MLCT, tip radius nom.: 20 nm, tip radius max.: 60 nm) with a nominal spring constant value of 0.01 N/m were used.

#### *Measurement protocol*

A glass slide used as a substrate was kept for 24 h in ethanol. Then, it was flushed with distilled water and dried by evaporation in the air at 20°C. A sample drop was put on the glass surface and kept for 12 h in the air at 20°C in the darkness. Then, it was flushed with the HEPES I buffer and finally covered with it. All samples were prepared in the same way. Images were collected in a contact mode at 20°C with a resolution of 515x512 points/line. The scan speed was 0.35 ln/s.

#### *Data analysis*

The images of thylakoid membranes were evaluated regarding changes in their organisation (under the influence of nanoparticles introduced into the system) using Gwyddion software. The computational analysis of the recorded data (histogram analysis applying the Gaussian function) was performed using MATLAB software. The results were presented in OriginLab software.



## 6. Results and discussion

### 6.1 The role of the extrinsic proteins on the heterogeneity of oxygen release

In the standard procedure for the measurement of oxygen release under short, saturating flashes using a fast three-electrode system, the time interval between the flashes is 300 ms, which provides optimal experimental conditions. Experimental and theoretical data of the flash-induced oxygen evolution in native and two or three extrinsic-protein-depleted PSII BBY are shown in Figure 34.

In this study, no external acceptors were introduced. Therefore, the total oscillatory oxygen release signal slightly decreases with an increasing number of flashes. This is due to the partial depletion of a natural acceptor (plastoquinone PQ-9), which reduces the number of active photosystems. In our case, this is determined by the  $C$  parameter, which is 1 for a fully functional system with a sufficient abundance of the acceptor, which means that the number of active centres is maintained (i.e.,  $\sum_{i=0}^4 S_i = 1$ , where  $S_i$  is a fraction of the OEC in a specific oxidized state  $i$ , Markov chain). The quenching of the total signal is stronger in PSII BBY – 16,23 than in the control sample because the elution of two external proteins reduced the available plastoquinone pool. In contrast, elution of three external proteins (16 kDa, 23 kDa, and 33 kDa), when the number of active centers is significantly reduced (maximum signal after the 3<sup>rd</sup> flash does not exceed 20-30% of the control sample), the effect of signal quenching due to PQ deficiency is much less pronounced (Table 7).

The failure rate  $\alpha$  of the trapping centers (called misses) leads to a redistribution of the  $S_i$  states and, consequently, to a damping of the oscillations of the  $O_2$  release. During prolonged darkness, the OEC is mainly in the  $S_1$  state. This is due to the oxidation of the  $S_0$  state by an electron carrier, Tyr D (tyrosine Tyr160 of peptide D2, Figure 8) (Bondar & Dau, 2012; Dismukes & Siderer, 1981; Mandal, Kawashima, Saito, & Ishikita, 2020; Sakashita, Watanabe, Ikeda, Saito, et al., 2017; Styring & Rutherford, 1987). It has been proposed that  $S_1$  is stable in the dark because the oxidation of Mn3(III) to Mn3(IV) forces the deprotonation of a  $\mu$ -hydroxo group at the O4 position in the  $Mn_4CaO_5$  cluster, and the proton is transferred along the O4 water channel (*broad* channel) up to  $\sim 13.5$  Å from O4 (Saito et al., 2015). So, the  $S_1$  state does not return to the ground state of  $S_0$  in the usual experimental time of a few minutes. Consequently, the occupancy of the  $S_0$  state is much lower (usually  $< 25\%$ ). Therefore, the first maximum is observed under the third flash. A small occupancy of the  $S_2$  state may also be detected (a small  $O_2$  yield was observed under the second flash), but the higher states are unstable (Burda & Schmid, 1996; Pokhrel, Service, Debus, & Brudvig, 2013; Yano & Yachandra, 2014). The

original Kok model assumed equal misses for light-driven transitions  $S_n \rightarrow S_{n+1}$  and additionally doubled effective excitation in a fraction  $\gamma$  of the centers, which are in the  $S_0$  and  $S_1$  states (called double hits and also equal). However, it has been shown that when this homogeneous model is used, there are significant discrepancies between the theoretical and experimental  $O_2$  yield patterns (Thibault, 1978).

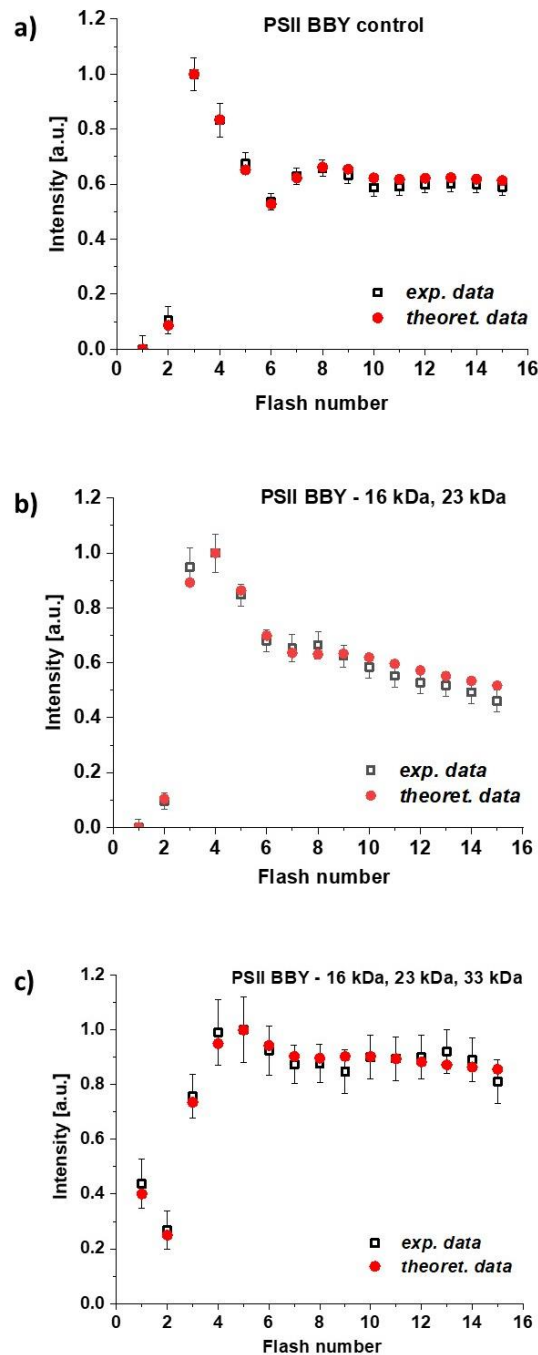


Figure 34 Flash-induced oxygen yield pattern in intact PSII BBY (a) and PSII BBY depleted of the extrinsic proteins by NaCl (b) and  $MgCl_2$  (c) washing. Samples were suspended in the HEPES I buffer pH 6.5. Amplitudes are always normalized to the amplitude of  $O_2$ -evolution under the third flash.

Moreover, it has been demonstrated that the progressive damping of the oscillations is mainly due to misses, and the heterogeneous model with different  $\alpha_i$

misses, omitting double hits, gives a better quantitative agreement with the experimental data obtained for other systems (Burda & Schmid, 1996; Delrieu, 1974, 1983; Lavorel, 1976, 1978). Unequal misses for  $S_n \rightarrow S_{n+1}$  transitions for  $n=0, 1, 2, 3, 4$  were also experimentally proven by EPR measurements (G. Han, Mamedov, & Styring, 2012). Furthermore, it was found that extending the Kok model to a 5S–state model by explicitly including the  $S_4$  state and introducing its longer-lived isomer resulted in an excellent reproduction of the experimentally observed patterns of  $O_2$  release (Burda & Schmid, 1996). The distinction between the short-lived and the metastable  $S_4$  state allowed to estimate the contribution of PSII involved in the fast and slow evolution of the oxygen molecule; see the scheme in Figure 11c. The results of the theoretical evaluation of the experimental data for the control sample, PSII BBY - 16,23 and PSII BBY – 16,23,33 kDa obtained using the 5S – state heterogeneous model are shown in Table 7.

*Table 7 Transition parameters and the initial S-state distribution estimated according to the 5S-state model (Burda & Schmid, 1996) for the PSII BBY control sample and PSII BBY depleted of two or three external proteins. Theoretical data are presented in Figure 34 (red-filled circles).*

Parameters	$\alpha_0$	$\alpha_1$	$\alpha_2$	$\alpha_3$	$d$	$S_0$	$S_1$	$S_2$	$S_3$	$C$
PSII BBY control	0.001	0.001	0.785	0.001	0.85	0.05	0.87	0.08	0.00	0.995
PSII BBY -16,23	0.55	0.28	0.78	0.12	0.30	0.04	0.88	0.08	0.00	0.967
PSII BBY -16,23, 33	0.51	0.27	0.79	0.16	0.02	0.282	0.530	0.130	0.058	0.990

The removal of the two outer 16 kDa and the 23 kDa proteins did not affect the initial occupancy of the  $S_i$  states in comparison to the control. In both samples, the  $S_3$  state occupancy was >86%, but a low  $S_2$  state occupancy comparable to the  $S_0$  state was also observed. However, in PSII BBY – 16,23, a significant decrease in transition efficiency between the  $S_i$  states was observed. There was an increase in the parameter  $\alpha_t$  (total miss:  $\alpha_t = \sum_{i=0}^3 \alpha_i$ ) mainly due to an increase in  $\alpha_0$  and  $\alpha_1$ , while the parameter  $\alpha_2$  remained unchanged. The value of parameter  $\alpha_3$  also increased, indicating that about 88% of the  $S_3$  states efficiently transitioned to  $S_4$  states. The probability of this transition in the control sample was nearly 100%. At the same time, the contribution of the fast mode to the  $O_2$  yield decreased (parameter  $d$  decreased almost threefold compared to the control sample). Removal of all three extracellular proteins did not affect the transition probability between  $S_i \rightarrow S_{i+1}$  states compared to PSII BBY – 16,23. However, the removal of the additional 33 kDa protein affected the initial distribution of  $S_i$  states and further reduced the  $d$  parameter to a value of about 0.02, indicating almost complete inactivation of the fast  $O_2$  release channel. It is noteworthy that in the case of the control sample, the misses came exclusively from  $\alpha_2$ , which maintained its value in samples lacking outer proteins of two or three, giving the highest contribution to  $\alpha_t$ . The lowest efficiency of the transition  $S_2 \rightarrow S_3$  is consistent with the unique character of this transition, confirmed by various measurements sensitive to the reorganization and

charge transfer changes during this step of the cyclic transformation of the OEC (Hussein et al., 2021; Ibrahim et al., 2020; Suga et al., 2017; Suga et al., 2019). EXAFS experiments implied significant structural changes during the  $S_2$  to  $S_3$  transition, observing the Mn-Mn and Mn-Ca distances (Liang et al., 2000; Pushkar, Ravari, Jensen, & M., 2019).

The structural changes observed around the  $Y_D$  under illumination with two flashes suggest a partial oxidation of the  $Y_D$ , probably due to an inefficient electron donation from the  $Mn_4CaO_5$  complex (Suga et al., 2017). The significant value of the miss parameter  $\alpha_2$  may reflect this. In addition, FTIR measurements showed that the binding of one of the substrate water molecules to the  $Mn_4CaO_5$  complex occurs during the  $S_2 \rightarrow S_3$  transition and the other during the  $S_3 \rightarrow (S_4) \rightarrow S_0$  transition (Noguchi & Sugiura, 2002; Suzuki, Sugiura, & Noguchi, 2009). It has been suggested that releasing a proton during the  $S_2 \rightarrow S_3$  transition could be a rate-limiting step in this transition (Takemoto, Sugiura, & Noguchi, 2019). The  $Mn_4CaO_5$  cluster consists of five oxo-/ hydroxo-bridges connecting Mn and Ca atoms and binds four water molecules. Two water molecules, called W1 and W2, are ligated to Mn4, and two others, W3 and W4, to Ca (Figure 10a). During the  $S_2$  to  $S_3$  transition, additional bridging oxygen (O6) ligated to Mn1 near O5 (probably a water molecule between Mn1 and Ca) was observed (Ibrahim et al., 2020; Kern et al., 2018; Suga et al., 2017; Suga et al., 2019).

The sixth oxygen bound to Mn1, presumably as an OH group, may originate from substrate water directly bound to Mn1 earlier in the  $S_1 \rightarrow S_2$  transition (Pushkar et al., 2019) or from a water molecule already present in the  $S_1$  state, proposed to be a Ca (W3) (C. J. Kim & Debus, 2017; P. E. M. Siegbahn, 2018; Ugur, Rutherford, & Kaila, 2016) or Mn4 (W1) ligand (Askerka, Wang, Vinyard, Brudvig, & Batista, 2016; Capone, Bovi, Narzi, & Guidoni, 2015; Narzi, Bovi, & Guidoni, 2014). In the latter case, when an additional water molecule is bound to the Ca or Mn4 ion (which requires Mn4(IV) in the  $S_2$  state) during the  $S_2 \rightarrow S_3$  transition, one of the internal water molecules (W1 or W3) moves to a new position, i.e. O6 (Cox & Messinger, 2013; P. E. M. Siegbahn, 2013; J. Wang, Askerka, Brudvig, & Batista, 2017).

Moreover, two redox isomers of the  $S_2$  state with distinctive EPR signals were detected (Casey & Sauer, 1984; Dismukes & Siderer, 1981; Hansson & Andréasson, 1982; Zimmermann & Rutherford, 1984). It was shown that the  $S_2$  state may exist in a low spin (LS) state characterized by a multiline signal with  $g \approx 2$  and in a high spin (HS) state with  $g \approx 4$ . These two states are isoenergetic and can be converted into each other. The transition between open (denoted A, LS) and closed (denoted B, HS)  $Mn_4CaO_5$  structures is associated with changes in the coupling between the Mn ions forming the manganese cluster, resulting in an  $Mn1(III)Mn4(IV) \leftrightarrow Mn1(IV)Mn4(III)$  electron exchange and O5 ligand displacement (Pantazis, Ames, Cox, Lubitz, & Neese, 2012). Recently, even two stable transient  $S_2$  closed conformers were suggested (Miyagawa et al.). The heterogeneity observed in  $S_2$  may already be the result of two different intermediate states  $S_2Y_Z^\bullet$  (where  $Y_Z^\bullet$  is a tyrosyl radical) (Sioros, Koulougliotis, Karapanagos, &

Petrouleas, 2007), for which two isomeric  $S_1$  states can coexist as a consequence of a quasi-reversible structure change induced by proton migration (Kusunoki, 2011). Two  $S_1$  conformations resembling  $S_2$  states have been proposed, closed and open (Narzi et al., 2017). Due to the orientational Jahn-Teller isomerism, they could convert to each other (open with LS = 1 and closed with HS = 3), and this would determine which Mn(III) (Mn1 or Mn4) would get oxidised (Campbell, Peloquin, Pham, Debus, & Britt, 1998; Dexheimer & Klein, 1992; Drosou, Zahariou, & Pantazis, 2021; Yamauchi, Mino, Matsukawa, Kawamori, & Ono, 1997). Two  $S_0$  isomers (Mn(III, IV, III, III)) with relatively similar energies analogous to the open and closed states of  $S_2$  were also considered. This time, a singly protonated O5 was assumed in both structures and assigned as a slow H<sub>2</sub>O-exchanging substrate (Hillier & Wydrzynski, 2004; Messinger, Badger, & Wydrzynski, 1995), but the open form of  $S_0$  was indicated as more preferred (Lohmiller et al., 2017). In the subsequent steps of the cyclic water oxidation, the  $S_3$  state, activated by two flashes, also shows isomerism. This is probably closely correlated with the two different conformations of the  $S_2$  state. In the  $S_3$  state, all manganates remain oxidized Mn(IV), but depending on whether Mn4(IV) is five- or six-coordinated, the Mn<sub>4</sub>CaO<sub>5</sub> complex adopts different spin and conformational states, respectively, a low spin state (S=3) with a stable closed cubane form and a high spin state (S=6) with a stable open cubane form (Boussac, Rutherford, & Sugiura, 2015; Cox et al., 2014; Drosou et al., 2021; V. Krewald et al., 2016). Thus, the  $S_1$ ,  $S_2$ , and  $S_3$  states can all adopt two potentially stable conformations, while it is proposed that the  $S_0$  state exists rather as an open cubane (V. Krewald et al., 2015; Lohmiller et al., 2017), see also Figure 10b.

In order to unravel the mystery of the mechanism of O-O bond formation and oxygen release, it seems crucial to know the last of the metastable states of the Kok cycle, i.e., the  $S_3$  state. Therefore, knowing the individual stages of the  $S_2$ - $S_3$  transition is as important as understanding the possible intermediate  $S_4$  states during the flash that triggers the  $S_3$ -( $S_4$ )- $S_0$  transition (Ananyev, Roy-Chowdhury, Gates, Fromme, & Dismukes, 2019; Bhowmick et al., 2023; Greife et al., 2023; Kern et al., 2018; Lubitz et al., 2023). It is now known that any electron uptake from Mn<sub>4</sub>CaO<sub>5</sub> is preceded by the oxidation of Y<sub>z</sub> and its deprotonation (Ibrahim et al., 2020; Retegan, Cox, Lubitz, Neese, & Pantazis, 2014) and that the accumulation of positive charges on the manganese cluster during the transitions between  $S_i \rightarrow S_{i+1}$  states requires a prior proton release (Haumann, Liebisch, et al., 2005; Klauss et al., 2012; Lavergne & Junge, 1993; Pushkar et al., 2019; Rappaport & Lavergne, 1991; Saito et al., 2015; Suzuki et al., 2009; Yang et al., 2021). The only exception is the transition from  $S_0 \rightarrow S_1$  when the transfer of electrons to Y<sub>z</sub><sup>•</sup> precedes the deprotonation (Klauss et al., 2012; Saito et al., 2015). There is consensus that at the  $S_0 \rightarrow S_1$  and  $S_1 \rightarrow S_2$  transitions, the oxidation is concentrated on Mn (Haumann, Müller, et al., 2005; Iuzzolino, Dittmer, Dörner, Meyer-Klaucke, & Dau, 1998), but there is no such consensus for the  $S_2 \rightarrow S_3$  transition, where some groups favor an interpretation of the data as Mn-centred oxidation (Cox et al., 2014; Dau, Iuzzolino, & Dittmer, 2001; Dau, Liebisch, & Haumann, 2003; Schuth et al., 2018) and

others as ligand-centered oxidation (Guiles et al., 1990; MacLachlan, Nugent, & Evans, 1994; Mandal, Kawashima, et al., 2020; Messinger et al., 2001; Roelofs et al., 1996).

There are several experimental approaches, combined with computational ones, that attempt to explain how the different conformational forms of the  $S_i$  states, in particular  $S_2$  and  $S_3$ , can affect the mechanism of oxygen release and its efficiency. At present, two pathways of O-O bond formation involving  $Mn_4CaO_5$  are the most commonly considered for reconstructing the Kok cycle. One of them assumes an oxo-oxyl radical coupling mechanism, where the  $S_4$  intermediate state may involve the electrophilic Mn(V)-oxo or Mn(IV)-oxyl radical (Haumann, Liebisch, et al., 2005; X. Li & Siegbahn, 2015; P. E. M. Siegbahn, 2009, 2017; Suga et al., 2017). The other one would involve a mechanism of nucleophilic attack by water (Barber, 2017; Guo, Messinger, Kloo, & Sun, 2022; Sproviero, Gascón, McEvoy, Brudvig, & Batista, 2008; Vinyard et al., 2015). A completely different mechanism has been proposed for O-O bond formation within the MnVII dioxo site on Mn4 (B. Zhang & Sun, 2018). Furthermore, different scenarios for the pathway leading to the formation of the O-O bond have been proposed, depending on the assumption of the conformation of the subsequent  $S_i$  states and the stage at which the second exchangeable substrate water is bound to the  $Mn_4CaO_5$  cluster. For example, one of the models considers additional  $H_2O$  binding during the  $S_2 \rightarrow S_3$  transition and only open structures of  $S_i$  states (Kern et al., 2018) while the other assumes structural changes of the  $Mn_4CaO_5$  complex (open  $\leftrightarrow$  close) for  $S_i$  states, facilitating coordination of substrate water binding, proton release and oxygen formation (Cox & Messinger, 2013; Guo et al., 2017; Lubitz et al., 2023; Suga et al., 2019; B. Zhang & Sun, 2018). The high degree of conformational variability of the individual  $S_i$  states may suggest an adaptive ability of the  $Mn_4CaO_5$  complex to maintain an optimal level of OEC activity under certain external conditions. However, it is currently impossible to determine whether the heterogeneity in the structures of the  $S_i$  states discussed above might indicate different pathways for forming O-O bonds, or rather a single pathway optimized during the cycle, leading to the release of  $O_2$  (Chrysin et al., 2019; Cox & Messinger, 2013; Cox, Pantazis, Neese, & Lubitz, 2013; Guo et al., 2017; Isobe, Shoji, Suzuki, Shen, & Yamaguchi, 2021; V. Krewald et al., 2015; Lubitz et al., 2023; Pushkar et al., 2019). In the latter case, the different conformations of the  $S_i$  would be transition states that occur in a single chain of events in the Kok cycle. For example, the topology of a high-spin closed cubane in the  $S_2$  state (formed, e.g., when  $H^+$  is released from the  $S_2Y^\bullet$  state) was proposed to be essential for the transition to the HS  $S_3$  (closed cubane) state, which changes to the low spin LS  $S_3$  (open cubane) state on the addition of  $H_2O$  (Orio & Pantazis, 2021; Zahariou, Ioannidis, Sanakis, & Pantazis, 2021). It is often suggested that the emergence of a high spin closed cubane topology in the  $S_2$  state is of mechanistic importance for the subsequent catalytic steps (Narzi et al., 2014; Retegan et al., 2014). However, the specific steps leading to the formation of O-O and the release of  $O_2$  may be much more complicated or different from those mentioned above. For example, the observed HS  $S_2$  may not result from conformational changes in the

Mn<sub>4</sub>CaO<sub>5</sub> complex but from the protonation of O4 in the open cubane form (Corry & O'Malley, 2019). Proton isomerism of the S<sub>2</sub> state has been independently suggested in (P. E. M. Siegbahn, 2018). Proton isomerism of high and low spin S<sub>3</sub> states has also been proposed (Isobe et al., 2021; Rogers et al., 2022).

Furthermore, the question arises as to the causal relationship between the changes in the manganese complex itself and the protein network of its proximal and distal environment. This point is crucial because of the need to synchronize the delivery of water, the reception of protons, and the release of O<sub>2</sub> with the cycling of the Mn<sub>4</sub>CaO<sub>5</sub> complex. Obtaining a complete picture of the process of OEC functioning is hampered because of, among other things, the insufficient resolution of PSII structures, the blurriness of the images obtained from them, the difficulty of capturing the various stages of the Kok cycle (mixing of S<sub>i</sub> states), the influence of the measurement conditions on the stability of the sample and the oxidation states of the manganese cluster or the preparation method on the functioning of PSII, the degree of its hydration and simplified theoretical models applied (Amin, Askerka, Batista, Brudvig, & Gunner, 2017; Guo et al., 2017; Y. Li et al., 2020; Mandal, Saito, et al., 2020; Nass, 2019; Nass et al., 2015; Sirohiwal & Pantazis, 2022; Suga et al., 2020; Tanaka, Fukushima, & Kamiya, 2017).

The coupling of PSII conformational changes, which can lead to a reorganisation of the immediate environment of the OEC, regulating substrate water access, proton release, and ultimately dioxygen formation, and thus affecting its enzyme activity, has been suggested many times, for example (Burda, 2007; Isobe et al., 2021; Linke & Ho, 2014; Suga et al., 2019). In addition to the protein network, the stability/variability of the hydrogen bonds between the water molecules, as well as between the water molecules and the amino acid residues, plays a vital role in this process [for review, see: (Linke & Ho, 2014)]. The presence of more water molecules in the vicinity of the manganese complex, which may be directly or indirectly involved in the oxygen evolution process, was predicted by EPR, mass spectroscopy, or FTIR measurements, among others (Burda, Bader, & Schmid, 2001; Hansson, Andréasson, & Vänngård, 1986; Suzuki et al., 2009), and further confirmed by structural studies of the OEC (Ferreira et al., 2004; Loll, Kern, Saenger, Zouni, & Biesiadka, 2005; Umena et al., 2011).

Due to the cyclic nature of the light-driving force-dependent operation of the Mn<sub>4</sub>CaO<sub>5</sub> cluster and its location and protection by external proteins on the luminal side of the thylakoids, it has been suggested that the pathways for the entry and exit of substrates (water molecules) and products (protons and O<sub>2</sub>) may be essential for the efficient functioning of PSII (Anderson, 2001; Anderson & Chow, 2002; Rutherford, 1989; Wydrzynski, Hillier, & Messinger, 1996). To date, based on theoretical studies, three water channels have been identified that have counterparts in cyanobacteria, algae, and higher plants (Hussein et al., 2021; Sakashita, Watanabe, Ikeda, Saito, et al., 2017). Two of them, *large* and *broad*, are branched and, using the nomenclature based on the entry point of each channel into the OEC region, are also known as the O1 and Cl1 channels,

respectively. The third one is a single *narrow* channel, also known as the O4 channel. In cyanobacteria, the O4 channel is formed by residues D1, D2, CP43, CP47, PsbO (a 33 kDa external protein, MSP - manganese stabilizing protein), and PsbU (external protein subunits). It connects O4 to the lumen with the participation of protonated D1-D61. But on the other side of D1-D61, there is the Cl1 channel that is at the interface of D2 and PsbO subunits (Ho & Styring, 2008; Umena et al., 2011; Vogt et al., 2015). *The Cl1 channel with its branching arms is indicated as an H-channel rather than a water delivery path* (Bondar & Dau, 2012; Guskov et al., 2009; Ishikita et al., 2006; Vogt et al., 2015) although the latter function cannot be ruled out either (Sakashita, Watanabe, Ikeda, Saito, et al., 2017; Umena et al., 2011). The O1 water chain, a branched network, is formed in cyanobacteria by the same protein subunits as the Cl1 channel, with one difference: instead of PsbO, the PsbV subunit is involved. This channel is thought to remove O<sub>2</sub> and/or deliver water to the OEC (A. G. Gabdulkhakov et al., 2015a, 2015b; Ho & Styring, 2008; Vassiliev et al., 2013). On the other hand, the sometimes recognized so-called *back* channel appears to be inaccessible to water but permeable to O<sub>2</sub> (Murray & Barber, 2007; Vassiliev et al., 2012). However, even if it were accessible to H<sub>2</sub>O, it would still be effective at O<sub>2</sub> removal (Ho & Styring, 2008). Among the many water channels reported in cyanobacteria or algae, the organization of amino acids of the Cl1 (*broad*) channel starting at Mn4, W1, W2, and W3 is the most evolutionary conserved. The recognized proton gate residues D1-E65/D2-E312/D1-R334/D1-335 associated with the proton network rearrangement along this channel were found in all photosynthetic species (Hussein et al., 2021). The O4 (*narrow*) channel is also very conservative at its entrance to the manganese complex near O4 and W1, including D1-D61, but shows a different orientation at its end near the surface. The O1 (*large*) channel, like the O4 channel, shows a high degree of conservatism in the vicinity of the Mn<sub>4</sub>CaO<sub>5</sub> complex, reaching Ca, O1, and W4, but at the same time, has different orientations at the end of the path close to the bulk, as well as different degrees of branching. For more details, see: (Hussein et al., 2023; Hussein et al., 2021; Sakashita, Watanabe, Ikeda, & Ishikita, 2017). In plants, however, fewer PSII subunits form the channels mentioned above. The subunits D1, CP43, PsbP (23 kDa external protein), and PsbQ (16 kDa external protein) are involved in forming the O1 water chain, D1, D2, CP43, CP47, and PsbP in forming the O4 water chain and only three subunits D1, D2 and PsbO (33 kDa external protein) in forming the Cl1 water chain (Hussein et al., 2023; Sakashita, Watanabe, Ikeda, & Ishikita, 2017). The small radius of the '*narrow channel*' (~1.4 Å) in all species suggests that water molecules are also arranged as a single chain in higher plants as well (Sakashita, Watanabe, Ikeda, & Ishikita, 2017). A rigid water chain with particularly strong hydrogen bonds between the initial water molecules near the Mn<sub>4</sub>CaO<sub>5</sub> cluster and with its O4 atom indicates that the *narrow* channel can transport protons via the Grotthuss mechanism since the activation energy of proton transfer is lowest when all water molecules are strongly bound in the H-bond network (Saito et al., 2015; Stuchebrukhov, 2009; Takaoka et al., 2016). Proton release during the S<sub>0</sub> → S<sub>1</sub> (Kern et al., 2018; Saito et

al., 2015; Shimizu, Sugiura, & Noguchi, 2018; Takaoka et al., 2016) and  $S_2 \rightarrow S_3$  transition via this channel was proposed (Suga et al., 2017). However, the involvement of the O4 channel in the removal of protons during the  $S_2 \rightarrow S_3$  transition was considered rather unlikely (Hussein et al., 2021; Kern et al., 2018), and the Cl1 channel has been proposed as a proton release pathway during this transition (Guerra, Siemers, Mielack, & Bondar, 2018; Kuroda et al., 2021; Okamoto, Shimada, Nagao, & Noguchi, 2021; Takemoto et al., 2019), with the D1-E65 (branch Cl1A) as the gate for proton transport to minimize the back reaction (Bhowmick et al., 2023; Hussein et al., 2021). On the other hand, the O4 channel is suggested to be responsible for supplying water to the OEC during the  $S_4 \rightarrow S_0$  transition (Guo et al., 2017). By analogy with the binding of ammonia to  $Mn_4CaO_5$ , water with similar structural and electrical properties was suggested to be supplied to  $Mn_4$  also through the O4 channel during the  $S_2 \rightarrow S_3$  transition (Askerka, Brudvig, & Batista, 2017; Askerka et al., 2016; Vassiliev et al., 2012). Especially in spinach, it is expected that the O4 channel is able to deliver water efficiently to the manganese complex. This is because the entrance to the channel is wider due to the presence of Ala in D1 at position 87 than in cyanobacteria, where Asn is found (Retegan & Pantazis, 2016, 2017). The competing hypothesis is that during the transition from  $S_2$  to  $S_3$ , a water molecule is introduced into  $Mn_4CaO_5$  through the O1 channel on the Ca side (Askerka et al., 2017; Bhowmick et al., 2023; Hussein et al., 2021; Ibrahim et al., 2020; Kern et al., 2018; Ugur et al., 2016). This channel has been shown to exhibit the highest water exchange rate (Hussein et al., 2021). It has also been proposed that in cyanobacteria, the O1 channel may supply water, and both O1 and Cl1 channels release protons in the  $S_2 \rightarrow S_3$  and  $S_3 \rightarrow (S_4) \rightarrow S_0$  transitions. But during the  $S_0 \rightarrow S_1$  transition, the O4 channel has been suggested to be the proton exit pathway, which was found to be disconnected in the  $S_2$  state and restored only in the  $S_0$  state (Kern et al., 2018). Recently, a fascinating observation has been made. Namely, glycerol (commonly used as a cryoprotectant and stabiliser of isolated PSII) incorporated into the O4 channel in cyanobacteria at a distance  $> 10 \text{ \AA}$  from the OEC affects the LS stabilization of the  $S_2$  state of the  $Mn_4CaO_5$  complex, which adopts the 'open' conformation (Figure 10b) as a result of disruption of the hydrogen bond network involving D1-D61 when it remains protonated. In the absence of glycerol (D1-61 becomes deprotonated), both states of  $S_2$ , i.e. LS and HS (open and closed conformations), are virtually isoenergetic (Flesher et al., 2022). An analogous effect of regulation of the  $Mn_4CaO_5$  complex by allosteric interactions may also occur in higher plants, as may be indicated by the usual occurrence in their case of both spin states of the  $S_2$  state and the disappearance of the HS signal with an increase in the concentration of glycerol (Zimmermann & Rutherford, 1986).

The search for water, proton, and  $O_2$  transport pathways has been and continues to be carried out by *in silico* experiments with various computational methods - including QM (quantum mechanics) / MM (molecular mechanics), MD (molecular dynamics), and CE (continuum electrostatics) / MC (Monte Carlo studies) using available PSII structures, even PSII thylakoid membrane model (Ogata et al., 2013). Various research groups have

pointed out similar patterns of water channels in cyanobacteria, but their purpose cannot always be clearly determined. Some counterparts have been found in higher plants, but even minor differences from cyanobacteria may be relevant to their distinct control of protons and O<sub>2</sub> output during water oxidation or water delivery to the OEC. Identifying these mechanisms is the greatest challenge. Learning about them is the key to getting a complete picture of how the OEC and PSII as a whole function. In general, water diffusion tends to require water-filled channels. Each water channel can potentially evacuate O<sub>2</sub>, but its diffusion can also occur through hydrophobic pathways. It has been suggested that lipid clusters within PSII, due to their predominantly hydrophobic nature, may serve as an oxygen drain and mediate efficient, PSII-safe, and rapid release of O<sub>2</sub> (A. Gabdulkhakov et al., 2009; Guskov et al., 2009). A highly conserved small hydrophobic pathway in cyanobacteria and algae (prokaryotes and eukaryotes) has been identified at the beginning of the O1 channel and has been suggested to be responsible for facilitating O<sub>2</sub> release from the OEC (Caspary et al., 2021; A. Gabdulkhakov et al., 2009). As can be seen, the factors regulating the process of water evolution by PSII are extremely complex. To understand them, it is necessary to consider not only the conformation of the OEC and its immediate environment but, most likely, the entire PSII, which is a dynamic system.

Based on the existing knowledge, we are able to identify the possible causes of the changes in the  $\alpha_i$  parameters due to the extraction of the two outer proteins, PsbP and PsbQ. As a first approximation, the removal of these two extracellular proteins should primarily be attributed to proton channel dysfunction. This is based on the assumption that the  $S_0 \rightarrow S_1$ ,  $S_1 \rightarrow S_2$ ,  $S_2 \rightarrow S_3$ , and  $S_3 \rightarrow (S_4) \rightarrow S_0$  transitions primarily require efficient proton extraction to minimize 'back reactions', mainly related to electron flow. This will, of course, be accompanied by changes in the coupling efficiency within the Mn<sub>4</sub>CaO<sub>5</sub> complex, as well as changes in its interaction with the immediate protein-water environment. They will certainly be reflected in the conformation and stability of the subsequent states resulting from these transitions. Referring to the proposed contribution of PsbP in stabilising O1B and O4 channel outlets and PsbQ in stabilizing O1A channel outlet recognized in higher plants (Hussein et al., 2023; Sakashita, Watanabe, Ikeda, & Ishikita, 2017), the observed increase in miss parameters very well reflects the changes in the activity of these channels. Thus, the lack of regulation of electron uptake at the output of the O4 water channel, which has been shown to be the main, if not the only, electron transfer channel for the  $S_0 \rightarrow S_1$  transition (Kern et al., 2018; Mandal, Kawashima, et al., 2020; Saito et al., 2015; Shimizu et al., 2018), translates into a high increase in  $\alpha_0$ . The dysfunction of both the O4 channel and the two branches of the O1 channel leads to an increase in  $\alpha_1$  and  $\alpha_3$  but to a much lesser extent. For  $S_1 \rightarrow S_2$  and  $S_3 \rightarrow S_0$  transitions,  $\alpha_1$  and  $\alpha_3$  are approximately 2 and more than 4 times lower than  $\alpha_0$ , respectively. This may indicate a smaller contribution of the O4 channel to deprotonation processes during these transitions, especially at the  $S_3 \rightarrow S_0$  transition, and a larger contribution of the other channels. It has been suggested

that the O4 channel is opened only during the  $S_0 \rightarrow S_1$  transition. It is also likely that the smaller changes in O1 channel function induced by the deletion of PsbQ and PsbP proteins are due to the specificity of this channel, which is wider than others, contains highly mobile water molecules over almost its entire surface, and may function primarily as a water channel (Hussein et al., 2021). Among the known channels, the Cl1 channel is the only one that is currently a candidate for these transitions. Since the extraction of all three outer proteins, i.e. PsbQ, PsbP, and PsbO, did not further alter the parameters  $\alpha_0$ ,  $\alpha_1$ , and  $\alpha_3$ , it can be expected that mainly the Cl1A branch is responsible for the reception of H<sup>+</sup> during the  $S_1 \rightarrow S_2$  and  $S_3 \rightarrow S_0$  transitions. It is also the most evolutionarily conserved water channel. It contains the very important conserved amino acid sequences E65/E312/R334, which are indicated as gates regulating the release of protons into the lumen (Service, Hillier, & Debus, 2010; Shimada, Sugiyama, Nagao, & Noguchi, 2022) as well as the possible uptake of water (de Lichtenberg, Kim, Chernev, Debus, & Messinger, 2021; Vassiliev et al., 2012). The Cl1 ion in this channel is also conserved in higher plants (Haumann et al., 2006; Lindberg & Andréasson, 1996; Olesen & Andréasson, 2003; Rivalta et al., 2011). Since no proton release to the bulk is observed during the  $S_1 \rightarrow S_2$  transition (Junge, Haumann, Ahlbrink, Mulkidjanian, & Clausen, 2002; Yang et al., 2021) it is proposed that in this case, the proton is temporarily stored in the form of hydronium in the hydrogen bond network in the vicinity of Ca (Polander & Barry, 2013; Tanaka et al., 2017) or in the Cl1 channel to which it can be transferred via D61 (Rivalta et al., 2011). For example, Asp 170 has been suggested to be involved (P. E. M. Siegbahn, 2009) in this process, but other deprotonation pathways of Mn<sub>4</sub>CaO<sub>5</sub> cannot be excluded. Indeed, the formation of a cationic water cluster was observed, which indicates transient storage of the proton in the  $S_2$  state in the form of the nH<sub>2</sub>O(H<sub>3</sub>O)<sup>+</sup> cluster, where n=5 (Barry et al., 2017). It should be noted here that the proton network of the Cl1 channel, which connects to the O4 channel in the vicinity of O4, extends through a network of hydrogen bonds involving unbound and bound water molecules on the Mn<sub>4</sub>CaO<sub>5</sub> cluster and neighboring amino acids up to TyrZ (Ho & Styring, 2008; Kern et al., 2018; Umena et al., 2011). On the opposite side of the manganese complex, close to Ca, water molecules can penetrate from the O1 channel (Kern et al., 2018). The highest value of  $\alpha_2$ , independent of the presence of external proteins, indicates the special nature of the  $S_2 \rightarrow S_3$  transition. As mentioned above, this transition requires large rearrangements of the Mn<sub>4</sub>CaO<sub>5</sub> cluster associated with substrate water binding. Water availability and binding it to a specific site for the required conformation of the complex may be the main reason for the low efficiency of this transition (de Lichtenberg, Kim, et al., 2021). The independence of the  $S_2 \rightarrow S_3$  transition from the presence of PsbQ, PsbP, and PsbO suggests that Cl1A could act as a water transport channel during this transition. This is consistent with previous predictions (Shimada et al., 2022). On the other hand, if access to substrate water is not the bottleneck for this transition, then perhaps the assumption of a mechanism ('carousel' or 'pivot') suggesting that the O6 position is occupied by one of the internal waters already present in the manganese

cluster, which changes its position, is correct (Askerka et al., 2017; Bovi, Narzi, & Guidoni, 2013; Ibrahim et al., 2020; Kawashima, Takaoka, Kimura, Saito, & Ishikita, 2018; Lubitz et al., 2023; Retegan et al., 2016). Then, the high stabilization of the  $S_2$  transient state before the electron flow to Yz and/or the instability of the  $S_3$  state would explain the low efficiency of this step of the Kok cycle. The much higher probability of the  $S_3 \rightarrow (S_4) \rightarrow S_0$  transition than in the previous step suggests that, in this case, the problem is not water access but deprotonation and probably O-O bond formation, the initial stage of which begins with the formation of the  $S_3$  state. This could mean that during the formation of the  $S_0$  state, the water molecule is already attached in the immediate vicinity of the  $Mn_4CaO_5$  cluster.

The deletion of the PsbQ and PsbP proteins did not affect the initial distribution of the  $S_i$  states. However, the additional removal of the PsbO protein significantly affected their distribution. On the one hand, it decreased the stability of the  $S_1$  state in the dark and, on the other hand, increased the stability of the  $S_2$  and  $S_3$  states. This observation is consistent with the fact that PsbO is an already-known MSP protein. As can be seen, it is responsible for stabilizing not only the  $Mn_4CaO_5$  complex but also the cluster's environment, including TyrD. The effect of increased stability of the higher states caused by the PSII depletion of PsbO is well known (Bricker, Roose, Fagerlund, Frankel, & Eaton-Rye, 2012; Popelkova & Yocum, 2011). We suspect that these changes observed by us are related to increased uncontrolled access of water molecules to the OEC.

The 5S – state model we have used has allowed us to investigate further the influence of external proteins on the heterogeneity of the oxygen evolution process. The decrease in the d parameter in samples without external proteins indicates a reduction in the contribution of the fast oxygen release pathway. Extracting PsbQ and PsbP reduced the contribution of the fast pathway to  $O_2$  evolution almost threefold. In the case of PSII lacking all three extracellular proteins, namely PsbQ, PsbP, and PsbO, the evolution of  $O_2$  occurred almost exclusively via the slow pathway (the metastable  $S_4'$  state).

To verify the heterogeneity of the oxygen release process in a direct measurement, we used a new protocol for measuring oxygen release using a fast electrode type, as presented in this paper. Two protocol variations were used, see Chapter 5.9, Figure 30. Figure 35 shows the dependence of the changes in the oxygen evolution after the third flash as a function of the flash interval when  $\Delta t_{1-2}$  (red symbols) and when  $\Delta t_{2-3}$  (black symbols) were changed. Note that for a given sample, whether the intervals between the first and second flashes or between the second and third flashes were altered, the dependence of the changes in oxygen evolution after the third flash on the flash interval is the same. This is in accordance with Kok's linear sequence of transitions between the  $S_i$  states. The experimental data were fitted using a dual

relaxation function, defined as the sum of two exponential relaxations (solid lines in Figure 35 a, b, and c):

$$Y_3 = A_{fast} \left( 1 - \exp\left(-\frac{t}{\tau_{fast}}\right) \right) + A_{slow} \left( 1 - \exp\left(-\frac{t}{\tau_{slow}}\right) \right), \quad (7)$$

where  $A_{fast}$  ( $A_{slow}$ ) and  $\tau_{fast}$  ( $\tau_{slow}$ ) are amplitudes and time constants characterizing the fast (slow)  $O_2$  release, respectively. For the data that were normalized to the amount of oxygen released when the time interval between flashes was 300 ms,  $A_{fast}$  and  $A_{slow}$  denote the contributions of the individual phases. The parameters  $A_{fast}$ ,  $A_{slow}$ ,  $\tau_{fast}$ , and  $\tau_{slow}$  obtained from the data for control PSII BBY and PSII depleted of two or three external proteins are listed in Table 8.

In the case of the control sample and PSII BBY – 16,23, two components were necessary to obtain a satisfactory fit to the experimental data, whereas in the case of PSII BBY – 16,23,33, one component was sufficient. This is consistent with the information obtained from the 5S – state model. The contribution of the fast amplitude corresponds to the fast phase of  $O_2$  release from the 5S – state model. It shows an excellent agreement with the values and the direction of the change of the  $d$  parameter obtained for the control sample and for the PSII sample with eluted proteins. The time constants of the fast and slow pathways of oxygen release in the samples studied were also determined using this experimental approach. For the control sample, the time constant of oxygen release in the slow (~44 ms) and fast (~4 ms) phases differs by an order of magnitude. In the sample lacking the two extrinsic proteins, PsbQ and PsbP, the difference is only about 3.5 times. This is because the fast phase is slowed down by about 2 ms, while the slow phase is twice as fast. The elution of all three proteins resulted in a further acceleration of the slow phase by a factor of about 1.7 (Table 8).

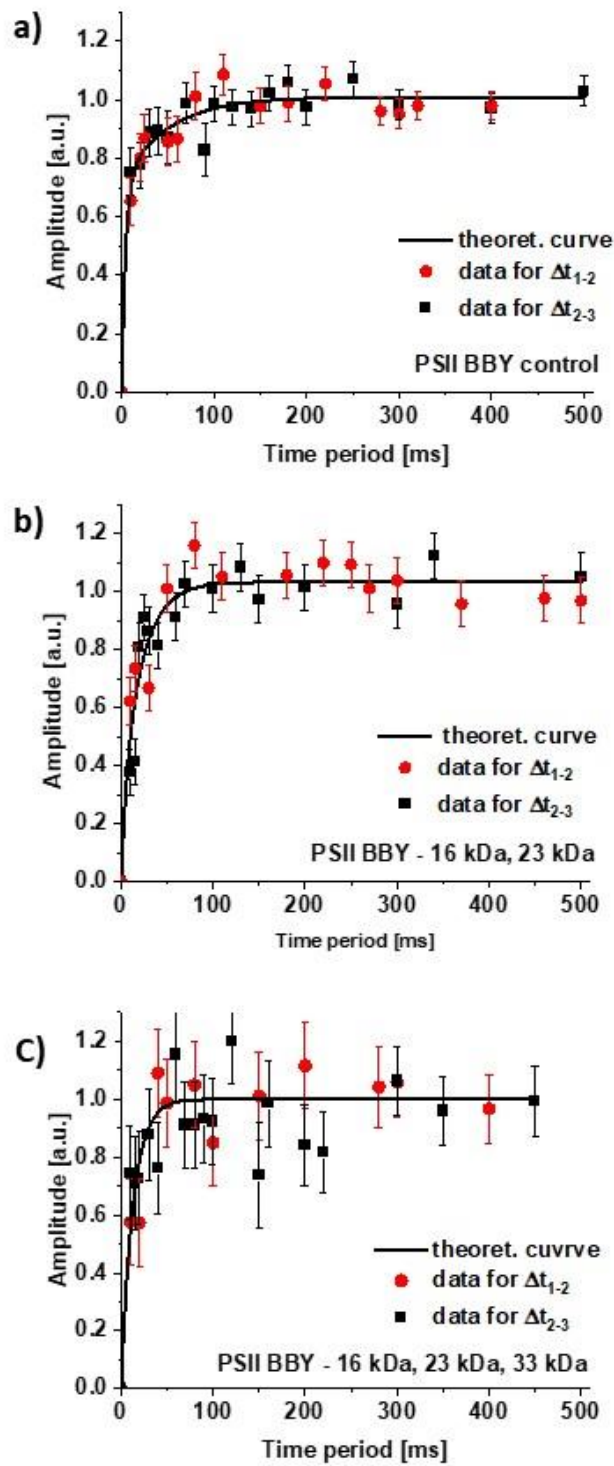


Figure 35 The dependence of  $O_2$  release under the third flash on the time interval between the first and second flashes (red symbols) and the second and third flashes (black symbols) for control PSII BBY (a), PSII-BBY – 16,23 (b) and PSII-BBY – 16,23,33 (c). Each experimental point is a mean of at least 3 independent measurements. Error bars represent the root mean square error. The theoretical curve shows the fit obtained using a biexponential function (eq. 1).

Table 8 Fitted parameters  $A_{fast}$ ,  $A_{slow}$ ,  $\tau_{fast}$ , and  $\tau_{slow}$  related to the amplitudes and time constants characterizing the fast and slow mode of  $O_2$  release. The dashed lines represent the mean values of the parameters obtained for the control samples.

Parameters	$A_{fast}$	$\tau_{fast}$ [ms]	$A_{slow}$	$\tau_{slow}$ [ms]
PSII BBY control	$0.73 \pm 0.08$	$4.1 \pm 1.8$	$0.27 \pm 0.08$	$44.2 \pm 14.7$
PSII BBY -16,23	$0.26 \pm 0.09$	$6.2 \pm 3.6$	$0.74 \pm 0.06$	$22.2 \pm 4.4$
PSII BBY -16,23,33	0	-----	$1.00 \pm 0.03$	$13 \pm 2$

Oxygen release times obtained using the fast polarographic method are typically in the range of 0.8 ms to 4 ms, depending on the measurement technique and conditions, type of the sample, and how the  $O_2$  release times are determined (Bouges-Bocquet, 1973; Canaani, Malkin, & Mauzerall, 1988; Etienne, 1968; Jursinic & Dennenberg, 1990; Lavergne, 1989; Mauzerall, 1990; Tang, Moussavi, & Dismukes, 1991). The lower limit of oxygen release, determined experimentally from EPR oximetry measurements and obtained by direct analysis of the signal after the third flash from the fast electrode, is approximately 500  $\mu$ s (Schulder, Burda, Strzalka, Bader, & Schmid, 1992; Strzalka, Walczak, Sarna, & Swartz, 1990). This limitation is also due to the electron transfer time between  $Q_A$  and  $Q_B$ , which depends on the  $Q_B$  redox state and the number of positive charges accumulated in the OEC (0.2  $\div$  0.8 ms) (de Wijn & van Gorkom, 2001; Vinyard et al., 2013). The transfer of an electron from  $Q_A^{\bullet-}$  to oxidized PQ bound at the  $Q_B$  site typically takes about 200-400  $\mu$ s and to  $Q_B^{\bullet-}$  about 500-800  $\mu$ s (Bowes, Crofts, & Arntzen, 1980; Robinson & Crofts, 1983; Weiss & Renger, 1984). If the observed specific PQ diffusion pathway between the membrane and the  $Q_B$  binding pocket allows the generation of an internal pool of quinones (Krivanek, Kern, Zouni, Dau, & Haumann, 2007; Loll et al., 2005) the acceptor side of PSII would not be a bottleneck in the kinetics of the oxygen release process. The approximately 10-fold slower time constant of the  $O_2$  signal observed here is comparable in magnitude to the oxygen release times observed for thylakoids isolated from *Synechocystis* sp. PCC6803 mutants: D1-V185N, D1-V185T, D1-D61N, and D1-61A, for which the time after which the oxygen release signal reached a maximum was about 29 ms, 20 ms, 23 ms, and 33 ms, respectively, at pH 6.5 (Bao & Burnap, 2015; Sugiura et al., 2018). It is important to note that these times are about 20 to 30 times longer than those obtained for the wild form of *Synechocystis* sp. PCC6803. The D1-D61 and D1-V185 mutants were selected because molecular modelling confirmed the hypothesis that they could mediate the release of protons from the OEC and the stabilisation of the water cluster adjacent to the O5 of the  $Mn_4CaO_5$  complex, respectively (Ho & Styring, 2008; Ishikita et al., 2006; Sproviero et al., 2008). This has also been confirmed by experiments (Debus, 2014; Dilbeck, Bao, Neveu, & Burnap, 2013; Dilbeck et al., 2012; Hundelt, Hays, Debus, & Junge, 1998; Sugiura et al., 2018). It has been suggested that the D1-V185 residue may be involved in tuning the effective relaxation processes of H-bond networks and/or proteins in the

vicinity of the OEC (Sugiura et al., 2018). The D1-V185 side chain is located about 3.7 Å from the  $Mn_4CaO_5$  complex and faces the Cl1 channel, which interacts with TyrZ, D1-Asp170, D1-D61, D2-K317 and contains water clusters. The hydrogen bonding network of these  $H_2O$  clusters probably facilitates low-energy hydrogen bonding between TyrZ and D1-H190. Thus, it is expected that D1-V185 mutations may modify the protonation/deprotonation processes of  $Mn_4CaO_5$  and the efficiency of electron transfer to TyrZ<sup>+</sup>. It has been shown that PSII point mutations at two separate sites on the D1 core protein, D1-D61A/N, and D1-V185N, but located close to the  $Mn_4CaO_5$  cluster and affecting OEC functioning differently, slowed oxygen release similarly. It has been, therefore, suggested that in these mutants, the  $Mn_4CaO_5$  complex has adopted a structural rearrangement and/or tautomerism that allows a similar mechanism of O-O bond formation and oxygen release (Bao & Burnap, 2015).

The following examples illustrate how difficult it is to pinpoint the leading cause that determines whether PSII will release oxygen at a fast or a slow rate, namely, by studying a mutant of *Synechocystis* sp. PCC 6803, when valine was replaced by threonine in the D1 subunit, D1-V185T, in one case, no effect of this mutation on the rate of  $O_2$  release ( $t_{1/2} \approx 1.5$  ms, similar to the control) was observed, except for a reduction in oxygen production efficiency of about 40% (Dilbeck et al., 2013). An independent experiment found a significant slowing of  $O_2$  release to  $t_{1/2} \approx 20$  ms (Sugiura et al., 2018). In the same work, it has also been shown that D1-V185 is involved in stabilizing the  $S_2$  state of the  $Mn_4CaO_5$  complex in the low spin state (LS,  $S = 1/2$ ), whereas, in the D1-V185T mutant, which released  $O_2$  slowly, the high spin  $S_2$  state (HS,  $S = 5/2$ ) was dominant. Therefore, it seems that stabilizing the  $Mn_4CaO_5$  complex in different conformations of the  $S_2$  state open and closed (Figure 10b), characterised by different magnetic properties LS and HS, respectively, is closely related to the fast and slow mechanism of oxygen release. However, for the  $S_2$  and  $S_3$  states, there are potentially more possible configurations if, in addition, differences in the hydration of the  $Mn_4CaO_5$  cluster are taken into account (Shoji, Isobe, Miyagawa, & Yamaguchi, 2019; Yamaguchi et al., 2022). In contrast to the V185T mutant (Sugiura et al., 2018), the  $Mn_4CaO_5$  complex in the V185N, D61A, and D61N mutants, for which slow  $O_2$  evolution was observed, gives rise to a multiband  $S_2$  state signal that is qualitatively similar to the  $S_2$ -LS state favored in wild-type cyanobacteria at pH ~6 (de Lichtenberg, Avramov, et al., 2021; Kaur et al., 2019; Oyala, Stich, Debus, & Britt, 2015). Nevertheless, it is unlikely that differences in the OEC due to the conformational heterogeneity of the  $S_2$  and/or  $S_3$  states themselves can explain the observed biphasic oxygen release. The magnetic state of the  $Mn_4CaO_5$  complex in the  $S_2$  state is apparently not unique for fast or slow oxygen release. Indeed, the elucidation of the reasons for the divergent values of  $O_2$  release times in the D1-V185T mutant obtained by the different groups significantly contributes to understanding the mechanism regulating the rate of this process.

Thus, based on the results obtained for the mutants mentioned above, it can be concluded that disruption of the hydrogen bond network in the immediate vicinity of the  $Mn_4CaO_5$  complex slows down the release of oxygen as a result of delayed proton and/or electron transfer. In contrast, studies of *Synechocystis* sp. PCC 6803 mutants, D1-N181A/S, have led to the conclusion that proton transfer is not impaired in their case and that the significant slowdown in oxygen yield is due to delayed O-O bond formation (Pokhrel, Debus, & Brudvig, 2015). Interestingly, the  $S_2$  state was observed in both the LS and HS states in these mutants. The authors suggested that the positions and dynamics of critical water molecules required for efficient O-O bond formation may be perturbed in these mutants. Similarly, in the case of the D1-V185 and D1-D61 mutants, it was suggested that the changes introduced could affect substrate water's movement and possibly the cluster's associated isomerisation (Dilbeck et al., 2013; Dilbeck et al., 2012). Mutations of hydrophobic D1-V185 and hydrophilic D1-N181 are located near water molecules situated between TyrZ and D1-D61 and disrupt the extensive hydrogen bonding network between water molecules in the Cl1 water chain (Ishikita et al., 2006). D1-N181 interacts with the chloride ion via hydrogen bonding and is one of the closest residues for water W2 bound to  $Mn_4$  (Pokhrel et al., 2015; Umena et al., 2011). The residue D1-D61 is directly hydrogen-bonded to the W1 ligand of  $Mn_4$  and is thought to be involved in proton removal from the OEC to the lumen and/or water entry (Dilbeck et al., 2012; Flesher et al., 2022; Ho & Styring, 2008; Vassiliev et al., 2013; Yang et al., 2021).

Thus, it is clear that many factors can determine whether the release of oxygen in PSII will be fast or slow. Identifying the sequence of events that make a system fast or slow is currently very difficult, especially as it is so far not even certain when and how the O-O bond is formed [for review, see: (Lubitz, Chrysina, & Cox, 2019; Lubitz et al., 2023; Orio & Pantazis, 2021; Pantazis, 2019)]. Some believe that the formation of a bond between two oxygen atoms is possible only after the accumulation of 4 positive charges, i.e., during the transition of the manganese complex to the  $S_4$  state (de Lichtenberg, Avramov, et al., 2021; Ibrahim et al., 2020; Kusunoki, 2007; Vinyard et al., 2015; B. Zhang & Sun, 2018), while others think that it can already happen during the formation of the  $S_3$  state, which, like the  $S_2$  state, shows heterogeneity (Corry & O'Malley, 2018; Cox et al., 2014; Klauss et al., 2012; Mandal, Saito, et al., 2020; Pantazis, 2019; Pérez-Navarro et al., 2016; Pushkar et al., 2018; Renger, 2012; Shoji et al., 2015; P. E. M. Siegbahn, 2008, 2009, 2018; Suga et al., 2017). Examples of possible  $Mn_4CaO_5$  cluster configurations that can coexist are shown in Figure 10. Each of the possible configurations of the  $Mn_4CaO_5$  complex at the various stages of its reorganization associated with the accumulation of positive charge, the attachment of further water molecules, and the release of protons is closely related to the valence changes of specific Mn ions, and consequently to the magnetic properties of the entire manganese cluster [for review see: (Pantazis, 2019)]. Due to the very short lifetime of the  $S_4$  state, one can only try to determine the organization of the OEC by modelling. This means that it is not

possible to state unequivocally what the actual stage of O-O formation and O<sub>2</sub> release is. How the reorganization of the Mn<sub>4</sub>CaO<sub>5</sub> cluster itself may occur during the Kok cycle has been the subject of many hypotheses [for review, see: (Hatakeyama et al., 2016; V. Krewald, Neese, & Pantazis, 2019; Retegan et al., 2016; Yamaguchi et al., 2022; Zahariou et al., 2021; B. Zhang & Sun, 2018)]. Recent studies of the S<sub>3</sub>→(S<sub>4</sub>)→S<sub>0</sub> transition kinetics using microsecond Fourier transform infrared (FTIR) spectroscopy (Greife et al., 2023) and serial femtosecond X-ray crystallography snapshots (Bhowmick et al., 2023) have allowed approximating the timescale of subsequent steps in the multistep O<sub>2</sub> formation process. At least a two-step deprotonation of Mn<sub>4</sub>CaO<sub>5</sub> was observed in the stage before Tyr<sub>Z</sub><sup>+</sup> reduction and after water binding refilling the vacant site created by O<sub>2</sub> release. Both experiments showed that the appearance of the peroxide after about 1.2 - 2.5 ms is the intermediate and slowest step before forming the O<sub>2</sub> molecule. Furthermore, in both works, the D1-D61 pathway (Cl1 channel) was identified as responsible for the exit of both protons from Mn<sub>4</sub>CaO<sub>5</sub> and D65/D312 as a regulator of these deprotonations. The mechanism of Mn<sub>4</sub>CaO<sub>5</sub> cluster reorganization and substrate water binding proposed by both groups is based on its open cubic structure. This structure is typically observed in cyanobacteria. In higher plants, high-spin S<sub>2</sub> and S<sub>3</sub> states are detected, which are often explained by the closed cubic structure of the Mn<sub>4</sub>CaO<sub>5</sub> complex (Zahariou et al., 2021). Consequently, there have also been theoretical proposals for a different pathway leading to O-O bond formation and O<sub>2</sub> release than the one proposed for example, in (Greife et al., 2023), involving Ca/Mn<sub>3</sub>/Mn<sub>4</sub> μ<sub>3</sub>-oxo (O5) and Mn1(IV)-oxyl (Ox), or in (Bhowmick et al., 2023), where different variants have been suggested, not excluding the possibility of the involvement of the Mn(V) state in the final transition step, i.e. in the S<sub>4</sub> state, prior to water binding to the substrate. A 'nucleophilic oxy-oxo coupling' mechanism between Mn4(V)=oxo and μ<sub>3</sub>-oxo (O5) has been proposed for the final S<sub>4</sub> state in the case of the closed cubic structure of the Mn<sub>4</sub>CaO<sub>5</sub> complex (Guo et al., 2022). However, even here, a second pathway for the open cubic structure in the S<sub>4</sub> state leading to an identifiable final S<sub>0</sub> state has not been ruled out.

Each of the proposed scenarios for O-O bond formation and O<sub>2</sub> release requires synchronized receipt of protons (H<sup>+</sup>) and O<sub>2</sub> and the binding of water to restore the S<sub>0</sub> state.

Both the theoretical approach to analysing the oxygen release sequence under the influence of short flashes, which takes into account the metastable state of S<sub>4</sub>, and the experimental approach, based on a time-dependent measurement of the increase in O<sub>2</sub> release under the influence of the third flash, allow us to conclude that the observed heterogeneity is due to the functioning of the OEC. The consistency of the observed changes in the proportions of fast and slow O<sub>2</sub> release pathways for the different samples, control, and PSII with external proteins removed allows us to relate the obtained times to the fast and slow release of the oxygen molecule and thus to the kinetics of the processes occurring on the donor side of PSII. The reduction of the fast

phase in the PSII – 23 kDa, 16 kDa water oxidation process indicates a destabilisation of the proton network of water inside the O4 and O1 channels due to the destruction of their outputs towards the lumen. This indicates not only an impairment of proton transport through these channels but also a reduced control of water access to the  $\text{Mn}_4\text{CaO}_5$  complex. The impairment of the proton uptake through these channels is also manifested by the hindered transitions between the  $S_0 \rightarrow S_1$ ,  $S_1 \rightarrow S_2$  and  $S_3 \rightarrow S_0$ . The additional extraction of the 33 kDa protein had no further effect on the efficiency of the transitions between the  $S_i \rightarrow S_{i+1}$  states. Still, it did result in the disappearance of the fast oxygen release phase. This means the transition between the  $S_3$  and  $S_0$  states in PSII - 33 kDa, 23 kDa, and 16 kDa occurs via the metastable  $S_4$  state. In this case, the only functional channel is Cl1A, as mentioned above, although some modifications of its functionality cannot be excluded. The 33 kDa protein has a region containing a hydrogen-bonding network near Cl-1 and a conserved residue R262 near the luminal side, which can interact with the  $\text{Mn}_4\text{CaO}_5$  cluster through a D1-D61-mediated hydrogen-bonding network extending to the PSII core proteins (Taguchi et al., 2020). So, the organizational modification of D1 and D2 on the donor side of PSII due to the extraction of external proteins, particularly the 33 kDa protein, is possible in several ways. The absence of this protein destabilizes the  $\text{Mn}_4\text{CaO}_5$  complex, affecting not only the organization of its protein ligands but also the entire proton network, to which water molecules and amino acids from the first and further coordination spheres contribute. The critical role of the hydrogen bonding network on the luminal side of PSII, not only in the immediate vicinity of the OEC, was discussed in (Vogt et al., 2015). The observed slowing of the fast phase in the sample lacking the 23 kDa and 16 kDa proteins compared to the control is not surprising, as one would expect that a disruption of the coordinated deprotonation with water binding would lead to a slowing of the  $\text{O}_2$  evolution. Disabling some channels and undoubtedly reducing their efficiency in both transport and gating contribute significantly to this effect. The structural change of the  $\text{Mn}_4\text{CaO}_5$  complex must also be considered. In contrast, the acceleration of oxygen release via the slow pathway may seem surprising. However, assuming that water is mainly supplied to the  $\text{Mn}_4\text{CaO}_5$  complex through the O1 channel, the lack of gating of the water flow as a result of modification of the channel is the simplest explanation for the observed effect. Such a mechanism to control water access to the O1 channel with D1-E329 has been proposed for cyanobacteria (Vassiliev et al., 2013). The above hypothesis is highly plausible if one assumes that water binding to the manganese complex is an equally important mechanism regulating OEC function in addition to proton extraction. The further significant acceleration of the oxygen release in PSII BBY – 16,23,33 - when open access of the  $\text{Mn}_4\text{CaO}_5$  complex to the aqueous environment is observed only supports this thesis. In addition, open access to the aquatic environment suggested that the aqueous network could provide an effective channel for the removal of oxygen molecules. On the other hand, if the hydrophobic matrix is responsible for the removal

of O<sub>2</sub>, this would imply that the penetration of the oxygen molecule into the lipid layer is enhanced.

However, a completely different scenario can be outlined to explain the observed changes in the contribution and rate of these two O<sub>2</sub> release pathways due to depletion of external proteins. EPR measurements showed that both LS and HS S<sub>2</sub> states exist in higher plants (Taguchi et al., 2020). This is attributed to the coexistence of two different isomers of the Mn<sub>4</sub>CaO<sub>5</sub> complex (see discussion above). The depletion of the two outer proteins PsbQ and PsbP led to a significant decrease in the ratio of the HS signal to the LS signal for the S<sub>2</sub> state. The depletion of all three outer proteins, i.e., including the PsbO protein, resulted in a complete loss of the HS signal for this state (Taguchi et al., 2020). These results provide evidence for a regulatory role of the external proteins in stabilizing the HS S<sub>2</sub> state. Thus, the fast transition pathway from S<sub>3</sub> to S<sub>0</sub> could be associated with the HS-S<sub>2</sub> state and the slow pathway, which requires consideration of the metastable S<sub>4</sub> state, with the LS S<sub>2</sub> state. We do not know how the following stages of the Kok cycle proceed. However, this direct correlation of the two S<sub>2</sub> spin states with the respective fractions of the two oxygen release pathways suggests that the bifurcation of the mechanism leading to O-O bond formation and O<sub>2</sub> release occurs at an earlier stage, than the final transition S<sub>3</sub> → S<sub>0</sub>.

Thus, taking into account the experimental and theoretical evidence for the existence of a relationship between the spin and protonation states of the S<sub>i</sub> states, it is clear that the O<sub>2</sub> evolution process cannot be considered without taking into account the interrelationships between the structural changes of the Mn<sub>4</sub>CaO<sub>5</sub> complex and the functioning of the channels. The influence of external proteins on the stabilisation and activity of the Mn<sub>4</sub>CaO<sub>5</sub> complex has been shown many times (Barry et al., 2017; Burnap, Shen, Jursinic, Inoue, & Sherman, 1992; Campbell, Gregor, et al., 1998; Enami et al., 2008; Ifuku & Noguchi, 2016; Nagao et al., 2015; Offenbacher, Polander, & Barry, 2013; Tomita, Ifuku, Sato, & Noguchi, 2009), but never in the context of PSII heterogeneity. Finally, it should be borne in mind that the oxygen release process is part of the dynamic protein-lipid-dye matrix, i.e. the PSII system. In addition to the local dynamics of the hydrogen network formed by amino acids and water near the OEC, the reorganization capacity of the entire PSII system, also near the acceptor side, is undoubtedly essential for oxygen release efficiency. Changes in the acceptor side have been observed to accompany structural changes in the donor side (Ibrahim et al., 2020; Kern et al., 2018; Suga et al., 2017). Considering the two-cycle acceptor side and the four-cycle donor side, it can be assumed that the exchange rate of PQ from the external quinone pool would be responsible for the heterogeneity of oxygen release. This aspect cannot be ignored. However, in PSII samples depleted of PsbQ, PsbP, and PsbO, it would be rather difficult to explain an acceleration of the slow path as a result of conformational changes of the Q<sub>B</sub> binding site. Moreover, no further changes in transfer probabilities between S<sub>i</sub> states were observed compared to the PsbQ and PsbP depleted sample. In this work, we did

not investigate the influence of  $\text{Cl}^-$  ions on the heterogeneity of the  $\text{O}_2$  evolution process. However, it cannot be ruled out that the release of the  $\text{Cl}^-$  ion could influence the observed effects (Boussac, Setif, & Rutherford, 1992; Saito, Rutherford, & Ishikita, 2013; van Vliet & Rutherford, 1996; Wincencjusz, van Gorkom, & Yocum, 1997). However, it appears that these modifications would primarily affect the activity of the Cl1 channel, i.e. its effectiveness in the uptake of protons from the  $\text{Mn}_4\text{CaO}_5$  complex and the delivery of water molecules to it.

The proposed method of measuring oxygen evolution time using fast polarography has significant advantages over the common use of the shape of the electrode response signal. As shown in (Schulder et al., 1992) the signal recorded on the electrode is strongly dependent on the contact of the sample with the electrode or its thickness, apart from the voltage applied to the electrode. However, the porosity of the sample and/or its external potential, which can change due to sample modification, also affect the signal's shape. This is demonstrated by the typical polarographic signals shown in Figure 36, obtained for the control PSII, PSII BBY – 16,23, and PSII BBY – 16,23,33 under the same experimental conditions.

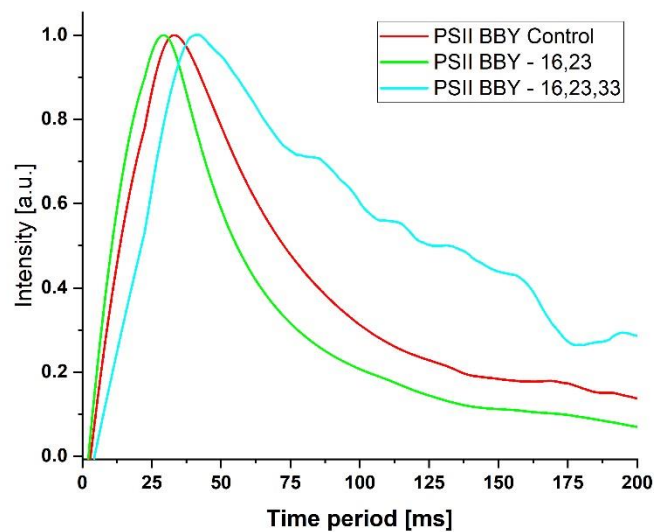


Figure 36 The typical polarographic signals of oxygen evolution after the 3<sup>rd</sup> flash of light (the first maximum of oxygen evolution) for the control PSII BBY, PSII BBY – 16,23, and PSII BBY – 16,23,33.

## 6.2 The action of WO<sub>3</sub> NPs on PSII BBY

### 6.2.1 WO<sub>3</sub> NPs influence on PSII organisation

Some data presented below have been already published in (Krysiak et al., 2023). Figure 37 shows a SEM image of the mWO<sub>3</sub> NPs used in the experiments provided by M. Gotić. Irregular NPs of about 100 nm in size predominate. The fine overlying structures in the magnifications suggest that these NPs may be formed from small, superfine nanoparticles. This was proved by the DLS results presented in Chapter 5.5.

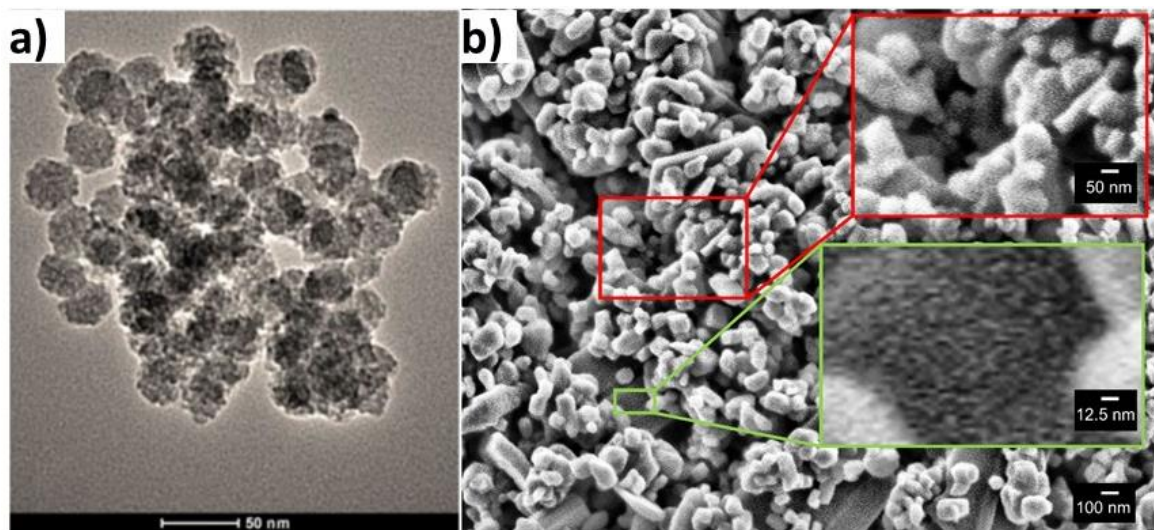


Figure 37 a) TEM image of sonicated WO<sub>3</sub> NPs. b) SEM image of the mWO<sub>3</sub> NPs used in our experiments.

The small nanoparticles ranging in size ~1-3 nm can easily penetrate PSII BBY membranes. To see how different concentrations of WO<sub>3</sub> NPs can affect the organization of PSII BBY, AFM topography measurements were performed. Figure 38a, c show example AFM images of PSII BBY untreated and treated with WO<sub>3</sub> NPs at a weight ratio of 1 µg NP/µg Chl. Visible protrusions ~0.3 nm high (Figure 38b, d) are the external proteins protecting OEC (see Figure 8) The heights of the protrusions and the heights of the concavities they form, estimated from AFM measurements carried out in an aqueous environment using the tapping mode, were about 2 nm and 1 nm, respectively (Stoichev et al., 2015; Sznee et al., 2011), while Cryo-EM allowed setting the upper limit of the protruding structure height at about 5 nm (Nield et al., 2000). The root mean square (RMS) roughness obtained for the PSII BBY control and NPs-treated samples (Table 9) show that the observed protrusions are similar in all cases, but their heights are lower than those found in other experiments. This is due to the fact that the AFM measurements were performed in a liquid environment in the contact mode and to the tip used. Thus, they indicate the distribution of PSII in the membranes studied. The results of the analysis of the distribution of PSII in the control sample and in samples

containing strictly defined concentrations of NPs are shown in Figure 38e. Parameters of the theoretical fits using modified Gaussian function are collected in Table 9. The deviations from the Gaussian shape are modelled by making the standard deviation linearly dependent on the argument:  $\sigma = \sigma_0(1 + \varepsilon(x - x_0))$ . This is an effective description that can be applied only in a specific range of  $x$ , i.e. when  $\varepsilon \leq \frac{1}{3}$  since  $\sigma$  has to be positive. This approach allowed us to simplify the description of the observed asymmetry of PSII separations.

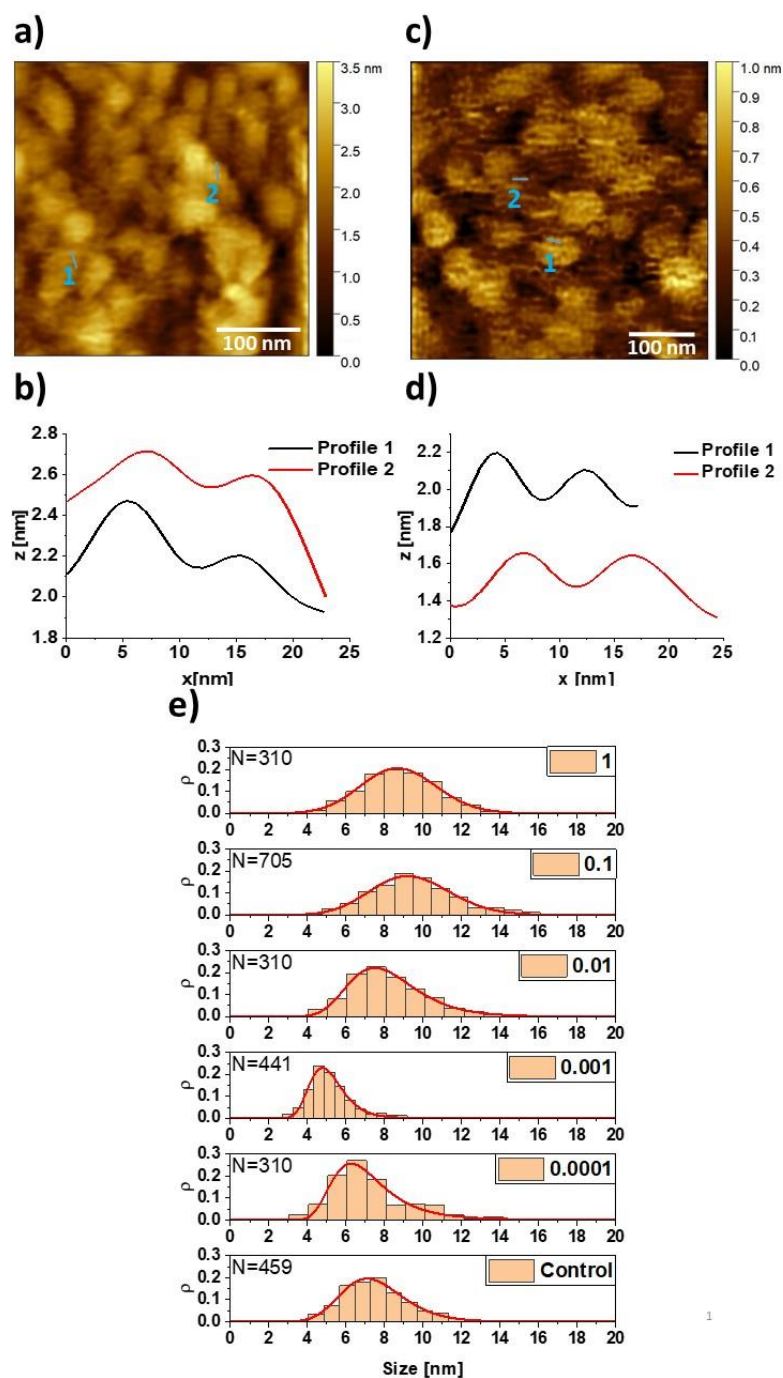


Figure 38 Example AFM image of PSII BBY untreated (a) and treated with  $m\text{WO}_3$  NPs at a weight ratio of  $1 \mu\text{g NPs}/\mu\text{g Chl}$  (b). Cross sections through the protrusions marked on the topographies are shown below the images (profiles 1 and 2). c) Distribution of PSII in the control sample of PSII BBY and samples containing indicated concentrations of NPs.

The lines are theoretical fits using a modified Gaussian function (as described in the text). The fitted parameters are summarized in Table 1. Measurements done in a contact mode using a liquid cell, in the Hepes I buffer.

Table 9 Parameters of the theoretical fits of the distribution of PSII in the PSII BBY (AFM experiments) using modified Gaussian function  $y = C * \exp(\frac{-(x-x_0)^2}{2\sigma^2})$ , where  $C$  is the amplitude,  $x_0$  is the abscissa of the maximum value,  $\sigma$  is the standard deviation linearly dependent on the argument  $\sigma = \sigma_0(1 + \varepsilon(x - x_0))$ . The last row contains the root mean square (RMS) roughness obtained for the PSII BBY control and NPs-treated samples

Concentration [ $\mu\text{g NPs}/\mu\text{g Chl}$ ]						
Parameters	0 control	0.0001	0.001	0.01	0.1	1
$C$	0.24	0.26	0.43	0.22	0.19	0.21
$x_0$ [nm]	7.09	6.26	4.77	7.49	9.19	8.66
$\sigma_0$ [nm]	1.57	1.32	0.83	1.69	2.05	1.95
$\varepsilon$ [nm <sup>-1</sup> ]	0.06	0.14	0.16	0.08	0.02	0.01
RMS [nm]	0.26	0.23	0.18	0.26	0.24	0.26

The estimated average PSII spacing was  $\sim 7.1$  nm in the control sample and varied with increasing concentrations of added  $\text{WO}_3$  NPs. The smallest distance of  $\sim 4.8$  nm was observed for a sample containing  $0.001 \mu\text{g NPs}/\mu\text{g Chl}$ . At higher concentrations of the NPs tested, the average separation between PSII complexes increased and was greater than that found for the control sample. The largest distance between the PSII complexes was observed to be  $\sim 9.2$  nm for a weight ratio of  $0.1 \mu\text{g NPs}/\mu\text{g Chl}$ . The parameter  $\varepsilon$ , which is related to the asymmetry of the distribution, has the highest values for the two lowest concentrations of NPs applied. It decreases as the concentration of nanoparticles increases. For the two highest NPs concentrations used, the PSII distance distributions are close to a Gaussian function.

At the same time, it is noteworthy that even at the highest concentrations of  $\text{WO}_3$  NPs used, fragments of the PSII-enriched thylakoids do not disintegrate (Figure 39). Due to the need for a contrast agent, it is not possible to indicate the fine  $\text{WO}_3$  NPs in thylakoid membranes, but this was possible on the observed isolated structures of LHCII-associated and LHCII-free PSII complexes,  $\text{C}_2\text{S}_2\text{M}_2$  (its size estimated on the high-resolution cryo-EM map:  $19.5 \text{ nm} \times 31.0 \text{ nm} \times 12.2 \text{ nm}$  : width x length x height) (van Bezouwen et al., 2017) and  $\text{C}_2$  (about  $10 \text{ nm} \times 19 \text{ nm} \times 11 \text{ nm}$ : width x length x height) (Boekema et al., 1995; Haniewicz et al., 2015; Nield & Barber, 2006; Umena et al., 2011), respectively, see inset in Figure 39d.

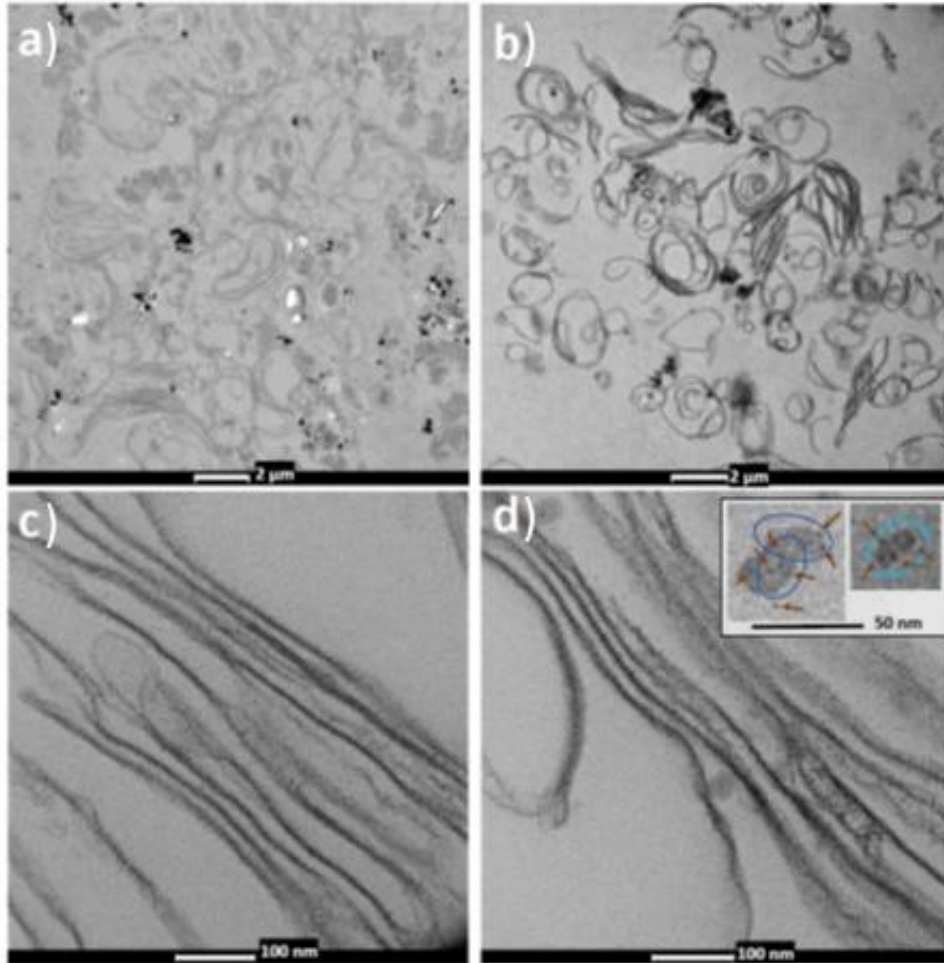


Figure 39 TEM images of BBY PSII: (a) and (c) untreated; (b) and (d) treated with  $1 \mu\text{g NPs}/\mu\text{g Chl}$ . In the inset of figure (d), the structures of PSII complexes with bound LHCII antennas ( $C_2S_2M_2$ , surrounded by a dark blue frame, the right image) and PSII dimer ( $C_2$ , surrounded by a light blue frame, the left image) are shown. Some of the visible superfine  $\text{WO}_3$  NPs embedded in these structures are indicated by red arrows.

## 6.2.2 $\text{WO}_3$ NPs influence on PSII functioning

### 6.6.2.1 Energy utilisation and photosynthetic efficiency

#### 6.6.2.1.1 Absorption and fluorescence measurements

Some data presented below have been already published in (Krysiak et al., 2023). Absorption spectra of the control sample and PSII BBY treated with different concentrations of  $\text{WO}_3$  NPs are shown in Figure 40. They show that the absorption is enhanced for samples containing 0.01 and  $0.1 \mu\text{g NPs}/\mu\text{g Chl}$ . All spectra show two absorption bands for pigments present in both the PSII and LHCII complexes. The first is visible in the range from 300 nm to about 525 nm. It is characteristic of Chls *a* and *b* (Soret B- bands) and carotenoids. (Lichtenthaler & Buschmann, 2001) The second band for wavelengths  $> 560$  nm comes from Chl *b* and Chl *a* (Q bands;  $Q_y$  bands at  $\lambda > 600$

nm): (i) Chl *a* and *b* from LHCII and the minor antenna with maxima at ~ 670-678 nm and ~ 640-654 nm, respectively, (ii) Chl *a* from the PSII complex with maxima at ~ 668 nm (accessory Chl *a* in the PSII core) and between 668 and 700 nm (PSII inner antenna: CP43 and CP47), and at ~ 654 nm (CP43), and (iii) a possible small contribution of Chl *a* from the PSI complex (in our case it is a possible minor contaminant) at around 690 to 705 nm (Alfonso, Montoya, Cases, Rodriguez, & Picorel, 1994; Bassi, Riconi, & Giacome, 1990; Groot et al., 1999; Groot, Peterman, van Stokkum, Dekker, & van Grondelle, 1995; Jennings, Zucchelli, & Garlaschi, 1990; Konermann & Holzwarth, 1996; Pan et al., 2017). To estimate the position of the bands of different dyes, data obtained for low-temperature spectra with higher resolution can be used because in the 650-690 nm wavelength range, the bands with energies  $< \sim 14760 \text{ cm}^{-1}$  ( $\lambda > \sim 677 \text{ nm}$ ) are blue-shifted, and at energies  $> \sim 14760$  ( $\lambda < \sim 677 \text{ nm}$ ) the higher energy components are red-shifted by no more than ~1 nm. Only the half-widths  $\Delta\lambda/2$  of the individual bands increase with increasing temperature from cryogenic to room temperature (up to 40%) (Konermann & Holzwarth, 1996). We can directly compare the spectra because all samples contained the same amount of Chl. From the differential spectra between NP-containing samples and control shown in Figure 40b, it can be seen that for the two lowest concentrations of WO<sub>3</sub> NPs, the contribution of LHCII pigments (chlorophylls *a* and *b* and carotenoids) in absorption spectra decreases (Bressan et al., 2016; Croce, Remelli, Varotto, Breton, & Bassi, 1999). An increase in absorbance was observed for the 0.01 and 0.1  $\mu\text{g NPs}/\mu\text{g Chl}$  weight ratios. In the first case, the shape of the differential spectrum is characteristic of PSII super-complexes with a few LHCII trimmers attached to them (Caffarri et al., 2009) and probably LHCII, as indicated by the absorption maximum at ~523 nm (Ruban, Rees, Pascal, & Horton, 1992). It seems that the higher concentration of WO<sub>3</sub> NPs resulted in an increased absorption only in the PSII RC since the peaks at 674 nm, 442 nm, and 419 nm were shifted to 677 nm, 438 nm, and 418 nm, respectively (Seibert, Picorel, Rubin, & Connolly, 1988). In this case, however, the effect of the increased absorption is less pronounced. For a sample containing 1  $\mu\text{g NPs}/\mu\text{g Chl}$ , an inverse trend of the changes in absorbance is observed when the absorbance decreases again in comparison to the control. The shape of the differential spectrum indicates a decrease in the absorption efficiency of the entire PSII-LHCII supercomplex. (Eshaghi, Andersson, & Barber, 1999).

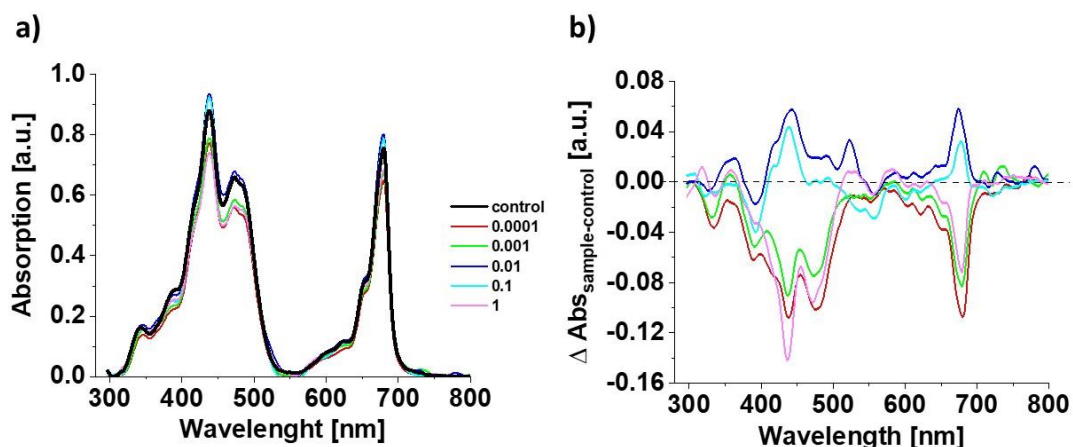


Figure 40 a) Absorption spectra of the control sample and PSII BBY treated with different concentrations of  $m\text{-WO}_3$  NPs indicated in the figure. The samples were suspended in the Hepes I buffer, pH 6.5. b) Differential absorption spectra between samples containing different concentrations of NPs and the control sample.

Steady-state fluorescence measurements were performed to investigate the influence of  $m\text{WO}_3$  NPs on the energy transfer efficiency of PSII BBY. Figure 41a-f shows an examples of excitation-emission spectra at room temperature. To obtain information on the energy transfer from LHCII and the minor antenna to PSII RC, we subtracted the fluorescence spectrum obtained by excitation at 440 nm (when equal excitation of Chl  $a$  and Chl  $b$  is expected) from the fluorescence spectrum excited at a wavelength specific for Chl  $b$ , i.e., 480 nm (E. Kim, Akimoto, Tokutsu, Yokono, & Minagawa, 2017; Mackinney, 1941). The emission spectra were previously normalized to a wavelength of 720 nm. At this wavelength, the fluorescence of Chl  $a$  from PSI dominates. These differential spectra for untreated and NP-treated PSII BBYs are shown in Figure 41g. These data provide information on light harvesting and energy transfer from the outer to the inner antenna and PSII core chlorophylls. The differential spectra obtained for the control and NP-containing samples are clearly different and depend on the concentration of  $\text{WO}_3$  NPs. In the control sample, there are some characteristic bands with maxima at about 657.5 nm, 662.5 nm, 677 nm, 684 nm, 690 nm, 700 nm, and 715 nm are visible (black line in Figure 41g). The two bands at the shortest wavelength are most likely related to Chls  $b$ , which could be observed in quenched PSII complexes, aggregated LHCII, and when Chls  $b$  are uncoupled in the light-harvesting antenna (Horton et al., 1991; Santabarbara, Neverov, Garlaschi, Zucchelli, & Jennings, 2001). Bands with maximum emission at about 677-680 nm are from Chl  $a$ , mainly from monomeric/isolated LHCII trimmers (Standfuss & Kühlbrandt, 2004), while at 700-715 nm from LHCII aggregates (Horton et al., 1991; Yamamoto et al., 2014). In the wavelength range of 680-700 nm, Chls  $a$  of the inner antenna emit radiation, but CP47 has a larger contribution in the emission at  $\lambda \geq 690$  nm, while CP43 has its maximum at  $\sim 683$ -685 nm (Alfonso et al., 1994; Andrizhiyevskaya et al., 2005; Andrizhiyevskaya, Frolov, van Grondelle, & Dekker, 2004;

Dang et al., 2008; Shibata, Nishi, Kawakami, Shen, & Renger, 2013). A fluorescence maximum that is usually observed at 693-695 nm is related to the fluorescence of the lowest excited state of CP47, most likely Chl 612 (Hall, Renger, Müh, Picorel, & Krausz, 2016). Core chlorophylls are expected to show fluorescence between 682-687 nm (Chen et al., 2015). Therefore, it is likely that the emission of Chls coupled to the PSII core and CP43 contributes to the band with a maximum at 684 nm, while the band with a maximum at 690 nm is dominated by the emission from the CP47 antenna. Therefore, it can be concluded that the LHCII is effectively transferring energy to the PSII reaction center and that there is good connectivity between the internal and external antennas, as well as with the PSII core. It turned out that even the lowest concentration of 0.0001  $\mu\text{g NPs}/\mu\text{g Chl}$  (red line in Figure 41g) caused a disruption of the energy transfer from LHCII to CP47 and from the PSII core to CP47 (which occurs when the reaction centres are closed), since the fluorescence at 684 nm decreased and, decreased in the whole range from 686 nm to 700 nm. In addition, there are two minima at these wavelengths, at 690 nm and 697 nm, characteristic of CP47. On the other hand, there are two strong bands with maxima at about 677 nm and 704 nm, which may indicate the monomerization and aggregation of the LHCII trimmers. A ten-fold higher concentration of NPs leads to an attenuation of the fluorescence over almost the whole range (green line in Figure 41g), indicating a disturbance of the energy transfer between LHCII and the two internal antennas, CP43 and CP47, in some PSII supercomplexes. For the concentration of 0.01  $\mu\text{g NPs}/\mu\text{g Chl}$  (dark blue line in Figure 41g), we observed the occurrence of positive bands at 680 nm and 686 nm, which can be attributed to LHCII and PSII core/ CP43, respectively, as well as a band at 708 nm which indicates antennas aggregation. The broad band at around 665-670 nm may come from decoupled Chls and/or aggregated Chls *b* as well as from minor complex antennas. This differential spectrum indicates an increase in absorption by LHCII and their partial aggregation, but also an effective transfer of energy to the PSII core, probably with the participation of CP43. However, the energy transfer from Chls, coupled to the PSII core, to CP43 is significantly reduced in comparison to the control sample. The differential fluorescence spectrum of the sample treated with a concentration of 0.1  $\mu\text{g NPs}/\mu\text{g Chl}$  (light blue line in Figure 41g) showed positive maxima at about 682 nm and 689 nm, indicating effective energy transfer from LHCII to both internal antennas, i.e. CP43 and CP47, respectively, and their good connectivity to PSII core Chls. The bands with maxima at about 660.6 nm and 674.4 nm are most likely derived from decoupled Chl *b* and Chl *a* within the LHCII. The two small bands at about 705 nm and 715 nm are associated with LHCII aggregates. The highest concentration applied (magenta line in Figure 41g) results in an increased fluorescence at about 680.5 nm, 688 nm, and 697 nm. The first band is from monomeric LHCII, while the other two are from CP47. The band at about 712 nm is probably related to some LHCII aggregates. The maximum band at 672 nm comes from decoupled Chls *a*, and these two bands at 651.5 nm and 660.5 nm are from decoupled

Chls *b*. The data indicates that the transfer of energy from the LHCII to the CP43 is disrupted but that the LHCII is able to transfer energy to the CP47.

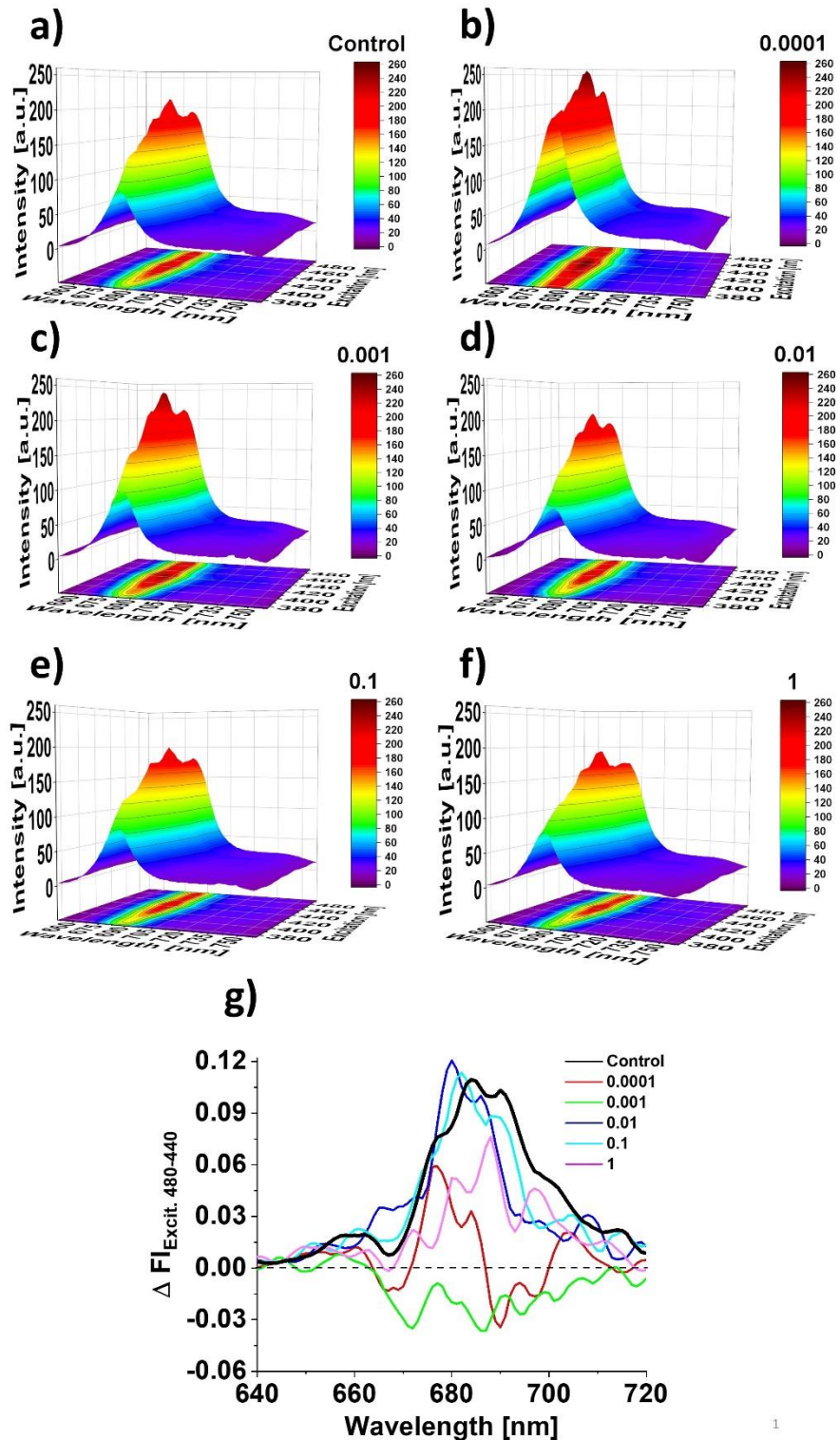


Figure 41 Room temperature excitation-emission spectra for a control sample of PSII BBY and treated with different concentrations of *m*-WO<sub>3</sub> NPs as indicated in the figures (a-f). g) Differential fluorescence emission spectra at 440 nm excitation (when equal excitation of Chl *a* and Chl *b* is expected) and at 480 nm (Chl *b* excitation) obtained for the control and PSII BBY treated with different concentrations of NPs. The samples were suspended in the HEPES I buffer, pH 6.5.

### 6.6.2.1.1 Variable fluorescence measurements (PAM fluorescence)

Variable changes in Chl *a* fluorescence measured in dark-adapted samples under continuous illumination, the so-called Kautsky effect, provide information about the photochemical quantum yield of PSII photochemistry and the activity of electron transfer within this reaction center (Figure 42) (Kautsky & Hirsch, 1931; Stirbet & Govindjee, 2011). In particular, we performed experiments in a time range not exceeding a few seconds to focus on the photosynthetic activity of water-plastoquinone oxidoreductase, i.e. the light-driven reaction localized within PSII RC depended on the state of its donor and acceptor side (see Figure 8), as our systems are enriched in PSII. Fluorescence is highest when the plastoquinone (PQ) bound to the Q<sub>A</sub> site (later named plastoquinone Q<sub>A</sub>) is in the reduced state. This is because Q<sub>A</sub> in the oxidized state is a known, highly efficient fluorescence quencher (van Gorkom, Pulles, & Étienne, 1978). PQ at the Q<sub>A</sub> site can only accept one electron. The non-photochemical quenching in our samples may be due to the oxidized PQ pool (unbound external quinones) (Vernotte, Etienne, & Briantais, 1979). In the dark-adapted samples, all quinone acceptors should be in the oxidized state, and these RCs are called 'open'. The small fraction of fluorescence that occurs immediately after exposure to light results from the light-driven accumulation of Q<sub>A</sub><sup>•-</sup> in PSII RCs due to charge separation that occurs in less than 300 ps after P680 excitation (Dau & Sauer, 1996; Grabolle & Dau, 2005). Reaction centers capable of further electron transfer beyond Q<sub>A</sub>, having oxidized PQ at the Q<sub>B</sub> site, contribute to this fastest phase. This phase saturates at the electron transfer rate from Q<sub>A</sub><sup>•-</sup> to Q<sub>B</sub> (Q<sub>A</sub><sup>•-</sup>Q<sub>B</sub> → Q<sub>A</sub>Q<sub>B</sub><sup>•-</sup>). They are referred to as active 'open' PSII and contribute to the fastest phase of the induction fluorescence curve, which is known as *F*<sub>0</sub> (Figure 42a). However, among PSII systems, one should also expect RCs with a single reduced PQ at the Q<sub>B</sub> site (Q<sub>B</sub><sup>•-</sup>) and an empty secondary quinone acceptor site or one occupied by Q<sub>B</sub><sup>2-</sup> (the plastoquinone bound at the Q<sub>B</sub> site can accept 2 electrons). Under prolonged illumination with saturating light, all Q<sub>A</sub>s are reduced within seconds since all quinone acceptors are reduced in PSII BBY, and such PSII RCs are called 'closed' active centres. The fluorescence intensity reaches its maximum, *F*<sub>*M*</sub>. The difference *F*<sub>*M*</sub> - *F*<sub>0</sub> = *F*<sub>*v*</sub> is called variable fluorescence and is related to the maximum quantum yield of primary PSII photochemistry (Genty, Briantais, & Baker, 1989). Our typical Kautsky curve (already normalized to *F*<sub>*M*</sub>) is shown in Figure 28, and one can see a characteristic plateau to which *F*<sub>0</sub> and fast variable fluorescence (*F*<sub>*fv*</sub>) contribute, *F*<sub>*p*</sub> = *F*<sub>0</sub> + *F*<sub>*fv*</sub>. Thus, when the Kautsky curve reaches its first plateau (at time < 1 ms), *F*<sub>*p*</sub> is a measure of the fluorescence value. A slow variable fluorescence (*F*<sub>*sv*</sub>) can be evaluated as indicated in the graph. However, in order to get a quantitative and qualitative insight into the process of Q<sub>A</sub> formation and its oxidation processes, we have fitted the experimental data with the following multi-exponential function:

$$y(t) = y_0 + \sum_{i=1}^n A_i \left( 1 - \exp\left(-\frac{t-t_0}{t_i}\right) \right), \quad (8)$$

where  $n$  is the minimum number of components required to obtain a reasonable fit,  $A_i$  is the contribution of each component, and  $t_i$  is a characteristic time constant,  $y_0$  is the background of the signal before illumination ( $y_0=0$  for normalized curves). In the end, we needed 4 components to get a reasonable fit to the experimental data.  $A_1$  and  $A_2$  correspond to the  $F_0$  and  $F_{fv}$  phases, respectively.  $A_3$  and  $A_4$  contribute to the slow variable fluorescence phase (a second plateau at time  $< \sim 5$  s but  $> 1$  ms), and we will now call them  $F_{sv1}$  and  $F_{sv2}$ , respectively, so that  $F_{sv} = F_{sv1} + F_{sv2}$ . The fluorescence induction curves were normalized to the  $F_M$  value before fitting, so the parameters  $F_0$ ,  $F_{fv}$ ,  $F_{sv1}$ , and  $F_{sv2}$  represent the contribution of the subsequent phases to the observed Kautsky effect. They are defined by the fluorescence growth times  $t_1=t_0$ ,  $t_2=t_{fv}$ ,  $t_3=t_{sv1}$ , and  $t_4=t_{sv2}$ , respectively. The fitted parameters  $F_0$ ,  $F_{fv}$ ,  $F_{sv1}$ , and  $F_{sv2}$  are shown in Figure 42a, and the time constants  $t_{fv}$ ,  $t_{sv1}$ , and  $t_{sv2}$  are shown in Figure 42b.

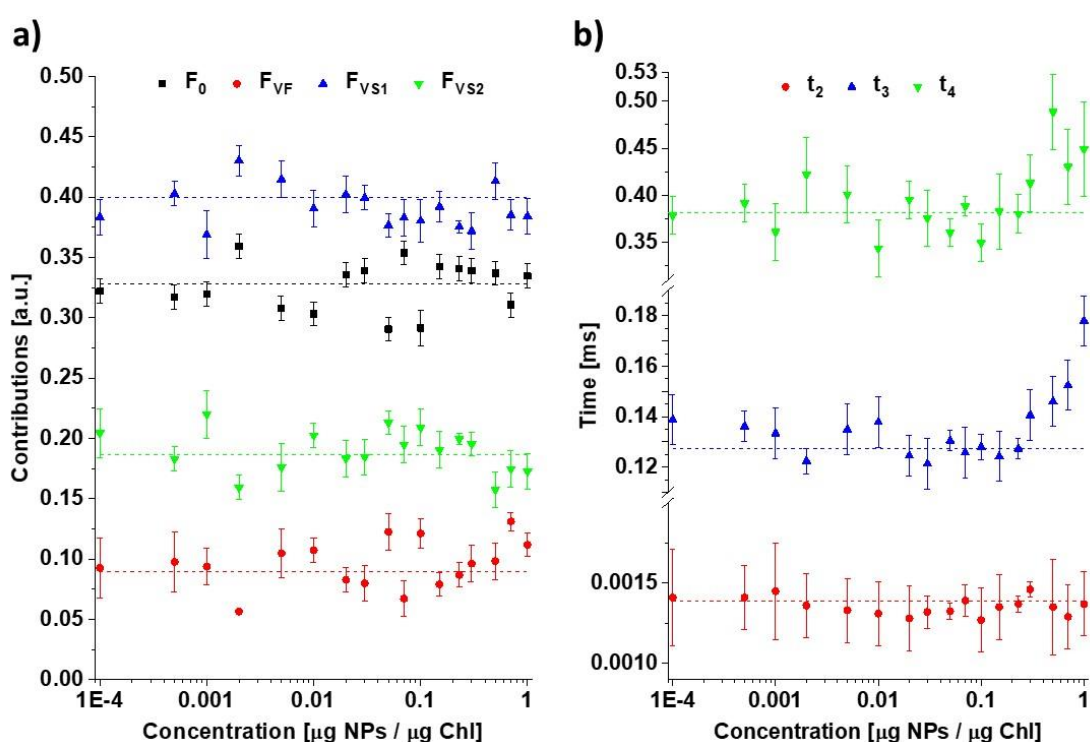


Figure 42 Fitted parameters  $F_0$ ,  $F_{fv}$ ,  $F_{sv1}$ , and  $F_{sv2}$  characterizing fast and slow phase contributions as a function of NPs concentrations. d) Time constants  $t_{fv}$ ,  $t_{sv1}$  and  $t_{sv2}$  describe each phase's kinetics versus NPs concentration. To get a good fit, a multi-exponential function assuming four components was sufficient. The dashed lines represent the mean values of the parameters obtained for the control samples. The values shown are the mean values of at least four independent measurements for the control samples and the samples containing different concentrations of NPs.

The mean values of  $t_0$ ,  $t_{fv}$ ,  $t_{sv1}$ , and  $t_{sv2}$  obtained for the control samples are  $478 \pm 36 \mu\text{s}$ ,  $1.39 \pm 0.12 \text{ ms}$ ,  $127 \pm 4 \text{ ms}$ , and  $381 \pm 15 \text{ ms}$ , respectively. These values indicate that the subsequent phases are undoubtedly due to oxidation of  $Q_A^{\bullet-}$  by: (i) oxidized PQ bound in the  $Q_B$  site ( $Q_A^{\bullet-}Q_B \rightarrow Q_AQ_B^{\bullet-}$ ) in the case of the fastest phase, (ii) already reduced  $PQ^{\bullet-}$  bound in the  $Q_B$  site ( $Q_A^{\bullet-}Q_B^{\bullet-} \rightarrow Q_AQ_B^{2\bullet-}$ ) for the phase characterized by the time constant of  $\sim 1 \text{ ms}$ , (iii) PQ, which must first bind to the empty  $Q_B$  site ( $Q_A^{\bullet-}\emptyset \rightarrow Q_A^{\bullet-}Q_B \rightarrow Q_AQ_B^{\bullet-}$ ) for the third phase saturating in  $\sim 100 \text{ ms}$  and (iv) PQ, which must replace  $Q_BH_2$  temporarily blocking the  $Q_B$  site ( $Q_A^{\bullet-}Q_BH_2 \rightarrow Q_A^{\bullet-}\emptyset \rightarrow Q_A^{\bullet-}Q_B \rightarrow Q_AQ_B^{\bullet-}$ ) in the case

of the slowest phase observed by us (de Wijn & van Gorkom, 2001). Slower values of the  $t_{sv1}$  and  $t_{sv2}$  constants in our experiments are due to the limited external plastoquinone pool available in PSII BBY.

The values of the parameters describing the fluorescence induction curves (Figure 42) show oscillations as a function of the applied concentration of  $WO_3$  NPs. The contributions of  $F_0$  and  $F_{fv}$  show opposite changes in monotonicity with increasing NPs' concentration. Similar complementary behaviour is observed for changes in the contributions of  $F_{sv1}$  and  $F_{sv2}$ . Interestingly, analogous oscillatory changes in  $F_0$  and  $F_{sv1}$  are observed in the NPs' concentration range  $0.001 \mu\text{g NPs}/\mu\text{g} \leq c_{\text{NPs}} \leq 0.3 \mu\text{g NPs}/\mu\text{g Chl}$ . Consequently, the same effect is also observed for the oscillations of  $F_{fv}$  and  $F_{sv2}$  in this concentration range. The time constants also show oscillatory changes with increasing NPs concentration and, in certain concentration ranges, are significant in relation to the values obtained for the control samples. Furthermore, changes in the values of  $t_{fv}$ ,  $t_{sv1}$ , and  $t_{sv2}$  in the concentration range from 0.001 to  $0.2 \mu\text{g NPs}/\mu\text{g Chl}$  show opposite monotonicity to the changes in the contributions of the phases characterized by these time constants, i.e.  $F_{fv}$ ,  $F_{sv1}$ , and  $F_{sv2}$ , respectively. This means that the growth of a given phase is accompanied by an increase in the flow rate of electrons. For  $c_{\text{NPs}} \geq 0.3 \mu\text{g NPs}/\mu\text{g}$ , the time constants of the slow phases increase with increasing NPs concentration. The time constant  $t_0$  showed no significant changes within the error limits. Its average value for the whole range of NPs concentrations is about  $514 \pm 24 \mu\text{s}$ .

#### 6.6.2.1 Oxygen evolution

The influence of  $WO_3$  NPs on the donor side of PSII, particularly the OEC action, was monitored by direct measurement of oxygen evolution under short saturating flashes using a fast three-electrode system. The polarographic method was developed by Joliot et al. (P. Joliot et al., 1969), who observed that oxygen production in dark-adapted PSII systems exhibits damped oscillations with a periodicity of four. Kok et al. (Kok et al., 1970). proposed a linear 4-step model that allowed coupling the four-electron oxidation of water to the single-electron turnover of the PSII reaction center components under a photon absorption by the RC chlorophylls. This model assumes the successive accumulation of four positive charges through OEC transient states called  $S_i$  states ( $i = 0, 1, 2, 3, 4$  and indicates the number of positive charges stored in the OEC on the  $Mn_4CaO_5$  complex). When sufficient oxidizing power is accumulated, water molecules are split, an O = O bond is formed, and  $O_2$  is released. The failure rate  $\alpha$  of the trapping centers (called misses) leads to a redistribution of the  $S_i$  states and, consequently, to a damping of the oscillations of the  $O_2$  release. In prolonged darkness, the OEC is mainly in the  $S_1$  state (usually  $\sim 75\%$ ) due to the oxidation of the  $S_0$  state by an electron carrier Tyr D (tyrosine of peptide D2, Figure 8) (Vermaas et al., 1984; Zimmermann & Rutherford, 1985). So the  $S_0$  state remains occupied at about 25%. Therefore, the first maximum is observed under the third flash. A small occupancy of

the  $S_2$  state is also detected (a small  $O_2$  yield is observed under the second flash), but the higher states are unstable (Burda & Schmid, 1996). The original Kok model assumed equal misses for light-driven transitions  $S_n \rightarrow S_{n+1}$  and additionally doubled effective excitation in a fraction  $\gamma$  of the centers, which are in the  $S_0$  and  $S_1$  states (called double hits and also equal). However, it has been shown that when this homogeneous model is used, there are significant discrepancies between the theoretical and experimental  $O_2$  yield patterns (Thibault, 1978). Moreover, it has been shown that the progressive damping of the oscillations is mainly due to misses, and the heterogeneous model with different  $\alpha_i$  misses, omitting double hits, gives a better quantitative agreement with the experimental data obtained for different systems (Burda & Schmid, 1996; Delrieu, 1974, 1983; Lavorel, 1976, 1978). Additionally, it was found that the extension of the 4S-state Kok model to the 5S-state model, when the  $S_4$  state is introduced explicitly and its longer living isomer is taken into account, results in a much better fit between the theoretical and experimental data (Burda & Schmid, 1996). The distinction between the short-lived and the metastable  $S_4$  state allowed us to estimate the contribution of the PSII CR involved in the fast ( $d$ ) and slow ( $1-d$ ) evolution of the oxygen molecule. The share of the fast and slow phases in the  $O_2$  yield depends on the species, cultivation, and experimental conditions. The contribution of the fast and slow phases to  $O_2$  evolution depends on the species, cultivation, and experimental conditions (Burda, He, Bader, & Schmid, 1996; Burda & Schmid, 2001).

The experimental data were evaluated using a double relaxation function given by Equation 6 in Chapter 5.  $A_{fast}$  ( $A_{slow}$ ) and  $\tau_{fast}$  ( $\tau_{slow}$ ) are amplitudes and time constants characterizing the fast (slow)  $O_2$  release, respectively. For data normalized to the amount of oxygen released, when the time interval between flashes was 300 ms,  $A_{fast}$  and  $A_{slow}$  denote the contributions of each phase. Their dependence on the increasing concentration of NPs  $WO_3$  in the samples is shown in Figure 43a. The time constants are shown in Figure 43b.

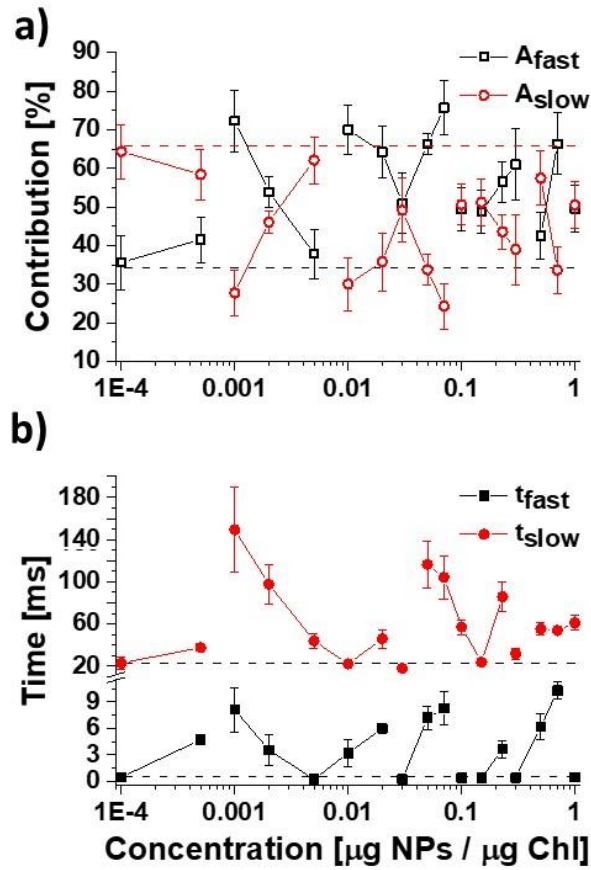


Figure 43 a) and b) Fitted parameters  $A_{fast}$  ( $A_{slow}$ ) and  $\tau_{fast}$  ( $\tau_{slow}$ ) related to the amplitudes and time constants characterizing the fast (slow)  $\text{O}_2$  release, respectively, versus NPs concentration. The dashed lines represent the mean values of the parameters obtained for the control samples

The values of the contributions and time constants oscillate in the range of the applied NPs' concentrations. At dilutions of NPs  $\leq 0.0005 \mu\text{g NPs}/\mu\text{g Chl}$ ,  $A_{fast}$  varies within  $\sim 38\div 76\%$  and is higher than in the control sample (black dashed line in Figure 43), while  $A_{slow}$  varies within  $\sim 24\div 62\%$  and is lower than in the control sample (red dashed line in Figure 43). The values of  $\tau_{fast}$  and  $\tau_{slow}$  are equal to or higher than those obtained for the control sample. The time constants  $\tau_{fast} \approx 564 \mu\text{s}$  and  $\tau_{slow} \approx 23 \text{ ms}$ , so the ratio  $r = \frac{\tau_{slow}}{\tau_{fast}} \cong 41$ . This ratio even increases to 150-200, resulting from the reduction of  $\tau_{fast}$  by a factor of 1.3-2.8 with a simultaneous increase of  $\tau_{slow}$  by a factor of 2.8-1.9. So high values of the  $r$  parameter are observed for the NPs dilutions: 0.005, 0.1, and  $1 \mu\text{g NPs}/\mu\text{g Chl}$ . Low values of the  $r$  parameter in the range of 5 to 8 (i.e. about 8 to 5 times lower than in the case of the control) were observed for NPs dilutions: 0.0005, 0.02, 0.01, 0.5, and  $0.7 \mu\text{g NPs}/\mu\text{g Chl}$ . This effect is associated with an increase in  $\tau_{fast}$  by order of magnitude and no change in  $\tau_{slow}$  or its increase by a factor not exceeding  $2.0 \pm 0.3$ . It is worth noting that monotonic changes in the fast phase contribution  $A_{fast}$  correlate with changes in the fast time constant in the following NPs concentration ranges:  $0.0001 \div 0.005 \mu\text{g NPs}/\mu\text{g Chl}$ ,  $0.03 \div 0.23 \mu\text{g NPs}/\mu\text{g Chl}$  and 0.5

$\div 1 \mu\text{g NPs}/\mu\text{g Chl}$ . However, taking into account the amount of oxygen released by the fast pathway, correlations between  $A_{fast}$  and  $\tau_{fast}$  are observed in the concentration range of  $0.005 \div 0.02 \mu\text{g NPs}/\mu\text{g Chl}$  (Figure 43). Similar monotonic changes of  $\tau_{fast}$  and  $\tau_{slow}$  are found in the range of NPs concentrations  $0.0001 \div 0.005 \mu\text{g NPs}/\mu\text{g Chl}$ ,  $0.07 \div 0.1 \mu\text{g NPs}/\mu\text{g Chl}$  and  $0.15 \div 0.5 \mu\text{g NPs}/\mu\text{g Chl}$  automatically indicating a negative correlation between  $\tau_{slow}$  and  $A_{n\_slow}$  for these concentrations of  $\text{WO}_3$  NPs.

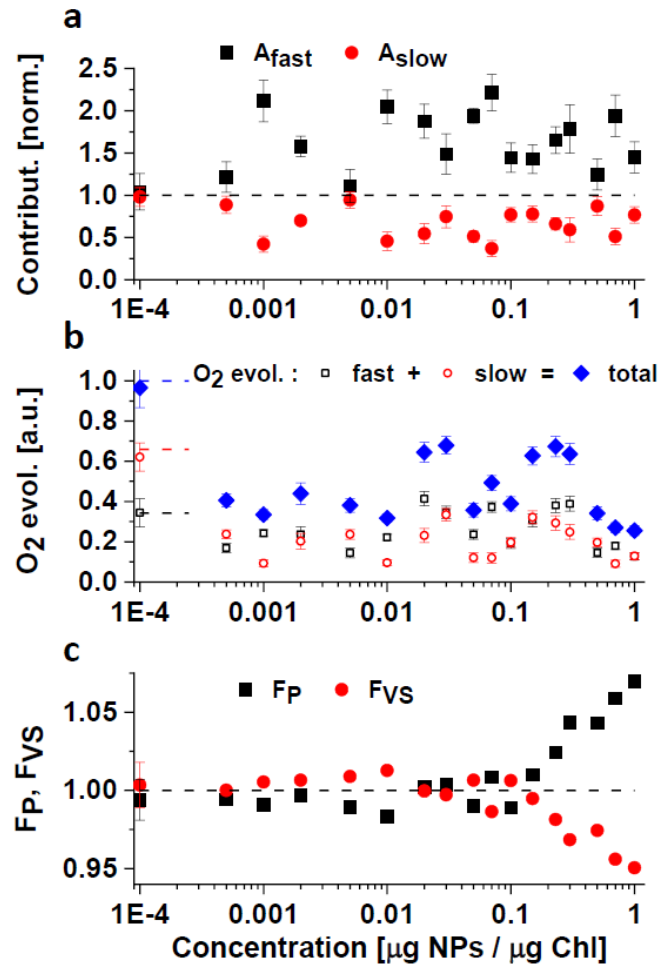


Figure 44 Changes in the amplitude of fast and slow  $\text{O}_2$  release,  $A_{fast}$  and  $A_{slow}$ , normalized to the values obtained for control samples as a function of NPs concentration. b) Dependence of the amount of total oxygen evolution (blue diamonds) and  $\text{O}_2$  released by the fast (black open squares) and slow (red open circles) pathways, normalized to the control samples, on the NPs concentration. The data shown (blue stars) are averages of the total amount of oxygen released during the 15 flashes (calculated from raw data normalized to the control - the average of 21 experimental points for one concentration of NPs) and after taking into account all measurements for different distances between the second and third flashes. The amount of oxygen released by the fast and slow pathways was determined after considering each phase's contribution based on the  $A_{fast}$  and  $A_{slow}$  parameters. Errors were defined as standard deviation. c) Changes in the  $F_p$  and  $F_{vs}$  parameters normalized to the control sample values versus the NPs concentration. The values shown are the mean values of at least four independent measurements for the control samples and the samples containing different concentrations of NPs. The apparent characteristic oscillations of  $F_p$  and  $F_{vs}$  are preserved even after averaging several independent measurements (data shown). In order to make their oscillations more apparent, the typical mean square error for the data shown has been plotted only for the point obtained for the lowest concentration of NPs used. The dashed lines indicate the level of control for each of the parameters shown in figures a, b, and c.

### 6.2.3. Discussion

Photosynthetic membranes are complex biological membranes enriched in proteins and pigments. Their macro-organization depends on environmental stimuli, so thylakoids are dynamic structures (Anderson et al., 2012; Dekker & Boekema, 2005). Their optimal architecture is determined by PSII supercomplexes, which can vary in size depending on the number of LHCII trimers attached. The largest supercomplex contains strongly and moderately - bound LHCII trimmers ( $C_2S_2M_2$ , Figure 6a), and the minimal unit ( $C_2S_2$ ) is separated from the two moderately - bound LHCII trimmers (2M), but intermediate states ( $C_2S_2M_1$ ,  $C_2S_1M_1$ ,  $C_2M_1$ ) and much smaller ones ( $C_2S_1$ ,  $C_2M_1$ ,  $C_2$ ,  $C_1S_1$ ) are possible (Caffarri et al., 2009), as well as larger supercomplexes (Pagliano et al., 2013). The transformation between these different forms of PSII supercomplexes and their temporal and spatial stabilization under specific conditions, depending on internal and external factors, aims to regulate and optimize the harvest and utilization of light, to facilitate diffusion processes inside and outside the membrane and to keep diffusion times short supporting the repair of light-damaged PSII [reviews: (Kirchhoff, 2008; Mullineaux, 2005)]. At the same time, LHCII aggregates may form (Johnson et al., 2011), and the reorganization of PSII core dimers can occur, even leading to PSII monomerization (Caffarri et al., 2009). Dissociation of the PSII supercomplex  $C_2S_2M_2$  is one of the photoprotective mechanisms essential for triggering non-photochemical fluorescence quenching (NPQ) (Betterle et al., 2009). A major challenge is to experimentally follow the different mechanisms that control the self-assembly of PSII-LHCII supercomplexes. In this case, the modeling approach has proven to be very helpful. Using a coarse-grained model of thylakoids, including two LHCII trimers (S2) strongly bound to the PSII core on antenna complexes CP26 and CP43 and two LHCII trimers (2M) moderately bound to the PSII core on antenna complexes CP24 and CP29, it was reported that there is a correlation between the free LHC:PSII ratios, the membrane protein packing fraction, and the transitions between the ordered and disordered PSII supercomplex structures. It has been shown that the shifts of the equilibrium states between the individual superstructures  $C_2S_2 + 2M \leftrightarrow C_2S_2M_1 + M \leftrightarrow C_2S_2M_2$  are reversible and that the long-range order depends on the fluidity of the membrane, and thus, in particular on temperature (C.-K. Lee et al., 2015a). In addition, different conformers may occur within the supercomplexes. For example, it has been shown that in eukaryotic PSII, a monomeric CP29 antenna can switch between two different  $C_2S_2$  conformations, stretched  $C_2S_2str$  and compact  $C_2S_2comp$ , by changing its orientation, each of which may exhibit additional structural heterogeneity (Caspy et al., 2021). This flexibility of the PSII dimer core most likely ensures its optimal functioning under global as well as local variable conditions, including (i) efficient utilization of light for charge separation, (ii) access of water and plastoquinones to the donor and acceptor PSII sides, respectively, and (iii) discharge of  $O_2$  and  $H^+$  outside the OEC.

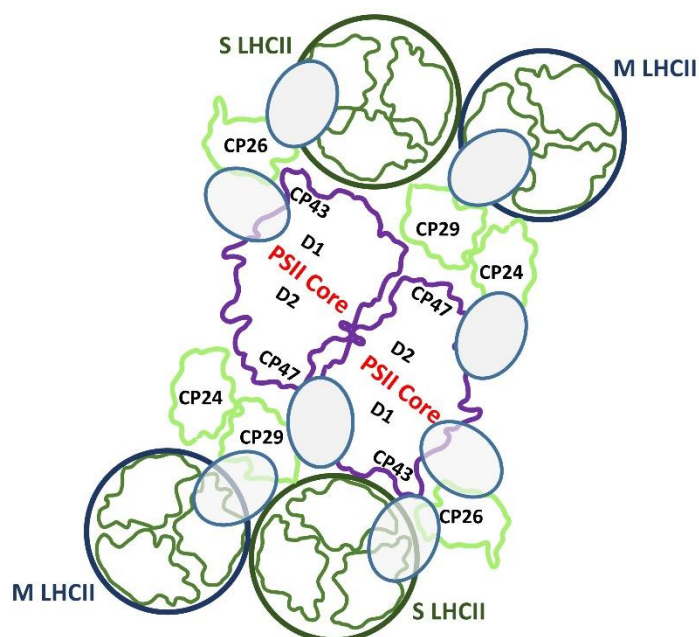


Figure 45 A Large supercomplex with strongly (S) and moderately-bound (M) trimer (C2S2M2). Prepared on (Dekker & Boekema, 2005; C.-K. Lee et al., 2015a), adopted from (Krysiak et al., 2023). Interaction sites of superfine  $\text{WO}_3$  NPs are indicated.

Our BBY PSII membranes contain almost exclusively PSII supercomplexes, as confirmed by the AFM measurements, absorption, and fluorescence experiments. Analysis of the distance between the protrusions corresponding to the external OEC protective proteins (Figure 38) observed in the AFM images of BBY PSII in their native liquid environment revealed structural changes in the PSII supercomplexes caused by the presence of superfine  $\text{WO}_3$  NPs embedded in the membranes. The mean distance between protrusions decreased in PSII BBY treated with  $0.0001 \mu\text{g NPs}/\mu\text{g Chl}$  ( $\sim 6.3 \text{ nm}$ ) compared to the control sample ( $\sim 7.1 \text{ nm}$ ). What's more, the PSII distribution obtained shows the greatest asymmetry with a simultaneous decrease of the standard deviation at the two lowest NPs concentration tested. However, the highest density of packing was observed at the concentration of  $0.001 \mu\text{g NPs}/\mu\text{g Chl}$  (distance  $\sim 4.8 \text{ nm}$ ), for which the standard deviation is the smallest, but the asymmetry of the distribution is large (Figure 38, Table 9). With further increase of NPs concentration, the separation between PSII cores increases. The standard deviation of the PSII distribution also increases and changes towards a Gaussian distribution as the asymmetry parameter decreases. All the above-described changes in the organization of PSII BBY under the influence of superfine  $\text{WO}_3$  NPs show that they strongly depend on the concentration of these nanoparticles. The observed differences in the distribution of PSII in supercomplexes are related to compositional and structural changes occurring within them and can therefore be expected to affect the efficiency of energy capture and transfer from external antennas to internal antennas and the PSII reaction center. Indeed, absorption and fluorescence measurements showed differences between the control sample and PSII BBY treated with NPs. For the two lowest concentrations of NPs, we observed a reduced contribution of chlorophylls *a* and *b* from LHCII in the absorption spectra (Bressan et al., 2016; Croce

et al., 1999). At a concentration of 0.0001  $\mu\text{g NPs}/\mu\text{g Chl}$ , this was accompanied by an attenuation of the energy transfer from LHCII to CP47, and at a concentration of 0.001  $\mu\text{g NPs}/\mu\text{g Chl}$ , the energy transfer between LHCII and both internal antennas of CP47 and CP43 within the PSII supercomplexes was impaired. At the same time, we observed monomerization and aggregation of LHCII trimers. The direction of these changes is consistent with the knowledge of how the disassembly of large PSII supercomplexes ( $\text{C}_2\text{S}_2\text{M}_2$ ) and the formation of smaller ones affect the energy transfer capabilities of its outer antenna complexes to the inner ones (Barera, Pagliano, Pape, Saracco, & Barber, 2012; Caffarri et al., 2009; Caspy et al., 2021; Wei et al., 2016). In samples treated with higher concentrations of 0.01  $\mu\text{g NPs}/\mu\text{g Chl}$  and 0.1  $\mu\text{g NPs}/\mu\text{g Chl}$ , the absorbance unexpectedly increased compared to the control. In the first case, the differential spectrum was characteristic of PSII supercomplexes lacking part of the LHCII trimer and the appearance of LHCII aggregates (Caffarri et al., 2009; Ruban et al., 1992). This is consistent with the observation of decoupling the LHCII trimers from CP47 and the appearance of antenna aggregates, disconnected Chls and disconnected minor antennas, and eventually aggregated Chls *b* resulting from the analysis of fluorescence spectra. However, the energy flow from LHCII to PSII RC involving CP43 was still efficient. At 10-fold higher concentrations, energy uptake by PSII core dimers increased. This was accompanied by an increase in the efficiency of energy transfer from LHCII to both CP43 and CP47. Other changes regarding the appearance of disconnected Chl *b/a* and the aggregation of LHCII and Chls observed at the lower NPs concentration also occur here and are intensified at the highest NPs concentration tested. At a concentration of 1  $\mu\text{g NPs}/\mu\text{g Chl}$ , the decrease in absorption was due to a decrease in the absorption efficiency of large PSII-LHCII supercomplexes. In this case, energy transfer from LHCII to CP43 was impaired but still possible to CP47.

The observed changes in light energy absorption and transfer from the external LHCII antenna complexes to the internal CP43 and CP47 and further to the PSII reaction center are undoubtedly dependent on these variable organizations of the PSII supercomplexes, but a direct effect of  $\text{WO}_3$  NPs on their individual components, i.e., antenna complexes and/or PSII core proteins, cannot be ruled out.

Knowing the ability of  $\text{WO}_3$  to oxidize water, the most intriguing problem was learning how these nanoparticles interact with a system that is the only one found in nature that can use light energy to extract electrons and protons from water. Self-organized  $\text{WO}_3$  NPs - PSII BBY biohybrids are a very good material to study the effect of these nanoparticles on the functioning of PSII and its efficiency in oxygen release. Moreover, the mechanism of water oxidation by PSII is not yet understood, and the interaction of tungsten oxide NPs with PSII may provide information that sheds new light on this process.

Our results from measurements of the Kautsky effect and oxygen evolution at short saturated flashes showed that superfine  $\text{WO}_3$  NPs could interact with both the

donor and acceptor sides of PSII. The quantum yield of PSII photochemistry and OEC activity strongly depend on the concentration of NPs ( $c_{NPs}$ ). Moreover, the parameters describing the operation of the acceptor and donor sides show an oscillatory dependence on  $c_{NPs}$  (Figure 42 and 43). We observed four phases of variable fluorescence, two of which we call fast, characterized by times  $\leq 1$  ms ( $F_0$  and  $F_{fv}$ ), and two slow with times  $\geq 100$  ms ( $F_{sv1}$  and  $F_{sv2}$ ). Plastoquinone  $Q_A$  can be efficiently reduced under light at photoactive PSII centers. When the  $Q_B$  site is inactive or empty, and there is no access for the oxidized PQ plastoquinone pool,  $Q_A^{\cdot-}$  accumulates very rapidly at  $< 500$  ps (Schatz, Brock, & Holzwarth, 1987; Shuvalov, V., Sharkov, Kryukov, & Bacon, 1979), and fluorescence reaches a maximum already in the fast phase. However, if  $Q_A^{\cdot-}$  can further transfer an electron to a quinone bound to the  $Q_B$  site, the fast fluorescence variable phase saturation occurs before it reaches a maximum. If  $Q_B$  is in the oxidized state, the transfer occurs in about 200-500  $\mu$ s, and if it is in the reduced  $Q_B^{\cdot-}$  state, the time is longer and is of the order of ms (Cao & Govindjee, 1990; A. Joliot & Joliot, 1964; Robinson & Crofts, 1983). This is consistent with our results. The slow phases result from the fact that the acceptor side works in a bicycle, i.e.,  $Q_B$ , after absorbing two electrons, binds two  $H^+$ , and is exchanged with oxidized PQ with the outer quinone pool (Figure 8). The  $t_{sv1}$  and  $t_{sv2}$  times may be slowed if, among other things: (i) the  $Q_B$  binding site undergoes conformational changes that prevent PQ binding and release; (ii) PQ access to the  $Q_B$  binding site is impeded; or (iii) PQ from the external pool is further reduced, and the number of available oxidized PQ decreases. This should be accompanied by increasing  $F_p = F_0 + F_{fv}$  and decreasing  $F_{sv} = F_{sv1} + F_{sv2}$ . We can see the above relationship by comparing the time dependencies for the slow fluorescence variable kinetics ( $t_{sv1}$  and  $t_{sv2}$ ) and the change in the proportion of fast and slow phases ( $F_p$  and  $F_{sv}$ ) as a function of NPs concentration (Figure 42a and b). In addition, it is noteworthy that the oscillations of  $t_{sv1}$  and  $t_{sv2}$  correspond to the oscillations of  $F_{sv2}$  and  $F_{sv1}$ , respectively, over the entire concentration range  $NPs < 0.3 \mu g NPs/\mu g Chl$ . On the one hand, this is a consequence of the limitation of the available pool of oxidized plastoquinones,  $PQ_{ox}$  (we did not use any external acceptors). Thus, accelerating the attachment of  $PQ_{ox}$  to an empty  $Q_B$  site ( $t_{sv1} \searrow$ ) decreases the probability of exchanging  $Q_B H_2$  for  $PQ_{ox}$  ( $F_{sv2} \searrow$  and  $F_{sv1} \nearrow$ ). In contrast, an increase in the exchange rate of  $Q_B H_2$  to  $PQ_{ox}$  ( $t_{sv2} \searrow$ ) results in an increase in the contribution of this process at the expense of  $PQ_{ox}$  binding to the empty  $Q_B$  site ( $F_{sv2} \nearrow$  and  $F_{sv1} \searrow$ ). These processes may additionally depend on the mechanism of PQ reduction and  $PQH_2$  exchange at the acceptor side of PSII, taking into account an additional PQ binding site, i.e.,  $Q_C$  coupled to the  $Q_B$  site, proposed in (Guskov et al., 2009). On the other hand, considering the very similar variation of  $F_0$  and  $F_{sv1}$  as a function of NPs concentration and the similar variation of  $F_{fv}$  and  $F_{sv2}$ , it can be concluded that the above effects are also influenced by the different actions of nanoparticles on the acceptor side depending on the state of the  $Q_B$  binding site, and in particular on whether the quinone bound there is reduced or not.

Using a new protocol for measuring oxygen evolution with applied a Joliot-type electrode, we have here demonstrated, for the first time in direct measurements, the heterogeneity of the oxygen evolution process. Previously, we proposed an extension of the Kok model to the metastable  $S'_4$  state, thus taking into account, in addition to the fast oxygen evolution pathway, a second slower one (Figure 31) (Burda & Schmid, 1996, 2001). Based on the oscillatory pattern of  $O_2$  release under the influence of short flashes, we were able to monitor the contribution of the two phases, fast and slow, in different photosynthetic systems under various experimental conditions (Burda et al., 1996; Burda & Schmid, 1996, 2001). For a control sample containing PSII BBY isolated from purchased spinach, the slow and fast phases of oxygen release were about 66% and 34%, respectively. We found that the  $O_2$  evolution time via the fast pathway was  $\sim 564 \mu s$ , and via the slow pathway was  $\sim 23 ms$ . The difficulty in identifying the main cause of why PSII releases oxygen via a fast or a slow pathway has been also discussed in the previous chapter. The rise times of the fast and slow  $O_2$  signal obtained after the third flash are consistent with literature reports, although agreement may result from other aspects, see discussion in chapter 6.1.

In this work, we showed that  $WO_3$  NPs have a strong concentration-dependent effect on regulating fast and slow oxygen release. They cause changes in the proportions of both phases as well as in the times of fast and slow  $O_2$  evolution. Only the lowest concentration of NPs used did not cause any change in the heterogeneity and activity of OEC compared to the control. All other concentrations of  $WO_3$  resulted in an increase in the fraction of the fast phase with a decrease in the fraction of the slow phase of  $O_2$  release. For concentrations of 0.001, 0.01, 0.02, 0.05, 0.07, and 0.7  $\mu g$  NPs/ $\mu g$  Chl, this increase in the contribution of the fast phase of oxygen release was even about twofold (Figure 43a and 8a). In addition, the already low concentration of 0.0005  $\mu g$  NPs/ $\mu g$  Chl caused a decrease in oxygen release by about 60%, and the two highest concentrations used even by about 75% compared to the control (Figure 44b). This suggests that  $WO_3$  NPs affect the activity of the donor side of PSII. Of particular interest is the oscillatory increase in oxygen release for certain ranges of NPs concentrations, namely: (i) an increase up to about 45% for a concentration of 0.002  $\mu g$  NPs/ $\mu g$  Chl and a monotonic decrease for increasing NPs concentrations up to 0.01  $\mu g$  NPs/ $\mu g$  Chl, (ii) an increase to about 50% for a concentration of 0.07  $\mu g$  NPs/ $\mu g$  Chl, and finally (iii) an increase to about 70% for concentrations of 0.02-0.03  $\mu g$  NPs/ $\mu g$  Chl and 0.15-0.3  $\mu g$  NPs/ $\mu g$  Chl of the control sample level. There is no correlation between the contribution of any of the phases or the times of fast or slow oxygen release on the performance of this process (Figure 44a and b). However, if the changes in the total amount of oxygen released under the influence of 15 short saturating flashes, obtained from polarographic measurements normalized to controls, are compared with the changes in the values of the parameters  $F_p$  and  $F_{vs}$ , also normalized, obtained from measurements of the Kautsky effect, a surprising regularity can be observed. For NPs concentrations  $\geq 0.0005 \mu g$  NPs/ $\mu g$  Chl, changes in the amount of oxygen released correlate with changes in  $F_p$

(Figure 44b and c). Such a course of  $F_p$  changes as a function of  $\text{WO}_3$  NPs concentration is determined primarily by  $F_0$  (Figure 42a). But plotting the sum of the fast phases  $F_p$  and the sum of the slow phases  $F_{sv}$  allows us to visualize an additional effect. Namely, the strongly increasing  $F_p$  (decreasing  $F_{sv}$ ) for  $c_{\text{NPs}} > 0.1 \mu\text{g NPs}/\mu\text{g Chl}$  clearly indicates the progressive depletion of the available electron acceptor,  $\text{PQ}_{\text{ox}}$ , as the NPs concentration increases in this range. This is why we observe such a strong decrease in oxygen release for the last two highest concentrations. The intriguing increase in oxygen release with a concomitant decrease in the maximum photochemical yield of dark-adapted PSII under the influence of superfine  $\text{WO}_3$  NPs can only be consistently explained in one way. It has been known for more than half a century that  $\text{WO}_3$  can oxidize water because the energy of its valence band has a much higher potential than the oxidation potential of water (see Figure 46). However, in order for this process to occur, an electron acceptor must be introduced into the system. To maintain the continuity of the process, the electron acceptor must be constantly replenished or regenerated in another independent cycle if it is a closed system. The reduction potential of the acceptor must be more positive than the conduction band of the  $\text{WO}_3$  NPs. The superfine  $\text{WO}_3$  NPs studied by us have a much higher energy band gap than bulk  $\text{WO}_3$ , which is  $\sim 3.4 \text{ eV}$  (Figure 23). Considering also that the redox potentials of the quinones bound at the  $\text{Q}_A$  and  $\text{Q}_B$  sites can be modified under the influence of even small changes in the organization of the PSII BBY induced by the presence of embedded small NPs, an additional electron flow involving NPs can take place in the formed hybrid system, as shown in Figure 45 and Figure 46. Potentially,  $\text{WO}_3$  NPs could receive electrons directly from the water. However, the fact that: (i) the heterogeneity of the oxygen evolution process is preserved, (ii) no background enhancement was observed on the electrode, (iii) and the amount of oxygen evolution shown in Figure 44b was determined as an area based on the  $\text{O}_2$  evolution pattern with a periodicity of 4, we can confidently conclude that the NPs receive electrons from the  $\text{Mn}_4\text{CaO}_5$  complex or water molecules connected to it. A single nanoparticle is too small to be in contact with both the  $\text{Mn}_4\text{CaO}_5$  cluster and  $\text{Q}_A$  or  $\text{Q}_B$ . Therefore, it is only when the reorganization of PSII BBY under the influence of NPs allows enough nanoparticles to be incorporated into a single PSII system that chain electron transfer from the  $\text{Mn}_4\text{CaO}_5$  complex via  $\text{WO}_3$  NPs to  $\text{Q}_A$  and  $\text{Q}_B$  can occur. At high concentrations of  $\text{WO}_3$  NPs, branched electron transfer pathways can form that extend to more distant regions of the thylakoid membrane, leading to PQ reduction from the extrinsic plastoquinone pool. Due to the increased accumulation of  $\text{PQ}_{\text{red}}$ , we observe an additional accumulation of reduced  $\text{Q}_A^{\bullet-}$  and  $\text{Q}_B^{\bullet-}$ , and consequently, a decrease in  $F_{sv}$  and the saturation rate of both its components ( $F_{sv1}$  and  $F_{sv2}$ ) for the highest applied concentrations of NPs. A scheme of the electron flow from the  $\text{Mn}_4\text{CaO}_5$  complex to the quinones bound at the  $\text{Q}_A$  and  $\text{Q}_B$  sites and to PQ from the external quinone pool through the NPs chain is shown in Figure 45. This is a tunnelling electron transfer process because it requires contact between NPs. Since the heterogeneity of oxygen evolution is the same whether the time intervals between the

first and second flashes or the second and third flashes were changed, the pattern of O<sub>2</sub> evolution was preserved, and it can be concluded that electrons were transferred from the OEC to NPs only when the Mn<sub>4</sub>CaO<sub>5</sub> complex was in the S<sub>3</sub>/S<sub>4</sub> state. Surprisingly, the increase in oxygen evolution stimulated by WO<sub>3</sub> NPs at their strict concentrations shows no correlation with either fast or slow O<sub>2</sub> release (Figure 44a and b). This means that the oxygen release efficiency depends on a variety of factors that determine the flexibility and structural changes of PSII within both its donor and acceptor sides. However, the influence of changes in the organization and dynamics of the entire WO<sub>3</sub> NPs - PSII BBY hybrid system cannot be overlooked either, as indicated by the results obtained by AFM, as well as absorption and fluorescence spectroscopy. For example, embedding NPs in PSII BBY may lead to local separation of protein and lipid structures, affecting the organization and packing of PSII supercomplexes and weakening the coupling of LHCII-PSII interactions, as well as modifying the lateral diffusion of PQ across the membrane and PQ access to the Q<sub>B</sub> binding site (Caspy et al., 2021; Haferkamp, Haase, Pascal, van Amerongen, & Kirchhoff, 2010; Kirchhoff, 2008).

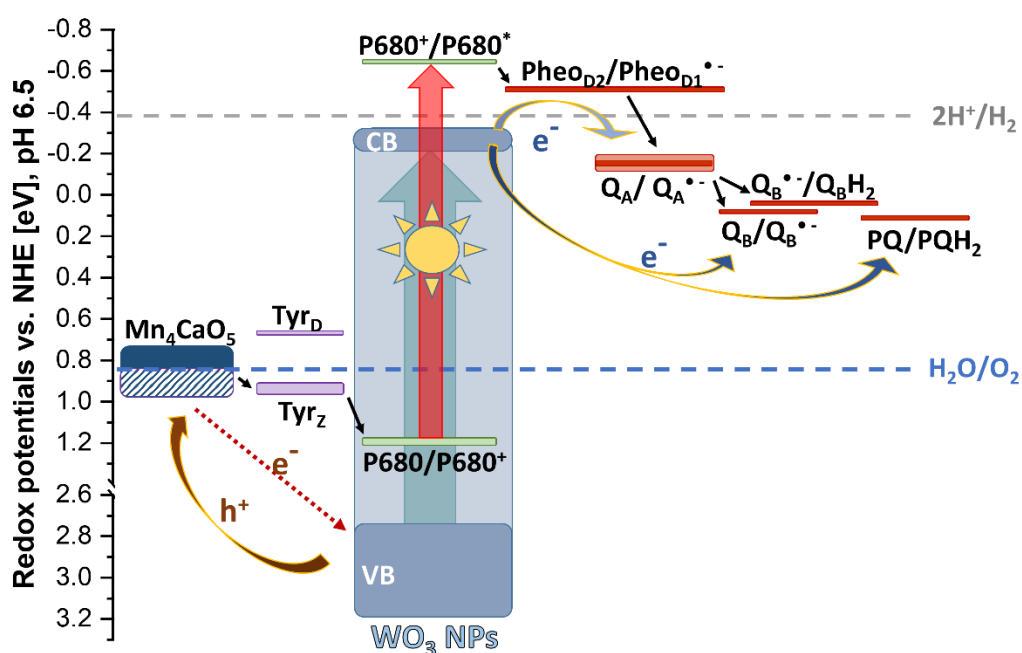


Figure 46 Schematic illustration of the proposed photogenerated carrier transfer mechanism in the nanohybrid system PSII BBY - mWO<sub>3</sub> NPs, occurring at specific NPs concentrations (see discussion). Redox potential values of PSII redox active components are taken from (De Causmseecker, Douglass, Fantuzzi, & Rutherford, 2019; Geijer, Morvaridi, & Styring, 2001; Golbeck & Kok, 1979; Ishikita & Knapp, 2006; Y. Kato, Sugiura, Oda, & Watanabe, 2009; Klimov, Allakhverdiev, Demeter, & Krasnovskii, 1979; Mandal, Kawashima, et al., 2020; Rich & Bendall, 1980; Rutherford & Faller, 2003; Rutherford, Mullet, & Crofts, 1981; Shibamoto, Kato, Sugiura, & Watanabe, 2009; Vass & Styring, 1991; Wraight, 2004). The energetic gap for superfine mWO<sub>3</sub> NPs is taken from the present work. The thick red line shows the excitation, the black arrow shows the forward electron transfer pathways within PSII, the dashed red arrow shows the electron transfer from the Mn<sub>4</sub>CaO<sub>5</sub> complex to the valence band of WO<sub>3</sub> NPs, and the thick yellow-red line shows the opposite hole H<sup>+</sup> transfer. The yellow-grey lines show the possible electron transfer pathways from the WO<sub>3</sub> NPs conducting band to the Q<sub>A</sub> and Q<sub>B</sub>-bound plastoquinones and PQ from the external plastoquinone pool. All redox potentials are set to pH 6.5.

Based on data from testing various Photosystem II-based hybrid systems for use in solar energy conversion, electricity generation, and O<sub>2</sub> (and H<sub>2</sub> in some systems) production, it was possible to determine the oxygen evolution efficiency per catalyst, in this case, PSII, to compare their ability to oxidize water. None of the systems (mesoporous indium tin oxide ITO-PSII (M. Kato et al., 2012), IO-mesoITO-PSII (Mersch et al., 2015), PSII anchoring polyethylenimine-coated microporous carbon (Tian et al., 2021), macroporous IO-TiO<sub>2</sub>/dpp/P<sub>O<sub>s</sub></sub> electrodes filled with a blend of PSII (Sokol et al., 2018), or CdS-PSII (Z. Li et al., 2017) showed comparable oxygen evolution efficiencies to natural PSII systems, despite the introduction of external electron acceptors involved in mediated electron transport. Their initial activity, when at its highest, ranged from about 2 mmol O<sub>2</sub>/ g<sub>CAT</sub> h<sup>-1</sup> to 30 mmol O<sub>2</sub>/ g<sub>CAT</sub> h<sup>-1</sup>. This is still 2-3 orders of magnitude lower than the activity of isolated free PSII structures in the presence of external acceptors. Only His-tagged PSII core complexes immobilized on Au NPs (diameter - 20 nm) via nickel-nitrilotriacetic acid (Ni-NTA) in the presence of two external acceptors, phenyl-p-benzoquinone and ferricyanide, showed an activity of about 2200 mmol O<sub>2</sub>/ g<sub>CAT</sub> h<sup>-1</sup>, i.e. about 23% of the activity measured for free PSII complexes (Noji et al., 2011). The lower O<sub>2</sub> evolution efficiency of the PSII-Au NPs system was explained by the need to remove Ca<sup>+2</sup> and Cl<sup>-</sup> ions from the reaction buffer in the case of the hybrid system to avoid aggregation of Au NPs. In the PSII BBY - WO<sub>3</sub> NPs systems we studied, we did not use any external acceptors. Superfine NPs were incorporated into PSII-enriched thylakoid membranes. The size of PSII of about 10.5 nm in depth, 20.5 nm in length, and 11.0 nm in width (Umena et al., 2011) provides enough space for such small NPs to build in between the structures of this photosystem. We obtained a self-assembling system that, at specific, well-defined concentrations of NPs, exhibited an oxygen-releasing capacity of up to 70% of the activity of untreated PSII BBY (control sample) under the same measurement conditions.



## 7. Conclusions

These studies were aimed at answering questions about how selected endogenous and exogenous factors affect photosystem II activity and what role they play in regulating oxygen-evolving complex heterogeneity. In particular, the research focused on the effect of (i) external proteins that stabilise the function of the oxygen-evolving complex on the donor side of PSII as an endogenous factor and (ii) monoclinic superfine WO<sub>3</sub> NPs, known to have n-type semiconductor properties, as an exogenous factor.

The 16 kDa (PsbQ), 23 kDa (PsbP) and 33 kDa (PsbO) proteins not only play a protective role for the OEC, but also provide a protein matrix with multiple cross-linked water channels, the functions of which have recently been widely discussed in the literature. Analysis of the oxygen release pattern measured under short saturating flashes of white light using a fast Joliot-type electrode with a standard measurement protocol showed that, compared to the control sample:

(a) deletion of the two outer proteins (16 kDa and 23 kDa) resulted in a decrease in the efficiency of the transitions between the  $S_i$  states of the Mn<sub>4</sub>CaO<sub>5</sub> complex (except for the  $S_2 \rightarrow S_3$  transition, which already showed low efficiency in the control sample) and a fourfold decrease in the probability of oxygen release via the fast pathway, which already showed low efficiency in the control sample) and a fourfold decrease in the probability of oxygen release via the fast pathway

(b) deletion of the three outer proteins (16 kDa, 23 kDa and 33 kDa) did not alter the probabilities of  $S_i \rightarrow S_{i+1}$  transitions, but affected the initial distribution of  $S_i$  states and caused the disappearance of the fast phase of O<sub>2</sub> evolution.

The heterogeneity of OEC operation was confirmed not only by the theoretical 5 – state model with consideration of the metastable  $S_4$  state, but also by an independent measurement using a new measurement protocol, which allows determination not only of the proportion of fast and slow oxygen release paths, but also of the kinetics of these processes. The contribution of the fast and slow oxygen evolution paths changed in the samples similarly to that determined from the theoretical model. However, with the elution of two and three proteins, the time constants of the two phases showed opposite changes. The fast phase became slower while the slow phase became much faster. For PSII BBY-16,23,33 the slow phase time constant was approximately 13 ms, whereas for the control it was approximately 44 ms. The observed changes in PSII BBY activity resulting from the removal of external proteins led to extensive discussion of what factors might determine the direction of changes in OEC functioning. A strong correlation was suggested between the Mn<sub>4</sub>CaO<sub>5</sub> complex reorganisation and uncontrolled water permeability through the remaining O4, O1 and Cl1 channel fragments. This is inextricably linked to a less efficient removal of the protons into the

lumen of the cell. It is evident that the absence or disruption of the recognised sites controlling water access to the OEC and the simultaneous destabilisation of hydrogen bonds, both near the  $Mn_4CaO_5$  cluster and at a distance greater than 10 Å, cause the disappearance of the fast phase of  $O_2$  evolution. The results of this experiment suggest that the entire water-protein network, linked by hydrogen bonds, influences the efficiency of OEC operation. This is also an indication that the dynamics of the system as a whole will play an important role in this process. Indeed, this seems to be confirmed by the results of the research carried out on how  $WO_3$  NPs affect the functioning of PSII BBY. The effect of  $WO_3$  NPs on changes in PSII BBY organisation and the fluctuations in photochemical yields accompanying oscillatory changes in the contributions and kinetics of the fast and slow  $O_2$  release pathways suggest a complex and multilevel regulation of the oxygen-evolving complex. It has to be emphasised that the heterogeneity of the oxygen evolution has also been observed in the PSII BBY isolated from spinach. In this case, about 35% of the reaction centres for the control sample showed a fast and 65% a slow release of oxygen with a time constant of about < 1 ms and 20 ms, respectively.

Another aspect of the work is a new approach to the design of biohybrid systems using PSII mechanisms that are essential for the optimisation of hybrid performance under near-natural, i.e. environmental, conditions. In particular, it was expected that the colloidal hybrid system PSII BBY -  $WO_3$  NPs would show significant efficiency in producing oxygen. The ease of fabrication is a major advantage over commonly studied 2D/3D semiconductor structures, which are limited in their ability to tightly pack biomolecules, especially large ones such as PSII complexes. A new approach to constructing hybrid systems based on natural PSII BBY was demonstrated, which exhibits the highest oxygen evolution capacity observed so far. Very fine  $WO_3$  NPs (~ 2 nm) were introduced into PSII BBY. It was observed that both the organisation of the membranes and the functioning of these systems showed a strong, oscillatory dependence on the NPs concentration. The process of  $O_2$  evolution showed the greatest changes caused by the effect of NPs. At concentrations of 0.02-0.03  $\mu\text{g NP}/\mu\text{g Chl}$  and 0.15-0.3  $\mu\text{g NP}/\mu\text{g Chl}$ , the maximum  $O_2$  yield achieved 70% of the control sample. There was a correlation with a slight decrease in photochemical yield, which led to the identification of the mechanism responsible for this phenomenon. It is suggested that In fact, at certain concentrations,  $WO_3$  NPs were able to form conductive chains between the donor and acceptor sides of PSII by forcing changes in the PSII BBY organisation. This facilitated the transfer of electrons from the  $Mn_4CaO_5$  complex to the quinones bound to the acceptor side of PSII. In addition, these NPs can alter the redox potentials of  $Q_A$  and  $Q_B$ . They can also interfere with the access of PQ from the external quinone pool to the  $Q_B$  binding site. It is very likely that the observed variable dependence of the oxygen release efficiency on the concentration of  $WO_3$  NPs is due to the variable flexibility / mobility of the whole system and that this is a dynamic effect.

On one hand, the above observations make a significant contribution to understanding the photosynthetic process of water oxidation. On the other hand, the

colloidal hybrid system PSII BBY -  $\text{WO}_3$  NPs was found to be very efficient. In the future, it may be possible to use it in more advanced systems that will be used in high performance solar reactors.



## 8. Prospects for the future

The complexity of the oxygen release process during photosynthesis is increasingly discussed in scientific papers. At present, there is no single model that can explain all the phenomena associated with the splitting of water by the different types of photosynthetic organisms. It is also unknown whether the heterogeneity we observe is due to the different states of the PSII complexes, and thus of the OECs, or whether there are at least two possible paths that each system can take at any given time through dynamic changes. However, it cannot be excluded that oxygen release in PSII can occur in different locations. Thus, further studies are needed to understand how PSII functions heterogeneously in different organisms. Further important observations may also be made by studying the effect of chloride or calcium ion deficiency on the fast and slow phases of oxygen evolution. There is also a need to answer the question of whether there is a relationship between the fast and slow binding of water to the  $Mn_4CaO_5$  cluster and the fast and slow pathways of  $O_2$  release.

In the context of further research on PSII BBY -  $WO_3$  NPs colloidal hybrids, one of the most important aspects will be the study of the stability of its functioning in various external conditions, including: light intensity and temperature.

Scientists are actively involved in the research and development of hybrid systems consisting of PSII and nanoparticles in order to overcome the challenges and improve their performance. The development of new and more efficient systems is not possible without a thorough understanding of the structure and functioning of the PSII. Optimising the architecture of hybrid materials can lead to significant improvements in their performance. PSII – NPs hybrids have the potential to contribute to the development of sustainable technologies for the conversion of energy.



# References

- Akella, A. K., Saini, R. P., & Sharma, M. P. (2009). Social, economical and environmental impacts of renewable energy systems. *Renew. Energ.*, *34*, 390-396. doi:10.1016/j.renene.2008.05.002
- Alfonso, M., Montoya, G., Cases, R., Rodriguez, R., & Picorel, R. (1994). Core Antenna Complexes, CP43 and CP47, of Higher Plant Photosystem II. Spectral Properties, Pigment Stoichiometry, and Amino Acid Composition. *Biochemistry*, *33*, 10494-10500. doi:10.1021/bi00200a034
- Allen, J. P., & Williams, J. C. (1998). Photosynthetic reaction centers. *FEBS Lett.*, *438*(1-2), 5-9. doi:10.1016/S0014-5793(98)01245-9
- Amin, M., Askerka, M., Batista, V. S., Brudvig, G. W., & Gunner, M. R. (2017). X-ray Free Electron Laser Radiation Damage through the S-State Cycle of the Oxygen-Evolving Complex of Photosystem II. *J Phys. Chem. B*, *121*(40), 9382-9388. doi:10.1021/acs.jpcc.7b08371
- Ananyev, G., Roy-Chowdhury, S., Gates, C., Fromme, P., & Dismukes, G. C. (2019). The Catalytic Cycle of Water Oxidation in Crystallized Photosystem II Complexes: Performance and Requirements for Formation of Intermediates. *ACS Catal.*, *9*(2), 1396-1407. doi:10.1021/acscatal.8b04513
- Anderson, J. M. (2001). Does functional photosystem II complex have an oxygen channel? *FEBS Lett.*, *488*(1-2), 1-4. doi:10.1016/s0014-5793(00)02358-9
- Anderson, J. M., & Chow, W. S. (2002). Structural and functional dynamics of plant photosystem II. *Philos. Trans. R Soc. Lond. B Biol. Sci.*, *357*(1426), 1421-1430; discussion 1469-1470. doi:10.1098/rstb.2002.1138
- Anderson, J. M., Horton, P., Kim, E.-H., & Chow, W. S. (2012). Towards elucidation of dynamic structural changes of plant thylakoid architecture. *Phil. Trans. R. Soc. B*, *367*, 3515-3524. doi:10.1098/rstb.2012.0373
- Andrzhijevskaya, E. G., Chojnicka, A., Bautista, J. A., Diner, B. A., van Grondelle, R., & Dekker, J. (2005). Origin of the F685 and F695 fluorescence in Photosystem II. *Photosynth Res*, *84*, 173-180. doi:10.1007/s11120-005-0478-7
- Andrzhijevskaya, E. G., Frolov, D., van Grondelle, R., & Dekker, J. P. (2004). On the role of the CP47 core antenna in the energy transfer and trapping dynamics of Photosystem II. *Phys. Chem. Chem. Phys.*, *6*, 4810-4819. doi:10.1039/B411977K
- Askerka, M., Brudvig, G. W., & Batista, V. S. (2017). The O<sub>2</sub>-Evolving Complex of Photosystem II: Recent Insights from Quantum Mechanics/Molecular Mechanics (QM/MM), Extended X-ray Absorption Fine Structure (EXAFS), and Femtosecond X-ray Crystallography Data. *Acc. Chem. Res.*, *50*(1), 41-48. doi:10.1021/acs.accounts.6b00405
- Askerka, M., Wang, J., Vinyard, D., Brudvig, G., & Batista, V. (2016). S<sub>3</sub> State of the O<sub>2</sub>-Evolving Complex of Photosystem II: Insights from QM/MM, EXAFS, and Femtosecond X-ray Diffraction. *Biochemistry*, *55*(7), 981-984. doi:10.1021/acs.biochem.6b00041
- Badura, A., Esper, B., Ataka, K., Grunwald, C., Woll, C., Kuhlmann, J., . . . Rogner, M. (2006). Light-Driven Water Splitting for (Bio-)Hydrogen Production: Photosystem 2 as the Central Part of a Bioelectrochemical Device. *Photochem. Photobiol.*, *82*, 1385-1390. doi:10.1562/2006-07-14-RC-969
- Bao, H., & Burnap, R. L. (2015). Structural rearrangements preceding dioxygen formation by the water oxidation complex of photosystem II. *PNAS*, *112*(45), E6139-E6147. doi:10.1073/pnas.1512008112

- Barber, J. (2017). A mechanism for water splitting and oxygen production in photosynthesis. *Nat. Plants*, 3, 17041. doi:10.1038/nplants.2017.41
- Barera, S., Pagliano, C., Pape, T., Saracco, G., & Barber, J. (2012). Characterization of PSII-LHCII supercomplexes isolated from pea thylakoid membrane by one-step treatment with  $\alpha$ - and  $\beta$ -dodecyl-d-maltoside. *Phil. Trans. R. Soc. B*, 367(1608), 3389-3399. doi:10.1098/rstb.2012.0056
- Barry, B. A., Brahmachari, U., & Guo, Z. (2017). Tracking Reactive Water and Hydrogen-Bonding Networks in Photosynthetic Oxygen Evolution. *Acc. Chem. Res.*, 5(8), 1937-1945. doi:10.1021/acs.accounts.7b00189
- Bassi, R., Riconi, F., & Giacome, G. M. (1990). Chlorophyll binding proteins with antenna function in higher plants and green algae. *Photochem. Photobiol.*, 52(6), 1187-1206. doi:10.1111/j.1751-1097.1990.tb08457.x
- Berne, B. J., & Pecora, R. (200). *Dynamic Light Scattering with Applications to Chemistry, Biology, and Physics*: New York: Dover Publications.
- Berthold, D. A., Babcock, G. T., & Yocum, C. F. (1981). A highly resolved, oxygen-evolving photosystem II preparation from spinach thylakoid membranes. *FEBS Lett.*, 134(2), 231-234. doi:10.1016/0014-5793(81)80608-4
- Betterle, N., Ballottari, M., Morosinotto, T., Zorzan, S., & Bassi, R. (2009). Light-induced Dissociation of an Antenna Hetero-oligomer Is Needed for Non-photochemical Quenching Induction. *J. Biol. Chem.*, 284(22), 15255-15266. doi:10.1074/jbc.M808625200
- Bhowmick, A., Hussein, R., Bogacz, I., Simon, P. S., Ibrahim, M., Chatterjee, R., . . . Yachandra, V. K. (2023). Structural evidence for intermediates during O<sub>2</sub> formation in photosystem II. *Nature*, 617, 629-636. doi:10.1038/s41586-023-06038-z
- Björn, L. O., & Govindjee, G. (2008). The Evolution of Photosynthesis and Its Environmental Impact. In L. O. Björn (Ed.), *Photobiology: The Science of Life and Light* (pp. 255-287). New York, NY: Springer New York.
- Björn, L. O., & Govindjee, G. (2009). The evolution of photosynthesis and chloroplasts. *Curr. Sci.*, 96(11), 1466-1474.
- Boekema, E. J., Hankamer, B., Bald, D., Kruij, J., Nield, J., Boonstra, A. F., . . . Rögner, M. (1995). Supramolecular structure of the photosystem II complex from green plants and cyanobacteria. *Proc. Natl. Acad. Sci. U.S.A.*, 92(1), 175-179. doi:10.1073/pnas.92.1.175
- Bondar, A.-N., & Dau, H. (2012). Extended protein/water H-bond networks in photosynthetic water oxidation. *Biochim. Biophys. Acta*, 1817, 1177-1190. doi:10.1016/j.bbabi.2012.03.031
- Bouges-Bocquet, B. (1973). Limiting steps in photosystem II and water decomposition in chlorella and spinach chloroplasts. *Biochim. Biophys. Acta*, 292(3), 772-785. doi:10.1016/0005-2728(73)90024-8
- Bourdin, M., Mjejri, I., Rougier, A., Labrugère, C., Cardinal, T., Messaddeq, Y., & Gaudon, M. (2020). Nano-particles (NPs) of WO<sub>3</sub>-type compounds by polyol route with enhanced electrochromic properties. *J. Alloys Compd.*, 823. doi:10.1016/j.jallcom.2020.153690
- Boussac, A., Rutherford, A. W., & Sugiura, M. (2015). Electron transfer pathways from the S<sub>2</sub>-states to the S<sub>3</sub>-states either after a Ca<sup>2+</sup>/Sr<sup>2+</sup> or a Cl<sup>-</sup>/I<sup>-</sup> exchange in Photosystem II from *Thermosynechococcus elongatus*. *Biochim. Biophys. Acta*, 1847(6-7), 576-586. doi:10.1016/j.bbabi.2015.03.006
- Boussac, A., Setif, P., & Rutherford, A. W. (1992). Inhibition of tyrosine Z photooxidation after formation of the S<sub>3</sub>-state in calcium-depleted and chloride-depleted photosystem-II. *Biochemistry*, 31(4), 1224-1234. doi:10.1021/bi00119a036

- Bovi, D., Narzi, D., & Guidoni, L. (2013). The S2 State of the Oxygen-Evolving Complex of Photosystem II Explored by QM/MM Dynamics: Spin Surfaces and Metastable States Suggest a Reaction Path Towards the S3 State. *Ang. Chem. Int. Ed.*, *52*(45), 11744-11749. doi:10.1002/anie.201306667
- Bowes, J., Crofts, A. R., & Arntzen, C. J. (1980). Redox Reactions on the Reducing Side of Photosystem II in Chloroplasts with Altered Herbicide Binding Properties. *Arch. Biochem. Biophys.*, *200*(2), 303-308. doi:10.1016/0003-9861(80)90359-8
- Bressan, M., Dall'Osto, L., Bargigia, I., Cerullo, G., D'Andrea, C., Bassi, R., . . . Ballottari, M. (2016). LHClI can substitute for LHCl as an antenna for photosystem I but with reduced light-harvesting capacity. *Nat. Plants*, *2*, 1-10. doi:10.1038/NPLANTS.2016.131
- Bricker, T. M., & Frankel, L. K. (1998). The structure and function of the 33 kDa extrinsic protein of Photosystem II: A critical assessment. *Photosynth. Res.*, *56*, 157-173. doi:10.1023/A:1006068615220
- Bricker, T. M., & Frankel, L. K. (2002). The structure and function of CP47 and CP43 in Photosystem II. *Photosynth. Res.*, *72*(2), 131-146. doi:10.1023/A:1016128715865
- Bricker, T. M., Roose, J. L., Fagerlund, R. D., Frankel, L. K., & Eaton-Rye, J. J. (2012). The extrinsic proteins of Photosystem II. *Biochim. Biophys. Acta*, *1817*(1), 121-142. doi:10.1016/j.bbabi.2011.07.006
- Burda, K. (2007). Dynamics of electron transfer in photosystem II. *Cell Biochem. Biophys.*, *47*(2), 271-284. doi:10.1007/s12013-007-0011-z
- Burda, K., Bader, K. P., & Schmid, G. H. (2001). An estimation of the size of the water cluster present at the cleavage site of the water splitting enzyme. *FEBS Lett.*, *491*(1-2), 81-84. doi:10.1016/S0014-5793(01)02175-5
- Burda, K., He, P., Bader, K. P., & Schmid, G. H. (1996). Temperature dependence of the O<sub>2</sub>-oscillation pattern in the filamentous cyanobacterium *Oscillatoria chalybea* and in *Chlorella kessleri*. *Z. Naturforsch.*, *51c*, 823-832. doi:10.1515/znc-1996-11-1210
- Burda, K., & Schmid, G. H. (1996). On the Determination of the 5-State Distribution in the Kok Model. *Z. Naturforsch.*, *51c*, 329-341. doi:10.1515/znc-1996-5-610
- Burda, K., & Schmid, G. H. (2001). Heterogeneity of the mechanism of water splitting in photosystem II. *Biochim. Biophys. Acta*, *1506*, 47-54. doi:10.1016/S0005-2728(01)00182-7
- Burda, K., Strzałka, K., & Schmid, G. H. (1995). Europium- and Dysprosium-Ions as Probes for the Study of Calcium Binding Sites in Photosystem II. *Z. Naturforsch.*, *50c*, 220-230. doi:10.1515/znc-1995-3-410
- Burheim, O. S. (2017). *Engineering Energy Storage*: Academic Press Elsevier.
- Burnap, R. L., Shen, J. R., Jursinic, P. A., Inoue, Y., & Sherman, L. A. (1992). Oxygen yield and thermoluminescence characteristics of a cyanobacterium lacking the manganese-stabilizing protein of photosystem II. *Biochemistry*, *31*(32), 7404-7410. doi:10.1021/bi00147a027
- Butler, M. A. (1977). Photoelectrolysis and physical properties of the semiconducting electrode WO<sub>2</sub>. *J. Appl. Phys.*, *48*(5), 1914-1920. doi:10.1063/1.323948
- Caffarri, S., Kouřil, R., Kereïche, S., Boekema, E. J., & Croce, R. (2009). Functional architecture of higher plant photosystem II supercomplexes. *EMBO J.*, *28*, 3052-3063. doi:10.1038/emboj.2009.232
- Cai, Z.-X., Li, H.-Y., Yang, X.-N., & Guo, X. (2015). NO sensing by single crystalline WO<sub>3</sub> nanowires. *Sens. Actuators B*, *219*, 346-353. doi:10.1016/j.snb.2015.05.036
- Cammarata, K. V., & Cheniae, G. M. (1987). Studies on 17,24 kD Depleted Photosystem II Membranes : I. Evidences for High and Low Affinity Calcium Sites in 17,24 kD Depleted

- PSII Membranes from Wheat versus Spinach. *Plant Physiol.*, *84*(3), 587-595. doi:10.1104/pp.84.3.587
- Campbell, K. A., Gregor, W., Pham, D. P., Peloquin, J. M., Debus, R. J., & Britt, R. D. (1998). The 23 and 17 kDa extrinsic proteins of photosystem II modulate the magnetic properties of the S1-state manganese cluster. *Biochemistry*, *37*(15), 5039-5045. doi:10.1021/bi9800552
- Campbell, K. A., Peloquin, J. M., Pham, D. P., Debus, R. J., & Britt, R. D. (1998). Parallel polarization EPR detection of an S1-state "multiline" EPR signal in Photosystem II particles from *Synechocystis* sp. PCC 6803. *J. Am. Chem. Soc.*, *120*(2), 447-448. doi:10.1021/ja972693y
- Canaani, O., Malkin, S., & Mauzerall, D. (1988). Pulsed photoacoustic detection of flash-induced oxygen evolution from intact leaves and its oscillations. *PNAS*, *85*(13), 4725-4729. doi:10.1073/pnas.85.13.472
- Cao, J., & Govindjee. (1990). Chlorophyll a fluorescence transient as an indicator of active and inactive Photosystem II in thylakoid membranes. *Biochim. Biophys. Acta*, *1015*(2), 180-188. doi:10.1016/0005-2728(90)90018-Y
- Capone, M., Bovi, D., Narzi, D., & Guidoni, L. (2015). Reorganization of Substrate Waters between the Closed and Open Cubane Conformers during the S<sub>2</sub> to S<sub>3</sub> Transition in the Oxygen Evolving Complex. *Biochemistry*, *54*(42), 6439-6442. doi:10.1021/acs.biochem.5b00782
- Casey, J. L., & Sauer, K. (1984). EPR detection of a cryogenically photogenerated intermediate in photosynthetic oxygen evolution. *Biochim. Biophys. Acta*, *767*(1), 21-28. doi:10.1016/0005-2728(84)90075-6
- Caspy, I., Fadeeva, M., Mazor, Y., & Nelson, N. (2021). Structure of Dunaliella Photosystem II reveals conformational flexibility of stacked and unstacked supercomplexes. In (2021.11.30 ed., pp. 1-29). biorxiv.
- Chang, X., Sun, S., Dong, L., Dong, Y., & Yansheng Yin, Y. (2014). Large-scale production of tungsten trioxide nanoparticles for electrochromic application. *RSC Adv.*, *4*, 8994-9002. doi:10.1039/c3ra47733a
- Chen, J., Kell, A., Acharya, K., Kupitz, C., Fromme, P., & Jankowiak, R. (2015). Critical assessment of the emission spectra of various photosystem II core complexes. *Photosynth Res*, *124*, 253-265. doi:10.1007/s11120-015-0128-7
- Chen, J., Yu, D., Liao, W., Zheng, M., Xiao, L., Zhu, H., . . . Yao, J. (2016). WO<sub>3</sub>-X nanoplates grown on carbon nanofibers for an efficient electrocatalytic hydrogen evolution reaction. *ACS Appl. Mater. Interfaces*, *8*(28), 18132-18139. doi:10.1021/acsami.6b05245
- Chou, L.-Y., Liu, R., He, W., Geh, N., Lin, Y., Hou, E. Y. F., . . . Hou, H. J. M. (2012). Direct oxygen and hydrogen production by photo water splitting using a robust bioinspired manganese-oxo oligomer complex/tungsten oxide catalytic system. *Int. J. Hydrog. Energy*, *37*, 8889-8896. doi:10.1016/j.ijhydene.2012.02.074
- Chrysin, M., Heyno, E., Kutin, Y., Reus, M., Nilsson, H., Nowaczyk, M. M., . . . Cox, N. (2019). Five-coordinate MnIV intermediate in the activation of nature's water splitting cofactor. *Proc. Natl. Acad. Sci.*, *116*(34), 16841-16846. doi:10.1073/pnas.1817526116
- Cinque, G., Croce, R., Holzwarth, A., & Bassi, R. (2000). Energy Transfer among CP29 Chlorophylls: Calculated Forster Rates and Experimental Transient Absorption at Room Temperature. *Biophys. J.*, *79*, 1706-1717. doi:10.1016/S0006-3495(00)76423-X
- Cong, S., Tian, T., Li, Q., Zhao, Z., & Geng, F. (2014). Single-Crystalline Tungsten Oxide Quantum Dots for Fast Pseudocapacitor and Electrochromic Applications. *Adv. Mater.*, *25*(26), 4260-4267. doi:10.1002/adma.201400447

- Corby, S., Francàs, L., Kafizas, A., & Durrant, J. R. (2020). Determining the role of oxygen vacancies in the photoelectrocatalytic performance of WO<sub>3</sub> for water oxidation. *Chem. Sci.*, *11*, 2907-2914. doi:10.1039/C9SC06325K
- Corry, T. A., & O'Malley, P. J. (2018). Evidence of O-O Bond Formation in the Final Metastable S<sub>3</sub> State of Nature's Water Oxidising Complex Implies a Novel Mechanism of Water Oxidation. *J. Phys. Chem. Lett.*, *9*(21), 6269-6274. doi:10.1021/acs.jpcclett.8b02793
- Corry, T. A., & O'Malley, P. J. (2019). Proton Isomers Rationalize the High- and Low-Spin Forms of the S<sub>2</sub> State Intermediate in the Water-Oxidizing Reaction of Photosystem II. *J. Phys. Chem. Lett.*, *10*(17), 5226-5230. doi:10.1021/acs.jpcclett.9b01372
- Cox, N., & Messinger, J. (2013). Reflections on substrate water and dioxygen formation. *Biochim. Biophys. Acta*, *1827*, 1020-1030. doi:10.1016/j.bbabi.2013.01.013
- Cox, N., Pantazis, D. A., Neese, F., & Lubitz, W. (2013). Biological Water Oxidation. *Acc. Chem. Res.*, *46*(7), 1588-1596. doi:10.1021/ar3003249
- Cox, N., Retegan, M., Neese, F., Pantazis, D. A., Bousac, A., & Lubitz, W. (2014). Electronic structure of the oxygenevolving complex in photosystem II prior to O-O bond formation. *Science*, *345*(6198), 804-808. doi:10.1126/science.1254910
- Croce, R., Remelli, R., Varotto, C., Breton, J., & Bassi, R. (1999). The neoxanthin binding site of the major light harvesting complex (LHCII) from higher plants. *FEBS Lett.*, *456*, 1-6. doi:10.1016/S0014-5793(99)00907-2
- Croce, R., & van Amerongen, H. (2011). Light-harvesting and structural organization of Photosystem II: From individual complexes to thylakoid membrane. *J. Photochem. Photobiol. B*, *104*, 142-153. doi:10.1016/j.jphotobiol.2011.02.015
- D., A. (2010). *Dynamic Light Scattering and application to proteins in solutions*. University of Ljubljana, Ljubljana.
- Dang, N. C., Zazubovich, V., Reppert, M., Neupane, B., Picorel, R., Seibert, M., & Jankowiak, R. (2008). The CP43 Proximal Antenna Complex of Higher Plant Photosystem II Revisited: Modeling and Hole Burning Study. I. *J. Phys. Chem. B*, *112*, 9921-9933. doi:10.1021/jp801373c
- Darwent, J. R., & Mills, A. (1982). Photo-oxidation of Water Sensitized by WO<sub>3</sub> Powder. *J. Chem. Soc., Faraday Trans.*, *78*, 359-367. doi:10.1039/F29827800359
- Dau, H., Iuzzolino, L., & Dittmer, J. (2001). The tetra-manganese complex of photosystem II during its redox cycle – X-ray absorption results and mechanistic implications. *Biochim. Biophys. Acta*, *1503*(1-2), 24-39. doi:10.1016/S0005-2728(00)00230-9
- Dau, H., Liebisch, P., & Haumann, M. (2003). X-ray absorption spectroscopy to analyze nuclear geometry and electronic structure of biological metal centers--potential and questions examined with special focus on the tetra-nuclear manganese complex of oxygenic photosynthesis. *Anal. Bioanal. Chem.*, *376*(5), 562-583. doi:10.1007/s00216-003-1982-2
- Dau, H., & Sauer, K. (1996). Exciton equilibration and Photosystem II exciton dynamics — a fluorescence study on Photosystem II membrane particles of spinach. *Biochim. Biophys. Acta*, *1273*(2), 175-190. doi:10.1016/0005-2728(95)00141-7
- De Causmsecker, S., Douglass, J. S., Fantuzzi, A., & Rutherford, A. W. (2019). Energetics of the exchangeable quinone, QB, in Photosystem II. *PNAS*, *116*(39), 19458-19463. doi:10.1073/pnas.1910675116
- De Las Rivas, J., Balsera, M., & Barber, J. (2004). Evolution of oxygenic photosynthesis: genome-wide analysis of the OEC extrinsic proteins. *Trends Plant Sci.*, *9*(1), 18-25. doi:10.1016/j.tplants.2003.11.007

- de Lichtenberg, C., Avramov, A. P., Zhang, M., Mamedov, F., Burnap, R. L., & Messinger, J. (2021). The D1-V185N mutation alters substrate water exchange by stabilizing alternative structures of the Mn<sub>4</sub>Ca-cluster in photosystem II. *Biochim. Biophys. Acta Bioenerg.*, *1862*. doi:10.1016/j.bbabi.2020.148319
- de Lichtenberg, C., Kim, C. J., Chernev, P., Debus, R. J., & Messinger, J. (2021). The exchange of the fast substrate water in the S<sub>2</sub> state of photosystem II is limited by diffusion of bulk water through channels – implications for the water oxidation mechanism. *Chem. Sci.*, *12*(38), 12763-12775. doi:10.1039/D1SC02265B
- de Wijn, R., & van Gorkom, H. J. (2001). Kinetics of Electron Transfer from Q<sub>A</sub> to Q<sub>B</sub> in Photosystem II. *Biochemistry*, *40*, 11912-11922. doi:10.1021/bi010852r
- Deb, S. K. (2008). Opportunities and challenges in science and technology of WO<sub>3</sub> for electrochromic and related applications. *Sol. Energy Mater. Sol. Cells*, *92*, 245-258. doi:10.1016/j.solmat.2007.01.026
- Debus, R. J. (2014). Evidence from FTIR Difference Spectroscopy that D1-Asp61 Influences the Water Reactions of the Oxygen-Evolving Mn<sub>4</sub>CaO<sub>5</sub> Cluster of Photosystem II. *Biochemistry*, *53*(18), 2941-2955. doi:10.1021/bi500309f
- Deepa, M., Srivastava, A. K., Kar, M., & Agnihotry, S. A. (2006). A case study of optical properties and structure of sol-gel derived nanocrystalline electrochromic WO<sub>3</sub> films. *J. Phys. D: Appl. Phys.*, *39*, 1885-1893. doi:10.1088/0022-3727/39/9/025
- Dekker, J. P., & Boekema, E. J. (2005). Supramolecular organization of thylakoid membrane proteins in green plants. *Biochim. Biophys. Acta*, *1706*, 12-39. doi:10.1016/j.bbabi.2004.09.009
- Delrieu, M.-J. (1974). Simple explanation of the misses in the cooperation of charges in photosynthetic O<sub>2</sub> evolution. *Photochem. Photobiol.*, *20*, 441-454. doi:10.1111/j.1751-1097.1974.tb06599.x
- Delrieu, M.-J. (1983). Evidence for Unequal Misses in Oxygen Flash Yield Sequence in Photosynthesis. *Z. Naturforsch.*, *38 c*, 247-258. doi:10.1515/znc-1983-3-415
- DeSantis, D., James, B. D., Houchins, C., Saur, G., & Lyubovskiy, M. (2021). Cost of long-distance energy transmission by different carriers. *iScience*, *24*, 1-24. doi:10.1016/j.isci.2021.103495
- Dexheimer, S. L., & Klein, M. P. (1992). Detection of a paramagnetic intermediate in the S<sub>1</sub> state of the photosynthetic oxygen-evolving complex. *J. Am. Chem. Soc.*, *114*(8), 2821-2826. doi:10.1021/ja00034a010
- Dilbeck, P. L., Bao, H., Neveu, C. L., & Burnap, R. L. (2013). Perturbing the water cavity surrounding the manganese cluster by mutating the residue D1-Valine 185 has a strong effect on the water oxidation mechanism of Photosystem II. *Biochemistry*, *52*(39), 6824-6833. doi:10.1021/bi400930g
- Dilbeck, P. L., Hwang, H. J., Zaharieva, I., Gerencser, L., Dau, H., & Burnap, R. L. (2012). The D1-D61N Mutation in *Synechocystis* sp. PCC 6803 Allows the Observation of pH-Sensitive Intermediates in the Formation and Release of O<sub>2</sub> from Photosystem II. *Biochemistry*, *51*, 1079-1091. doi:10.1021/bi201659f
- Dismukes, G. C., & Siderer, Y. (1981). Intermediates of a polynuclear manganese center involved in photosynthetic oxidation of water. *Proc. Natl. Acad. Sci.*, *78*(1), 274-278. doi:10.1073/pnas.78.1.274
- Dittrich, K. (1988). *Absorpcyjna Spektrometria Atomowa*. Warszawa: PWN.
- Drosou, M., Zahariou, G., & Pantazis, D. A. (2021). Orientational Jahn–Teller Isomerism in the Dark-Stable State of Nature's Water Oxidase. *Angew. Chem. Int. Ed.*, *60*(24), 13493-13499. doi:10.1002/anie.202103425

- Enami, I., Okumura, A., Nagao, R., Suzuki, T., Iwai, M., & Shen, J. R. (2008). Structures and functions of the extrinsic proteins of photosystem II from different species. *Photosynth. Res.*, *98*(1-3), 349-363. doi:10.1007/s11120-008-9343-9
- Enami, I., Tomo, T., Kitamura, M., & Katoh, S. (1994). Immobilization of the three extrinsic proteins in spinach oxygen-evolving Photosystem II membranes: roles of the proteins in stabilization of binding of Mn and Ca<sup>2+</sup>. *Biochim. Biophys. Acta*, *1185*(1), 75-80. doi:10.1016/0005-2728(94)90195-3
- Eshaghi, S., Andersson, B., & Barber, J. (1999). Isolation of a highly active PSII-LHCII supercomplex from thylakoid membranes by a direct method. *FEBS Lett.*, *446*, 23-26. doi:10.1016/S0014-5793(99)00149-0
- Etienne, A. L. (1968). Étude de l'étape thermique de l'émission photosynthétique d'oxygène par une méthode d'écoulement. *Biochim. Biophys. Acta*, *153*, 895-897. doi:10.1016/0005-2728(68)90018-2
- Ferreira, K. N., Iverson, T. M., Maghlaoui, K., Barber, J., & Iwata, S. (2004). Architecture of the Photosynthetic Oxygen-Evolving Center. *Science*, *303*(5665), 1831-1838. doi:10.1126/science.1093087
- Flesher, D. A., Liu, J., Wiwczar, J. M., Reiss, K., Yang, K. R., Wang, J., . . . Brudvig, G. W. (2022). Glycerol binding at the narrow channel of photosystem II stabilizes the low-spin S<sub>2</sub> state of the oxygen-evolving complex. *Photosynth Res*, *152*(2), 167-175. doi:10.1007/s11120-022-00911-0
- Fujishima, A., & Honda, K. (1972). Electrochemical Photolysis of Water at a Semiconductor Electrode. *Nature*, *238*, 37-38. doi:10.1038/238037a0
- Gabdulkhakov, A., Guskov, A., Broser, M., Kern, J., Müh, F., Saenger, W., & Zouni, A. (2009). Probing the Accessibility of the Mn<sub>4</sub>Ca Cluster in Photosystem II: Channels Calculation, Noble Gas Derivatization, and CocrySTALLIZATION with DMSO. *Structure*, *17*, 1223-1234. doi:10.1016/j.str.2009.07.010
- Gabdulkhakov, A. G., Kljashtorny, V. G., & Dontsova, M. V. (2015a). Analysis of Molecular Oxygen Exit Pathways in Cyanobacterial Photosystem II: Molecular Dynamics Studies. *Kristallografiya*, *60*(6), 926-931. doi:10.1134/S1063774515060085
- Gabdulkhakov, A. G., Kljashtorny, V. G., & Dontsova, M. V. (2015b). Molecular Dynamics Studies of Pathways of Water Movement in Cyanobacterial Photosystem II. *Kristallografiya*, *60*(1), 91-97. doi:10.1134/S1063774515010083
- Geijer, P., Morvaridi, F., & Styring, S. (2001). The S(3) state of the oxygen-evolving complex in photosystem II is converted to the S(2)Y(Z)\* state at alkaline pH. *Biochemistry*, *40*(36), 10881-10891. doi:10.1021/bi010040v
- Genty, B., Briantais, J.-M., & Baker, N. R. (1989). The relationship between the quantum yield of photosynthetic electron transport and quenching of chlorophyll fluorescence. *Biochim. Biophys. Acta*, *990*, 87-92. doi:10.1016/S0304-4165(89)80016-9
- Ghanotakis, F., & Yocum, C. F. (1986). Characterization of a photosystem II reaction center complex isolated by exposure of PSII membrane to a non-ionic detergent and high concentration of NaCl. *Photosynth. Res.*, *10*, 483-488. doi:10.1007/BF00118314
- Golbeck, J. H., & Kok, B. (1979). Redox titration of electron acceptor Q and the plastoquinone pool in Photosystem II. *Biochim. Biophys. Acta*, *547*(2), 347-360. doi:10.1016/0005-2728(79)90016-1
- Gonçalves Silva, C. C., de Moura Torquato, L. D., de Araújo, B. C., Rojas Mantilla, H. D., Boldrin Zaroni, M. V., & Santesso Garrido, S. (2022). Assessment of WO<sub>3</sub> electrode modified with intact chloroplasts as a novel biohybrid platform for photocurrent improvement. *Bioelectrochemistry*, *147*, 108177. doi:10.1016/j.bioelechem.2022.108177

- Gotic, M., Ivanda, M., Popovic, S., & Music, S. (2000). Synthesis of tungsten trioxide hydrates and their structural properties. *J. Mater. Sci. Eng. B*, *77*(2), 193-201. doi:10.1016/S0921-5107(00)00488-8
- Grabolle, M., & Dau, H. (2005). Energetics of primary and secondary electron transfer in Photosystem II membrane particles of spinach revisited on basis of recombination-fluorescence measurements. *Biochim. Biophys. Acta*, *1708*(2), 209-218. doi:10.1016/j.bbabi.2005.03.007
- Graça, A. T., Hall, M., Persson, K., & Schröder, W. P. (2021). High-resolution model of Arabidopsis Photosystem II reveals the structural consequences of digitonin-extraction. *Sci. Rep.*, *11*(1), 15534. doi:10.1038/s41598-021-94914-x
- Granqvist, C. G., Arvizu, M. A., Pehlivan, I. B., Qu, H.-Y., Wen, R.-T., & Niklasson, G. A. (2018). Electrochromic materials and devices for energy efficiency and human comfort in buildings: A critical review. *Electrochim. Acta*, *259*, 1170-1182. doi:10.1016/j.electacta.2017.11.169
- Grätzel, M. (2001). Photoelectrochemical cells. *Nature*, *414*, 338-344. doi:10.1142/9789814317665\_0003
- Greife, P., Schönborn, M., Capone, M., Assunção, R., Narzi, D., Guidoni, L., & Dau, H. (2023). The electron–proton bottleneck of photosynthetic oxygen evolution. *Nature*, *617*, 623-628. doi:10.1038/s41586-023-06008-5
- Grimme, R. A., Lubner, C. E., Bryant, D. A., & Golbeck, J. H. (2008). Photosystem I/Molecular Wire/Metal Nanoparticle Bioconjugates for the Photocatalytic Production of H<sub>2</sub>. *J. Am. Chem. Soc.*, *130*, 6308-6309. doi:10.1021/ja800923y
- Groot, M.-L., Frese, R. N., de Weerd, F. L., Bromek, K., Pettersson, Å., Peterman, E. J. G., . . . Dekker, J. P. (1999). Spectroscopic Properties of the CP43 Core Antenna Protein of Photosystem II. *Biophys. J.*, *77*, 3328-3340. doi:10.1016/S0006-3495(99)77164-X
- Groot, M.-L., Peterman, E. J. G., van Stokkum, I. H. M., Dekker, J. P., & van Grondelle, R. (1995). Triplet and Fluorescing States of the CP47 Antenna Complex of Photosystem II Studied as a Function of Temperature. *Biophys. J.*, *68*, 281-290. doi:10.1016/S0006-3495(95)80186-4
- Guerra, F., Siemers, M., Mielack, C., & Bondar, A.-N. (2018). Dynamics of Long-Distance Hydrogen-Bond Networks in Photosystem II. *J Phys. Chem. B*, *122*(17), 4625-4641. doi:10.1021/acs.jpcc.8b00649
- Guiles, R. D., Zimmermann, J. L., McDermott, A. E., Yachandra, V. K., Cole, J. L., Dexheimer, S. L., . . . Klein, M. P. (1990). The S<sub>3</sub> state of photosystem II: differences between the structure of the manganese complex in the S<sub>2</sub> and S<sub>3</sub> states determined by x-ray absorption spectroscopy. *Biochemistry*, *29*(2), 471-485. doi:10.1021/bi00454a023
- Gullapalli, S. K., Vemuri, R. S., & Ramana, C. V. (2010). Structural transformation induced changes in the optical properties of nanocrystalline tungsten oxide thin films. *Appl. Phys. Lett.*, *96*, 1-3. doi:10.1063/1.3421540
- Guo, Y., Li, H., He, L.-L., Zhao, D.-X., Gong, L.-D., & Yang, Z.-Z. (2017). Theoretical reflections on the structural polymorphism of the oxygen-evolving complex in the S<sub>2</sub> state and the correlations to substrate water exchange and water oxidation mechanism in photosynthesis. *Biochim. Biophys. Acta*, *1858*(10), 833-846. doi:10.1016/j.bbabi.2017.08.001
- Guo, Y., Messinger, J., Kloo, L., & Sun, L. (2022). Reversible Structural Isomerization of Nature's Water Oxidation Catalyst Prior to O–O Bond Formation. *J. Am. Chem. Soc.*, *144*(26), 11736-11747. doi:10.1021/jacs.2c03528

- Guo, Y., Messinger, J., Kloo, L., & Sun, L. (2023). Alternative Mechanism for O<sub>2</sub> Formation in Natural Photosynthesis via Nucleophilic Oxo–Oxo Coupling. *J. Am. Chem. Soc.*, *145*(7), 4129-4141. doi:10.1021/jacs.2c12174
- Guskov, A., Kern, J., Gabdulkhakov, A., Broser, M., Zouni, A., & Saenger, W. (2009). Cyanobacterial photosystem II at 2.9Å resolution and the role of quinones, lipids, channels and chloride. *Nat. Struct. Mol. Biol.*, *16*(3), 334-342. doi:10.1038/nsmb.1559
- Gust, D., Moore, T. A., & Moore, A. L. (2009). Solar Fuels via Artificial Photosynthesis. *Acc. Chem. Res.*, *42*(12), 1890-1898. doi:10.1021/ar900209b
- Haferkamp, S., Haase, W., Pascal, A. A., van Amerongen, H., & Kirchhoff, H. (2010). Efficient Light Harvesting by Photosystem II Requires an Optimized Protein Packing Density in Grana Thylakoids. *J. Biol. Chem.*, *285*(22), 17020-17028. doi:10.1074/jbc.M109.077750
- Hall, J., Renger, T., Müh, F., Picorel, R., & Krausz, E. (2016). The lowest-energy chlorophyll of photosystem II is adjacent to the peripheral antenna: Emitting states of CP47 assigned via circularly polarized luminescence. *Biochim. Biophys. Acta*, *1857*, 1580-1593. doi:10.1016/j.bbabi.2016.06.007
- Han, G., Mamedov, F., & Styring, S. (2012). Misses during Water Oxidation in Photosystem II Are S State-dependent. *J. Biol. Chem.*, *287*(16), 13422-13429. doi:10.1074/jbc.M112.342543
- Han, Z., Qiu, F., Eisenberg, R., Holland, P. L., & Krauss, T. D. (2012). Robust Photogeneration of H<sub>2</sub> in Water Using Semiconductor Nanocrystals and a Nickel Catalyst. *Science*, *338*(6112), 1321-1324. doi:10.1126/science.1227775
- Haniewicz, P., Floris, D., Farci, D., Kirkpatrick, J., Loi, M. C., Büchel, C., . . . Piano, D. (2015). Isolation of Plant Photosystem II Complexes by Fractional Solubilization. *Front. Plant. Sci.*, *6*, 1100. doi:10.3389/fpls.2015.01100
- Hansson, Ö., & Andréasson, L.-E. (1982). EPR-detectable magnetically interacting manganese ions in the photosynthetic oxygen-evolving system after continuous illumination. *Biochim. Biophys. Acta*, *679*(2), 261-268. doi:10.1016/0005-2728(82)90296-1
- Hansson, Ö., Andréasson, L.-E., & Vänngård, T. (1986). Oxygen from water is coordinated to manganese in the S<sub>2</sub> state of photosystem II. *FEBS Lett.*, *195*(1-2), 151-154. doi:10.1016/0014-5793(86)80150-8
- Hardee, K. L., & Bard, A. J. (1977). Semiconductor Electrodes: X. Photoelectrochemical Behavior of Several Polycrystalline Metal Oxide Electrodes in Aqueous Solutions. *J. Electrochem. Soc.*, *124*, 215-224. doi:10.1149/1.2133269
- Hatakeyama, M., Ogata, K., Fujii, K., Yachandra, V. K., Yano, J., & Nakamura, S. (2016). Structural changes in the S<sub>3</sub> state of the oxygen evolving complex in photosystem II. *Chem. Phys. Lett.*, *651*, 243-250. doi:10.1016/j.cplett.2016.03.010
- Haumann, M., Barra, M., Loja, P., Löscher, S., Krivanek, R., Grundmeier, A., . . . Dau, H. (2006). Bromide does not bind to the Mn<sub>4</sub>Ca complex in its S<sub>1</sub> state in Cl(-)-depleted and Br(-)-reconstituted oxygen-evolving photosystem II: evidence from X-ray absorption spectroscopy at the Br K-edge. *Biochemistry*, *45*(43), 13101-13107. doi:10.1021/bi061308r
- Haumann, M., Liebisch, P., Müller, C., Barra, M., Grabolle, M., & Dau, H. (2005). Photosynthetic O<sub>2</sub> formation tracked by time-resolved x-ray experiments. *Science*, *310*(5750), 1019-1021. doi:10.1126/science.1117551
- Haumann, M., Müller, C., Liebisch, P., Iuzzolino, L., Dittmer, J., Grabolle, M., . . . Dau, H. (2005). Structural and Oxidation State Changes of the Photosystem II Manganese Complex in Four Transitions of the Water Oxidation Cycle (S<sub>0</sub> → S<sub>1</sub>, S<sub>1</sub> → S<sub>2</sub>, S<sub>2</sub> → S<sub>3</sub>, and S<sub>3,4</sub> → S<sub>0</sub>) Characterized by X-ray Absorption Spectroscopy at 20 K and Room Temperature. *Biochemistry*, *44*(6), 1894-1908. doi:10.1021/bi048697e

- He, W., Zhao, K.-H., & Hou, H. J. M. (2013). Toward Solar Fuel Production using Manganese/Semiconductor Systems to Mimic Photosynthesis. *NanoPhotoBioSciences*, *1*, 63-78.
- Heathcote, P., & Jones, M. R. (2012). 8.7 *The Structure-Function Relationships of Photosynthetic Reaction Centers*.
- Hill, J. C., & Choi, K.-S. (2012). Effect of Electrolytes on the Selectivity and Stability of n-type WO<sub>3</sub> Photoelectrodes for Use in Solar Water Oxidation. *J. Phys. Chem. C*, *116*, 7612-7620. doi:10.1021/jp209909b
- Hillier, W., & Wydrzynski, T. (2004). Substrate water interactions within the Photosystem II oxygen evolving complex. *Phys. Chem. Chem. Phys.*, *6*, 4882-4889. doi:10.1039/B407269C
- Ho, F. M., & Styring, S. (2008). Access channels and methanol binding site to the CaMn<sub>4</sub> cluster in Photosystem II based on solvent accessibility simulations, with implications for substrate water access. *Biochim. Biophys. Acta*, *1777*, 140-153. doi:10.1016/j.bbabi.2007.08.009
- Horton, P., Ruban, A. V., Rees, D., Pascal, A. A., Noctor, G., & Young, A. J. (1991). Control of the light-harvesting function of chloroplast membranes by aggregation of the LHClI chlorophyll-protein complex. *FEBS J.*, *292*(1,2), 1-4. doi:10.1016/0014-5793(91)80819-o
- Hou, H. J. M. (2017). Hydrogen energy production using manganese/semiconductor system inspired by photosynthesis. *Int. J. Hydrog. Energy*, *42*(12), 8530-8538. doi:10.1016/j.ijhydene.2017.01.100
- Hryniewicz, Z., & Rokita, E. (2013). *Fizyczne metody badań w biologii, medycynie i ochronie środowiska*: PWN.
- Huang, Z.-F., Song, J., Pan, L., Zhang, X., Wang, L., & Zou, J.-J. (2015). Tungsten Oxides for Photocatalysis, Electrochemistry, and Phototherapy. *Adv. Mater.*, *27*(36), 5309-5327. doi:10.1002/adma.201501217
- Hundelt, M., Hays, A.-M. A., Debus, R. J., & Junge, W. (1998). Oxygenic Photosystem II: The Mutation D1-D61N in *Synechocystis* sp. PCC 6803 Retards S-State Transitions without Affecting Electron Transfer from Y<sub>2</sub> to P680\*. *Biochemistry*, *37*(41), 14450-14456. doi:10.1021/bi981164j
- Hussein, R., Ibrahim, M., Bhowmick, A., Simon, P. S., Bogacz, I., Doyle, M. D., . . . Yano, J. (2023). Evolutionary diversity of proton and water channels on the oxidizing side of photosystem II and their relevance to function. *Photosynth. Res.* doi:10.1007/s11120-023-01018-w
- Hussein, R., Ibrahim, M., Bhowmick, A., Simon, P. S., Chatterjee, R., Lassalle, L., . . . Yano, J. (2021). Structural dynamics in the water and proton channels of photosystem II during the S<sub>2</sub> to S<sub>3</sub> transition. *Nat. Commun.*, *12*, 6531. doi:10.1038/s41467-021-26781-z
- Ibrahim, M., Fransson, T., Chatterjee, R., Cheah, M. H., Hussein, R., Lassalle, L., . . . Yano, J. (2020). Untangling the sequence of events during the S<sub>2</sub> → S<sub>3</sub> transition in photosystem II and implications for the water oxidation mechanism. *PNAS*, *117*(23), 12624-12635. doi:10.1073/pnas.2000529117
- Ifuku, K., & Noguchi, T. (2016). Structural Coupling of Extrinsic Proteins with the Oxygen-Evolving Center in Photosystem II. *Front. Plant Sci.*, *7*(84). doi:10.3389/fpls.2016.00084
- Ihara, M., Nishihara, H., Yoon, K.-S., Lenz, O., Friedrich, B., Nakamoto, H., . . . Okura, I. (2006). Light-driven Hydrogen Production by a Hybrid Complex of a [NiFe]-Hydrogenase and the Cyanobacterial Photosystem I. *Photochem. Photobiol.*, *82*, 676-682. doi:10.1562/2006-01-16-RA-778

- Ikeuchi, M., Yuasa, M., & Inoue, Y. (1985). Simple and discrete isolation of an O<sub>2</sub>-evolving PS II reaction center complex retaining Mn and the extrinsic 33 kDa protein. *FEBS Lett.*, *185*(2), 316-322. doi:10.1016/0014-5793(85)80930-3
- Isari, A. A., Mehregan, M., Mehregan, S., Hayati, F., Kalantary, R. R., & Kakavandi, B. (2020). Sono-photocatalytic degradation of tetracycline and pharmaceutical wastewater using WO<sub>3</sub>/CNT heterojunction nanocomposite under US and visible light irradiations: A novel hybrid system. *J. Hazard. Mat.*, *390*. doi:10.1016/j.jhazmat.2020.122050
- Ishikita, H., & Knapp, E.-W. (2006). Function of Redox-Active Tyrosine in Photosystem II. *Biophys. J.*, *90*(11), 3886-3896. doi:10.1529/biophysj.105.076984
- Ishikita, H., Saenger, W., Loll, B., Biesiadka, J., & Knapp, E.-W. (2006). Energetics of a Possible Proton Exit Pathway for Water Oxidation in Photosystem II. *Biochemistry*, *45*, 2063-2071. doi:10.1021/bi051615h
- Isobe, H., Shoji, M., Suzuki, T., Shen, J.-R., & Yamaguchi, K. (2021). Exploring reaction pathways for the structural rearrangements of the Mn cluster induced by water binding in the S3 state of the oxygen evolving complex of photosystem II. *J. Photochem. Photobiol. A*, *405*, 112905. doi:10.1016/j.jphotochem.2020.112905
- Iuzzolino, L., Dittmer, J., Dörner, W., Meyer-Klaucke, W., & Dau, H. (1998). X-ray absorption spectroscopy on layered photosystem II membrane particles suggests manganese-centered oxidation of the oxygen-evolving complex for the S<sub>0</sub>-S<sub>1</sub>, S<sub>1</sub>-S<sub>2</sub>, and S<sub>2</sub>-S<sub>3</sub> transitions of the water oxidation cycle. *Biochemistry*, *37*(49), 17112-17119. doi:10.1021/bi9817360
- Iwuchukwu, I. J., Vaughn, M., Myers, N., O'Neill, H., Frymier, P., & Bruce, B. D. (2010). Self-organized photosynthetic nanoparticle for cell-free hydrogen production. *Nat. Nanotechnol.*, *5*, 73-79. doi:10.1038/NNANO.2009.315
- Jafari, T., Moharrerri, E., Amin, A. S., Miao, R., Song, W., & Suib, S. L. (2016). Photocatalytic Water Splitting - The Untamed Dream: A Review of Recent Advances. *Molecules*, *21*, 1-29. doi:10.3390/molecules21070900
- Jennings, R. C., Zucchelli, G., & Garlaschi, F. M. (1990). Excitation energy transfer from the chlorophyll spectral forms to Photosystem II reaction centres: a fluorescence induction study. *Biochim. Biophys. Acta*, *1016*(2), 259-265. doi:10.1016/0005-2728(90)90067-E
- Johnson, M. P., Goral, T. K., Duffy, C. D. P., Brain, A. P. R., Mullineaux, C. W., & Ruban, A. V. (2011). Photoprotective Energy Dissipation Involves the Reorganization of Photosystem II Light-Harvesting Complexes in the Grana Membranes of Spinach Chloroplasts. *Plant Cell*, *23*, 1468-1479. doi:10.1105/tpc.110.081646
- Joliot, A., & Joliot, P. (1964). Etude cinétique de la réaction photochimique libérant l'oxygène au cours de la photosynthèse. *C. R. Acad. Sci. Paris*, *258*, 4622-4625.
- Joliot, P., Barbieri, G., & Chabaud, R. (1969). Un nouveau modele des centres photochimiques du systeme II. *Photochem. Photobiol.*, *10*, 309-329. doi:10.1111/j.1751-1097.1969.tb05696.x
- Joya, K. S., Joya, Y. F., Ocakoglu, K., & van de Krol, R. (2013). Water-Splitting Catalysis and Solar Fuel Devices: Artificial Leaves on the Move. *Angew. Chem. Int. Ed.*, *52*, 2-14. doi:10.1002/anie.201300136
- Juelsholt, M., Anker, A. S., Christiansen, T. L., Jørgensen, M. R. V., Kantor, I., Sørensen, D. R., & Jensen, K. M. Ø. (2021). Size-induced amorphous structure in tungsten oxide nanoparticles. *Nanoscale*, *13*(47), 20144-20156. doi:10.1039/D1NR05991B
- Junge, W., Haumann, M., Ahlbrink, R., Mulikidjanian, A., & Clausen, J. (2002). Electrostatics and proton transfer in photosynthetic water oxidation. *Philos. Trans. R Soc. Lond. B Biol. Sci.*, *357*(1426), 1407-1417; discussion 1417-1420. doi:10.1098/rstb.2002.1137

- Jursinic, P. A., & Dennenberg, R. J. (1090). Oxygen release time in leaf discs and thylakoids of peas and Photosystem II membrane fragments of spinach. *Biochim. Biophys. Acta*, *1020*, 195-206. doi:10.1016/0005-2728(90)90051-5
- Kato, M., Cardona, T., Rutherford, A. W., & Reisner, E. (2012). Photoelectrochemical Water Oxidation with Photosystem II Integrated in a Mesoporous Indium–Tin Oxide Electrode. *J. Am. Chem. Soc.*, *134*, 8332-8335. doi:10.1021/ja301488d
- Kato, M., Cardona, T., Rutherford, A. W., & Reisner, E. (2013). Covalent Immobilization of Oriented Photosystem II on a Nanostructured Electrode for Solar Water Oxidation. *J. Am. Chem. Soc.*, *135*(29), 10610-10613. doi:10.1021/ja404699h
- Kato, Y., Sugiura, M., Oda, A., & Watanabe, T. (2009). Spectroelectrochemical determination of the redox potential of pheophytin a, the primary electron acceptor in photosystem II. *Proc. Natl. Acad. Sci. U.S.A.*, *106*(41), 17365–17370. doi:10.1073/pnas.0905388106
- Kaur, D., Szejgis, W., Mao, J., Amin, M., Reiss, K. M., Askerka, M., . . . Gunner, M. R. (2019). Relative stability of the S<sub>2</sub> isomers of the oxygen evolving complex of photosystem II. *Photosynth Res*, *141*, 331-341. doi:10.1007/s11120-019-00637-6
- Kautsky, H., & Hirsch, A. (1931). Neue Versuche zur Kohlensäureassimilation. *Naturwissenschaften*, *19*, 964. doi:10.1007/BF01516164
- Kawahara, K., Inoue-Kahino, N., Namie, K., Kato, Y., Tomo, T., Shibata, Y., . . . Noguchi, T. (2020). A gold nanoparticle conjugate with photosystem I and photosystem II for development of a biohybrid water-splitting photocatalyst. *Biomed. Spectrosc. Imaging*, *9*(1-2), 73-81. doi:10.3233/BSI-200200
- Kawashima, K., Takaoka, T., Kimura, H., Saito, K., & Ishikita, H. (2018). O<sub>2</sub> evolution and recovery of the water-oxidizing enzyme. *Nat. Com.*, *9*(1), 1247. doi:10.1038/s41467-018-03545-w
- Ke, B. (2001). *Photosynthesis Photochemistry and Photobiophysics* (Vol. 10): Kluwer Academic Publishers.
- Keereeta, Y., Thongtem, S., & T., T. (2015). Enhanced photocatalytic degradation of methylene blue by WO<sub>3</sub>/ZnWO<sub>4</sub> composites synthesized by a combination of microwave-solvothermal method and incipient wetness procedure. *Powder Technol.*, *284*, 85-94. doi:10.1016/j.powtec.2015.06.046
- Kern, J., Chatterjee, R., Young, I. D., Fuller, F. D., Lassalle, L., Ibrahim, M., . . . Yachandra, V. K. (2018). Structures of the intermediates of Kok's photosynthetic water oxidation clock. *Nature*, *563*, 421-425. doi:10.1038/s41586-018-0681-2
- Kim, C. J., & Debus, R. J. (2017). Evidence from FTIR Difference Spectroscopy That a Substrate H<sub>2</sub>O Molecule for O<sub>2</sub> Formation in Photosystem II Is Provided by the Ca Ion of the Catalytic Mn<sub>4</sub>CaO<sub>5</sub> Cluster. *Biochemistry*, *56*(20), 2558-2570. doi:10.1021/acs.biochem.6b01278
- Kim, D., Sakimoto, K. K., Hong, D., & Yang, P. (2015). Artificial Photosynthesis for Sustainable Fuel and Chemical Production. *Angew. Chem. Int. Ed.*, *54*, 2-10. doi:10.1002/anie.201409116
- Kim, E., Akimoto, S., Tokutsu, R., Yokono, M., & Minagawa, J. (2017). Fluorescence lifetime analyses reveal how the high light-responsive protein LHCSR3 transforms PSII light-harvesting complexes into an energy-dissipative state. *J Biol. Chem.*, *292*(46), 18951-18960. doi:10.1074/jbc.M117.805192
- Kirchhoff, H. (2008). Molecular crowding and order in photosynthetic membranes. *Trends Plant Sci.*, *13*(5), 201-207. doi:10.1016/j.tplants.2008.03.001

- Klauss, A., Haumann, M., & Dau, H. (2012). Alternating electron and proton transfer steps in photosynthetic water oxidation. *PNAS*, *109*(40), 16035-16040. doi:10.1073/pnas.1206266109
- Klepser, B. M., & Bartlett, B. M. (2014). Anchoring a Molecular Iron Catalyst to Solar-Responsive WO<sub>3</sub> Improves the Rate and Selectivity of Photoelectrochemical Water Oxidation. *J. Am. Chem. Soc.*, *136*(5), 1694-1697. doi:10.1021/ja4086808
- Klimov, V. V., Allakhverdiev, S. I., Demeter, S., & Krasnovskii, A. A. (1979). Photoreduction of pheophytin in the photosystem 2 of chloroplasts depending on the oxidation-reduction potential of the medium. *Doklady*, *249*(1), 227-230.
- Knoppová, J., Sobotka, R., Yu, J., Bečková, M., Pilný, J., Trinugroho, J. P., . . . Komenda, J. (2022). Assembly of D1/D2 complexes of photosystem II: Binding of pigments and a network of auxiliary proteins. *Plant Physiol*, *189*(2), 790-804. doi:10.1093/plphys/kiac045
- Koffyberg, F. P., Dwight, K., & Wold, A. (1979). Interband transitions of semiconducting oxides determined from photoelectrolysis spectra. *Solid State Commun.*, *30*, 433-437. doi:10.1016/0038-1098(79)91182-7
- Kok, B., Forbush, B., & McGloin, M. (1970). Cooperation of charges in photosynthetic O<sub>2</sub> evolution-I. A linear four step mechanism. *Photochem. Photobiol.*, *11*(6), 457-475. doi:10.1111/j.1751-1097.1970.tb06017.x
- Konermann, L., & Holzwarth, A. R. (1996). Analysis of the Absorption Spectrum of Photosystem II Reaction Centers: Temperature Dependence, Pigment Assignment, and Inhomogeneous Broadening. *Biochemistry*, *35*, 829-842. doi:10.1021/bi9513158
- Kouřil, R., Oostergetel, G. T., & Boekema, E. J. (2011). Fine structure of granal thylakoid membrane organization using cryo electron tomography. *Biochim. Biophys. Acta*, *1807*(3), 368-374. doi:10.1016/j.bbabi.2010.11.007
- Kozak, L., & Niedzielski, P. (2011). Podstawy teoretyczne absorpcyjnej spektrometrii atomowej. *LAB*, *16*(3), 12-14. doi:bwmeta1.element.baztech-article-LOD7-0026-0002
- Krasnovskii, A. A., & Brin, G. P. (1962). Inorganic models of Hill's reaction. *Dokl. Akad. Nauk SSSR Ser. Khim.*, *147*, 656-659.
- Krewald, V., Neese, F., & Pantazis, D. A. (2019). Implications of structural heterogeneity for the electronic structure of the final oxygen-evolving intermediate in photosystem II. *J. Inorg. Biochem.*, *199*. doi:10.1016/j.jinorgbio.2019.110797
- Krewald, V., Retegan, M., Cox, N., Messinger, J., Lubitz, W., DeBeer, S., . . . Pantazis, D. A. (2015). Metal oxidation states in biological water splitting. *Chem. Sci.*, *6*, 1676-1695. doi:10.1039/c4sc03720k
- Krewald, V., Retegan, M., Neese, F., Lubitz, W., Pantazis, D. A., & Cox, N. (2016). Spin State as a Marker for the Structural Evolution of Nature's Water-Splitting Catalyst. *Inorg. Chem.*, *55*(2), 488-501. doi:10.1021/acs.inorgchem.5b02578
- Krivanek, R., Kern, J., Zouni, A., Dau, H., & Haumann, M. (2007). Spare quinones in the QB cavity of crystallized photosystem II from *Thermosynechococcus elongatus*. *Biochim. Biophys. Acta*, *1767*(6), 520-527. doi:10.1016/j.bbabi.2007.02.013
- Kruk, J., Burda, K., Jemioła-Rzemińska, M., & K., S. (2003). The 33 kDa protein of photosystem II is a low-affinity calcium- and lanthanide-binding protein. *Biochemistry*, *42*(50), 14862-14867. doi:10.1021/bi0351413
- Krysiak, S., Gotić, M., Madej, E., Moreno Maldonado, A. C., Goya, G. F., Spiridis, N., & Burda, K. (2023). The effect of ultrafine WO<sub>3</sub> nanoparticles on the organization of thylakoids enriched in photosystem II and energy transfer in photosystem II complexes. *Microsc. Res. Tech.*, *n/a*(*n/a*). doi:10.1002/jemt.24394

- Kuroda, H., Kawashima, K., Ueda, K., Ikeda, T., Saito, K., Ninomiya, R., . . . Ishikita, H. (2021). Proton transfer pathway from the oxygen-evolving complex in photosystem II substantiated by extensive mutagenesis. *Biochim Biophys Acta Bioenerg.*, *1862*(1), 148329. doi:10.1016/j.bbabi.2020.148329
- Kusunoki, M. (2007). Mono-manganese mechanism of the photosystem II water splitting reaction by a unique  $Mn_4Ca$  cluster. *Biochim. Biophys. Acta*, *1767*, 484-492. doi:10.1016/j.bbabi.2007.03.012
- Kusunoki, M. (2011).  $S_1$ -state  $Mn_4Ca$  complex of Photosystem II exists in equilibrium between the two most-stable isomeric substates: XRD and EXAFS evidence. *J. Photochem. Photobiol. B*, *104*(1-2), 100-110. doi:10.1016/j.jphotobiol.2011.03.002
- Laemmli, U. K. (1970). Cleavage of Structural Proteins during the Assembly of the Head of Bacteriophage T4. *Nature*, *227*(5259), 680-685. doi:10.1038/227680a0
- Lavergne, J. (1989). Mitochondrial responses to intracellular pulses of photosynthetic oxygen. *PNAS*, *86*(22), 8768-8772. doi:10.1073/pnas.86.22.8768
- Lavergne, J., & Junge, W. (1993). Proton release during the redox cycle of the water oxidase. *Photosynth. Res.*, *38*, 279-296. doi:10.1007/BF00046752
- Lavorel, J. (1976). Matrix analysis of the oxygen evolving system of photosynthesis. *J. Theor. Biol.*, *57*, 171-185. doi:10.1016/S0022-5193(76)80011-2
- Lavorel, J. (1978). *On the origin of the damping of the  $O_2$  yield in sequences of flashes*. New York: Academic Press.
- Lee, B.-H., Park, S., Kim, M., Sinha, A. K., Lee, S. C., Jung, E., . . . Hyeon, T. (2019). Reversible and cooperative photoactivation of single-atom Cu/TiO<sub>2</sub> photocatalysts. *Nat. Mater.*, *18*, 620-626. doi:10.1038/s41563-019-0344-1
- Lee, C.-K., Pao, C.-W., & Smit, B. (2015a). PSII-LHCII Supercomplex Organizations in Photosynthetic Membrane by Coarse-Grained Simulation. *J. Phys. Chem. B*, *119*(10), 3999-4008. doi:10.1021/jp511277c
- Lee, C.-K., Pao, C.-W., & Smit, B. (2015b). PSII-LHCII Supercomplex Organizations in Photosynthetic Membrane by Coarse-Grained Simulation. *J. Phys. Chem. B*, *119*(10), 3999-4008. doi:10.1021/jp511277c
- Lee, S.-H., Deshpande, R., Parilla, P. A., Jones, K. M., To, B., Mahan, A. H., & Dillon, A. C. (2006). Crystalline WO<sub>3</sub> Nanoparticles for Highly Improved Electrochromic Applications. *Adv. Mater.*, *18*, 763-766. doi:10.1002/adma.200501953
- Lewis, N. S., & Nocera, D. G. (2006). Powering the planet: Chemical challenges in solar energy utilization. *PNAS* *103*(43), 15729-15735. doi:10.1073/pnas.0603395103
- Li, B., Sun, L., Bian, J., Sun, N., Sun, J., Chen, L., . . . Jing, L. (2020). Controlled synthesis of novel Z-scheme iron phthalocyanine/porous WO<sub>3</sub> nanocomposites as efficient photocatalysts for CO<sub>2</sub> reduction. *Appl. Catal. B*, *270*. doi:10.1016/j.apcatb.2020.118849
- Li, J., Feng, X., Fei, J., Cai, P., Huang, J., & Li, J. (2016). Integrating photosystem II into a porous TiO<sub>2</sub> nanotube network toward highly efficient photo-bioelectrochemical cells. *J. Mater. Chem. A*, *4*, 12197-12204. doi:10.1039/C6TA04964H
- Li, M., Mukhopadhyay, R., Svoboda, V., Oung, H. M. O., Mullendore, D. L., & Kirchhoff, H. (2020). Measuring the dynamic response of the thylakoid architecture in plant leaves by electron microscopy. *Plant Direct*, *4*(11), e00280. doi:10.1002/pld3.280
- Li, X., & Siegbahn, P. E. M. (2015). Alternative mechanisms for O<sub>2</sub> release and O–O bond formation in the oxygen evolving complex of photosystem II. *Phys. Chem. Chem. Phys.*, *17*, 12168-12174. doi:10.1039/c5cp00138b
- Li, Y., & Tsang, S. C. E. (2020). Recent progress and strategies for enhancing photocatalytic water splitting. *Materials Today Sustainability*, *9*, 1-10. doi:10.1016/j.mtsust.2020.100032

- Li, Y., Yao, R., Chen, Y., Xu, B., Chen, C., & Zhang, C. (2020). Mimicking the Catalytic Center for the Water-Splitting Reaction in Photosystem II. *Catalysts*, *10*. doi:10.3390/catal10020185
- Li, Z., Wang, W., Ding, C., Wang, Z., Liao, S., & Li, C. (2017). Biomimetic electron transport via multiredox shuttles from photosystem II to a photoelectrochemical cell for solar water splitting. *Energy Environ. Sci.*, *10*, 765-771 doi:10.1039/c6ee03401b
- Liang, W., Roelofs, T. A., Cinco, R. M., Rompel, A., Latimer, M. J., Yu, W. O., . . . Yachandra, V. K. (2000). Structural change of the Mn cluster during the  $S_2 \rightarrow S_3$  state transition of the oxygen-evolving complex of Photosystem II. Does it reflect the onset of water/substrate oxidation? Determination by Mn X-ray absorption spectroscopy. *J Am Chem Soc.*, *122*, 3399-3412. doi:10.1021/ja992501u
- Lichtenthaler, H. K., & Buschmann, C. (2001). Chlorophylls and Carotenoids: Measurement and Characterization by UV-VIS Spectroscopy. In *Current Protocols in Food Analytical Chemistry*.
- Lim, J., Yeap, S. P., Che, H. X., & Low, S. C. (2013). Characterization of magnetic nanoparticle by dynamic light scattering. *Nano. Research Lett.*, *8*(1), 381. doi:10.1186/1556-276X-8-381
- Limburg, J., Vrettos, J. S., Liable-Sands, L. M., Rheingold, A. L., Crabtree, R. H., & Brudvig, G., W. (1999). A Functional Model for O-O Bond Formation by the  $O_2$ -Evolving Complex in Photosystem II. *Science*, *283*, 1524-1527. doi:10.1126/science.283.5407.1524
- Lindberg, K., & Andréasson, L. E. (1996). A one-site, two-state model for the binding of anions in photosystem II. *Biochemistry*, *35*(45), 14259-14267. doi:10.1021/bi961244s
- Linke, K., & Ho, F. M. (2014). Water in Photosystem II: Structural, functional and mechanistic considerations. *Biochim. Biophys. Acta*, *1837*, 14-32. doi:10.1016/j.bbabi.2013.08.003
- Liu, J., & van Iersel, M. W. (2021). Photosynthetic Physiology of Blue, Green, and Red Light: Light Intensity Effects and Underlying Mechanisms. *Front. Plant Sci.*, *12*. doi:10.3389/fpls.2021.619987
- Liu, R., Lin, Y., Chou, L.-Y., Sheehan, S. W., He, W., Zhang, F., . . . Wang, D. (2011). Water Splitting by Tungsten Oxide Prepared by Atomic Layer Deposition and Decorated with an Oxygen-Evolving Catalyst. *Angew. Chem. Int. Ed.*, *50*, 499-502. doi:10.1002/anie.201004801
- Liu, Y., Daye, J., Jenson, D., & Fong, S. (2018). Evaluating the efficiency of a photoelectrochemical electrode constructed with photosystem II-enriched thylakoid membrane fragments. *Bioelectrochemistry*, *124*, 22-27. doi:10.1016/j.bioelechem.2018.06.007
- Lohmiller, T., Krewald, V., Sedoud, A., Rutherford, A. W., Neese, F., Lubitz, W., . . . Cox, N. (2017). The First State in the Catalytic Cycle of the Water-Oxidizing Enzyme: Identification of a Water-Derived  $\mu$ -Hydroxo Bridge. *J. Am. Chem. Soc.*, *139*(41), 14412-14424. doi:10.1021/jacs.7b05263
- Loll, B., Kern, J., Saenger, W., Zouni, A., & Biesiadka, J. (2005). Towards complete cofactor arrangement in the 3.0 Å resolution structure of photosystem II. *Nature*, *438*, 1040-1044. doi:10.1038/nature04224
- Loopstra, B. O., & Boldrini, P. (1966). Neutron diffraction investigation of  $WO_3$ . *Acta Cryst.*, *21*, 158-162. doi:10.1107/S0365110X66002469
- Lubitz, W., Chrysina, M., & Cox, N. (2019). Water oxidation in photosystem II. *Photosynth Res*, *142*, 105-125. doi:10.1007/s11120-019-00648-3
- Lubitz, W., Pantazis, D. A., & Cox, N. (2023). Water oxidation in oxygenic photosynthesis studied by magnetic resonance techniques. *FEBS Lett.*, *597*, 6-29. doi:10.1002/1873-3468.14543
- Mackinney, G. (1941). Absorption of light by chlorophyll solutions. *J. Biol. Chem.*, *140*(2), 315-322. doi:10.1016/S0021-9258(18)51320-X

- MacLachlan, D. J., Nugent, J. H. A., & Evans, M. C. W. (1994). A XANES study of the manganese complex of inhibited PS II membranes indicates manganese redox changes between the modified  $S_1$ ,  $S_2$  and  $S_3$  states. *Biochim. Biophys. Acta*, *1185*(1), 103-111. doi:10.1016/0005-2728(94)90200-3
- Maeda, K., Higashi, M., Lu, D., Abe, R., & Domen, K. (2010). Efficient Nonsacrificial Water Splitting through Two-Step Photoexcitation by Visible Light using a Modified Oxynitride as a Hydrogen Evolution Photocatalyst. *J. Am. Chem. Soc.*, *132*, 5858-5868. doi:10.1021/ja1009025
- Mandal, M., Kawashima, K., Saito, K., & Ishikita, H. (2020). Redox Potential of the Oxygen-Evolving Complex in the Electron Transfer Cascade of Photosystem II. *J. Phys. Chem. Lett.*, *11*, 249–255. doi:10.1021/acs.jpcclett.9b02831
- Mandal, M., Saito, K., & Ishikita, H. (2020). The Nature of the Short Oxygen–Oxygen Distance in the  $Mn_4CaO_6$  Complex of Photosystem II Crystals. *J. Phys. Chem. Lett.*, *11*, 10262-10268. doi:10.1021/acs.jpcclett.0c02868
- Martin, D. J., Reardon, P. J. T., Moniz, S. J. A., & Tang, J. (2014). Visible Light-Driven Pure Water Splitting by a Nature-Inspired Organic Semiconductor-Based System. *J. Am. Chem. Soc.*, *136*, 12568-12571. doi:10.1021/ja506386e
- Mauzerall, D. (1990). Determination of Oxygen Emission and Uptake in Leaves by Pulsed, Time Resolved Photoacoustics. *Plant Physiol.*, *94*(1), 278-283. doi:10.1104/pp.94.1.278
- Maxwell, K., & Johnson, G. N. (2000). Chlorophyll fluorescence—a practical guide. *J. Experimen. Bot.*, *51*(345), 659-668. doi:10.1093/jexbot/51.345.659
- McConnell, I., Li, G., & Brudvig, G. W. (2010). Energy Conversion in Natural and Artificial Photosynthesis. *Chem. Biol.*, *17*, 434-447. doi:10.1016/j.chembiol.2010.05.005
- McCree, K. J. (1972). The action spectrum, absorptance and quantum yield of photosynthesis in crop plants. *Agric. Meteorol.*, *9*, 191-216. doi:10.1016/0002-1571(71)90022-7
- Mersch, D., Lee, C.-Y., Zhang, J. Z., Brinkert, K., Fontecilla-Camps, J. C., Rutherford, A. W., & Reisner, E. (2015). Wiring of Photosystem II to Hydrogenase for Photoelectrochemical Water Splitting. *J. Am. Chem. Soc.*, *137*(26), 8541-8549. doi:10.1021/jacs.5b03737
- Messinger, J., Badger, J., & Wydrzynski, T. (1995). Detection of one slowly exchanging substrate water molecule in the  $S_3$  state of photosystem II. *Proc. Natl. Acad. Sci.*, *92*(8), 3209-3213. doi:10.1073/pnas.92.8.3209
- Messinger, J., Robblee, J. H., Bergmann, U., Fernandez, C., Glatzel, P., Visser, H., . . . Yachandra, V. K. (2001). Absence of Mn-Centered Oxidation in the  $S_2 \rightarrow S_3$  Transition: Implications for the Mechanism of Photosynthetic Water Oxidation. *J. Am. Chem. Soc.*, *123*(32), 7804-7820. doi:10.1021/ja004307+
- Mills, A., & Valenzuela, M. A. (2004). Photo-oxidation of water sensitized by  $TiO_2$  and  $WO_3$  in presence of different electron acceptors. *Rev. Mex. Fis.*, *50*(3), 287-296.
- Miyachi, M., Ikehira, S., Nishiori, D., Yamanoi, Y., Yamada, M., Iwai, M., . . . Nishihara, H. (2017). Photocurrent generation of reconstituted photosystem II on self-assembled gold film. *Langmuir*, *33*(6), 1351-1358. doi:10.1021/acs.langmuir.6b03499
- Miyagawa, K., Kawakami, T., Suzuki, Y., Isobe, H., Shoji, M., Yamanaka, S., . . . Yamaguchi, K. Relative stability among intermediate structures in  $S_2$  state of  $CaMn_4O_5$  cluster in PSII by using hybrid-DFT and DLPNO-CC methods and evaluation of magnetic interactions between Mn ions. *J. Photochem. Photobiol. A*, *405*(15), 112923. doi:10.1016/j.jphotochem.2020.112923
- Müh, F., & Zouni, A. (2020). Structural basis of light-harvesting in the photosystem II core complex. *Protein Sci.*, *29*, 1090-1119. doi:10.1002/pro.3841

- Mullineaux, C. W. (2005). Function and evolution of grana. *Trends Plant Sci.*, *10*(11), 521-525. doi:10.1016/j.tplants.2005.09.001
- Murray, J. W., & Barber, J. (2007). Structural characteristics of channels and pathways in photosystem II including the identification of an oxygen channel. *J. Struct. Biol.*, *159*, 228-237. doi:10.1016/j.jsb.2007.01.016
- Nagakawa, H., Takeuchi, A., Takekuma, Y., Noji, T., Kawakami, K., Kamiya, N., . . . Nagata, M. (2019). Efficient hydrogen production using photosystem I enhanced by artificial light harvesting dye. *Photochem. Photobiol. Sci.*, *18*, 309-313 doi:10.1039/c8pp00426a
- Nagao, R., Tomo, T., & Noguchi, T. (2015). Effects of extrinsic proteins on the protein conformation of the oxygen-evolving center in cyanobacterial photosystem II as revealed by Fourier transform infrared spectroscopy. *Biochemistry*, *54*(11), 2022-2031. doi:10.1021/acs.biochem.5b00053
- Narzi, D., Bovi, D., & Guidoni, L. (2014). Pathway for Mn-cluster oxidation by tyrosine-Z in the S<sub>2</sub> state of photosystem II. *Proc. Natl. Acad. Sci. U.S.A.*, *111*(24), 8723-8728. doi:10.1073/pnas.1401719111
- Narzi, D., Mattioli, G., Bovi, D., & Guidoni, L. (2017). A Spotlight on the Compatibility between XFEL and Ab Initio Structures of the Oxygen Evolving Complex in Photosystem II. *Chem. Eur. J.*, *23*(29), 6969-6973. doi:10.1002/chem.201700722
- Nass, K. (2019). Radiation damage in protein crystallography at X-ray free-electron lasers. *Acta Cryst.*, *75*(2), 211-218. doi:doi:10.1107/S2059798319000317
- Nass, K., Foucar, L., Barends, T. R., Hartmann, E., Botha, S., Shoeman, R. L., . . . Schlichting, I. (2015). Indications of radiation damage in ferredoxin microcrystals using high-intensity X-FEL beams. *J Synchrotron Radiat.*, *22*(2), 225-238. doi:10.1107/s1600577515002349
- Nield, J., & Barber, J. (2006). Refinement of the structural model for the Photosystem II supercomplex of higher plants. *Biochim. Biophys. Acta*, *1757*(5-6), 353-361. doi:10.1016/j.bbabi.2006.03.019
- Nield, J., Orlova, E. V., Morris, E. P., Gowen, B., van Heel, M., & Barber, J. (2000). 3D map of the plant photosystem II supercomplex obtained by cryoelectron microscopy and single particle analysis. *Nat. Struct. Biol.*, *7*(1), 44-47. doi:10.1038/71242
- Noguchi, T., & Sugiura, M. (2002). Flash-induced FTIR difference spectra of the water oxidizing complex in moderately hydrated photosystem II core films: effect of hydration extent on S-state transitions. *Biochemistry*, *41*(7), 2322-2330. doi:10.1021/bi011954k
- Noji, T., Suzuki, H., Gotoh, T., Iwai, M., Ikeuchi, M., Tomo, T., & Noguchi, T. (2011). Photosystem II-Gold Nanoparticle Conjugate as a Nanodevice for the Development of Artificial Light-Driven Water-Splitting Systems. *J. Phys. Chem. Lett.*, *2*, 2448-2452. doi:10.1021/jz201172y
- Offenbacher, A. R., Polander, B. C., & Barry, B. A. (2013). An intrinsically disordered photosystem II subunit, PsbO, provides a structural template and a sensor of the hydrogen-bonding network in photosynthetic water oxidation. *J. Biol. Chem.*, *288*(40), 29056-29068. doi:10.1074/jbc.M113.487561
- Ogata, K., Yuki, T., Hatakeyama, M., Uchida, W., & Nakamura, S. (2013). All-Atom Molecular Dynamics Simulation of Photosystem II Embedded in Thylakoid Membrane. *J. Am. Chem. Soc.*, *135*(42), 15670-15673. doi:10.1021/ja404317d
- Okamoto, Y., Shimada, Y., Nagao, R., & Noguchi, T. (2021). Proton and Water Transfer Pathways in the S<sub>2</sub> → S<sub>3</sub> Transition of the Water-Oxidizing Complex in Photosystem II: Time-Resolved Infrared Analysis of the Effects of D1-N298A Mutation and NO<sub>3</sub>- Substitution. *J. Photochem. Photobiol. B*, *125*(25), 6864-6873. doi:10.1021/acs.jpccb.1c03386

- Olesen, K., & Andréasson, L. E. (2003). The function of the chloride ion in photosynthetic oxygen evolution. *Biochemistry*, *42*(7), 2025-2035. doi:10.1021/bi026175y
- Ono, T.-A., & Inoue, Y. (1983). Mn-preserving extraction of 33-, 24- and 16-kDa proteins from O<sub>2</sub>-evolving PS II particles by divalent salt-washing. *FEBS Lett.*, *164*(2), 255-260. doi:10.1016/0014-5793(83)80297-X
- Orio, M., & Pantazis, D. A. (2021). Successes, challenges, and opportunities for quantum chemistry in understanding metalloenzymes for solar fuels research. *Chem. Commun.*, *57*(33), 33952-33974. doi:10.1039/d1cc00705j
- Oyala, P. H., Stich, T. A., Debus, R. J., & Britt, R. D. (2015). Ammonia Binds to the Dangler Manganese of the Photosystem II Oxygen Evolving Complex. *J. Am. Chem. Soc.*, *137*(27), 8829-8837. doi:10.1021/jacs.5b04768
- Pagliano, C., Saracco, G., & Barber, J. (2013). Structural, functional and auxiliary proteins of photosystem II. *Photosynth Res*, *116*, 167-188. doi:10.1007/s11120-013-9803-8
- Pan, J., Gelzinis, A., Chorošajev, V., Vengris, M., Senlik, S. S., Shen, J.-R., . . . Ogilvie, J. P. (2017). Ultrafast energy transfer within the photosystem II core complex. *Phys. Chem. Chem. Phys.*, *19*(23), 15356-15367. doi:10.1039/C7CP01673E
- Pang, H., Zhao, G., Liu, G., Zhang, H., Hai, X., Wang, S., . . . Ye, J. (2018). Interfacing photosynthetic membrane protein with mesoporous WO<sub>3</sub> photoelectrode for solar water oxidation. *Small*, *14*(19), 1-10. doi:10.1002/sml.201800104
- Pantazis, D. A. (2018). Missing Pieces in the Puzzle of Biological Water Oxidation. *Catalysis*, *8*(10), 9477-9507. doi:10.1021/acscatal.8b01928
- Pantazis, D. A. (2019). The S<sub>3</sub> State of the Oxygen-Evolving Complex: Overview of Spectroscopy and XFEL Crystallography with a Critical Evaluation of Early-Onset Models for O–O Bond Formation. *Inorganics*, *7*(4), 55-85. doi:10.3390/inorganics7040055
- Pantazis, D. A. (2023). Clues to how water splits during photosynthesis. *Nature*, *617*, 468. doi:10.1038/d41586-023-01388-0
- Pantazis, D. A., Ames, W., Cox, N., Lubitz, W., & Neese, F. (2012). Two Interconvertible Structures that Explain the Spectroscopic Properties of the Oxygen-Evolving Complex of Photosystem II in the S<sub>2</sub> State. *Angew. Chem. Int. Ed.*, *51*(39), 9935-9940. doi:10.1002/anie.201204705
- Park, M., Seo, J. H., Kim, J. H., Park, G., Park, J. Y., Seo, W. S., . . . Nam, K. M. (2018). Effective Formation of WO<sub>3</sub> Nanoparticle/BiS Nanowire Composite for Improved Photoelectrochemical Performance. *J. Phys. Chem. C*, *122*, 17676-17685. doi:10.1021/acs.jpcc.8b05555
- Pecoraro, V. L., Baldwin, M. J., Caudle, M. T., Hsieh, W.-Y., & Law, N. A. (1998). A proposal for water oxidation in photosystem II. *Pure & Appl. Chem.*, *70*(4), 925-929. doi:10.1351/pac199870040925
- Pérez-Navarro, M., Neese, F., Lubitz, W., Pantazis, D. A., & Cox, N. (2016). Recent developments in biological water oxidation. *Curr Opin Chem Biol*, *31*, 113-119. doi:10.1016/j.cbpa.2016.02.007
- Pokhrel, R., Debus, R. J., & Brudvig, G. W. (2015). Probing the Effect of Mutations of Asparagine 181 in the D1 Subunit of Photosystem II. *Biochemistry*, *54*(8), 1663-1672. doi:10.1021/bi501468h
- Pokhrel, R., Service, R. J., Debus, R. J., & Brudvig, G. W. (2013). Mutation of Lysine 317 in the D2 Subunit of Photosystem II Alters Chloride Binding and Proton Transport. *Biochemistry*, *52*(28), 4758-4773. doi:10.1021/bi301700u

- Polander, B. C., & Barry, B. A. (2013). Detection of an intermediary, protonated water cluster in photosynthetic oxygen evolution. *PNAS*, *110*(26), 10634-10639. doi:10.1073/pnas.1306532110
- Popelkova, H., & Yocum, C. F. (2011). PsbO, the manganese-stabilizing protein: Analysis of the structure–function relations that provide insights into its role in photosystem II. *J. Photochem. Photobiol. B*, *104*(1), 179-190. doi:10.1016/j.jphotobiol.2011.01.015
- Pushkar, Y., Davis, K. M., & Palenik, M. C. (2018). Model of the Oxygen Evolving Complex Which is Highly Predisposed to O–O Bond Formation. *J. Phys. Chem. Lett.*, *9*(12), 3525-3531. doi:10.1021/acs.jpcclett.8b00800
- Pushkar, Y., Ravari, A. K., Jensen, S. C., & M., P. (2019). Early Binding of Substrate Oxygen Is Responsible for a Spectroscopically Distinct S2 State in Photosystem II. *J. Phys. Chem. Lett.*, *10*(17), 5284-5291. doi:10.1021/acs.jpcclett.9b01255
- Rappaport, F., & Lavergne, J. (1991). Proton release during successive oxidation steps of the photosynthetic water oxidation process: stoichiometries and pH dependence. *Biochemistry*, *30*(41), 10004-10012. doi:10.1021/bi00105a027
- Raziq, F., Aligayev, A., Shen, H., Ali, S., Shah, R., Ali, S., . . . Qiao, L. (2022). Exceptional Photocatalytic Activities of rGO Modified (B,N) Co-Doped WO<sub>3</sub>, Coupled with CdSe QDs for One Photon Z-Scheme System: A Joint Experimental and DFT Study. *Adv. Sci.*, *9*. doi:10.1002/advs.202102530
- Renger, G. (2012). Mechanism of light induced water splitting in Photosystem II of oxygen evolving photosynthetic organisms. *Biochim. Biophys. Acta*, *1817*, 1164-1176. doi:10.1016/j.bbabi.2012.02.005
- Retegan, M., Cox, N., Lubitz, W., Neese, F., & Pantazis, D. A. (2014). The first tyrosyl radical intermediate formed in the S<sub>2</sub>–S<sub>3</sub> transition of photosystem II. *Phys. Chem. Chem. Phys.*, *16*, 11901-11910. doi:10.1039/c4cp00696h
- Retegan, M., Krewald, V., Mamedov, F., Neese, F., Lubitz, W., Cox, N., & Pantazis, D. A. (2016). A five-coordinate Mn(IV) intermediate in biological water oxidation: spectroscopic signature and a pivot mechanism for water binding. *Chem. Sci.*, *7*(1), 72-84. doi:10.1039/C5SC03124A
- Retegan, M., & Pantazis, D. A. (2016). Interaction of methanol with the oxygen-evolving complex: atomistic models, channel identification, species dependence, and mechanistic implications. *Chem. Sci.*, *7*(10), 6463-6476. doi:10.1039/C6SC02340A
- Retegan, M., & Pantazis, D. A. (2017). Differences in the Active Site of Water Oxidation among Photosynthetic Organisms. *J. Am. Chem. Soc.*, *139*(41), 14340-14343. doi:10.1021/jacs.7b06351
- Rich, P. R., & Bendall, D. S. (1980). The kinetics and thermodynamics of the reduction of cytochrome c by substituted p-benzoquinols in solution. *Biochim. Biophys. Acta*, *592*(3), 506-518. doi:10.1016/0005-2728(80)90095-X
- Riedel, M., Wersig, J., Ruff, A., Schuhmann, W., Zouni, A., & Lisdat, F. (2019). A Z-scheme inspired photobioelectrochemical H<sub>2</sub>O/O<sub>2</sub> cell with 1V open-circuit voltage combining photosystem II and PbS quantum dots. *Angew. Chem. Int. Ed.*, *131*(3), 811-815. doi:10.1002/ange.201811172
- Rivalta, I., Amin, M., Lubner, S., Vassiliev, S., Pokhrel, R., Umena, Y., . . . Batista, V. S. (2011). Structural–Functional Role of Chloride in Photosystem II. *Biochemistry*, *50*(29), 6312-6315. doi:10.1021/bi200685w
- Robinson, H. H., & Crofts, A. R. (1983). Kinetics of the oxidation-reduction reactions of the photosystem II quinone acceptor complex, and the pathway for deactivation. *FEBS Lett.*, *153*(1), 221-226. doi:10.1016/0014-5793(83)80152-5

- Roelofs, T. A., Liang, W., Latimer, M. J., Cinco, R. M., Rompel, A., Andrews, J. C., . . . Klein, M. P. (1996). Oxidation states of the manganese cluster during the flash-induced S-state cycle of the photosynthetic oxygen-evolving complex. *Proc. Natl. Acad. Sci. USA*, *93*(8), 3335-3340. doi:10.1073/pnas.93.8.3335
- Rogers, C. J., Hardwick, O., Corry, T. A., Rummel, F., Collison, D., Bowen, A. M., & O'Malley, P. J. (2022). Magnetic and Electronic Structural Properties of the S<sub>3</sub> State of Nature's Water Oxidizing Complex: A Combined Study in ELDOR-Detected Nuclear Magnetic Resonance Spectral Simulation and Broken-Symmetry Density Functional Theory. *ACS Omega*, *7*(45), 41783-41788. doi:10.1021/acsomega.2c06151
- Ruban, A. V., Rees, D., Pascal, A. A., & Horton, P. (1992). Mechanism of ΔpH-dependent dissipation of absorbed excitation energy by photosynthetic membranes. II. The relationship between LHCII aggregation in vitro and qE in isolated thylakoids. *Biochim. Biophys. Acta*, *1102*, 39-44. doi:10.1016/0005-2728(92)90062-7
- Rutherford, A. W. (1989). Photosystem II, the water-splitting enzyme. *Trends in Biochemical Sciences*, *14*(6), 227-232. doi:10.1016/0968-0004(89)90032-7
- Rutherford, A. W., & Faller, P. (2003). Photosystem II: evolutionary perspectives. *Phil. Trans. R. Soc. B*, *358*(1429), 245-253. doi:10.1098/rstb.2002.1186
- Rutherford, A. W., Mullet, J. E., & Crofts, A. R. (1981). Measurement of the midpoint potential of the pheophytin acceptor of photosystem II. *FEBS Lett.*, *123*, 235-237.
- Sager, J. C., Smith, W. O., Edwards, J. L., & Cyr, K. L. (1988). Photosynthetic Efficiency and Phytochrome Photoequilibria Determination Using Spectral Data. *Trans. ASAE*, *31*(6), 1882-1889. doi:10.13031/2013.30952
- Saito, K., Kikuchi, T., Nakayama, M., Mukai, K., & Sumi, H. (2006). A single chlorophyll in each of the core antennas CP43 and CP47 transferring excitation energies to the reaction center in Photosystem II of photosynthesis. *J. Photochem. Photobiol. A*, *178*, 271-280. doi:10.1016/j.jphotochem.2005.10.038
- Saito, K., Rutherford, A. W., & Ishikita, H. (2013). Mechanism of tyrosine D oxidation in Photosystem II. *Proc. Natl. Acad. Sci. U.S.A.*, *110*(19), 7690-7695. doi:10.1073/pnas.1300817110
- Saito, K., Rutherford, A. W., & Ishikita, H. (2015). Energetics of proton release on the first oxidation step in the water-oxidizing enzyme. *Nat. Commun.*, *6*, 1-10. doi:10.1038/ncomms9488
- Sakashita, N., Watanabe, H. C., Ikeda, T., & Ishikita, H. (2017). Structurally conserved channels in cyanobacterial and plant photosystem II. *Photosynth Res*, *133*, 75-85. doi:10.1007/s11120-017-0347-1
- Sakashita, N., Watanabe, H. C., Ikeda, T., Saito, K., & Ishikita, H. (2017). Origins of Water Molecules in the Photosystem II Crystal Structure. *Biochemistry*, *56*, 3049-3057. doi:10.1021/acs.biochem.7b00220
- Sánchez Martínez, D., Martínez-de la Cruz, A., & López Cuéllar, E. (2011). Photocatalytic properties of WO<sub>3</sub> nanoparticles obtained by precipitation in presence of urea as complexing agent. *Appl. Catal. A*, *398*, 179-186. doi:10.1016/j.apcata.2011.03.034
- Santabarbara, S., Neverov, K. V., Garlaschi, F. M., Zucchelli, G., & Jennings, R. C. (2001). Involvement of uncoupled antenna chlorophylls in photoinhibition in thylakoids. *FEBS Lett.*, *491*, 109-113. doi:10.1016/S0014-5793(01)02174-3
- Schatz, G. H., Brock, H., & Holzwarth, A. R. (1987). Picosecond kinetics of fluorescence and absorbance changes in photosystem II particles excited at low photon density. *PNAS*, *88*, 8414-8418. doi:10.1073/pnas.84.23.8414

- Schmid, G. H. (1971). Origin and properties of mutant plants: Yellow tobacco. In *Methods in Enzymology* (Vol. 23, pp. 171-194): Academic Press.
- Schmid, G. H., & Thibault, P. (1979). Evidence for a Rapid Oxygen-Uptake in Tobacco Chloroplasts. *Z. Naturforsch.*, *34c*, 414-418.
- Schmid, V. H. R. (2008). Light-harvesting complexes of vascular plants. *Cell. Mol. Life Sci.*, 3619-3639. doi:10.1007/s00018-008-8333-6
- Schulder, R., Burda, K., Strzałka, K., Bader, K. P., & Schmid, G. H. (1992). Study on the Parameters Affecting Oxygen Release Time Measurements by Amperometry. *Z. Naturforsch.*, *47c*, 465-473. doi:10.1515/znc-1992-0622
- Schuth, N., Zaharieva, I., Chernev, P., Berggren, G., Anderlund, N., Styring, S., . . . Haumann, M. (2018).  $K\alpha$  X-ray Emission Spectroscopy on the Photosynthetic Oxygen-Evolving Complex Supports Manganese Oxidation and Water Binding in the  $S_3$  State. *Inorg. Chem.*, *57*(16), 10424-10430. doi:10.1021/acs.inorgchem.8b01674
- Sclafani, A. P., L., Marci, G., & Venezia, A. M. (1998). Influence of platinum on catalytic activity of polycrystalline  $WO_3$  employed for phenol photodegradation in aqueous suspension. *Sol. Energy Mater Sol. Cells*, *51*, 203-219. doi:10.1016/S0927-0248(97)00215-8
- Seibert, M., Picorel, R., Rubin, A. B., & Connolly, J. S. (1988). Spectral, Photophysical, and Stability Properties of Isolated Photosystem II Reaction Center. *Plant Physiol.*, *87*, 303-306. doi:10.1104/pp.87.2.303
- Service, R. J., Hillier, W., & Debus, R. J. (2010). Evidence from FTIR Difference Spectroscopy of an Extensive Network of Hydrogen Bonds near the Oxygen-Evolving  $Mn_4Ca$  Cluster of Photosystem II Involving D1-Glu65, D2-Glu312, and D1-Glu329. *Biochemistry*, *49*(31), 6655-6669. doi:10.1021/bi100730d
- Shahsavari, A., & Akbari, M. (2018). Potential of solar energy in developing countries for reducing energy-related emissions. *Renew. Sustain. Energy Rev.*, *90*, 275-291. doi:10.1016/j.rser.2018.03.065
- Shevela, D., Kern, J. F., Govindjee, G., & Messinger, J. (2023). Solar energy conversion by photosystem II: principles and structures. *Photosynth. Res.*, *156*, 279-307. doi:10.1007/s11120-022-00991-y
- Shi, W., Guo, X., Cui, C., Jiang, K., Li, Z., Qu, L., & Wang, J.-C. (2019). Controllable synthesis of  $Cu_2O$  decorated  $WO_3$  nanosheets with dominant (0 0 1) facets for photocatalytic  $CO_2$  reduction under visible-light irradiation. *Appl. Catal. B*, *243*, 236-242. doi:10.1016/j.apcatb.2018.09.076
- Shibamoto, T., Kato, Y., Sugiura, M., & Watanabe, T. (2009). Redox potential of the primary plastoquinone electron acceptor Q(A) in photosystem II from *Thermosynechococcus elongatus* determined by spectroelectrochemistry. *Biochemistry*, *48*(45), 10682. doi:10.1021/bi901691j
- Shibata, Y., Nishi, S., Kawakami, K., Shen, J.-R., & Renger, T. (2013). Photosystem II Does Not Possess a Simple Excitation Energy Funnel: Time-Resolved Fluorescence Spectroscopy Meets Theory. *J. Am. Chem. Soc.*, *135*, 6903-6914. doi:10.1021/ja312586p
- Shikanai, T., & Yamamoto, H. (2017). Contribution of Cyclic and Pseudo-cyclic Electron Transport to the Formation of Proton Motive Force in Chloroplasts. *Mol. Plant.*, *10*, 20-29. doi:10.1016/j.molp.2016.08.004
- Shimada, Y., Sugiyama, A., Nagao, R., & Noguchi, T. (2022). Role of D1-Glu65 in Proton Transfer during Photosynthetic Water Oxidation in Photosystem II. *J. Phys. Chem. B*, *126*(41), 8202-8213. doi:10.1021/acs.jpcc.2c05869
- Shimizu, T., Sugiura, M., & Noguchi, T. (2018). Mechanism of Proton-Coupled Electron Transfer in the  $S_0$ -to- $S_1$  Transition of Photosynthetic Water Oxidation As Revealed by Time-

- Resolved Infrared Spectroscopy. *J. Phys. Chem. B*, 122(41), 9460-9470. doi:10.1021/acs.jpcc.8b07455
- Shoji, M., Isobe, H., Miyagawa, K., & Yamaguchi, K. (2019). Possibility of the right-opened Mn-oxo intermediate (R-oxo(4444)) among all nine intermediates in the S<sub>3</sub> state of the oxygen-evolving complex of photosystem II revealed by large-scale QM/MM calculations. *Chem. Phys.*, 518, 81-90. doi:10.1016/j.chemphys.2018.11.003
- Shoji, M., Isobe, H., & Yamaguchi, K. (2015). QM/MM Study of the S<sub>2</sub> to S<sub>3</sub> Transition Reaction in the Oxygen-Evolving Complex of Photosystem II. *Chem. Phys. Lett.*, 636, 172-179. doi:10.1016/j.cplett.2015.07.039
- Shuvalov, V. A., V., K. A., Sharkov, A. V., Kryukov, P. G., & Bacon, K. E. (1979). Picosecond spectroscopy of photosystem I reaction centers. *FEBS Lett.*, 107(2), 313-316. doi:10.1016/0014-5793(79)80397-x
- Siegbahn, K., & Edvarson, K. (1956).  $\beta$ -Ray spectroscopy in the precision range of 1 : 105. *Nuclear Physics*, 1(8), 137-159. doi:10.1016/S0029-5582(56)80022-9
- Siegbahn, P. E. M. (2008). A Structure-Consistent Mechanism for Dioxygen Formation in Photosystem II. *Eur. J. Chem.*, 14(27), 8290-8302. doi:10.1002/chem.200800445
- Siegbahn, P. E. M. (2009). Structures and Energetics for O<sub>2</sub> Formation in Photosystem II. *Acc. Chem. Res.*, 42(12), 1871-1880. doi:10.1021/ar900117k
- Siegbahn, P. E. M. (2013). Substrate Water Exchange for the Oxygen Evolving Complex in PSII in the S<sub>1</sub>, S<sub>2</sub>, and S<sub>3</sub> States. *J. Am. Chem. Soc.*, 135(25), 9442-9449. doi:10.1021/ja401517e
- Siegbahn, P. E. M. (2017). Nucleophilic water attack is not a possible mechanism for O–O bond formation in photosystem II. *Proc. Natl. Acad. Sci.*, 114(19), 4966-4968. doi:10.1073/pnas.1617843114
- Siegbahn, P. E. M. (2018). The S<sub>2</sub> to S<sub>3</sub> transition for water oxidation in PSII (Photosystem II), revisited. *Phys. Chem. Chem. Phys.*, 20, 22926-22931. doi:10.1039/C8CP03720E
- Sioros, G., Koulougliotis, D., Karapanagos, G., & Petrouleas, V. (2007). The S<sub>1</sub>Y<sub>2</sub><sup>\*</sup> Metalloradical EPR Signal of Photosystem II Contains Two Distinct Components That Advance Respectively to the Multiline and g = 4.1 Conformations of S<sub>2</sub>. *Biochemistry*, 46(1), 210-217. doi:10.1021/bi061224i
- Sirohiwal, A., & Pantazis, D. A. (2022). Functional Water Networks in Fully Hydrated Photosystem II. *J. Am. Chem. Soc.*, 144(48), 22035-22050. doi:10.1021/jacs.2c09121
- Sokol, K. P., Ruff, A., Zhang, J. Z., Robinson, W. E., Warnan, J., Kornienko, N., . . . Reisner, E. (2018). Bias-free photoelectrochemical water splitting with photosystem II on a dye-sensitized photoanode wired to hydrogenase. *Nat. Energy*, 3, 944-951. doi:10.1038/s41560-018-0232-y
- Sproviero, E. M., Gascón, J. A., McEvoy, J. P., Brudvig, G. W., & Batista, V. S. (2008). Quantum Mechanics/Molecular Mechanics Study of the Catalytic Cycle of Water Splitting in Photosystem II. *J. Am. Chem. Soc.*, 130, 3428-3442. doi:10.1021/ja076130q
- Staehelein, L. A., & Paolillo, D. J. (2020). A brief history of how microscopic studies led to the elucidation of the 3D architecture and macromolecular organization of higher plant thylakoids. *Photosynth. Res.*, 145(3), 237-258. doi:10.1007/s11120-020-00782-3
- Standfuss, J., & Kühlbrandt, W. (2004). The Three Isoforms of the Light-harvesting Complex II: SPECTROSCOPIC FEATURES, TRIMER FORMATION, AND FUNCTIONAL ROLES. *J. Biol. Chem.*, 279(35), 36884-36891. doi:10.1074/jbc.M402348200
- Stirbet, A., & Govindjee. (2011). On the relation between the Kautsky effect (chlorophyll a fluorescence induction) and Photosystem II: Basics and applications of the OJIP fluorescence transient *J. Photochem. Photobiol.*, 104, 236-257. doi:10.1016/j.jphotobiol.2010.12.010

- Stoichev, S., Krumova, S. B., Andreeva, T., Busto, J. V., Todinova, S., Balashev, K., . . . Taneva, S. G. (2015). Low pH modulates the macroorganization and thermal stability of PSII supercomplexes in grana membranes. *Biophys. J.*, *108*(4), 844-853. doi:10.1016/j.bpj.2014.12.042
- Strzalka, K., Walczak, T., Sarna, T., & Swartz, H. M. (1990). Measurement of Time-Resolved Oxygen Concentration Changes in Photosynthetic Systems by Nitroxide-Based EPR Oximetry. *Arch. Biochem. Biophys.*, *281*(2), 312-318. doi:10.1016/0003-9861(90)90449-9
- Stuchebrukhov, A. A. (2009). Mechanisms of proton transfer in proteins: Localized charge transfer versus delocalized soliton transfer. *Phys. Rev. E*, *79*. doi:10.1103/PhysRevE.79.031927
- Styring, S., & Rutherford, A. W. (1987). In the oxygen-evolving complex of photosystem II the S0 state is oxidized to the S1 state by D<sup>+</sup> (signal IIslow). *Biochemistry*, *26*(9), 2401-2405. doi:10.1021/bi00383a001
- Suga, M., Akita, F., Sugahara, M., Kubo, M., Nakajima, Y., Nakane, T., . . . Shen, J.-R. (2017). Light-induced structural changes and the site of O=O bond formation in PSII caught by XFEL. *Nature*, *543*, 131-135. doi:10.1038/nature21400
- Suga, M., Akita, F., Yamashita, K., Nakajima, Y., Ueno, G., Li, H., . . . Shen, J.-R. (2019). An oxyl/oxo mechanism for oxygen-oxygen coupling in PSII revealed by an x-ray free-electron laser. *Science*, *366*(6463), 334–338. doi:10.1126/science.aax6998
- Suga, M., Shimada, A., Akita, F., Shen, J.-R., Toshi, T., & Sugimoto, H. (2020). Time-resolved studies of metalloproteins using X-ray free electron laser radiation at SACLA. *Biochim. Biophys. Acta*, *1864*(2), 129466. doi:10.1016/j.bbagen.2019.129466
- Sugiura, M., Tibiletti, T., Takachi, I., Hara, Y., Kanawaku, S., Sellés, J., & Boussac, A. (2018). Probing the role of Valine 185 of the D1 protein in the Photosystem II oxygen evolution. *Biochim. Biophys. Acta Bioenerg.*, *1859*(12), 1259-1273. doi:10.1016/j.bbabi.2018.10.003
- Sumathi, M., Prakasam, A., & Anbarasan, P. M. (2019). High capable visible light driven photocatalytic activity of WO<sub>3</sub>/g-C<sub>3</sub>N<sub>4</sub> heterostructure catalysts synthesized by a novel one step microwave irradiation route. *J. Mater. Sci.: Mater. Electron.*, *30*, 3294–3304. doi:10.1007/s10854-018-00602-4
- Suzuki, H., Sugiura, M., & Noguchi, T. (2009). Monitoring Water Reactions during the S-State Cycle of the Photosynthetic Water-Oxidizing Center: Detection of the DOD Bending Vibrations by Means of Fourier Transform Infrared Spectroscopy. *Biochemistry*, *47*(42), 11024-11030. doi:10.1021/bi801580e
- Sznee, K., Dekker, J. P., Dame, R. T., van Roon, H., Wuite, G. J. L., & Frese, R. N. (2011). Jumping Mode Atomic Force Microscopy on Grana Membranes from Spinach. *J. Biol. Chem.*, *286*(45), 39164-39171. doi:10.1074/jbc.M111.284844
- Tachibana, Y., Vayssieres, L., & Durrant, J. R. (2012). Artificial photosynthesis for solar water-splitting. *Nat. Photonics*, *6*, 511-518. doi:10.1038/NPHOTON.2012.175
- Taguchi, S., Shen, L., Han, G., Umena, Y., Shen, J.-R., Noguchi, T., & Mino, H. (2020). Formation of the High-Spin S2 State Related to the Extrinsic Proteins in the Oxygen Evolving Complex of Photosystem II. *J. Phys. Chem. Lett.*, *11*(20), 8908-8913. doi:10.1021/acs.jpcllett.0c02411
- Tahara, K., Mohamed, A., Kawahara, K., Nagao, R., Kato, Y., Fukumura, H., . . . Noguchi, T. (2017). Fluorescence property of photosystem II protein complexes bound to a gold nanoparticle. *Faraday Discuss.*, *198*, 121-134. doi:10.1039/C6FD00188B

- Takaoka, T., Sakashita, N., Saito, K., & Ishikita, H. (2016). pK<sub>a</sub> of a Proton-Conducting Water Chain in Photosystem II. *J. Phys. Chem. Lett.*, *7*, 1925-1932. doi:10.1021/acs.jpcclett.6b00656
- Takemoto, H., Sugiura, M., & Noguchi, T. (2019). Proton Release Process during the S<sub>2</sub>-to-S<sub>3</sub> Transition of Photosynthetic Water Oxidation As Revealed by the pH Dependence of Kinetics Monitored by Time-Resolved Infrared Spectroscopy. *Biochemistry*, *58*(42), 4276-4283. doi:10.1021/acs.biochem.9b00680
- Tanaka, A., Fukushima, Y., & Kamiya, N. (2017). Two different structures of the oxygen-evolving complex in the same polypeptide frameworks of photosystem II. *J. Am. Chem. Soc.*, *139*(5), 1718-1721. doi:10.1021/jacs.6b09666
- Tang, X. S., Moussavi, M., & Dismukes, G. C. (1991). Monitoring oxygen concentration in solution by ESR oximetry using lithium phthalocyanine: application to photosynthesis. *J. Am. Chem. Soc.*, *113*(15), 5914-5915. doi:10.1021/ja00015a085
- Tanisaki, S. (1960). Crystal Structure of Monoclinic Tungsten Trioxide at Room Temperature. *J. Phys. Soc. Jpn.*, *15*, 573-581. doi:10.1143/JPSJ.15.573
- Terasaki, N., Iwai, M., Yamamoto, N., Hiraga, T., S., Y., & Inoue, Y. (2008). Photocurrent generation properties of Histag-photosystem II immobilized on nanostructured gold electrode. *Thin Solid Films* *516*(9), 2553-2557.
- Thanh Truc, N. T., Giang Bach, L., Thi Hanh, N., Pham, T.-D., Thi Phuong Le Chie, N., Tran, D. T., . . . Nguyen, V. N. (2019). The superior photocatalytic activity of Nb doped TiO<sub>2</sub>/g-C<sub>3</sub>N<sub>4</sub> direct Z-scheme system for efficient conversion of CO<sub>2</sub> into valuable fuels. *J. Colloid Interface Sci.*, *540*, 1-8. doi:10.1016/j.jcis.2019.01.005
- Thibault, P. (1978). A new attempt to study the oxygen evolving system of photosynthesis: Determination of transition probabilities of a state i. *J. Theor. Biol.*, *73*(2), 271-284. doi:10.1016/0022-5193(78)90190-X
- Tian, W., Zhang, H., Sibbons, J., Sun, H., Wang, H., & Wang, S. (2021). Photoelectrochemical Water Oxidation and Longevous Photoelectric Conversion by a Photosystem II Electrode. *Adv. Energy Mater.*, *11*(30). doi:10.1002/aenm.202100911
- Tomita, M., Ifuku, K., Sato, F., & Noguchi, T. (2009). FTIR evidence that the PsbP extrinsic protein induces protein conformational changes around the oxygen-evolving Mn cluster in photosystem II. *Biochemistry*, *48*(27), 6318-6325. doi:10.1021/bi9006308
- Trtilek, M., Kramer, D. M., Koblizek, M., & Nedbal, L. (1997). Dual-modulation LED kinetic fluorometer. *J. Lumin.*, *72-74*, 597-599. doi:10.1016/S0022-2313(97)00066-5
- Ugur, I., Rutherford, A. W., & Kaila, V. R. I. (2016). Redox-coupled substrate water reorganization in the active site of Photosystem II—The role of calcium in substrate water delivery. *Biochim. Biophys. Acta*, *1857*(6), 740-748. doi:10.1016/j.bbabi.2016.01.015
- Umena, Y., Kawakami, K., Shen, J.-R., & Kamiya, N. (2011). Crystal structure of oxygen-evolving photosystem II at a resolution of 1.9 Å. *Nature*, *473*, 55-61. doi:10.1038/nature09913
- Utschig, L. M., Dimitrijevic, N. M., Poluektov, O. G., Chemerisov, S. C., Mulfort, K. L., & Tiede, D. M. (2011). Photocatalytic Hydrogen Production from Noncovalent Biohybrid Photosystem I/Pt Nanoparticle Complexes. *J. Phys. Chem. Lett.*, *2*, 236-241. doi:10.1021/jz101728v
- van Bezouwen, L. S., Caffarri, S., Kale, R. S., Kouřil, R., Thunnissen, A.-M. W. H., Oostergetel, G. T., & Boekema, E. J. (2017). Subunit and chlorophyll organization of the plant photosystem II supercomplex. *Nat. Plants*, *3*, 17080. doi:10.1038/nplants.2017.80
- van Gorkom, H. J., Pulles, M. P. J., & Étienne, A.-L. (1978). Fluorescence and absorbance changes in Tris-washed chloroplasts. In H. Metzner (Ed.), *Photosynthetic Oxygen evolution* (pp. 135-145). London, UK: Academic Press.

- van Vliet, P., & Rutherford, A. W. (1996). Properties of the chloride-depleted oxygen-evolving complex of photosystem II studied by electron paramagnetic resonance. *Biochemistry*, 35(6), 1829-1839. doi:10.1021/bi9514471
- Vass, I., Ono, T., & Inoue, Y. (1987). Removal of 33 kDa extrinsic protein specifically stabilizes the S<sub>2</sub>Q<sub>A</sub><sup>-</sup> charge pair in photosystem II. *FEBS Lett.*, 211(2), 215-220. doi:10.1016/0014-5793(87)81439-4
- Vass, I., & Styring, S. (1991). pH-dependent charge equilibria between tyrosine-D and the S states in photosystem II. Estimation of relative midpoint redox potentials. *Biochemistry*, 30(3), 830-839. doi:10.1021/bi00217a037
- Vassiliev, S., Zaraiskaya, T., & Bruce, D. (2012). Exploring the energetics of water permeation in photosystem II by multiple steered molecular dynamics simulations. *Biochim. Biophys. Acta*, 1817, 1671-1678. doi:10.1016/j.bbabi.2012.05.016
- Vassiliev, S., Zaraiskaya, T., & Bruce, D. (2013). Molecular dynamics simulations reveal highly permeable oxygen exit channels shared with water uptake channels in photosystem II. *Biochim. Biophys. Acta*, 1827, 1148-1155. doi:10.1016/j.bbabi.2013.06.008
- Vermaas, W. F. J., Renger, G., & Dohnt, G. (1984). The reduction of the oxygen-evolving system in chloroplasts by thylakoid components. *Biochim. Biophys. Acta*, 764, 192-202. doi:10.1016/0005-2728(84)90028-8
- Vernotte, C., Etienne, A. L., & Briantais, J.-M. (1979). Quenching of the System II chlorophyll fluorescence by the plastoquinone pool. *Biochim. Biophys. Acta*, 545(3), 519-527. doi:10.1016/0005-2728(79)90160-9
- Vinyard, D. J., Ananyev, G. M., & Dismukes, G. C. (2013). Photosystem II: The Reaction Center of Oxygenic Photosynthesis. *Annu. Rev. Biochem.*, 82, 577-606. doi:10.1146/annurev-biochem-070511-100425
- Vinyard, D. J., Khan, S., & Brudvig, G. W. (2015). Photosynthetic water oxidation: binding and activation of substrate waters for O–O bond formation. *Faraday Discuss.*, 185, 37-50. doi:10.1039/c5fd00087d
- Vittadello, M., Gorbunov, M. G., Mastrogiovanni, D. T., Wielunski, L. S., Garfunkel, E. L., Guerrero, F., . . . Falkowski, P. G. (2010). Photoelectron Generation by Photosystem II Core Complexes Tethered to Gold Surfaces. *ChemSusChem*, 3, 471 -475. doi:10.1002/cssc.200900255
- Vogt, L., Vinyard, D. J., Khan, S., & Brudvig, G. W. (2015). Oxygen-evolving complex of Photosystem II: an analysis of second-shell residues and hydrogen-bonding networks. *Curr Opin Chem Biol*, 25, 152-158. doi:10.1016/j.cbpa.2014.12.040
- Voloshin, R. A., Shumilova, S. M., Zadneprovskaya, E. V., Zharmukhamedov, S. K., Alwasel, S., Hou, H. J. M., & Allakhverdiev, S. I. (2022). Photosystem II in bio-photovoltaic devices. *Photosynthetica*, 60(1), 121-135. doi:10.32615/ps.2022.010
- Walkowiak B., & V., K. (2002). Elektroforeza. Przykłady zastosowań. *Amersham Biosciences*.
- Wang, C.-K., Lin, C.-K., Wu, C.-L., Brahma, S., Wang, S.-C., & Huang, J.-L. (2013). Characterization of electrochromic tungsten oxide film from electrochemical anodized RF-sputtered tungsten films. *Ceram. Int.*, 39(4), 4293-4298. doi:10.1016/j.ceramint.2012.11.010
- Wang, J., Askerka, M., Brudvig, G. W., & Batista, V. S. (2017). Crystallographic Data Support the Carousel Mechanism of Water Supply to the Oxygen-Evolving Complex of Photosystem II. *ACS Energy Lett.*, 2(10), 2299-2306. doi:10.1021/acseenergylett.7b00750
- Wang, W., Wang, H., Zhu, Q., Qin, W., Han, G., Shen, J.-R., . . . Li, C. (2016). Spatially Separated Photosystem II and a Silicon Photoelectrochemical Cell for Overall Water Splitting: A Natural–Artificial Photosynthetic Hybrid. *Angew. Chem. Int. Ed.*, 55, 1-6. doi:10.1002/anie.201604091

- Wang, W., Wang, Z., Zhu, Q., Han, G., Ding, C., Chen, J., . . . Li, C. (2015). Direct electron transfer from photosystem II to hematite in a hybrid photoelectrochemical cell. *Chem. Commun.*, *51*(95), 16952-16955. doi:10.1039/C5CC06900A
- Wang, Y., Chen, D., Hu, Y., Qin, L., Liang, J., Sun, X., & Huang, Y. (2020). An artificially constructed direct Z-scheme heterojunction: WO<sub>3</sub> nanoparticle decorated ZnIn<sub>2</sub>S<sub>4</sub> for efficient photocatalytic hydrogen production. *Sustain. Energy Fuels*, *4*, 1681-1692. doi:10.1039/C9SE01158G
- Wang, Z. G., Xu, T. H., Liu, C., & Yang, C. H. (2010). Fast isolation of highly active photosystem II core complexes from spinach. *J. Integr. Plant Biol.*, *52*(9), 793-800. doi:10.1111/j.1744-7909.2010.00971.x
- Washizu, E., Yamamoto, A., Abe, Y., Kawamura, M., & Sasaki, K. (2003). Optical and electrochromic properties of RF reactively sputtered WO<sub>3</sub> films. *Solid State Ion.*, *165*, 175-180. doi:10.1016/j.ssi.2003.08.030
- Wasilewski, M. R. (2009). Self-Assembly Strategies for Integrating Light Harvesting and Charge Separation in Artificial Photosynthetic Systems. *Acc. Chem. Res.*, *42*(12), 1910-1921. doi:10.1021/ar9001735
- Wei, X., Su, X., Cao, P., Liu, X., Chang, W., Li, M., . . . Liu, Z. (2016). Structure of spinach photosystem II-LHCII supercomplex at 3.2 Å resolution. *Nature*, *534*, 69-74. doi:10.1038/nature18020
- Weiss, W., & Renger, G. (1984). UV-spectral characterization in Tris-washed chloroplasts of the redox component D1 which functionally connects the reaction center with the water-oxidizing enzyme system Y in photosynthesis. *FEBS*, *169*(2), 219-223. doi:10.1016/0014-5793(84)80322-1
- Wietrzynski, W., Schaffer, M., Tegenov, D., Albert, S., Kanazawa, A., Plitzko, J. M., . . . Engel, B. D. (2020). Charting the native architecture of Chlamydomonas thylakoid membranes with single-molecule precision. *eLife*, *9*, e53740. doi:10.7554/eLife.53740
- Wincencjusz, H., van Gorkom, H. J., & Yocum, C. F. (1997). The photosynthetic oxygen evolving complex requires chloride for its redox state S<sub>2</sub>-->S<sub>3</sub> and S<sub>3</sub>-->S<sub>0</sub> transitions but not for S<sub>0</sub>-->S<sub>1</sub> or S<sub>1</sub>-->S<sub>2</sub> transitions. *Biochemistry*, *36*(12), 3663-3670. doi:10.1021/bi9626719
- Wraight, C. A. (2004). Proton and electron transfer in the acceptor quinone complex of photosynthetic reaction centers from Rhodospirillum rubrum. *Front Biosci.*, *1*(9), 303-337. doi:10.2741/1236
- Wydrzynski, T., Hillier, W., & Messinger, J. (1996). On the functional significance of substrate accessibility in the photosynthetic water oxidation mechanism. *Physiologia Plantarum*, *96*(2), 342-350. doi:10.1111/j.1399-3054.1996.tb00224.x
- Xu, X., Wang, Z., Qiao, W., Luo, F., Hu, J., Wang, D., & Zhou, Y. (2021). Refined Z-scheme charge transfer in facet-selective BiVO<sub>4</sub>/Au/CdS heterostructure for solar overall water splitting. *Int. J. Hydrog. Energy*, *46*(12), 8531-8538. doi:10.1016/j.ijhydene.2020.12.047
- Xu, Y., Li, A., Yao, T., Ma, C., Zhang, X., Shah, J. H., & Han, H. (2017). Strategies for Efficient Charge Separation and Transfer in Artificial Photosynthesis of Solar Fuels. *ChemSusChem*, *10*, 4277-4305. doi:10.1002/cssc.201701598
- Yamaguchi, K., Shoji, M., Isobe, H., Kawakami, T., Miyagawa, K., Suga, M., . . . Shen, J.-R. (2022). Geometric, electronic and spin structures of the CaMn<sub>4</sub>O<sub>5</sub> catalyst for water oxidation in oxygen-evolving photosystem II. Interplay between experiments and theoretical computations. *Coord. Chem. Rev.*, *471*(15). doi:10.1016/j.ccr.2022.214742
- Yamamoto, Y., Kai, S., Ohnishi, A., Tsumura, N., Ishikawa, T., Hori, H., . . . Ishikawa, Y. (2014). Quality Control of PSII: Behavior of PSII in the Highly Crowded Grana Thylakoids Under Excessive Light. *Plant Cell Physiol.*, *55*(7), 1206-1215. doi:10.1093/pcp/pcu043

- Yamauchi, T., Mino, H., Matsukawa, T., Kawamori, A., & Ono, T.-A. (1997). Parallel polarization electron paramagnetic resonance studies of the S<sub>1</sub>-state manganese cluster in the photosynthetic oxygen-evolving system. *Biochemistry*, *36*(24), 7520-7526. doi:10.1021/bi962791g
- Yang, K. R., Lakshmi, K. V., Brudvig, G. W., & Batista, V. S. (2021). Is Deprotonation of the Oxygen-Evolving Complex of Photosystem II during the S<sub>1</sub> → S<sub>2</sub> Transition Suppressed by Proton Quantum Delocalization? *J. Am. Chem. Soc.*, *143*, 8324-8332. doi:10.1021/jacs.1c00633
- Yano, J., & Yachandra, V. (2014). Mn<sub>4</sub>Ca Cluster in Photosynthesis: Where and How Water is Oxidized to Dioxygen. *Chem. Rev.*, *114*(8), 4175-4205. doi:10.1021/cr4004874
- Yehezkeili, O., Tel-Vered, R., Wasserman, J., Trifonov, A., Michaeli, D., Nechushtai, R., & Willner, I. (2012). Integrated photosystem II-based photo-bioelectrochemical cells. *Nat. Commun.*, *3*. doi:10.1038/ncomms1741
- Yehezkeili, O., Willner, I., Tel-Vered, R., Michaeli, D., & Nechushtai, R. (2014). Photosynthetic reaction center-functionalized electrodes for photo-bioelectrochemical cells. *Photosynth. Res.*, *120*, 71-85. doi:10.1007/s11120-013-9796-3
- Zahariou, G., Ioannidis, N., Sanakis, Y., & Pantazis, D. A. (2021). Arrested Substrate Binding Resolves Catalytic Intermediates in Higher-Plant Water Oxidation. *Angew. Chem. Int. Ed.*, *60*, 3156-3162. doi:doi.org/10.1002/anie.202012304
- Zamaraev, K. I., & Parmon, V. N. (1980). Potential Methods and Perspectives of Solar Energy Conversion via Photocatalytic Processes. *Catal. Rev. Sci. Eng.*, *22*(2), 261-324. doi:10.1080/03602458008066536
- Zeradjanin, A. R., Masa, J., Spanos, I., & Schlögl, R. (2021). Activity and Stability of Oxides During Oxygen Evolution Reaction - From Mechanistic Controversies Toward Relevant Electrocatalytic Descriptors. *Front. Energy Res.*, *8*. doi:10.3389/fenrg.2020.613092
- Zhang, B., & Sun, L. (2018). Why nature chose the Mn<sub>4</sub>CaO<sub>5</sub> cluster as water-splitting catalyst in photosystem II: a new hypothesis for the mechanism of O–O bond formation. *Dalton Trans.*, *47*, 14381-14387. doi:10.1039/c8dt01931b
- Zhang, J. Z., & Reisner, E. (2020). Advancing photosystem II photoelectrochemistry for semi-artificial photosynthesis. *Nat. Rev. Chem.*, *4*, 6-21. doi:10.1038/s41570-019-0149-4
- Zhang, L., Tang, X., Lu, Z., Wang, Z., Li, L., & Xiao, Y. (2011). Facile synthesis and photocatalytic activity of hierarchical WO<sub>3</sub> core-shell microspheres. *258*, 1719-1724. doi:10.1016/j.apsusc.2011.10.022
- Zhao, D., Wang, Y., Dong, C.-L., Huang, Y.-C., Shen, S., & Guo, L. (2021). Boron-doped nitrogen-deficient carbon nitride-based Z-scheme heterostructures for photocatalytic overall water splitting. *Nat. Energy*, *6*, 388-397. doi:10.1038/s41560-021-00795-9
- Zheng, H., Zhen Ou, J., Strano, M. S., Kaner, R. B., Mitchell, A., & Kalantar-zadeh, K. (2011). Nanostructured Tungsten Oxide – Properties, Synthesis, and Applications *Adv. Funct. Mater.*, *21*, 2175–2196. doi:10.1002/adfm.201002477
- Zimmermann, J. L., & Rutherford, A. W. (1984). EPR studies of the oxygen-evolving enzyme of Photosystem II. *Biochim. Biophys. Acta*, *767*(1), 160-167. doi:10.1016/0005-2728(84)90091-4
- Zimmermann, J. L., & Rutherford, A. W. (1985). The O<sub>2</sub>-evolving of photosystem II. Recent advances. *Physiol. Veg.*, *23*, 425-434.
- Zimmermann, J. L., & Rutherford, A. W. (1986). Electron paramagnetic resonance properties of the S<sub>2</sub> state of the oxygen-evolving complex of photosystem II. *Biochemistry*, *25*(16), 4609-4615. doi:10.1021/bi00364a023